Fast frequency control in low inertia electrical power systems using doubly fed induction generator

A thesis submitted to the University of Manchester for the degree of

Doctor of Philosophy

in the Faculty of Science and Engineering

2020

Yi Cheng

School of Electrical and Electronic Engineering

List of Contents

Word Count: 40,030

List of Figures

List of Tables

Nomenclature

List of Symbols

A	Blade-swept area
$C_p(\lambda, \beta)$	Power coefficient
$C_{P,Betz}$	Betz power coefficient
$C_{P,de}$	Deloading power coefficient
D_s	Mutual damping coefficient
D_r	Damping coefficient of lumped shaft model
D_t	Damping coefficient of turbine rotor
D	Damping coefficient of generator rotor
D_{shaft}	Total shaft damping coefficient
d	Deloading factor
E_k	Kinetic energy
$\underline{E}_s, \underline{E}'_{rs}$	Induced emf in the stator and rotor
f_i	frequency at which the *i*th stage is accomplished
f_{COI}	COI frequency
$f_{COI,RoCoF}$	COI RoCoF
G_{re}	Remaining generation left in the system
$H_{i,sys}$	Inertia constant of i^{th} synchronous machine
H_{in}	Synthetic inertia constant
H_{sys}	Total system inertia

H_{APE}	Inertia constant of actual penetration level
H_{PPE}	Inertia constant of presumed penetration level
$\underline{I}_s, \underline{I}_r^{'}$	Induced stator and rotor current
i_{dr_ref}	Reference d-axis rotor current
i_{qr_ref}	Reference q-axis rotor current
J	Moment of inertia
J_r	Total inertia of the lumped shaft model
J_T	Turbine rotor inertia
J_G	Generator rotor inertia
K_s	Mutual stiffness coefficient
K_{in}	Inertia constant
K_{shaft}	Total shaft stiffness
k_{adap}	Adaptive gain
L	Excess load factor
$L_{\max}$	largest possible generation loss
$L_{\sigma r}$	Rotor leakage inductance referred to the stator
L_m	Magnetizing inductance of the machine
M	Generation margin of wind turbines
N_s, N_r	Stator and rotor winding's number of turns per phase
P_{boost}	Reserved generation of deloaded wind turbine
P_m	Mechanical power
P_e	Electrical power

P_{extra}	Extra power
P_{MPPT}	MPPT power
P_{del}	Deloading power
P_{droop}	Temporary droop power
P_{in}	Synthetic inertia active power
P_{rec}	Restoration power of rotor speed
$\frac{1}{R}$	Droop coefficient
R	Droop parameter
$R(df/dt)$	Dynamic droop parameter
R_{blade}	Blade length
$R_s, R_r^{'}$	Stator and rotor resistance
T_1	Over-production period
T_2	Rotor speed recovery period
T_a	Driving torque
T_e	Electromagnetic torque of the generator
T_m	Mechanical torque
T_s	Reaction torque from the low-speed shaft
t_{dis}	Disturbance start time
t_{ter}	Termination time of synthetic inertia control
t_{re}	Restoration time of rotor speed
th_i	frequency threshold at which the *i*th stage is accomplished
$\underline{V}_s, \underline{V}_r^{'}$	Supplied stator and rotor voltage

$X_{\sigma s}, X'_{\sigma s}$	Stator and rotor leakage impedance
δ	Angular position of rotor angle
θ	Angular position of rotor
θ_s	Torsional twist between turbine and generator rotor
$d\beta^*$	Reference rate of change of pitch angle
β	Pitch angle
ρ	Air density
v_w	Wind speed
λ	Tip-speed ratio
λ_{del}	Tip-speed ratio at the deloading level
ω	Base value of angular speed
ω^*	Optimum rotor speed
ω_r	Rotor speed
ω_T	Turbine rotor speed
ω_G	Generator rotor speed
$\omega_{\max}$	Maximum rotor speed following MPPT curve
ω_{de}	Rotor speed at the deloading level
Δt	Maximum time delay
Δf	Frequency safety margin

Acronyms

AGC	Automatic generation control
APE	Actual penetration level
APR	Active power reserve

ASG	Asynchronous generator
AVR	Automatic voltage regulator
COI	Centre of inertia
DFIG	Doubly fed induction generator
DPL	DIgSILENT programming language
DSL	DIgSILENT simulation language
FN	Frequency nadir
FRCG	Fully rated converter generator
GSC	Grid-side converter
HVDC	High voltage direct current
IES	Integrated energy system
KE	Kinetic energy
LSA	Load shedding amount
OOS	Out-of-step
PE	Power electronic
PPE	Presumed penetration level
PWM	Pulse-width modulation
RES	Renewable energy source
RSC	Rotor side converter
SCADA	Supervisory control and data acquisition
SFD	Secondary frequency dip
SIPS	Protection integrity protection scheme
SSR	Subsynchronous resonance
TSR	Tip-speed ratio
UFLS	Underfrequency load shedding

UVLS	Undervoltage load shedding
VSC	Voltage source converter
VSWT	Variable speed wind turbine
WPP	Wind power plant
WT	Wind turbine
WTG	Wind turbine generator

Abstract

Fast frequency control in low inertia electrical power systems using doubly fed induction generators

Mr Yi Cheng, The University of Manchester, September 2020.

Increased penetration of renewable energy sources in modern electrical power systems is contributing to a reduction in carbon emissions, thereby reducing the level of air pollution, climate change and finally supporting the quality of life on the Earth. In this context, energy conversion systems realised using wind turbine generators have been and are still the focus of extensive research on different system aspects, from planning, exploitation, monitoring, control and protection perspectives. However, connecting modern wind turbine generators to the main grid over converters can cause a number of consequences. One of them is reduction of system inertia. The reduction of system inertia imposes serious technical challenges in preserving system frequency stability. As it is known, inertia is one of the key factors determining the robustness of power systems against sudden active power imbalances caused by different types of frequency events. A reduction in synchronous power reserves further intensifies this problem by reducing the system ability to maintain the frequency within a permissible range following frequency events. Considering the effects of the integration of WECSs, enhancing the frequency support capability of wind turbines by emulating the behaviour of synchronous generators to some extent and participating in (fast) frequency control is needed.

Wind turbines usually operate at the maximum power point tracking curve, and their active power can be temporarily increased by using synthetic inertia control for supporting system frequency. However, the support period cannot last long because the rotor speed of wind turbine will decrease to its minimum, which tiggers the rotor protection. In this context, the output of wind turbines reduces. Hence, another imbalance between generation and consumption occurs leading a secondary frequency dip. Sometimes, the magnitude of secondary frequency dip is even lower than the first

frequency nadir caused by a frequency event. Motivated by solving the problem, this thesis is investigated from the perspectives of enhancing the power system frequency stability, improving the magnitude of secondary frequency dips, maintaining the DFIGs stable operation and increasing the annual profit of wind farms.

Two novel controls are discussed at wind turbine level and wind farm level, respectively. The first control presented in this thesis is to design a novel frequency control for wind turbines that provides fast frequency support. A novel frequency control called dynamic-droop based control is proposed, which utilise as much as possible the available energy from wind turbines in a wind farm and at the same time to provide a smart, fast and reliable primary frequency response without imposing adverse impacts on the power system. The mitigation of secondary frequency dip can be achieved by employing a droop control based on the information of rate of change of frequency. In this way, the magnitude of power reduction brough by the termination of temporary energy reserves can be reduced, which results in a smaller secondary frequency dip and a more gradual power transition.

Secondly, another novel frequency control scheme that consecutively utilises wind turbines working under various operating conditions is proposed. This control is proposed based on employing temporary and persistent energy reserve-based approaches, which enhances the frequency response in power systems with high penetration of converter interfaced generation. Also, it improves the frequency nadir, mitigates the secondary frequency dip, and prevent power systems from frequency collapse. In addition, this novel control also satisfies the anticipation of system operators based on functionality and economical requirements.

In first two chapters, the introduction and a summary of power system stability are presented, which identifies the research direction of this thesis. In the chapter three and four, the created wind turbine models are depicted, and existing controls of wind turbines used for fast frequency support are reviewed. The synthetic inertia control is accessed in the chapter five. Also, this chapter presents and discusses the performance of proposed dynamic-droop based control of wind turbines. In chapter six, a consecutive power dispatch in wind farms is proposed and evaluated. Then, the work relating to the underfrequency load shedding scheme is presented. The last but not the

least, chapter eight summarises the research presented in this thesis, its contribution, and some potential research areas for further development of this research.

Declaration

No portion of the work referred to in the thesis has been submitted in support of an application for another degree or qualification of this or any other university or any other institute of learning.

Copyright Statement

Acknowledgements

I would like to express my sincere gratitude to my supervisor Prof Vladimir Terzija for his guidance I received from him during my PhD research and thank him for funding my PhD project. He provided me a great opportunity to explore one of the most interesting area in the power system. Without his endless support, constant supervision as well as professional advice, this PhD could not have been accomplished.

My sincere thanks also go to my colleagues and friends at The University of Manchester. Especially to Dr Sadegh Azizi who helped me having a smooth beginning of my Ph. D research and Dr. Rasoul Azizipanah-Abarghooee who provided me productive suggestions during this project. Also, Dr. Mingyu Sun and Dr. Gaoyuan Liu had great contribution to my tactical skills. Also, I will never forget the interesting discussions, collaborations, and joy time I had with others in Manchester.

Particular thanks are to Prof Lei Ding, Shandong University, Jinan, China, who has been permanently supporting my research progress.

Last but not the least, I would like to express my thankfulness to my parents for their spiritual and financial support during this research. I would also like to thank to my wife, Yuyuan. It is their understanding and unconditional love that encourage me through the whole process of pursuing this degree.

To my Family

Chapter 1 Introduction

This chapter presents objectives, background and motivation, specific goals, methodology and contributions of this research. The principal objectives of the research are described in Section 1.1, the main background and motivation in Section 1.2, the primary goals in Section 1.3, the methodology in Section 1.4, a summary of the contributions made by this research in Section 1.5 and the content of the following chapters summarised in Section 1.6.

1.1. Research objectives

The objective of this research was to develop a frequency control approach suitable for WECSs and capable of providing faster frequency response. Another objective was to design an efficient UFLS scheme that copes with potential frequency instability issues associated with integrated wind power systems. The key aspect of the deployment of frequency control was to demonstrate the frequency response capability of a WECSs to mitigate the adverse impacts associated with the reduction of power system inertia. In addition, the design of the UFLS had to be capable of protecting the entire power system from minimizing the level of disconnection of loads.

1.1.1. Demonstration of the frequency response capability of a WECS

The system frequency response will be affected by the frequency control capability of WECSs. Before examining this, the impact of different synchronous generator parameters, such as inertia constant, damping factor, active power reserve and governor response on the system response, will be discussed because the key issue of replacing synchronous generation with WECSs reduces frequency stability. Naturally, wind turbines do not contribute to system inertia because the wind turbine rotor is electrically-decoupled from system frequency. In addition, wind turbines normally

operate at MPPT mode, which does not have any spinning reserves. Therefore, wind turbines are required to mimic the behaviour of synchronous generators to provide frequency support in case of experiencing unexpected frequency events. During the over-production stage, the incremental active power output of wind turbines are carried out. Moreover, the governing parameters of synchronous generators will be modified accordingly. During the under-production or rotor speed recovery stage, how to control the power of wind turbines and the synchronous generator to facilitate rotor speed recovery is an essential issue. This can be achieved by adding various supplementary control loops. The potential capability of wind turbines in terms of speed and time are and will be evaluated and demonstrated using frequency deviation and/or a RoCoF-based controlled loop. The synthetic inertia control will be accessed to measure the capability of DFIG-based wind turbines to provide frequency support. On the other hand, the overspeed-based deloading control will be evaluated to test the wind turbine ability of supporting system frequency. Consequently, a novel frequency control should be able to compromise disadvantages of other controls. The intent of this research is to coordinate the available energy captured by WECS to mitigate the occurrence of the SFD and to retain wind farm profitability.

1.1.2. Designing UFLS relay

Frequency stability of a power system should be accessed from both the generation and load sides perspective. Therefore, designing a suitable UFLS scheme will help to effectively protect transmission lines and transformers from thermal overloading. After a disturbance occurs within the system, the frequency excursion causes continuous frequency swings, resulting in tripping of the generation or load. As the penetration level of RESs increases, system frequency is easily prone to drop outside of the permissible range due to the reduction in system inertia. A specific focus is placed on the largest possible generation loss and presumed penetration level of the system, which is valuable for conducting the frequency thresholds at each step of UFLS. Also, the implantation of the protection scheme requires fast action when sensing frequency excursion. Thereby, existing concerns about communication delay or trip delays also need to be included.

1.2. Background and motivations

Electric power systems, considered as one of the key subsystems belonging to large scale integrated energy systems (IESs), have been rapidly developing over the last few decades. Integration of RESs has often been at the top of the agenda of this development [1]. Electrical energy has been mainly generated from primary energy sources, such as coal, oil, water or natural gas. Nonetheless, traditional fossil fuel-fired power plants cause air pollution and carbon dioxide emissions when generating electricity [2]. In order to meet the requirements of the Paris Agreement on a 40% greenhouse gas emissions reduction by 2030 [3], many countries are today replacing their conventional generators with RESs. For example, more than 40% of electricity is expected to originate from RESs in Spain by 2020 [4]. In 2017, China installed 19.7 GW wind capacity, which is 37% of the total world's installed wind capacity [5]. In 2017, Danish government had already achieved 44% electricity production from wind energy [6]. In the third quarter of 2019, some 40% of the entire UK electricity generation originated from RESs, which was more than the electricity generated by conventional plants [7]

With permanently increasing wind energy penetration, the conventional operation, control and protection paradigms employed for the secure operation of the power system are becoming increasingly inappropriate. This is due to the different dynamic characteristics caused by RESs, such as wind turbines [8]. This is adversely impacting the performance of the approaches traditionally used for the design, operation and control of energy production, transmission and distribution. To this end, a large volume of ongoing research being focused on aspects and prospects associated with transition towards 100% renewable-based energy vectors in general, and electrical energy in particular, is well justified as a timely response to these fundamental system changes [9]–[12].

The main motivation of the most research activities is to contribute to improved approaches that ensure system frequency stability [13]. Frequency stability is the ability of power networks to maintain the frequency within statutory limits and to keep balancing power generation and consumption following a frequency event. However, the increased penetration of RESs is negatively affecting system stability. For this reason, to reduce the risk of potential cascading events and catastrophic blackouts,

electricity system operators define a maximum permissible level for instantaneously operating renewable generation. For instance, the permissible renewable penetration level in Ireland is 55% of the total energy generation [14]. Strengthening the transmission system in Ireland is thought of as a viable solution to overcoming this problem to help achieve higher decarbonisation targets [4][15].

Synchronous generators contribute to the compensation of power imbalances by releasing or absorbing their kinetic energy following an imbalance. Since their rotor is decoupled from the grid side frequency variation, WECSs do not inherently exhibit the inertial response like that in synchronous generators. Therefore, the power system cannot expect any instantaneous extra active power contribution from WECSs. Therefore, the increased penetration of RESs and the displacement of conventional generating units decrease the total system inertia and active power reserves. This decreases the power system's ability to adequately respond to frequency events, e.g. generation outages. This is why the RoCoF is much higher in modern power systems with reduced system inertia when compared to those of conventional power systems dominated by synchronous generators [16]. Therefore, in low inertia systems, the frequency nadir is more likely to fall outside of statutory limits following contingencies of the same size. To guarantee a more secure operating system, as well as to weaken the impacts caused by integrating wind power, wind turbine control loops have to be adapted to the needs of the system. Thus, by providing inertial control similar to what conventional generators provide during contingencies is necessary to ensure stable system operation in a high penetration of PEs generation [17].

Secondly, the inertia in modern power systems will not always only be reduced and may vary depending on the share of renewable generation from the whole generation mix at a specific time instant. This volatility in system inertia will introduce technical challenges when designing and setting system integrity protection schemes, e.g. UFLS. The functionality of some of these schemes may need to be carefully redefined in response to the increasing levels of RESs in the power system.

So far, a number of innovative solutions has been proposed addressing these emerging challenges directly related to reduced and even variable system inertia. Recent examples include new solutions introduced within the Enhanced Frequency Control Capability (EFCC) and Massive InteGRATion of power Electronic devices

(MIGRATE) projects led by UK National Grid and TenneT, respectively (see [18], [19]). Furthermore, an assessment of the technological capabilities for the fast frequency response project was conducted by GE for an Australian energy market operator [20]. Additionally, a new project, Interconnection Frequency Response, proposed a set of options to maintain reliable interconnection frequency response in the USA [21]. The operational theory and power system planning of power systems with high penetration levels of RESs, formed part of China's national key research and development programme [22]. EirGrid and System Operator for Northern Ireland (SONI) investigated a series of cases related to increased RoCoF [23]. All these studies indicate or prove that applying additional and adequate frequency control mechanisms is unavoidable. One of the most important requirements is that WECSs ought to provide frequency support that is normally delivered by conventional synchronously operating generating units. How a WECS responds to a frequency event and provides optimal active power support is a complex technical question, with its answer depending on the system's operational characteristics.

1.3. Goals

The main goal of this research is to develop an enhanced frequency control in a wind turbine to deal with the shortcomings presented in the literature, e.g. significant reduction in system inertia. Achieving this main goal can be divided into the following sub-goals:

1) Review relevant power system stability concepts published in the open literature, with a specific emphasis on frequency stability.
2) Review relevant WECS modelling literature.
3) Review relevant literature on frequency controls and identify their advantages and disadvantages.
4) Review relevant literature on SIPS, especially related to UFLS.
5) Understand the frequency responses in conventional power systems and the impacts of power system stability brought by the integration of RESs.
6) Build and discuss the functional structure of existing frequency controls that provide frequency support, which is accessed by conducting simulations that are suitable for evaluating their performance under different system conditions with various contingencies.

7) Validate the proposed method created using simulated power system models in DIgSILENT PowerFactory under various conditions.
8) Demonstrate the benefits of the proposed method for fast frequency response in the form mitigate the SFD in which adopting wind turbines as the frequency response service provider.
9) Validate the designed UFLS created using the GB 29-zone system built in DIgSILENT PowerFactory under different conditions.
10) Demonstrate the benefits of the designed UFLS for protecting frequency stability in the RES integrated GB 29-zone system.

1.4. Methodology

All research work presented in this PhD. project has been conducted using DIgSILENT PowerFactory and MATLAB software packages run on an Intel Core i7-6700 CPU, 3.41 GHz processor within a 16.00 GB RAM, 64 bit Windows 10 system.

DIgSILENT PowerFactory software is a computer-aided engineering tool for the analysis of transmission, distribution and industrial electrical power systems. This software has been designed as advanced software focused on power system modelling and control analysis to accomplish the main planning and operation optimisation objectives. Also, DIgSILENT PowerFactory is integrated with a graphical single-line interface consisting of features such as drawing elements, editing capability and appropriate static and dynamic calculations. The system model and proposed controls in this research project will be conducted using this software.

MATLAB is the most commonly adopted programming language/interface in the electrical engineering field and will allow for an unknown number of obtained simulation results to be processed. In addition, calculation speed, data processing and drawn figures are all facilitated. For example, the parameters set for wind turbine modelling, UFLS relay, etc, in DIgSILENT PowerFactory need to be carried out using MATLAB.

1.5. Contributions

This research focuses on the frequency support control of wind turbines that explicitly satisfies both functional and economic requirements. Main contributions of this research are as follows:

In order to figure out the role of wind turbine in frequency response, it is essential to have a precise model that satisfies the simulation requirements. The impacts of integrating high penetration level of wind power are firstly investigated, and the accuracy of model is verified. In addition, new control blocks need to be added in the wind turbine model in DIgSILENT PowerFactory. The added controls such as synthetic inertia control and dynamic droop-based control aim to investigate the performance of temporary energy reserves in improving the secondary frequency dip, which identifies the limitation of utilising temporary energy supports.

Then, the over-speeding control based deloading control of wind turbine is also built in wind turbine model, which is used to discuss the impacts of persistent energy reserves on the frequency support. Moreover, a power dispatch based on the combination of temporary energy and persistent energy reserves is proposed, which fills the research gap that solves the problem of secondary frequency dip at wind farm level.

Last but not least, the work relating to modelling a GB 29-zone transmission system based on National Grid data is accomplished to support future power system research. As the integration of RESs bringing the system inertia down, the system frequency is prone to fall outside of the permissible range regulated by the Grid Code. This modelling work not only evaluates the setting of UFLS but also the interaction of wind turbine and UFLS on the frequency support, because a lower nadir and a larger RoCoF modern system having now severely threaten the system frequency stability. Thus, this research assesses the performance of UFLS under high penetration level of RESs, which provides a train of thought for further consideration of designing UFLS schemes.

1.6. Outline of the thesis

The thesis is comprised of eight chapters. The first chapter is an introduction to this study, with the remaining chapters briefly described below:

Chapter 2 : A summary of power system stability

This chapter primarily reviews power system stabilities and presents their definition and classification. Also, the corresponding time scales for various stabilities are presented. Understanding PE interfaced device related stabilities is critical to access the dynamic system response in RES integrated power systems. More importantly, the

impact of integrating the frequency stability of WECSs is discussed from various perspectives.

Chapter 3 : Modelling and controlling the DFIG

This chapter introduces the modelling and control of the DFIG-based variable speed wind turbine. The configuration of the DFIG can be divided into two systems: mechanical system and electrical system. To understand the basic functional structure, a working algorithm is essential to enhance the frequency support capability of wind turbines. In addition, the DFIG modelling and relevant controls are built in the DIgSILENT PowerFactory for disturbance analysis.

Chapter 4 : A summary of smart frequency control

This chapter elaborates on existing smart frequency control schemes in the literature. The frequency controls are classified and determined by the energy type, and then systematically reviewed. Appropriate well-designed models are important to ensure power system security. Additionally, SFD occurrences are also explored in the chapter, which extend the research area in which frequency control of wind turbines. Furthermore, proposed controls in Chapter 5 and Chapter 6 are discussed based on the advantages and disadvantages of reviewed frequency controls.

Chapter 5 : Synthetic inertia control

This chapter introduces a synthetic inertia control for WECSs to participate in frequency control by making them temporary releasing the kinetic energy emulating from the inertial response in the synchronous generators. A dynamic droop-based control is then described, which will help mitigate the disadvantages of synthetic inertia control causing SFD occurrence. A number of simulation tests are conducted to investigate the effect of different parameters in this method’s performance.

Chapter 6 : A consecutive power dispatch in wind farms

This chapter proposes a consecutive power dispatch in wind farms to mitigate secondary frequency dips by collaborating the temporary and persistent energy of wind turbines. All wind turbines in a wind farm are required to be divided into two groups. One group consists of the wind turbines having temporary energy reserve and the other group consists of the wind turbine having persistent energy reserve. The main

mechanism of this proposed control is to subsequently trigger these two groups of wind turbines. The comparison of this proposed control and other frequency controls will be carried out under different system conditions.

Chapter 7 : SIPS – Underfrequency load shedding

This chapter presents theoretical background of SIPSs from the perspective of their definition, classification and typical architecture. The emphasis is focused on UFLS. Therefore, an UFLS scheme based on the systematic approach will be investigated. This UFLS uses the presumed inertia constant and largest possible active power loss in the system as inputs. The simulation is carried out on the two-area test system and the GB 29-zone transmission system. Accordingly, the impacts of the system inertia, frequency thresholds and communication delay on the UFLS performance will be discussed.

Chapter 8 : Thesis Summary

This chapter summarises the research presented in this thesis, its contribution and some potential research areas for further development of this research.

Chapter 2 Frequency Stability Challenges Faced by Modern Power Systems

Power system stability has been considered as an evident challenge for secure system operation since 1920s [24]. In [25], the issue of power system stability definition and classification has been addressed from its fundamental perspective. However, the discussion was published in 2004, with the dynamic response of conventional power systems dominated by synchronous generating units and their controls, as well as the dynamic response of the loads. Accordingly, [25] presented how to cope with the relatively slow, electromechanical phenomena that exists in conventional power systems. However, the fairly fast dynamic response related to modern systems that integrate converter interfaced generations are not considered.

With the rapid increase in converter interfaced generations (e.g. wind units, photovoltaic, battery energy storage systems and smart induction motors), PE interfaced loads and HVDC links, the dynamic response of modern power systems has gradually become more dependent on these converter-interfaced generation methods. This transformation in power systems has focused research attention on the reclassification of power system stability. In this chapter, reclassification is discussed based on [26]. The definition of power system stability in conventional and converter-driven power systems will be elaborated on. The emphasis on frequency stability in low inertia power systems will also discussed from different perspectives.

2.1. Definition of power system stability

[25] defines that:

"Power system stability is the ability of an electric power system, for a given initial operating condition, to regain a state of operating equilibrium after being subjected to a physical disturbance, with most system variables bounded so that practically the entire system remains intact."

Power system stability in conventional systems is directly determined by the operating status of the power systems and the nature of contingencies. As the above power system stability definition suggests, instability can occur when two opposing forces are affected after being subjected to a disturbance. The system will either return to the operating condition before the contingencies or pursue a new equilibrium point. During the operation of a power system, if a small disturbance such as a continuously changing load occurring, the system is able to react to the changes accordingly. However, if a large disturbance occurs in the system, such as sudden loss of a synchronous generator, it can result in a severe failure in the system. On the other hand, system protection devices will be tripped to quickly protect other connected units within the system. In this context, the other units must regain a new state of equilibrium and maintain a balance between generation and load [13].

Power systems consist of a large number of components that have the potential to generate disturbances. It is intensively costly to deploy a power system that remains stable under all possible contingencies. A more practical way is to presume the contingencies that can occur in a system by taking all potential occurrences into account. Since different energy sources are integrated in modern power systems, the dynamic responses of a power system may contain many components, with each able to potentially lead the power system into a cascading failure [27].

2.2. Classification of power system stability in conventional power systems

In a conventional power system, power system related stability issues should include different types of instability and corresponding factors. Various forms of instability problems can be caused by different factors, requiring different approaches to be used by the system operator to facilitate stable operation. There are three types of stability commonly considered [13]:

i). The physical nature of the disturbance that causes the instability that can be observed by the main system variables.

ii). The size of the disturbance that influences the approaches used to calculate and predict instability.

iii). The time scale, processes and components considered during the disturbance.

Fig. 2.1 presents the classification of power system stability, including its categories and subcategories.

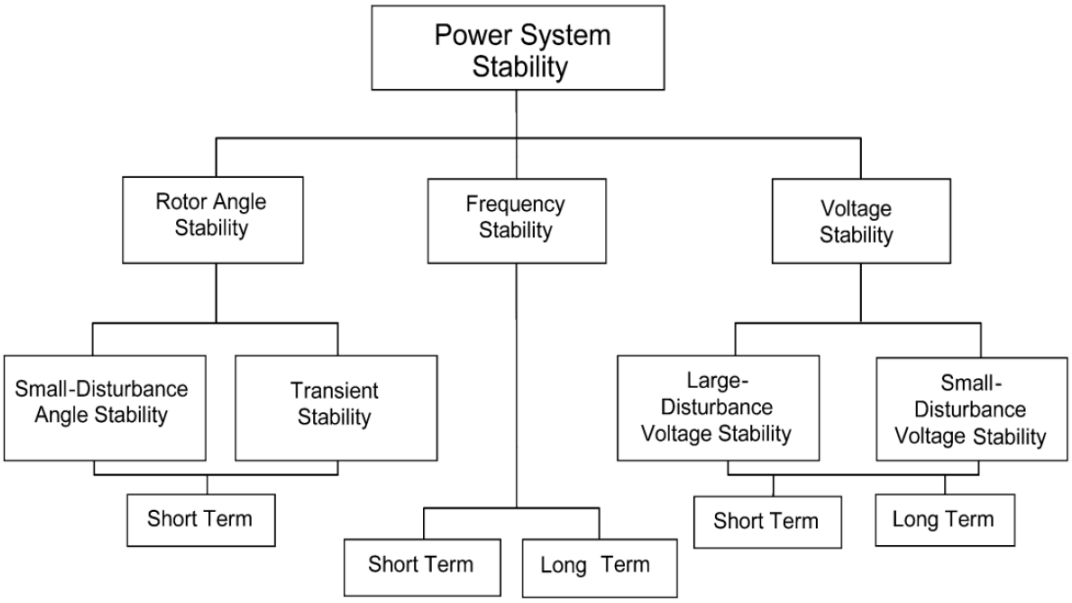

Fig. 2.1: Classification of power system stability [28].

2.2.1. Rotor angle stability

Rotor angle stability refers to the ability of the synchronous machines in an interconnected power system to remain in synchronism after being subjected to a disturbance. Rotor angle stability is dependent on the ability to restore/maintain equilibrium between electromagnetic torque and mechanical torque in every synchronous machine in the system. When instability occurs, the angular swings in some generators may result in a loss of synchronism [28].

The rotor angle stability issue concerns the study of electromechanical oscillations in power systems. The primary factor to consider is the change in the active power output of synchronous generators influencing the rotor angle change. For example, during a

steady-state condition, the input mechanical torque and the output electromagnetic torque of each generator are in equilibrium, with the speed remaining constant. On the other hand, if the system is disturbed, the equilibrium balance between input and output torques can be upset, resulting in the affected rotors either accelerating or decelerating. If this happens, the angular separation between two generators depends on the power-angle relationship that is highly nonlinear. Once the certain limit is reached, an increase in angular separation is accompanied by a decrease in power transfer so that the angular separation can increase further. Under any given condition, the angular stability of the power system relies on whether or not the system is able to absorb the kinetic energy caused by rotor speed differences [28]. Finally, angular stability can occur between one synchronous machine and the rest of the system, or between a number of machines, with synchronism remaining.

Two restoring torques are extremely important to counter against rotor angle instability: synchronising torque and damping torque, in phase with rotor angle deviation and speed deviation, respectively. Furthermore, lacking synchronising torque can lead to aperiodic instability, whist lacking damping torque can result in oscillatory instability.

Fig. 2.1 shows that small-disturbance angle stability and transient stability are derived from rotor angle stability, which is determined by the size of the disturbance.

Small-disturbance angle stability refers to the ability of a power system to remain in synchronism when experiencing a relatively small size disturbance, with the power system able to be linearised for the sake of analysis. In a conventional power system, a small-disturbance rotor angle stability problem is usually caused by insufficient damping of oscillations. The aperiodic instability problem has been mostly dealt with through the implementation of Automatic Voltage Regulators (AVR). However, this problem still exists, since generators operate with constant excitation that is associated with excitation limiters. Also, the time scale in small-disturbance stability studies when failure occurs is approximately 10 to 20 seconds after being subjected to a disturbance.

Small-disturbance rotor angle stability can be categorised into both local and global problems:

i) Local problems are associated with the rotor angle oscillations of a small portion of the system, or even a single synchronous machine. The damping of the oscillations is determined by the strength of the transmission system.

ii) Global problems depend on interaction among different groups of generators. For example, the oscillations of a group of generators in an area swing against a group of generators in another area, which is also known as interarea mode oscillation. Compared to local problems, global problems are more complex and important.

Transient stability, also termed *large-disturbance rotor angle stability*, relates to the ability of the power system after being subjected to a severe disturbance (e.g. short circuit, loss of large generation). Instability generally shows in the form of aperiodic angular separation due to insufficient synchronising torque. The time scale of interest for transient stability is usually 3 to 5 seconds after being subjected to a disturbance. In the case of a large disturbance, the time span can take up to 10 to 20 seconds.

As Fig. 2.1 shows, small-disturbance rotor angle stability and transient stability are classified as short term phenomena.

2.2.2. Frequency stability

Frequency stability is associated with the ability of the power system to keep the frequency at a constant value after being subjected to a frequency event. A frequency event can result in a significant imbalance between generation and load. Frequency instability can cause continuous frequency swings that result in tripping of generators or loads [25], [28].

A severe frequency event can cause a frequency to drop out of the permissible range required by the system operator. Thus, the magnitude of the frequency, power flow, bus voltage and other system variables will lead to tripping the protective action scheme (e.g. underfrequency load shedding (UFLS), undervoltage load shedding schemes (UVLS).) However, the inherent reaction of synchronous generators is relative slow due to slow boiler dynamics [29]. More severe, a large interconnected power system can be split into islands following frequency instability, with stability under this condition depending on the mean frequency of all split islands rather than the relative motion of the machines. In general, frequency stability is related to the

response of turbine-governor control, insufficient generation reserves, total system inertia and the amount of inherent load damping. It is noted that frequency responses are more sensitive in a power system with lower inertia.

During frequency excursions, the time span of the processes and involved devices ranges from a fraction of seconds (e.g. generator controls, protection schemes) to several minutes (e.g. prime mover energy supply system, load voltage regulators). As Fig. 2.1 presents, frequency stability can be categorised into either short term or long term phenomena.

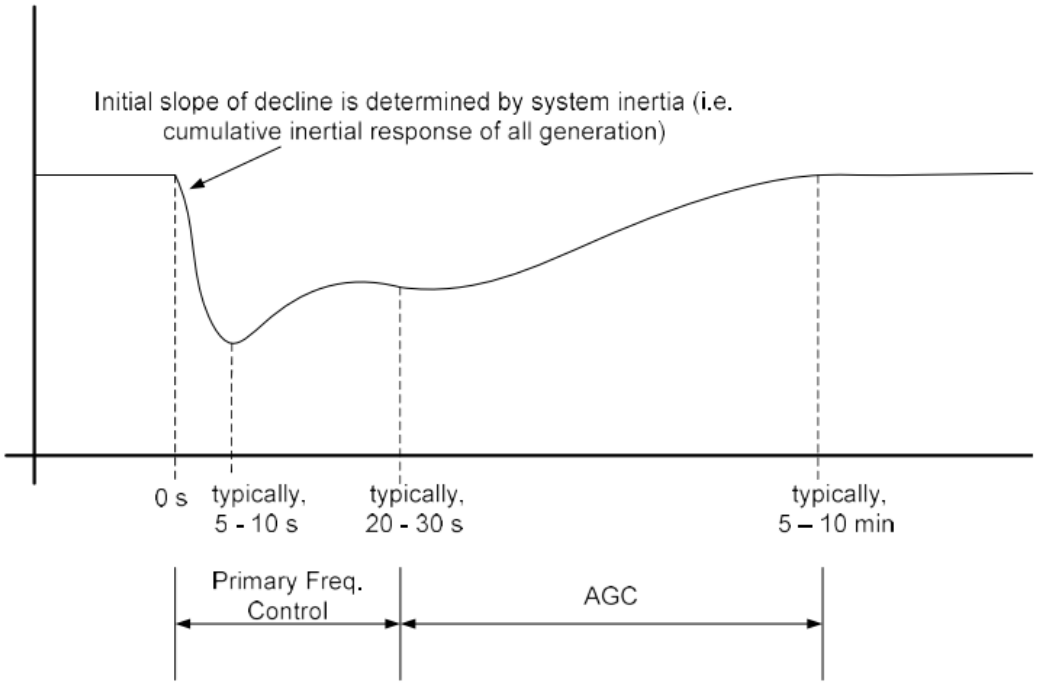

Fig. 2.2: An illustration of power system frequency response to a major loss of generation [30].

Fig. 2.2 presents an overview of a power system response to a major loss of generation. The first response phase is contributed to by the inherent inertial response of the synchronous generators since the laws of physical and not control actions. If no controls are employed on any of the synchronous generators, the system frequency will continuously decrease until protection is tripped, and proper load size is shed. In order to maintain stable system operation, synchronous generators are required to carry some active power reserves. During contingencies, the active power output of the synchronous generator increases to compensate the power imbalance between

generation and load, ensuring the system reaches a new operating state equilibrium. The second phase is normally known as the primary frequency response that is achieved by the turbine governor frequency response [30]. Then, Automatic Generation Control (AGC) takes over the third phase, bringing the system frequency back to the pre-disturbance value.

2.2.3. Voltage stability

Voltage stability can be defined as the system's ability to maintain all bus voltages in a steady voltage range following a disturbance [25][31]. Many factors contribute to voltage instability, such as a sudden increase in demand, loss of transmission lines and unexpected generator loss. The result of the aforementioned problems is that a voltage drop happens in which active power and reactive power flow through the transmission lines, with the voltage drop potentially causing voltage collapses and resulting in devastating cascading system outages [32]. The time window of interest for voltage stability can vary from very fast if using induction motors, or high-voltage direct current transmission system (HVDC) considered or change very slow if mechanical tap changer and generator current limiters considered. Accordingly, the voltage stability time window can be divided into two sub-categories: short term (few seconds) and long term (tens of minutes) phenomena, as shown in Fig. 2.1.

i). Large disturbance voltage stability describes the ability of a power system to maintain all bus voltages in a steady voltage range following a severe disturbance, such as a system fault, transmission line disconnection or loss of generation. The ability directly depends on the system characteristics and load modelling, and the interaction between various controls and the protection schemes. The requirement to set the large disturbance stability criteria means examining the nonlinear response of the power system through a predefined time scale to ascertain the performance of devices, such as induction motors, mechanical tap changer and generator current limiters.

ii) Small disturbance voltage stability describes the ability of a power system to maintain all bus voltages in a steady voltage range following a small disturbance, such as a small step-up load increase. Small disturbance voltage stability depends on the load modelling and system controls at an

instantaneous period. In order to linearise the system equation properly, computation identifies those factors that impact on voltage stability and captures the response of the system voltage for the voltage stability analysis [25].

Furthermore, the most severe voltage instability condition is voltage collapse, which can lead an unexpected blackout or an unacceptable low voltage profile.

2.3. Time scales of power system dynamic response

The time span for different categories of dynamic response in power system is presented in Fig. 2.3. It is noteworthy that the time span involved in the controls for converter interfaced generators range from a few microseconds to several milliseconds, and consist of wave and electromagnetic phenomena. Considering the increase in converter interfaced generator integration, faster dynamic responses play an important role in the analysis of modern power systems. Emphasis on the time span of electromechanical transients can simplify the modelling and representation of modern power systems. A major aspect of simplified models is the assumption that voltage and current waveforms are dominated by the fundamental frequency component of the power system (50 or 60 Hz) [26]. Fast responses, such as switching off PE converters, are only represented by either the steady-state model or simplified dynamic model, indicating that fast phenomena, and the operation cannot be captured. In power systems integrating converter interfaced generations, the time scales focus on faster dynamic responses.

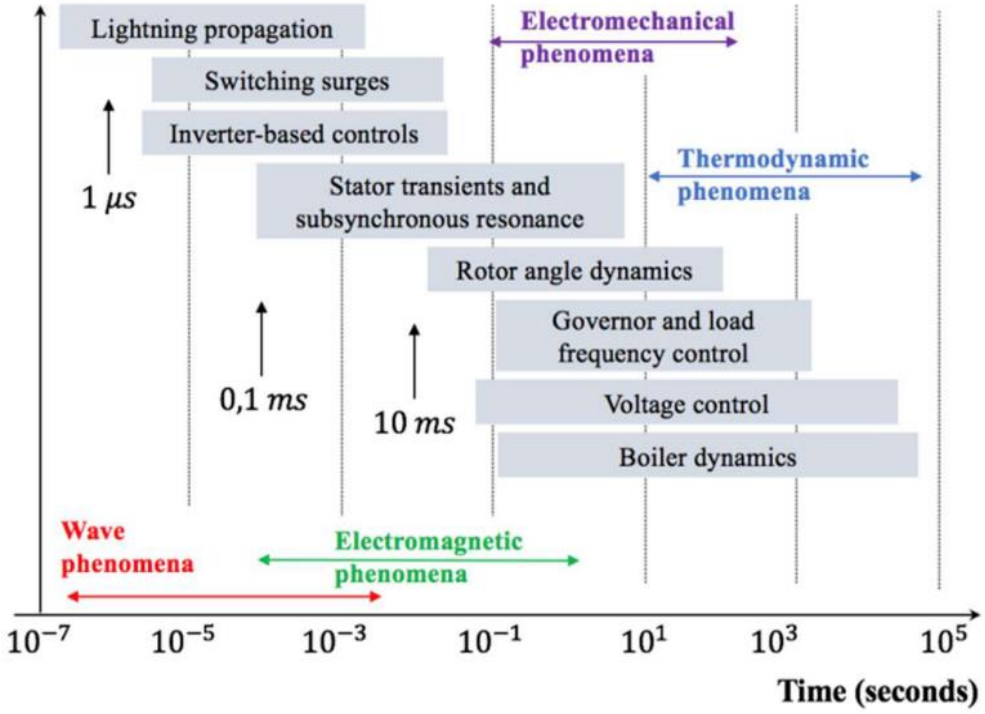

Fig. 2.3: Power systems time scales [26].

2.4. Classification of power system stability in power systems that integrate converter interfaced generations

On top of the discussion in Chapter 2.2, power system stability is enhanced based on the original classification presented in Fig. 2.1. Two additional stabilities, *Resonance stability* and *Converter-driven stability*, are introduced as well. The motivation to add these two stabilities is due to the increase in converter interfaced generations in power systems.

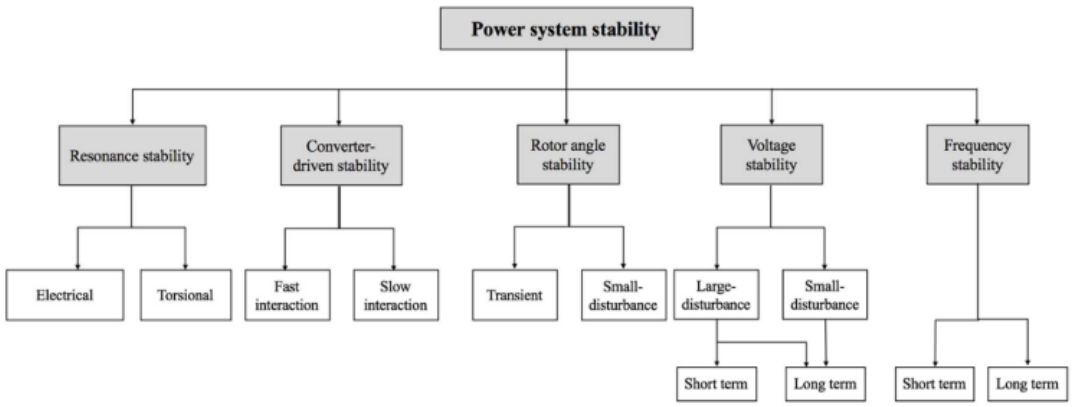

Fig. 2.4: Classification of power system stability in an converter interfaced generation integrated power system [26].

2.4.1. Resonance stability

Resonance stability consists of subsynchronous resonance (SSR), a condition in which a series capacitor compensated system exchanges significant energy with a turbine-generator at a frequency below the synchronous frequency [33], [34]. SSR is either related to electromechanical resonance or entirely electrical resonance. As elaborated in [35], SSR can be divided into two classes:

i) Resonance between the turbine-generator mechanical shaft and passive system component (e.g. series capacitor).
ii) Resonance between the electrical characteristics of the turbine-generator and active system component (e.g. HVDC transmission equipment controls, static VAR system control).

Resonance stability can also be classified into two categories:

Electrical resonance related to subsynchronous resonance (SSR) concerns torsional interaction and resonance in conventional power systems. The electrical resonance is also termed as the induction generator effect [36]. Variable speed induction generators adopted in DFIG based wind turbine generators are highly susceptible to induction generator effect self-exaction type SSR [33]. This problem was reported in a DFIG wind farm nearby series capacitors. An induction generator directly connected to the grid causes electrical resonance, leading to net negative resistance occurring since the induction generator rotor has inherent negative resistance. As the DFIG controls the converter connected between the stator and rotor circuit, negative resistance also occurs on the stator side. If the total negative resistance exceeds the positive resistance of the circuit around the resonant frequency, self-excitation SSR occurs [26].

Torsional resonance occurs due to the interaction between the turbine-generator mechanical shaft and series compensated line. According to [35], subsynchronous oscillation are divided into SSR and device-dependent subsynchronous oscillations.

SSR occurs in a power system when the mechanical system of generators exchanges significant energy with the electrical network [36]. The oscillations range from poorly damped, undamped or even negatively damped and growing, thereby worsening the mechanical system of the generators. On the other hand, device-dependent subsynchronous oscillations occurs due to the interaction between fast acting control devices (e.g. HVDC transmission lines, static Var compensator (SVC), static synchronous compensator (STACOM) and power system stabilizer (PSS)) and the torsional mechanical modes of nearby turbine-generators [33].

2.4.2. Converter-driven stability

The dynamic performance of a converter interfaced generation is different from a synchronous generator because the voltage source converter based interface connects the generator to the grid. As mentioned in the introduction, converter interfaced generations have relatively faster response times than conventional generators due to the implemented control loop and algorithms, such as the phase locked loop (PLL), inner-current control loop and the high-level control loop. In this situation, the time span of converter interfaced generations covers both the electromechanical dynamics of machines and the electromagnetic transient of networks [26]. The subcategory of *Converter-driven stability* is classified into *fast-interaction converter-driven stability* (e.g. less than 10 Hz) and *slow-interaction converter-driven stability* (e.g. tens to hundreds of Hz, up to kHz) according to the frequencies of the observed phenomena.

Slow-interaction converter-driven stability [26] consists of system-wide instabilities and is caused by the slow dynamic interaction of the control systems that are adapted in the slow response devices such as electromechanical response and generator controllers.

This converter-driven stability subcategory is similar to the voltage stability discussed in the previous section. Voltage stability is more dominated by load, whilst converter-driven stability is usually caused by PE device controls. For example, the maximum power transfer between a converter and the rest of the system. If the generated power exceeds the maximum power that can be transmitted, the equilibrium does not exist; in addition, the phase angle increases and leads an unstable system response.

Fast-interaction converter-driven stability [26] refers to the system-wide stability problems caused by the fast dynamic responses in the control systems of converter-interfaced devices, such as converter interfaced generations, HVDC links, etc. Fast-interaction converter-driven instability can be caused in different ways. For example, the fast control of an electric power converter can cause interactions between the converter and the grid.

Synthetic inertia control that mimics the response of a synchronous generator is adopted in wind turbines, providing fast frequency response and potentially causing interactions.

2.5. Frequency stability in a wind power integrated system

A system frequency response is used to analyse the frequency control capability of a power system. System frequency is a continuously changing variable that depends on the active power balance between system generation and load. If generation exceeds the load, system frequency increases. In this section, frequency stability in wind integrated systems will be discussed in detail. Moreover, the effects of various parameters, such as system inertia constant, damping factor and active power reserves, will also be discussed.

2.5.1. The swing equation

During steady state operation, there exists an equilibrium between two opposing torques: the mechanical input torque and the electrical output torque. They maintain generator's constant speed, ensuring nominal system frequency and stable operation of a multimachine power system. The rotating shafts of synchronous generators absorb the electrical energy when the electrical power exceeds the system's requirement, whereas the rotating shafts of the synchronous generators release the electrical energy when electrical power is less than the system requires [13]. The swing equation shown in (2.1) is derived from the equation of a rotating machine, describing the relationship between mechanical power and electrical power with respect to the frequency operation of power systems [37][38].

$$\frac{2H}{\omega_s}\frac{d^2\delta}{dt^2} = P_m - P_e \tag{2.1}$$

where H represents the inertia constant in seconds, ω_s is the synchronous speed in rad/s, δ is the angular position of rotor angle in rad referring to the synchronously rotating frame, t represents the time in seconds, P_m and P_e are the mechanical power and electrical power in *pu* [39].

The remaining parts of this chapter show how to derive the swing equation. As shown in (2.2), the equation for motion can be expressed as the total moment of inertia of the prime mover and generator:

$$J\frac{d^2\theta}{dt^2} = T_a \tag{2.2}$$

where J represents the moment of inertia of wind turbine and generator in kgm^2, θ is the angular position of rotor in rad and T_a represents the accelerating torque in Nm. The mismatch between the mechanical torque and electromagnetic torque results in a net acceleration (or deceleration) in the power system [40]:

$$T_a = T_m - T_e \tag{2.3}$$

where, T_m and T_e are mechanical torque and electrical torque in Nm respectively.

The angular position θ is measured with a stationary reference frame, and should be expressed in a synchronously rotating frame:

$$\theta = \omega_s t + \delta \tag{2.4}$$

The angular speed of the rotor can be defined as:

$$\omega_r = \frac{d\theta}{dt} \tag{2.5}$$

$$\omega_r - \omega_s = \frac{d\delta}{dt} \tag{2.6}$$

where ω_r represents the rotor angular speed in rad/s.

Multiplying Equation (2.2) by ω_m, the equation can be written as:

$$J\omega_r\frac{d^2\delta}{dt^2} = P_m - P_e \tag{2.7}$$

Then the inertia constant H can be expressed as the following with respect to the synchronous angular velocity ω_s in rad/s:

$$H = \frac{1}{2}\frac{J\omega_s^2}{VA_{base}} \tag{2.8}$$

Substituting Equation (2.8) into Equation (2.7),

$$2H\frac{S_{rated}}{\omega_s^2}\omega_r\frac{d^2\delta}{dt^2} = P_m - P_e \tag{2.9}$$

During the steady operating condition, ω_r is equal to ω_s, the right hand side of Equation (2.9) needs to be divided by S_{rated}, therefore, the swing equation can be written as Equation (2.1).

If the P_m is larger than P_e, the rotor of the generation accelerates, causing frequency increases in the system. Whereas P_m is smaller than P_e, the generator's rotor decelerates, causing frequency to decrease in the system.

2.5.2. Rate of change of frequency

Next to frequency, rate of change of frequency (RoCoF) is one of the most significant variables used to study frequency stability in power systems. The RoCoF depends on the imbalance magnitude in the level of the system inertia. The lower the system inertia is, the higher the RoCoF will be after a disturbance (e.g. active power imbalance) in the system. Owing to the Swing equation (2.1), the RoCoF is proportional to the difference between the mechanical power and electrical powers, and inversely proportional to the system inertia, expressed through its inertia constant. In [41], the Irish government policy has set a target to provide 40% of electrical energy by wind generation by 2020. Also, the RoCoF criteria is set to be 0.5Hz/s Hz/s in the Ireland Grid Code [37]. Conventional generation is to be replaced by an increasing amount of wind generation, which will result in lower system inertia and even higher RoCoF because WTs are connected to the grid via a back-to-back converter, which decouples electrically the generator frequency and grid frequency [42]. In the latter chapters, the effects of the penetration level of wind generation on the RoCoF will be analysed based on the obtained simulation results.

2.5.3. The swing equation of multi-machine systems

In 2.5.1, the swing equation is discussed based on the assumption that the entire power system can be equivalented with a single machine. However, during the transient period, the synchronous generators connected to a multi-machine power system would be slightly different, leading to relative rotor movements. If the small system stability is satisfied, all relative rotor movements will be eliminated, leading to a single frequency of all generators.

In order to derive the swing equation for a multi-machine power system (e.g. *n* generating units), an equivalent model is needed to present the average frequency of all generators at the same time, which is termed the centre of inertia frequency (COI) [43]. In [40], the COI frequency is elaborated as a presumed dynamic position measured by the weighted average of the instantaneous rotor angles of all the synchronous generators in the system.

Normally, inertia constant H of the synchronous machine is normalised based on its own ratings. Before calculating the COI frequency of a power system, all the synchronous machines need to convert their ratings into a common system MVA base:

$$H_{i,sys} = H_i(\frac{S_i}{S_{base}}) \tag{2.10}$$

where S_{base} represents the common power system base, S_i represents the power base for i^{th} synchronous machine, H_i represents the inertia constant of the i^{th} synchronous machines based on its S_i, and $H_{i,sys}$ represents the inertia constant of i^{th} synchronous machine based on S_{base}.

Therefore, the COI frequency f_{COI}, COI RoCoF $f_{COI,RoCoF}$ and total system inertia H_{sys} are represented as follows:

$$f_{COI} = \frac{(\sum_{i=1}^{n} f_i H_{i,sys})}{(\sum_{i=1}^{n} H_{i,sys})} \tag{2.11}$$

$$f_{COI,RoCoF} = \frac{(\sum_{i=1}^{n} f_{i,RoCoF} H_{i,sys})}{(\sum_{i=1}^{n} H_{i,sys})} \tag{2.12}$$

$$H_{sys} = \sum_{i=1}^{n} H_{i,sys} \tag{2.13}$$

During the contingency, the frequency of each synchronous machine is easily disturbed by inter-area oscillations. This is the reason why f_{COI} is required to present the simulation results due to the various disturbances that exist in the system. The RoCoF at each bus in the system are even more obvious when compared to the frequency.

The frequency of a power system has a unique value among the entire system at steady state conditions. However, the frequency cannot be maintained at a constant value in case of having a frequency event, since the frequency will have different values at different parts of the power system for a specific time point. To be more detail, the frequency deviation will be monitored sooner at the parts of the grid which are electrically closer to the disturbance and the oscillations due to the disturbance will be visible at these parts first. Therefore, different frequency measurements from various location throughout the system are needed, so that the system's average frequency can be accurately represented as discussed in the previous contents. The COI frequency of a system can be introduced to represent the system's average frequency. The COI frequency of a system can be considered to be a fictitious bus, where all generators of the system are connected. Therefore, assuming a complex system, the COI frequency does not present any oscillations and it accurately represents the average frequency of the system. Nevertheless, measurements from each generator are not available in current power systems. Therefore, the employment of Phasor Measurement Units (PMUs) has made it feasible to acquire this kind of measurements in a fast and accurate manner. However, there will be a certain amount of time before a satisfactory number of PMUs is installed in the power systems. Therefore, inertia estimation methods should be able to provide accurate results, even with limited observability. Also, the communication time of exchanging the data among various PMUs has a direct impact to accuracy of COI frequencies [44], which still is an intractable problem to be dealt with.

2.6. Droop characteristic

The primary frequency control phase is based on adjusting the active power output of generating units according to system frequency variations. In a case where a generator is supplying an isolated load when only one generator is required to respond to the load change, a speed governor can be used to adjust the generator's active power output. However, when all the generators in a multi-machine system are required to respond to the changes, the droop characteristic must be employed to avoid conflict between different generators [45]. Furthermore, the droop characteristic contributes to the stable load division between two or more parallel generating units.

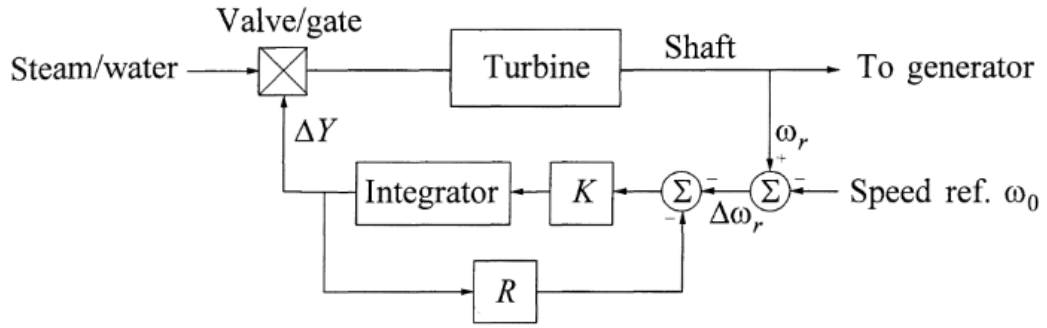

Fig. 2.5: Schematic for a speed governor with droop control [45].

Fig. 2.5 presents the schematic of a speed governor with droop control. The measured rotor speed ω_r is compared with the reference rotor speed ω_0. Then the speed deviation $\Delta\omega_r$ is amplified by a value of K and integrated to produce a control signal ΔY which adjusts the main power output. The droop parameter R determines the steady-state speed versus load characteristic of the generating units connected to the power system.

Droop parameter R can be expressed in a percentage as follows [45]:

$$\begin{aligned} \text{Percent } R &= \frac{\text{percent speed or frequency change}}{\text{percent power output change}} \times 100 \\ &= \left(\frac{\omega_{NL} - \omega_{FL}}{\omega_0} \right) \times 100 \end{aligned} \tag{2.14}$$

where ω_{NL} represents the steady state at no load, ω_{FL} represents the steady-state speed at full load and ω_0 represents the nominal speed.

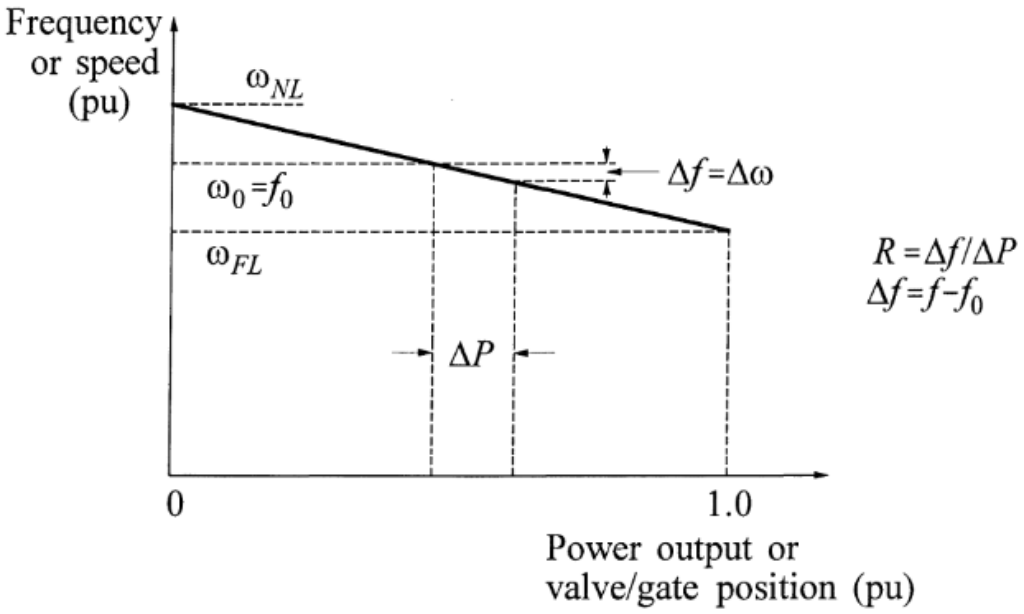

Fig. 2.6: Steady-state characteristics of a governor with droop characteristics [45].

As Fig. 2.6 shows, a 5% droop means that a 5% frequency deviation can cause a 100% active power change. If more than one generator with a droop characteristic are connected in a system and share the load in parallel, the final frequency will reach the same frequency following an active power event. For example, two generators operate at same nominal frequency f_0 with output power P_1 and P_2, respectively. When there is a load increase event ΔP_L occurring in the system, the rotor speed of the generators decreases and in turn causes frequency declines. The governors increase the output power until the generators reach a new state of equilibrium. The amount of load shared by each generator is determined by the droop characteristic:

$$\Delta P_1 = P_1^{'} - P_1 = \frac{\Delta f}{R_1} \tag{2.15}$$

$$\Delta P_2 = P_2^{'} - P_2 = \frac{\Delta f}{R_2} \tag{2.16}$$

Therefore,

$$\frac{\Delta P_1}{\Delta P_2} = \frac{R_2}{R_1} \tag{2.17}$$

If the droops for different generators connected in the power system are approximately same, the change in their active power outputs will be nearly in proportion to their ratings [45].

The turbine-governor model used in the simulation will be presented in the latter chapter 5.2.1.

2.7. Impacts of a wind integrated plant on system frequency response

DFIGs (type 3) and FRCGs (type 4) are currently used in wind-integrated power plants. Although WECSs have a good amount of kinetic energy stored in the rotating mass of blades, this kinetic energy will not automatically participate in the frequency response due to the connection over power electrics. This is because the wind turbine generators are connected to the grid via AC/DC/AC power electric converters. Different to conventional plants, the DC voltage bus electrically decouples the rotor of the wind turbines from the grid frequency. Therefore, it is a lost opportunity if the wind turbines kinetic energy is left unused as it could be repurposed to help maintain grid stability. Indeed, synchronous generator speed cannot fall below 0.95 *pu*, DFIGs can operate under a wide range of generator speed between 0.7 to 1.2 *pu*, FRCGs can operate within an even wider range of 0.5 to 1.2 *pu* [46].

As above discussed, the progressive deployment of WECSs not only decreases total system inertia but also reduces the active power reserves in the system. Fig. 2.7 shows the frequency response for various system inertia and active power reserves when the system is subjected to a generation loss of the same size. As can be observed, system frequency declines at a higher rate and reaches the lowest FN f_3 in the system with the smallest inertia (5 s). Fig. 2.7 also shows the frequency response for power systems with the same inertia (10 s) and different active power reserve levels, with system frequency decreasing at a lower rate and reaching a higher FN f_1 when the active power reserve is larger. It follows that under a higher penetration of RESs, frequency stability deteriorates, with the wear and tear of machines [47] more likely to occur.

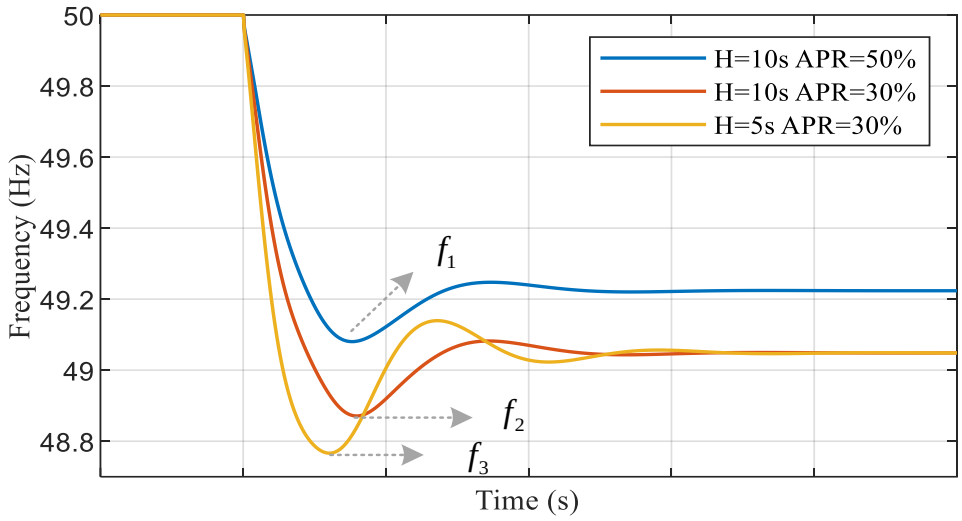

Fig. 2.7: System frequency response for different system inertia (*H*) and active power reserve levels.

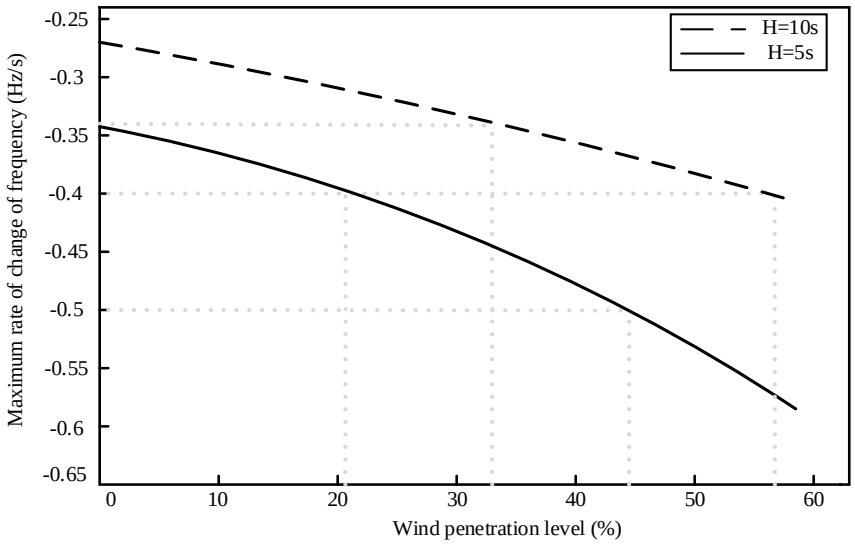

Fig. 2.8: Comparison of RoCoF for different system inertia levels [48].

In order to further explore the effects of wind power integration, Fig. 2.8 presents a comparison of initial RoCoFs for different wind penetration levels. The two curves represent two different systems with various inertia levels. As can be concluded, following a loss of identical generation, the initial RoCoF is larger in the system with smaller inertia. Additionally, the RoCoF increases faster as the penetration level increases. This high RoCoF causes technical challenges when applying system integrity protection schemes, e.g. UFLS [49]–[52], or intentional controlled system islanding [53]–[57].

2.8. Chapter summary

This chapter introduced the definition of power system stability in conventional and converter integrated generation power systems. With the ongoing trend towards a sustainable and green energy future, conventional fossil synchronous generators will be replaced by converter integrated generators. Frequency response is a vital aspect of power system performance explored in this study.

The key problem with frequency stability in the power system is that this type of generation does not contribute to system inertia. In a conventional system, the release of kinetic energy stored in the rotating mass will slow the frequency decay. However, converter integrated generation is decoupled from the frequency change due to the deployment of VSC. Next, the impact of the wind integrated energy plant on the system frequency response was discussed from the perspective of both frequency responses and RoCoF. In order to make converter integrated generation acting like synchronous generators responding to frequency change in the system, a proper droop or synthetic inertia control is required, which will be discussed in the latter chapter 5.2.

Chapter 3 Modelling and Control of a DFIG Wind Turbine System

To investigate the power quality issues of grid-connected wind turbines and their interaction with the grid, a full understanding of DFIGs in both the steady-state model and dynamic model is essential. This chapter introduces the physical and mathematical background for the simulation model and explains the assumptions made in the process.

3.1. An overview of a DFIG based wind turbine system

Fig. 3.1 shows the layout of a typical DFIG wind turbine. It is composed of blade pitch, gearbox, induction generator and two back-to-back voltage source converters rated at about 30% of nominal generator power. Also, the speed adjustable range is limited to ±30% approximately synchronous speed [58] which is generally 0.7 *pu* to 1.25 *pu* [59], [60].

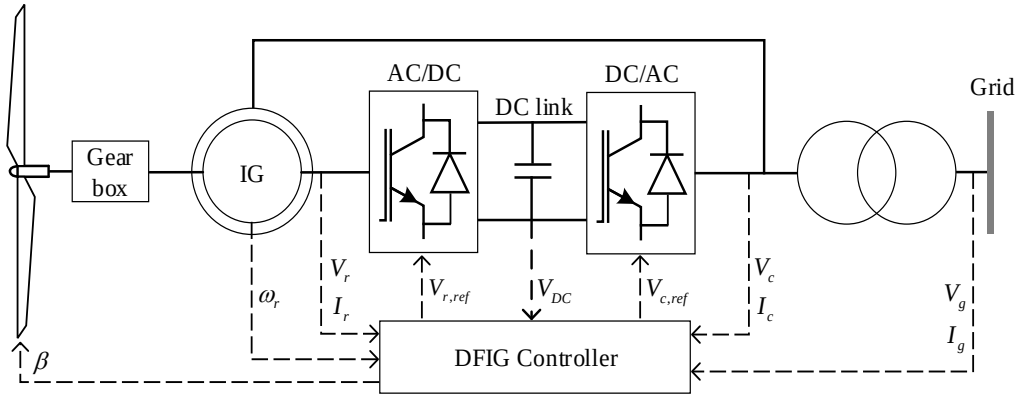

Fig. 3.1: Block diagram of a typical DFIG wind turbine.

As shown in the following figure, the DFIGs stator is connected directly to the grid, whereas the DFIGs rotor is connected to the grid through a voltage source converter.

Moreover, the rotor side converter and filter can generate a three-phase voltage with variable amplitude and frequency, which controls the generator torque and the reactive power exchanged between the stator and grid. However, the grid side converter and filter can exchange the active power extracted or injected by the rotor with the grid. The output frequency will be constant; however, the output voltage will change to modify the exchanged active and reactive power, respectively.

The following sub-sections will focus on the modelling of DFIGs. As shown in Fig. 3.2, it consists of mechanical, electrical and control systems.

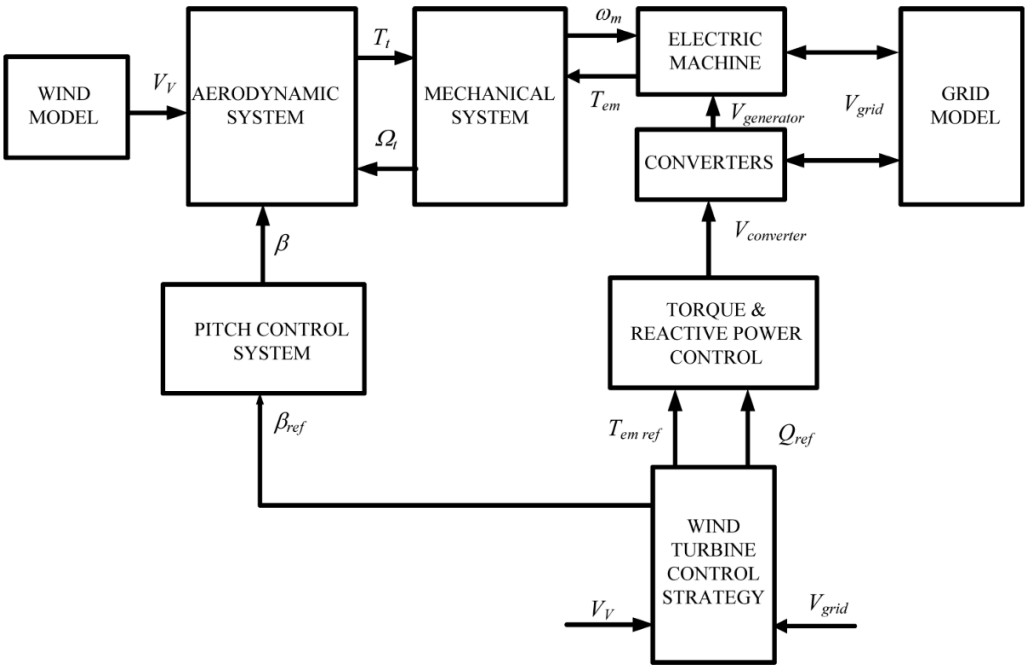

Fig. 3.2: Block scheme of a variable speed wind turbine model [61].

3.2. Mechanical system

The mechanical system of wind turbine generators consists of an aerodynamic system, shaft and pitch system. The wind turbine blades are used to generate aerodynamic torque from the wind, thus transferring it to the shaft system and generator. With the development of the wind turbine generators, the blades of the MW level wind turbines can be pitched to limit the mechanical power. Generally, there are three schemes to limit the power through the blades: fixed stall, active stall and pitch control (i.e. the aerodynamic design of the rotor blade will regulate the power of the wind turbine.). Comparing these schemes, the pitch control produces the least mechanical stress on the drive-train system [62].

3.2.1. Aerodynamic system

According to aerodynamic theory, the mechanical power P_m extracted from wind at any given wind speed is defined as λ.

$$P_m = \frac{1}{2}\rho A v_w^3 C_p(\lambda,\beta) \tag{3.1}$$

where ρ is the air density in kg/m^3, A is the blade-swept area in m^2, v_w is the wind speed in m/s, $C_p(\lambda,\beta)$ is the power coefficient, which is determined by λ the tip-speed ratio (TSR), $\lambda = \omega_r R_{blade} / v_w$ the pitch angle and ω_r the rotor speed. $C_p(\lambda,\beta)$ is dependent on the aerodynamic design [63] and issued by the turbine manufacturer [64]. This nonlinear relationship between C_p and can be described as

$$C_p(\lambda,\beta) = 0.22(116\lambda_i - 0.4\beta - 5)e^{-12.5\lambda_i} \tag{3.2}$$

$$\lambda_i = \frac{1}{\lambda + 0.08\beta} - \frac{0.035}{\beta^3 + 1} \tag{3.3}$$

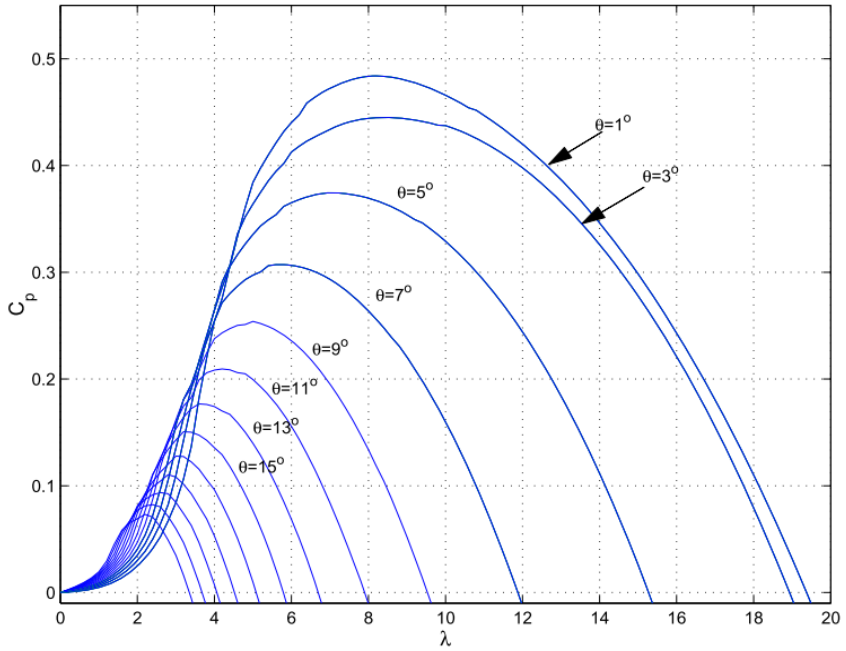

Fig. 3.3: Power coefficient-TSR of a wind turbine generator for various pitch angles [65].

Fig. 3.3 shows the power performance of wind turbine generator is the curve for various pitch angles. It clearly presents the TSR relationship in terms of $\lambda = \omega_r R_{blade} / v_w$.

Moreover, the theoretical optimum for using wind power by decreasing the velocity was initially discovered by Betz. Based on Betz suggestion, the maximum power can be captured from the wind and expressed as follows

$$P_{Betz} = \frac{1}{2}\rho A v_W^3 C_{P,Betz} = \frac{1}{2}\rho A v_W^3 \times 0.59 \tag{3.4}$$

Therefore, even though power captured without any losses is feasible, only 59% of wind power can be converted and used by a wind turbine [66].

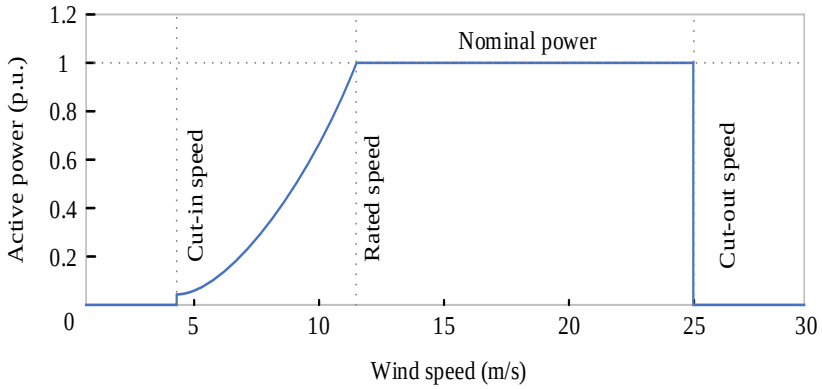

Fig. 3.4: Power-wind speed curve of a DFIG [67].

Fig. 3.4 shows a typical power-wind speed curve for the DFIG used in this project. The blue curve is divided into four regions depending on the various wind speeds. The cut-in, rated and cut-out speeds of the used DFIG are 4 m/s, 11 m/s, and 25 m/s, respectively. In addition, the power captured by the wind turbine generators is limited to nominal power to mitigate the mechanical stress on the wind turbine generators. However, in extreme weather conditions, i.e., wind turbine generators sensing the wind speed is larger than the cut out speed, they have to terminate their operation to prevent further damage.

3.2.2. Drive train model

The shaft model is also known as the drive-train model and can be presented as a two-mass model (see Fig. 3.5). The assumption of this model is obtained by integrating gearbox inertia with either the turbine rotor or generator rotor.

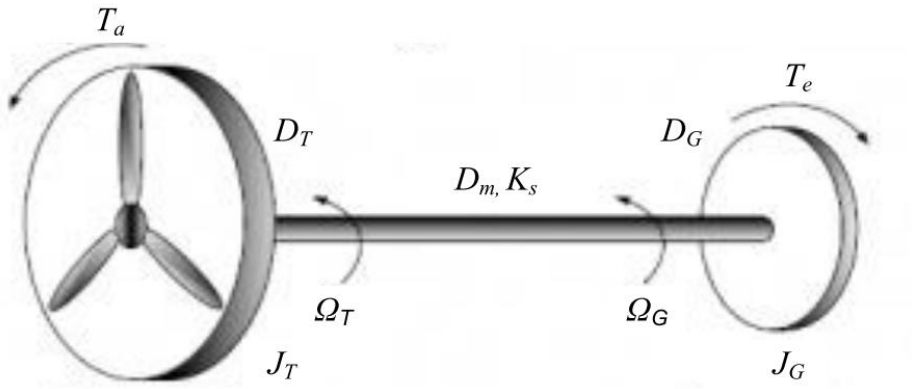

Fig. 3.5: A two mass mechanical model [62].

All the mechanical parameters are included in this turbine rotor model. K_s and D_s are the mutual stiffness coefficient and mutual damping coefficient, respectively. If the two inertias J_t and J_G are considered as a single rotating mass, the lumped shaft model can be expressed as

$$J_r \frac{d\omega_r}{dt} = T_a - T_e - D_r\omega_r \tag{3.5}$$

where J_r represents the total inertia of the lumped shaft model, T_a and T_e represent driving torque and electromagnetic torque of the generator, respectively. And D_r represents the total damping coefficient of the lumped shaft model.

However, if the shaft model is considered as a two-mass shaft model, the following equations are used to describe the model

$$\begin{aligned} J_T \frac{d\omega_T}{dt} &= T_a - T_s - D_T\omega_T \\ J_G \frac{d\omega_G}{dt} &= T_s - T_e - D_G\omega_G \\ T_s &= K_s\theta_s + D_s(\omega_T - \omega_G) \\ \frac{d\theta_s}{dt} &= \omega(\omega_T - \omega_G) \end{aligned} \tag{3.6}$$

where J_T and J_G represent the turbine rotor and generator rotor inertia, ω_T and ω_G represent the angular speed of turbine rotor and generator rotor, D_T and D_G represent the damping coefficient of turbine rotor and generator rotor, T_s represents the reaction

torque from the low-speed shaft, θ_s represents the torsional twist between turbine and generator rotor, and ω represents the base value of angular speed [68].

3.2.3. Pitch system

The pitch system is necessary for all the blades to rotate at similar or different angles. Independent regulation extends the flexibility of the control system, decreasing mechanical stresses in extreme weather conditions (i.e. high wind speed) [69]. Fig. 3.6 shows the layout of a general pitch system. The input signal of this system is the pitch angle deviation that passes a PI controller and generates a reference rate of change of pitch angle $d\beta^*$. Next, a first-order system provides the dynamic behaviours of speed control of pitch variation. Thus, the pitch angle β is then attained by integrating the variation of the angle.

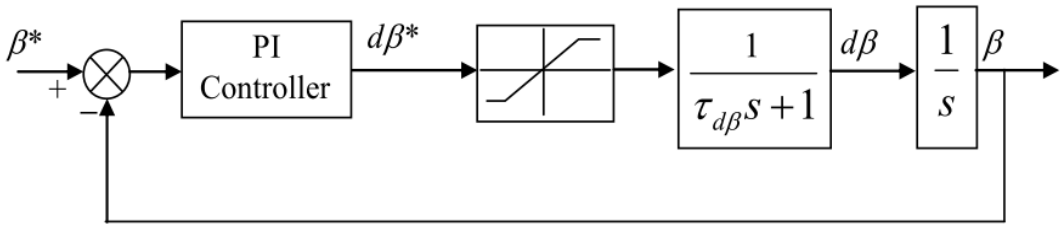

Fig. 3.6: Pitch system [61].

It is crucial to model the rate of change of the pitch angle as the blades contribute a continued effect on the variation of the pitch [70].

3.3. Electrical system

The configuration of DFIG implemented in this study is shown in Fig. 3.1. The stator winding connects to the grid directly, whereas the rotor winding connects to the grid though a voltage source converter. In the following sub-sections, the electrical system, i.e., the generator, converter, transformer and crowbar portion, will be respectively introduced.

3.3.1. Generator

The most common generator used for wind turbines is the converter interfaced generation, which is also called an induction generator. Induction generators have several advantages over synchronous generators, such as their robustness and mechanical simplicity [66]. However, the major disadvantage is that the stator requires

a reactive magnetising current due to the induction generator not having permanent magnets and not being separately excited. Thus, an induction generator has to receive and then consume the reactive power from another source (i.e., grid or reactive compensator). In this context, this will establish the magnetic field in the generator.

As Fig. 3.1 shows, the stator winding is supplied at a constant frequency and three-phase amplitude due to the direct connection. The rotor winding is supplied by a PE converter capable of feeding the DFIG with a variable voltage and frequency three-phase voltages. In addition, the converter adopted in the DFIG only needs to deal with approximately 30% of the power coming from the generator, which means the cost can be dramatically decreased when compared to a FRCG.

For DFIGs, the term 'doubly fed' means that the voltage on the stator is supplied from the grid, whereas the voltage on the rotor is induced by the VSC. The purpose of the VSC is to compensate for the difference between the mechanical and electrical frequency by injecting a rotor current with a variable frequency [66]. More specifically, the RSC controls active and reactive power by controlling the rotor current components. On the other hand, the GSC controls the DC-link voltage and guarantees the converter operation at unity power factor. Moreover, the stator always contributes energy to the grid. However, the power flows to the grid at super-synchronous speed, while power is fed back to the rotor at sub-synchronous speed.

3.3.2. Converter

In recent years, the development of converter topologies has been explored and utilised in wind turbines. There are five categories targeted as becoming mainstream use: multilevel converters, back-to-back PWM converters, matrix converters, tandem converters and resonant converters. In this sub-section, the back-to-back PWM converter, as the most popular among the mentioned converters, will be introduced in detail.

In order to properly control DFIGs, it is important to understand the working principle and characteristics of the converter. The back-to-back PWM converter consists of a grid side converter and a rotor side converter with an intermediate DC voltage link. The GSC controls the DC-link voltage and reactive power fed from the grid or converter, whereas the RSC separately controls the active and reactive power of the

induction generator [71]. Fig. 3.7 shows a simplified layout of a RSC; the active power and reactive power control are achieved by controlling the reference d-axis rotor current i_{dr_ref} and reference the q-axis rotor current i_{qr_ref}.

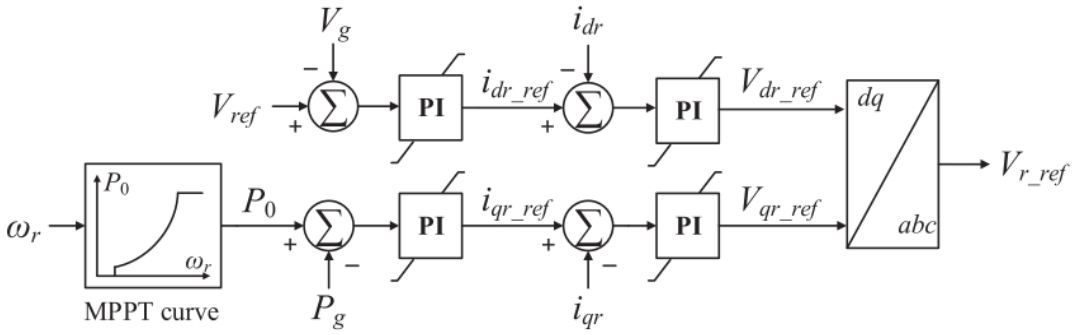

Fig. 3.7: Layout of a rotor side converter [72].

The size of the converter does not depend on the total power output from the generator but on the selected speed range and hence to the slip power. Thus, the cost of the converter increases when the speed range around the synchronous speed widens. The selection of the speed range is therefore based on the economic optimisation of investment costs and on increased efficiency [66].

Furthermore, the most suitable and common model for electromechanical stability analysis in a large power system is the average model. This approach ignores the switching dynamic of converters and represents it as a three-phase voltage source at the voltage source converter terminal.

Fig. 3.8 shows a basic three-phase voltage source converter model. Since phase voltage is used in the figure, the phase lock loop (PLL) angle θ_{PLL} is needed for the transformations between the abc and dq reference frame. The control system behind this voltage source (shown in Fig. 3.8) is achieved by linear control strategies. The dynamic equation of the electric circuits as well as the linearised control are depicted in synchronous frame dq. If the direct axis aligns to phase A of the terminal converter voltage, then the active power injection control is decoupled from the reactive power injection control.

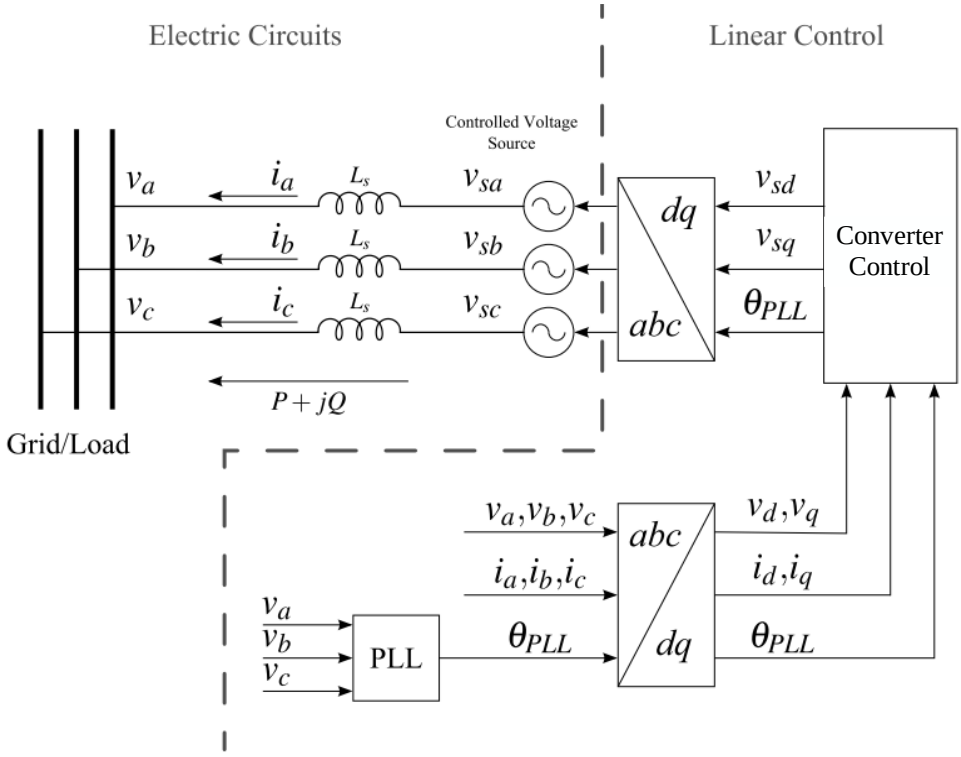

Fig. 3.8: A three-phase voltage source converter – a basic model [73].

The transformation between three-phase reference frame *abc* and synchronous reference frame *dq* can be presented as follows:

$$\begin{bmatrix} v_d \\ v_q \end{bmatrix} = \frac{2}{3}\begin{bmatrix} \sin\theta & \sin(\theta-\frac{2}{3}\pi) & \sin(\theta+\frac{2}{3}\pi) \\ \cos\theta & \cos(\theta-\frac{2}{3}\pi) & \cos(\theta+\frac{2}{3}\pi) \end{bmatrix} \cdot \begin{bmatrix} v_a \\ v_b \\ v_c \end{bmatrix} \tag{3.7}$$

3.3.3. Transformer

The output voltage of wind turbines is not adapted for a low or medium voltage network. However, the turbine voltage of wind turbines is normally fitted for low voltage levels [74]. Therefore, a transformer is required to connect the turbine voltage with an external grid. Fig. 3.9 shows three different types of transformer connections, each of which has its advantages and disadvantages. The first type is a single secondary winding transformer, which adapts different low voltage range to the external network. However, the size of the transformer needs to satisfy the full power of the DFIG. The second type of transformer is only rated at approximately 30% of the wind turbine power due to the connection of rotor and grid. However, the voltage level of the stator winding needs to be the same as the external network, which is the

main inflexibility of this transformer. The last configuration is the most complicated and expensive one among these three types because the stator voltage and PEs utilised have to be fit to accommodate various voltage levels [75]

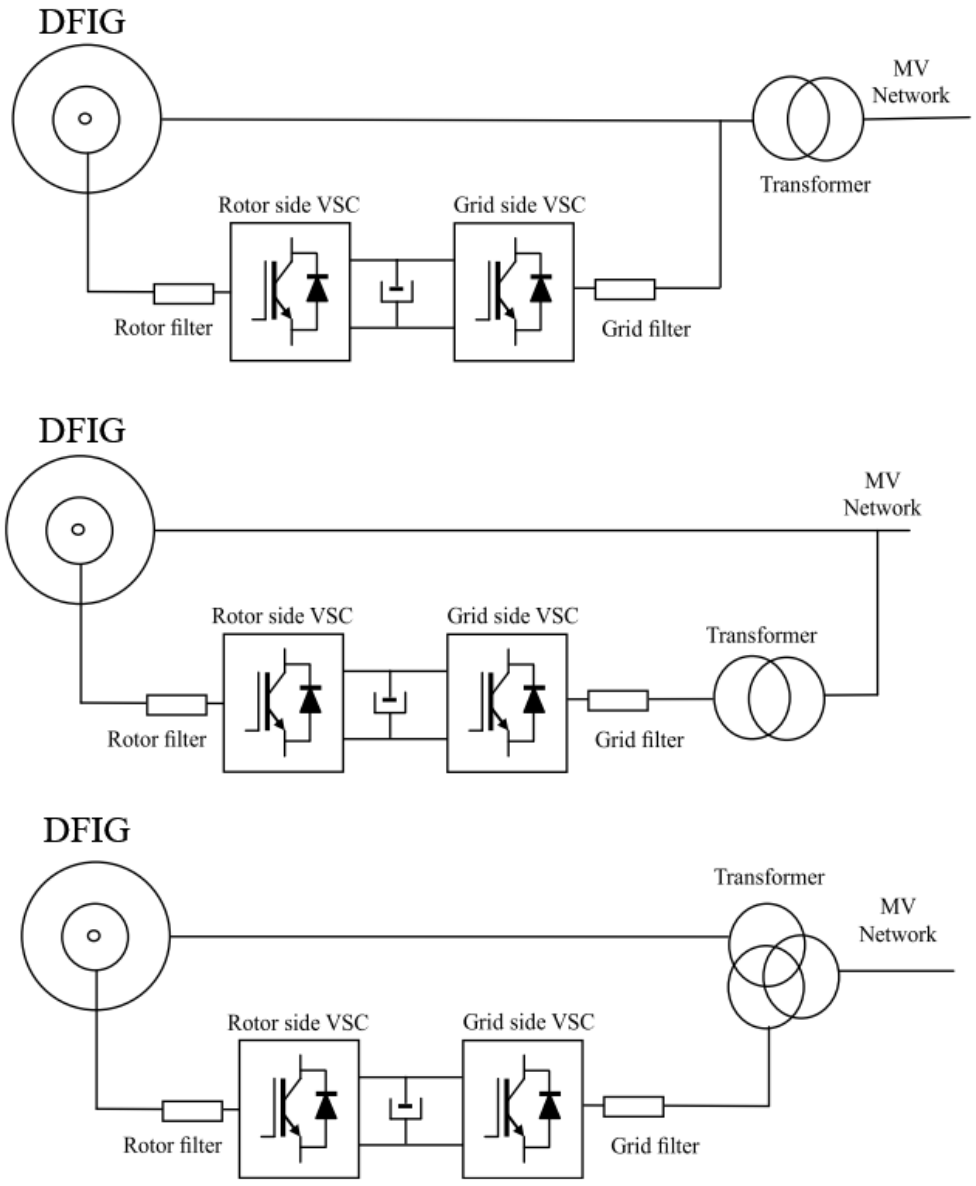

Fig. 3.9: Three types of transformer connection [61].

3.3.4. Crowbar protection

A crowbar is implemented to protect the RSC during the fault period (i.e. voltage dip), in which the DFIG operates at a fix speed mode and absorbs a large amount of reactive power from the grid or other sources [76].

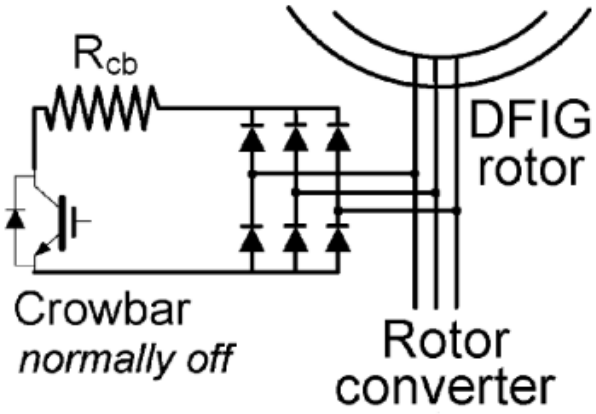

Fig. 3.10: Crowbar circuit [77].

As Fig. 3.10 shows, the crowbar is connected to the rotor windings of the DFIG in a closed circuit at a designated resistance, diverting current from the RSC and quickly deenergising the rotor. Under normal conditions, the switch is open. When a rotor current or DC-link voltage exceeds their maximum reference values, the switch is closed to protect the RSC. The activation period typically lasts for approximately 120 ms, which can result in a 100 ms postfault period of at least 50% reactive power abortion and associated voltage suppression [77].

3.4. Steady state DFIG model

The induction generator is a key component of a variable speed drive system. In this section, the steady state equivalent circuit of a DFIG is presented in detail (see Fig. 3.11). For simplicity purposes, only one phase of the stator and rotor three-phase windings will be described. Under normal operating conditions, the induced voltages and currents in the rotor windings have f_r frequency, whereas the applied voltages and currents in the rotor also have f_r frequency. Also, the relations between the stator frequency f_s and rotor frequency can be represented as:

$$f_r = sf_s \tag{3.8}$$

where s is the slip. In general, f_s is constant since the stator winding of the DFIG is directly connected to the grid and the rotor frequency is a variable which is determined by (3.8). Thus, impedance $X'_{\sigma s}$ also relies on the speed of the generator.

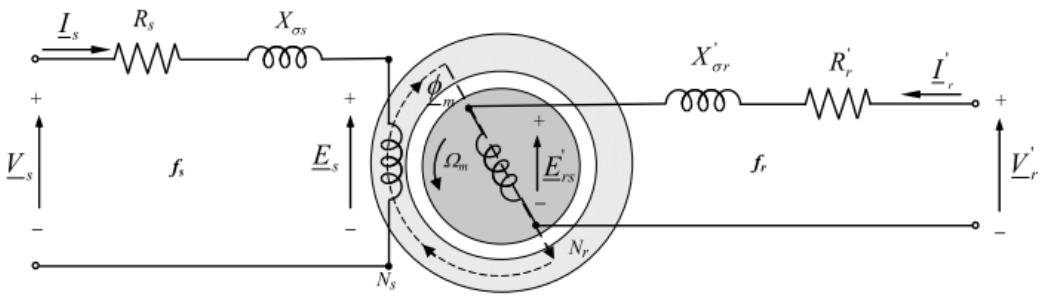

Fig. 3.11: One phase steady state equivalent of a DFIG with various stator and rotor frequencies [70].

To describe the steady state voltage and current magnitudes, the following classic phasor theory parameters are used:

$\underline{V}_s, \underline{V}'_r$ Supplied stator and rotor voltage

$\underline{I}_s, \underline{I}'_r$ Induced stator and rotor current

$\underline{E}_s, \underline{E}'_{rs}$ Induced emf in the stator and rotor

And electric parameters of the stator and rotor are depicted as:

R_s, R'_r Stator and rotor resistance

$X_{\sigma s}, X'_{\sigma s}$ Stator and rotor leakage impedance

N_s, N_r Stator and rotor winding's number of turns per phase

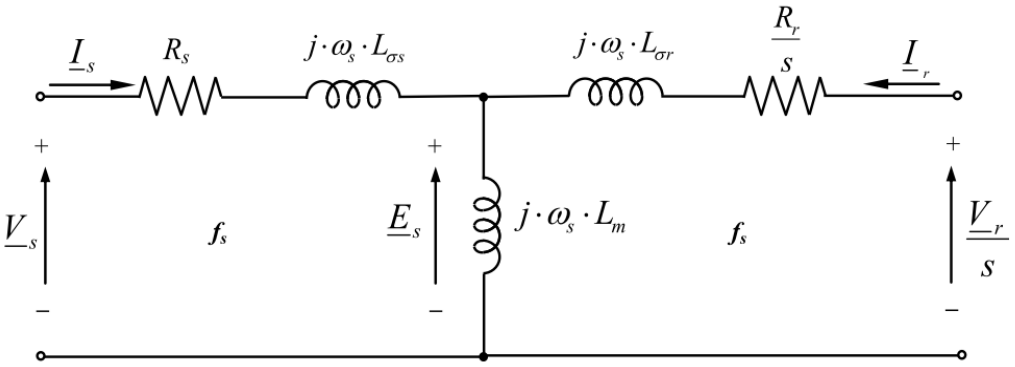

Fig. 3.12: One phase steady state equivalent circuit of the DFIG referred to the stator [70].

The induced voltage E is determined by the flux $\varnothing$ variation and number of turns N. Therefore, the induced voltage $\underline{E}_s$ in the stator windings and induced voltage in the rotor windings $\underline{E}_r^{'}$ can be expressed as:

$$\underline{E}_s = \sqrt{2}\pi K_s N_s f_s \ \varnothing(V_{rms}) \tag{3.9}$$

$$\underline{E}_r^{'} = \sqrt{2}\pi K_r N_r f_r \varnothing(V_{rms}) \text{ EMBED Equation.DSMT4} \tag{3.10}$$

where $\varnothing$ represents the magnetising flux and K_s, and K_r represents the stator and rotor winding factor, respectively.

Two parameters K_s and K_r are approximately identity in the general cases. While in the standstill case, when slip $s=1$, the relation between induced voltages in the stator and rotor windings can be expressed as:

$$n = \frac{\overline{E}_r}{\overline{E}_s} = \frac{N_r}{N_s} \tag{3.11}$$

Therefore, all the parameters in the rotor windings need to be referred to that in the stator windings. (3.12) and (3.13) show the relations between stator and rotor emf from rotor frequency and stator frequency, respectively:

$$\underline{V}_r - sE_s = (R_r + js\omega_s L_{\sigma r})\underline{I}_r \text{ at } f_r \tag{3.12}$$

$$\frac{\underline{V}_r}{s} - E_s = (\frac{R_r}{s} + j\omega_s L_{\sigma r})\underline{I}_r \text{ at } f_s \tag{3.13}$$

where $L_{\sigma r}$ represents the rotor leakage inductance referred to the stator, $\underline{I}_r$ represents the rotor current referred to the stator. Thus, the stator induced emf can be expressed as:

$$E_s = j\omega_s L_m(\underline{I}_s + \underline{I}_r) \text{ at } f_s \tag{3.14}$$

where L_m represents the magnetising inductance of the machine.

3.5. Dynamic modelling of a DFIG

In this section, a dynamic model of a DFIG is presented in [62][78]. The simplified model can be presented as three windings in the stator and rotor, respectively (as shown in Fig. 3.13). The windings are an ideal representation of a real generator, which is used to derive an equivalent electric circuit (as shown in Fig. 3.14).

Therefore, the stator voltage, current and fluxes of the generator can be represented as the following:

$$\begin{aligned} v_{as}(t) &= R_s i_{as} + \frac{d\psi_{as}(t)}{dt} \\ v_{bs}(t) &= R_s i_{bs} + \frac{d\psi_{bs}(t)}{dt} \\ v_{cs}(t) &= R_s i_{cs} + \frac{d\psi_{cs}(t)}{dt} \end{aligned} \tag{3.15}$$

where R_s represents the stator resistance, i_{as}, i_{bs} and i_{cs} represent the stator currents in phase a, b and c, respectively. v_{as}, v_{bs} and v_{cs} represent the applied stator voltages. Also, ψ_{as}, ψ_{bs} and ψ_{cs} represent the stator fluxes.

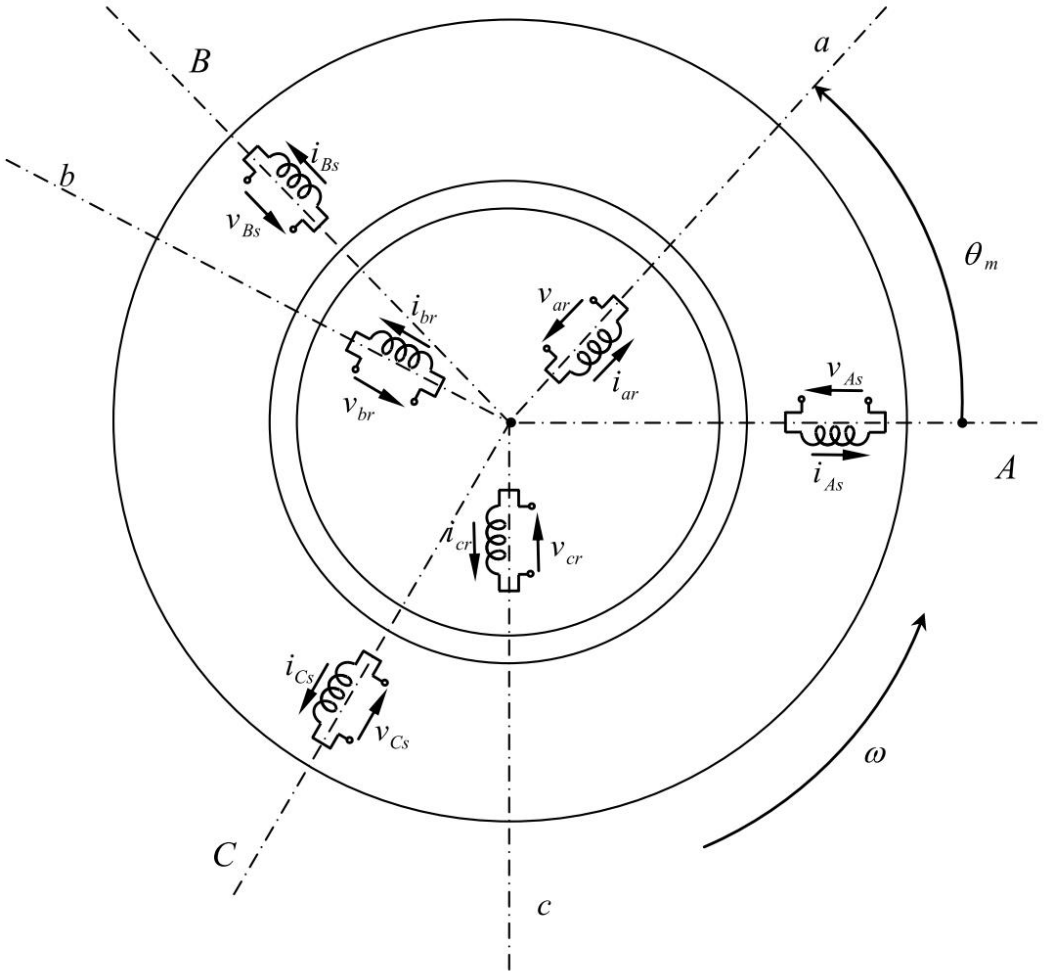

Fig. 3.13: Ideal three-phase windings (stator and rotor) of a DFIG [79].

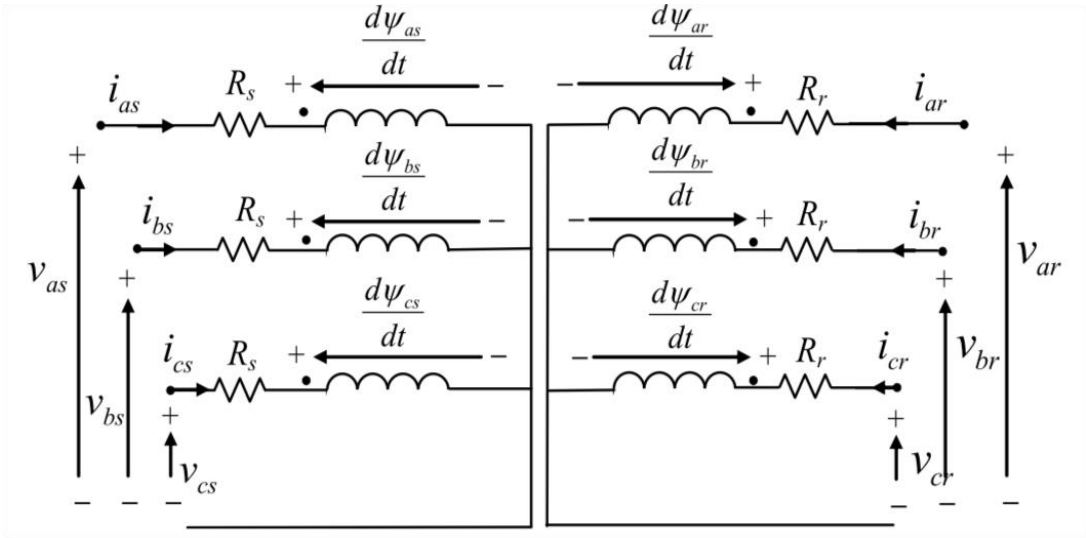

Fig. 3.14: Electric equivalent of a DFIG.

In a steady state, the electric magnitudes mentioned in the stator side have a constant angular frequency imposed by the network.

Also, the electric magnitudes in the rotor can be represented as similar to those in the stator:

$$\begin{aligned} v_{ar}(t) &= R_r i_{ar} + \frac{d\psi_{ar}(t)}{dt} \\ v_{br}(t) &= R_r i_{br} + \frac{d\psi_{br}(t)}{dt} \\ v_{cr}(t) &= R_r i_{cr} + \frac{d\psi_{cr}(t)}{dt} \end{aligned} \tag{3.16}$$

where R_r represents the rotor resistance referred to the stator, i_{ar}, i_{br} and i_{cr} represent the rotor currents referred to the stator in phase a, b and c, respectively. v_{ar}, v_{br} and v_{cr} represent the applied rotor voltages referred to the stator. Also, ψ_{ar}, ψ_{br} and ψ_{cr} represent the rotor fluxes.

3.5.1. Space vector representation

In this section, the differential equations representing the DFIG model are discussed, using the space vector representation notated in the stator reference frame, which is shown as follows:

$$\vec{v}_s^{\,s} = R_s \vec{i}_s^{\,s} + \frac{d\vec{\psi}_s^{\,s}}{dt} \tag{3.17}$$

$$\vec{v}_r^{\,r} = R_r \vec{i}_r^{\,r} + \frac{d\vec{\psi}_r^{\,r}}{dt} \tag{3.18}$$

where $\vec{v}_s^{\,s}$ represents the stator voltage space vector, $\vec{i}_s^{\,s}$ represents the stator current space vector and $\vec{\psi}_s^{\,s}$ represents the stator flux space vector. $\vec{v}_r^{\,r}$ represents the rotor voltage space vector, $\vec{i}_r^{\,r}$ represents the rotor current space vector and $\vec{\psi}_r^{\,r}$ represents the rotor flux space vector. Equation (3.17) is represented in the $\alpha\beta$ reference frame (stator coordinates), while Equation (3.18) is represented in the DQ reference frame (rotor coordinates).

Also, the relation between fluxes and current represented in the space vector can be described by:

$$\vec{\psi}_s^{\,s} = L_s \vec{i}_s^{\,s} + L_m \vec{i}_r^{\,s} \tag{3.19}$$

$$\vec{\psi}_r^{\,r} = L_m \vec{i}_s^{\,r} + L_r \vec{i}_r^{\,r} \tag{3.20}$$

where L_s and L_r represent the stator and rotor inductances, respectively, and L_m represents the magnetising inductance.

3.5.2. The *dq* model

To convert the Equation (3.17) and (3.18) from space reference frame to the synchronous reference frame, multiply each equation by $e^{-j\theta_s}$ and $e^{-j\theta_r}$, respectively. Thus, the stator and rotor voltage can be described as:

$$\vec{v}_s^{\,a} = R_s \vec{i}_s^{\,a} + \frac{d\vec{\psi}_s^{\,a}}{dt} + j\omega_s \vec{\psi}_s^{\,a} \tag{3.21}$$

$$\vec{v}_r^{\,a} = R_r \vec{i}_r^{\,a} + \frac{d\vec{\psi}_r^{\,a}}{dt} + j\omega_r \vec{\psi}_r^{\,a} \tag{3.22}$$

Moreover, the relation between fluxes and current represented in the synchronous reference frame is the same as Equations (3.19) and (3.20):

$$\vec{\psi}_s^{\,a} = L_s \vec{i}_s^{\,a} + L_m \vec{i}_r^{\,a} \tag{3.23}$$

$$\vec{\psi}_r^{\,a} = L_m \vec{i}_s^{\,a} + L_r \vec{i}_r^{\,a} \tag{3.24}$$

In the above equations, the super script "*a*" means space vectors referred to the synchronous reference frame. In a steady state, the voltage, current and flux magnitudes are maintained at a constant in the *dq* modelling. However, the voltage,

current and flux magnitudes are sinusoidal magnitudes in the space vector representation.

3.6. DFIG modelling in DIgSILENT PowerFactory

According to the discussion above, a DFIG based wind farm is modelled in DIgSILENT PowerFactory and used for simulation. Therefore, the modelling is quite important for frequency response studies. Additionally, the wind turbine aerodynamic is accurately remodelled to ensure the precision of simulation results. In this study, smart frequency controls contributed by wind turbines are one of the main research directions considered. In addition, the aerodynamic system of DFIGs is of importance and simplified using DSL. Different inertial controls (e.g. synthetic inertia control, droop control) are derived based on [80] in this section.

The adopted framework of the DFIG based on the WECS is shown in Fig. 3.15. The main framework consists of four main parts: mechanical controllers, electrical controllers, mechanical parts and electrical parts. The framework is built in DIgSILENT for the sake of dynamic response studies. It can be seen that the electrical part is represented as a ‘DFIG’ block, which includes the electrical generator and voltage source converters employed. In other words, the ‘DFIG’ block can be treated as a static generator in DIgSILENT. Compared to conventional generators, the active power reference of a DFIG depends on wind speed, aerodynamic system and MPPT strategy. The MPPT strategy is then determined by pitch angle and blade length, with the pitch angle depicted in Equation (3.2) and Equation (3.3). Next, the response speed of the MPPT control is determined by the time constant of mechanical parts, which is circled by the blue dash line. It is also noted that this mechanism is only considered for those times that follow a power deficit event. In more detail, the response time of the adopted MPPT strategy is the same as that of the conventional strategy in a normal conventional system due to the constant pitch angle always used during the simulation. Moreover, the ‘Inertia emulator’ block will be discussed in the latter chapter 5.2 as the type of block will be changed in different studies.

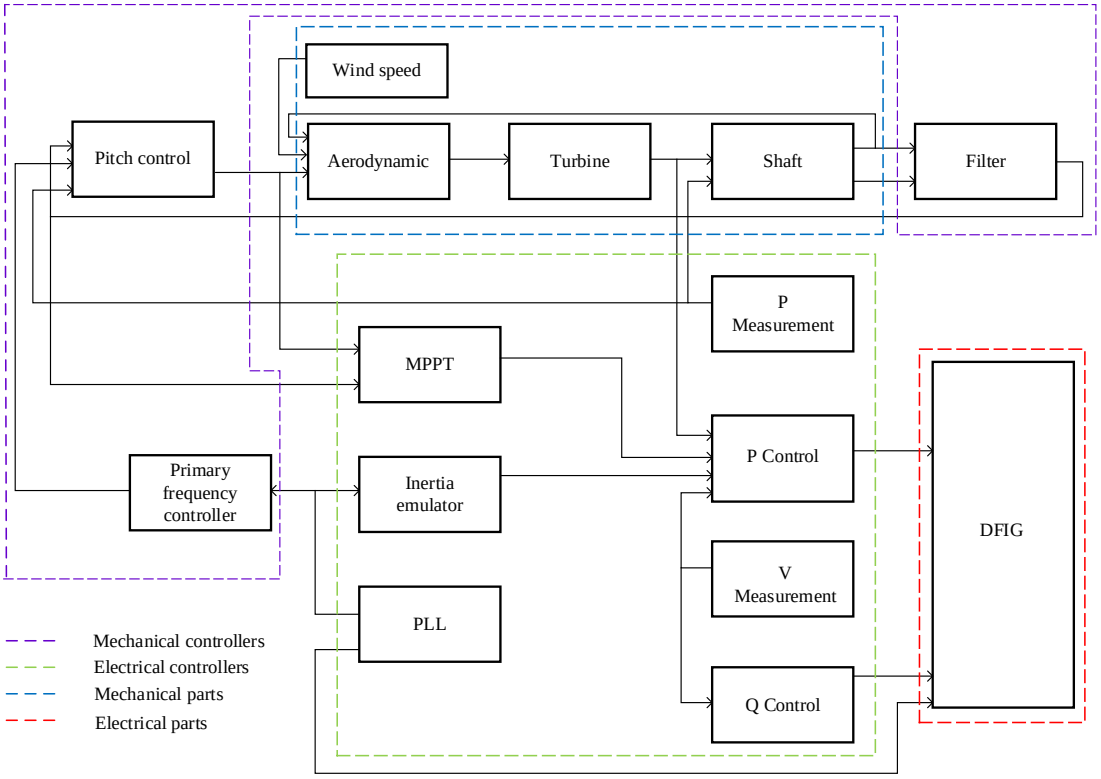

Fig. 3.15: Framework of the DFIG based the WECS modelled in DIgSILENT.

3.6.1. Primary frequency controller of the WECS

The primary frequency controller of the WECS shown in Fig. 3.16 is similar to the governor in a synchronous generator. The input signal is the frequency deviation from its nominal value and *R* is the droop parameter. A deadband is used first. Tdelay represents a governor time delay and ymax represents the maximum reserve power of a wind turbine. The rate of change of active power is restricted by a 'Rate Limits' block. The primary frequency controller parameters are shown in Table 3.1.

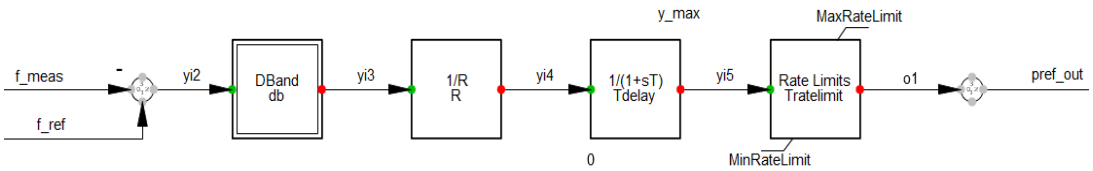

Fig. 3.16: Schematic of the primary frequency controller modelled in DIgSILENT.

Table 3.1: Parameters of the primary frequency controller.

Parameter	Value	Unit
db	0.0001	*pu*

Tdelay	1	s
MaxRateLimit	0.1	*pu*/s
MinRateLimit	-1	*pu*/s
R	0.05	*pu*
Tratelimit	0.02	s
ymax	0.1	*pu*

3.6.2. Pitch controller for the WECS

A schematic of the pitch controller for the WECS is modelled in Fig. 3.17. The input signal for the pitch controller is the speed deviation between the measured and reference generator speed. Then, the beta_speed representing the reference angle is obtained by using the blade angle controller. dbeta is the angle deviation between the reference and measured angle. Then, the servo motor spins the blades with the amount of reference angle and Tp is the servo time constant. The beta is finally obtained after applying the restriction to the rate of change of the angle and angle change range.

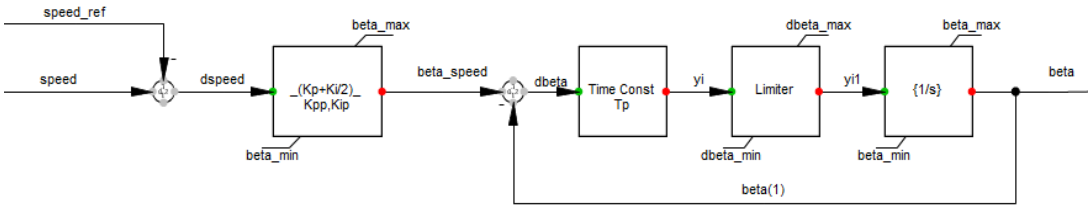

Fig. 3.17: Schematic of the pitch controller modelled in DIgSILENT.

Table 3.2: Parameters of the pitch angle controller.

Parameter	Value	Unit
Kpp	150	*pu*
Kip	25	s
speed_max	1.2	*pu*
beta_max	10	degree/s
beta_min	-10	degree/s
Tp	0.01	s
dbeta_max	27	degree
dbeta_min	0	degree

It should be noted that the pitch angle does not change instantaneously but only at a finite rate (as shown in Fig. 3.17). This is because the size of blades is rather large in modern wind turbines. Also, the blades drives are usually made as small as possible to save costs. Furthermore, the pitch angle controller is active when wind farms experience high wind speeds. In this regard, the rotor speed is no longer controlled by increasing the generated active power due to potential generator overload. The pitch angle is used to limit the aerodynamic efficiency of the rotor, which prevents the rotor speed from reaching its maximum limit.

3.6.3. Aerodynamic system of the WECS

The aerodynamic system of the WECS is modelled in the 'aerodynamic' block in Fig. 3.15.

The equation used to calculate the active power of turbine $P_{turbine}$ is shown as follows:

$$P_{turbine} = \frac{1}{2}\pi\rho\frac{C_{pmax}}{\lambda_{opt}^3}R_{blade}^5\omega_t^3 \tag{3.25}$$

where C_{pmax} is the maximum aerodynamic coefficient and λ_{opt} is the optimum tip speed ratio.

3.6.4. Drive train of the WECS

The drive train system of the WECS consists of 'Turbine' and 'Shaft' blocks (as shown in Fig. 3.15). The wind turbine blades are installed hub directly connected to the wind turbine's shaft. For a wind turbine, the wind turbine shaft rotates slower than the generator shaft. Therefore, a gear box is connected to two of these shafts. Table 3.3 shows the parameters of the drive train modelled in DIgSILENT. K_{shaft} and D_{shaft} represent the total shaft stiffness and total shaft damping coefficient, respectively. In the simulations, K_{shaft} will be set as a small value to reduce the frequency oscillations.

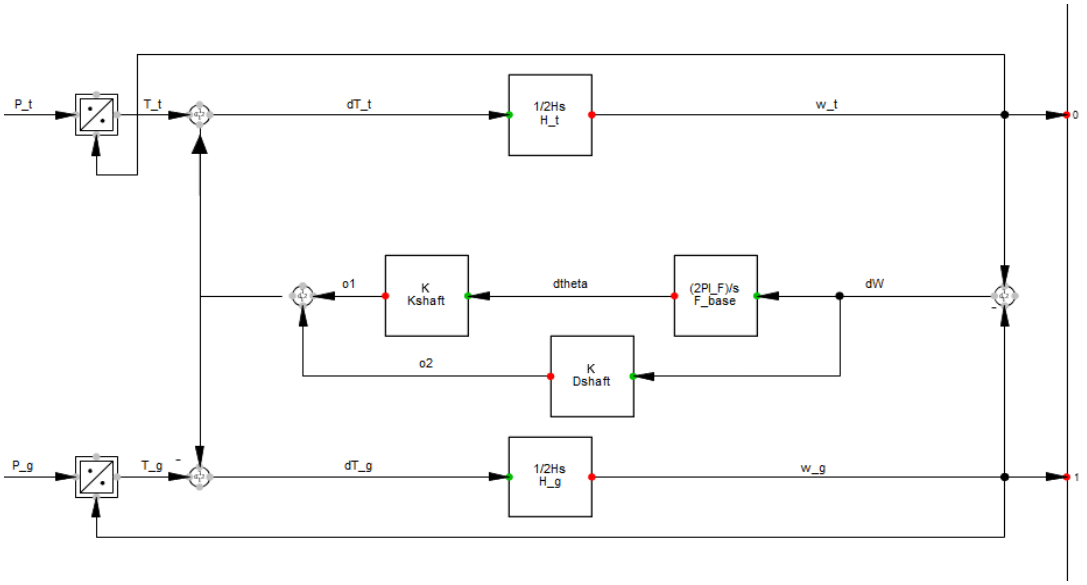

Fig. 3.18: Schematic of a drive train modelled in DIgSILENT.

Table 3.3: Parameters of the drive train.

Parameter	Value	Unit
F_base	50	Hz
Kshaft	80.27	*pu*/rad
Dshaft	1.5	*pu*
H_g	0.75	s
H_t	4.02	s

3.6.5. Filter for the WECS

High-frequency speed variation are continuously occurring, particularly when wind speed variations are frequent. The ‘Filter’ block shown in Fig. 3.15 is a low pass filter with a time constant T_filter of 0.2.

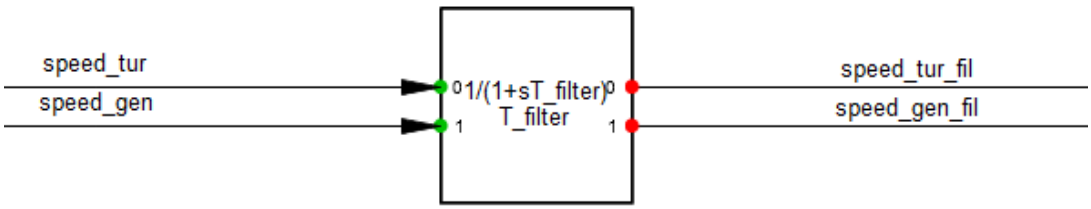

Fig. 3.19: Schematic of the filter modelled in DIgSILENT.

3.6.6. MPPT for the WECS

In this section, the main part of the 'MPPT' block is shown and introduced. The P_{mpt} is dependent on the following equations:

$$P_{mpt}=\begin{cases}0 & 0<\omega_r<\omega_{\min}\\ k_{opt}\omega_r^3 & \omega_{\min}<\omega_r<\omega_1\\ \dfrac{P_{max}-k_{opt}\omega_1^3}{\omega_{max}-\omega_1}(\omega_1-\omega_{max})+P_{max} & \omega_1<\omega_r<\omega_{\max}\\ P_{max} & \omega_r>\omega_{\max}\end{cases} \tag{3.26}$$

$$k_{opt}=\frac{1}{2}\pi\rho\frac{C_{pmax}}{\lambda_{opt}^3}R^5 \tag{3.27}$$

The input signal is the filtered generator speed ω_{gen_fil} and pitch angle β. Also, P_{mpt} is determined by the rotor speed value. The relationship between ω and active power output of wind turbines P is shown in Fig. 3.20. $\omega_{\min}$ is the start-up rotor speed of wind turbines. ω_1 is the maximum rotor speed when the wind turbine operation follows the MPPT curve. $\omega_{\max}$ is the maximum limit of the rotor speed during operation, which is slightly larger than ω_1. Furthermore, a 'Rate limiter' block is needed, with the MaxRateLimit and MinRateLimit 0.1 *pu*/s and -1 *pu*/s, respectively. The wind turbine model provided by PowerFactory DIgSILENT is not accurate enough to implement simulations. When $\omega_r>\omega_{\max}$, the $P_{\max}$ is neglected in the existing model.

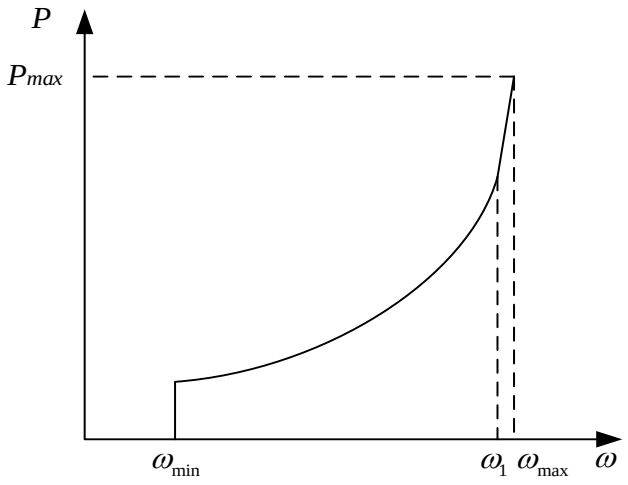

Fig. 3.20: Relationship between ω and active power output of wind turbines P.

3.6.7. Dynamic-droop based control of the WECS

In the later Chapter 5.3, a dynamic droop based control is built in the WECS, which aims to provide temporary energy support on the information of RoCoF. And the impacts of built control on the mitigation of SFD will be evaluated. The following equations shown as follows are added in control block.

$$\Delta P = -\frac{1}{R(df/dt)}(f_{mea} - f_{nom})$$

$$R = \begin{cases} R1 & RoCoF \le -0.1Hz \\ R2 & RoCoF > -0.1Hz \end{cases}$$

The ΔP represents the wind power output, and droop parameter R changes according to the RoCoF. To be more specific, R1 is a relatively small value if the RoCoF is less and equal to -0.1 Hz due to a large ΔP is needed to fast decline the frequency dip. On the contrary, a large value of R2 is used to reduce the temporary increased wind power, which leads a smoother power transition.

3.6.8. Phase-locked loop (PLL) of the WECS

The PLL of the WECS is used to measure the terminal voltage angle and frequency of wind turbines. The schematic of the PLL is shown in Fig. 3.21. The K_p and K_i parameters of this PLL are 5 and 100, respectively.

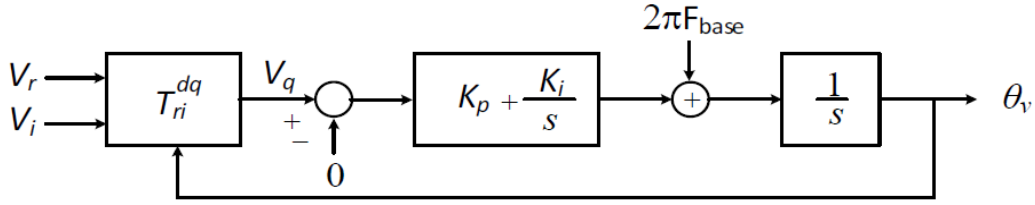

Fig. 3.21: Schematic of the PLL modelled in DIgSILENT.

3.6.9. P control of the WECS

As shown in Fig. 3.22, the schematic of the P control is modelled in DIgSILENT. For the sake of simplicity in studying the system response of a large system, this block removes the current and power control loops in electrical controllers related to the VSC. The input signals are the MPPT power, reference power output from the 'Inertia

emulator' block (shown in Fig. 3.15), and the terminal voltage of the wind turbines. Therefore, the current component of the *d*-axis of the generator can be obtained.

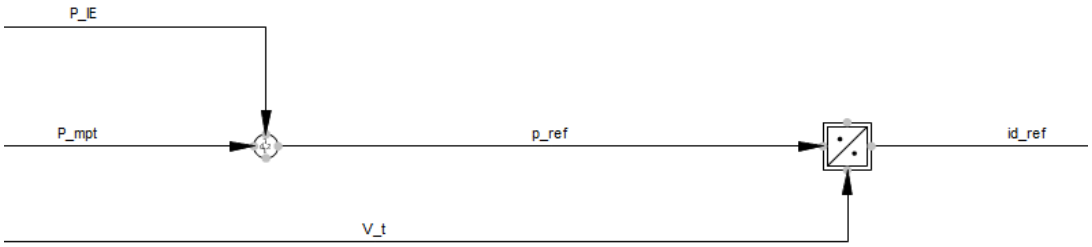

Fig. 3.22: Schematic of the P control modelled in DIgSILENT.

3.6.10. Q control of the WECS

The Q control of WECS (shown in Fig. 3.23) is used to obtain the reference reactive power. The input signals are the terminal reference and measured voltage of the turbine, and the initial reactive power. Also, parameter K can be zero or non-zero and the WECS can be either the PQ or PV type in turn [81]. The parameters of the Q control are presented in Table 3.1

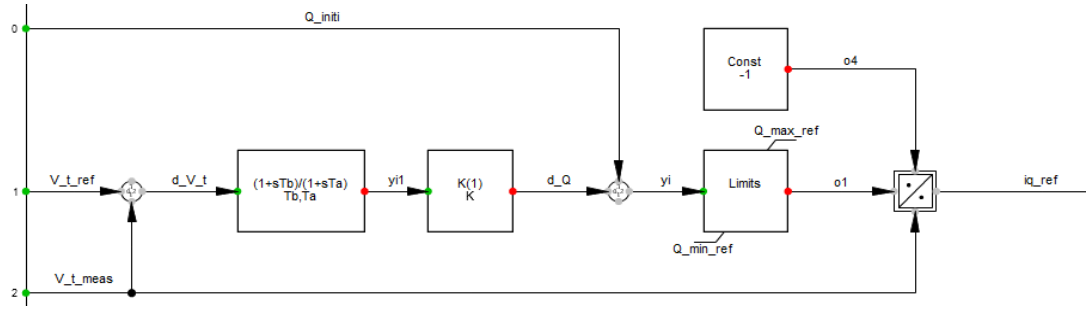

Fig. 3.23: Schematic of the Q control modelled in DIgSILENT.

Table 3.4: Parameters of the Q control.

Parameter	Value	Unit
Ta	1	s
Tb	10	s
K	200	/
Q_ref_max	0.435	*pu*
Q_ref_min	-0.435	*pu*

3.7. Chapter summary

This chapter has discussed the general structure and characteristic aspects of DFIG, presenting the basic ideas and concepts to understand the working principle of doubly fed induction generators. Next, the adopted models mainly focused on the mechanical system and electric system are in help of creating simulation dynamic models, to execute the computer-based simulations in DIgSILENT. A steady state model was discussed with an equivalent circuit. On the other hand, the dynamic model of DFIG has been derived and presented from different referential frames. In addition, the adopted models utilised in DIgSILENT were also introduced in detail.

Chapter 4 Smart Frequency Control of DFIGs

To investigate the capability of existing smart frequency control schemes, this chapter summarises different control approaches based on reserved kinetic energy types. All these studies indicate, or prove that applying additional and adequate frequency control mechanisms enhances the frequency stability when the power system is subjected to a frequency event, e.g. loss of a generator or the sudden connection of a large load. One of the most important requirements is that the WECS should provide frequency support that is normally delivered by conventional synchronously operating generating units. Fig. 4.1 shows the frequency response techniques presented in this chapter.

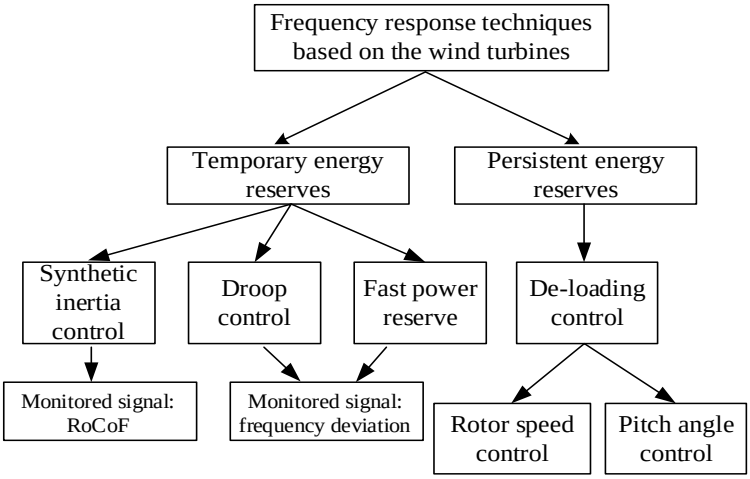

Fig. 4.1: Classification of frequency response techniques.

Section 4.1 presents the maximum power point tracking technique that wind turbines operate at. Section 4.2 presents a brief introduction to synthetic inertia control and indicates the differences between them. Section 4.3 introduces the primary frequency

responses of wind power integrated power systems. Also, the sub-sections in Section 4.3 are classified into temporary energy reserves and persistent energy reserves. Section 4.4 presents the emerging control techniques to arrest secondary frequency dips brought by the termination of primary frequency support. Section 4.5 concludes this chapter.

4.1. Maximum power point tracking

In this section, the *MPPT technique*, based on the wind speed estimation, is introduced [82], [83]. This technique is used to determine the maximum power that can be delivered from a wind turbine under different wind speeds. The MPPT curve shown in Fig. 4.2, i.e. the blue curve, can be divided into four operational sections. The first section (M-N) corresponds to conditions in which the active power contributed by the wind turbine follows a linear trend. Then, the wind turbine starts operating at its MPPT mode (N-P), contributing maximum power to the grid. In the third section (P-Q), the wind turbine operates at a constant rotor speed regime in order to avoid rotor overspeed. It is worth noting that the wind power available at high speeds may exceed the power indicated by the MPPT curve. If wind speed exceeds the rated value (Q), the constant power mode is switched on to guarantee a rated output power.

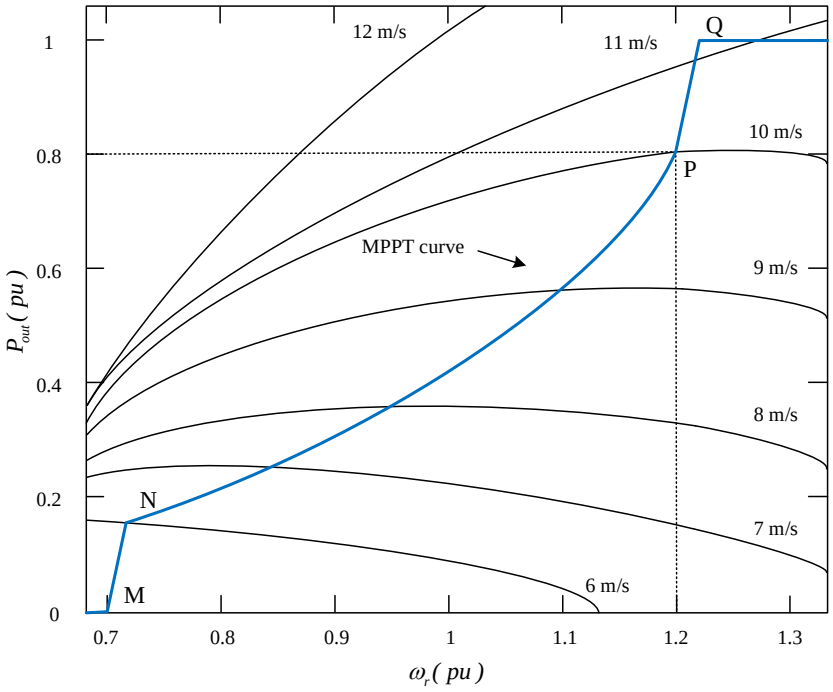

Fig. 4.2: Active power-rotor speed curve of a DFIG under different wind speeds [84].

Considering the intermittence of captured wind power [85], the reduction of turbine mechanical stress [86], interaction between conventional and renewable power plants [87] and wind direction conditions [88], more precise MPPT model can be deployed to improve wind energy production.

4.2. Synthetic inertia control

It is a well-established fact that the kinetic energy stored in the rotating blades of a wind turbine will not automatically participate in regulating frequencies in the power system. Nevertheless, variable speed wind turbines can easily emulate a similar inertial response to that of synchronous generating units by implementing appropriate control mechanisms [89]. Therefore, the synthetic inertia control is also known as natural inertial control [83]. This is to maintain system frequency within a permissible range upon generation losses resulting in an active power imbalance in the power system. This can be accomplished by monitoring the RoCoF and properly adjusting the active power delivered to the grid. In [90], the term synthetic inertia is defined as controlling active power from a unit such that it is proportional to the RoCoF at the terminal of that unit. A one-loop inertial response and two-loop inertial response are two common designs frequently addressed. The extra active power delivered by the one-loop control is proportional only to the measured RoCoF [90]–[94]. Detecting both the RoCoF and frequency deviations will be required in the two-loop control design [95], [96]. A one-loop control design is presented in Fig. 4.3. The synthetic inertia active power P_{in} contributed from the additional control loop is shown in the upper dashed block. Being proportional to the RoCoF and synthetic inertia constant H_{in}, this power is calculated as follows:

$$P_{in} = 2H_{in} \times \frac{d\omega_{sys}}{dt} \times \omega_{sys} \tag{4.1}$$

The lower block represents how the active power is delivered by the wind turbine. Denoted by P_{MPPT}, this power is determined by a PI controller that compares the measured rotor speed, $\omega_{r,meas}$, with a reference rotor speed, $\omega_{r,ref}$.

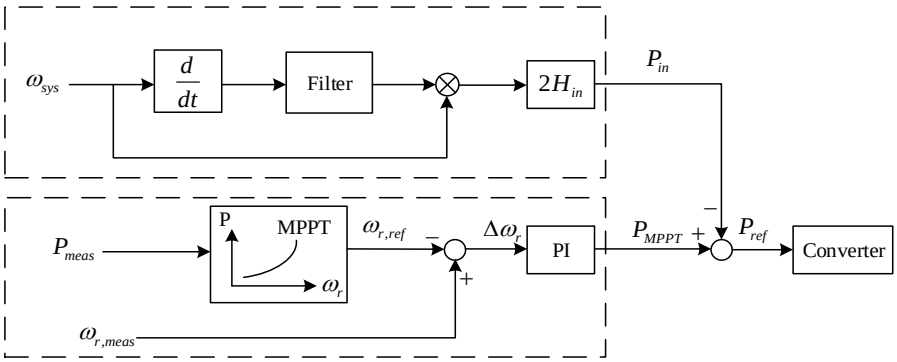

Fig. 4.3: Synthetic inertia one-loop control design [97].

In [98], the authors propose an advanced two-loop synthetic inertia control approach. In this design, the extra active power, P_{extra}, is determined by two loops, i.e., the RoCoF loop and the droop loop, as shown in Fig. 4.4. As demonstrated in the upper block in Fig. 4.4., the RoCoF and the frequency deviation Δf are obtained by directly measuring the grid frequency. Here it is essential to have an accurate approach to measure its frequency and its rate of change. Among a number of numerical algorithms for their measurement, those based on parameter estimations demonstrate a high level of robustness and accuracy [99]–[103]. The synthetic inertia is proportional to the inertia constant K_{in}, as shown below:

$$P_{in} = -K_{in}\frac{df}{dt} \tag{4.2}$$

The second control loop adds additional power, P_d, which is calculated as follows:

$$P_d = -\frac{1}{R}\Delta f = -K_d \Delta f \tag{4.3}$$

In this respect, an activation scheme is proposed in [98] that uses an 'over/under frequency trigger' and 'maximum frequency gradient trigger' to provide better frequency control following a generation disturbance.

RoCoF, as one of the inputs of synthetic inertia controls, its measurement accuracy plays an important role. As with any measurand, a user would ideally wish for noise- and error-free data which is available with minimum delay (or latency). However, the measurement of frequency and RoCoF is particularly sensitive to power system disturbances and noise. Since they respectively are the first and second derivative of the measured phase, any noise in the phase measurement is amplified in the frequency

and RoCoF measurement. This can lead to erroneous control and protection actions, such as false tripping of distributed generation and false load shedding when used as inputs to power balance management schemes. In this research, the natural inertial response originated from conventional generation decreases as the increase of wind power source, which limiting the frequency response ability of power systems to respond to sudden disturbances. The performance of synthetic inertia control providing the "Synthetic Inertia" highly depends on the RoCoF measurement, which must be able to identify a genuine RoCoF caused by disturbances. This requires the use of long filtering windows of the order 500 ms to provide robust data such that there is no doubt that the synthetic inertia will operate when required to do so, while continuing normal service during spurious disturbance events [104]. This filtering delay unfortunately prevents an active power response within the window latency, which in turn delays the onset of the "inertial" response of the converter. Yet, synthetic inertia control still contributes kinetic energy before the primary response of the synchronous machine governors and thus doing so with a higher ramp rate. Therefore, this generator response is able to fast contribute needed power to decline the frequency drop caused by the disturbance. Moreover, ENTSO-E recommends that accuracies for frequency of the order of 10 mHz [105].

There are a number of advantages to applying one- or two-loop synthetic inertia controls. Both enable the wind turbine to participate in the frequency control process, thereby reducing the RoCoF and delaying/removing the need for UFLS in the system. Nonetheless, the two-loop control provides additional power proportional to frequency deviation Δf , which more precisely emulates synchronous generators' behaviour and guarantees returning the grid frequency back to nominal frequency as much as possible. This method is implemented based on the real-time measurement of the frequency magnitude or RoCoF value.

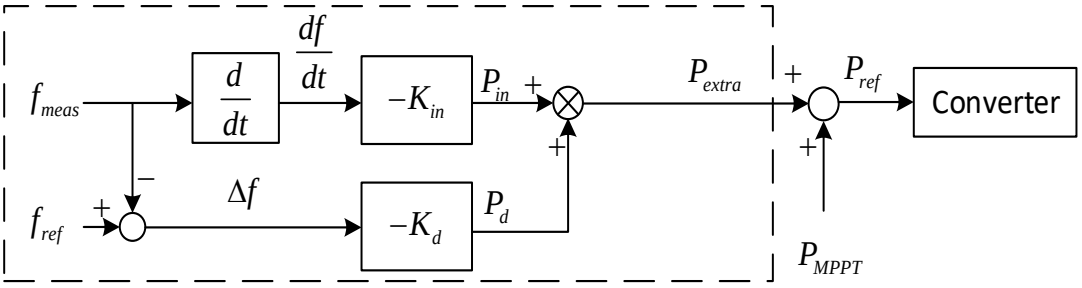

Fig. 4.4: Synthetic inertia two-loop control design [98].

Compared to the non-synchronous generators, synchronous generating units as such nuclear power, thermal power and hydroelectric power plant have a relatively slow response speed of power generation, which significantly limits the capability of providing such services. Therefore, the frequency can be brought back to nominal frequency in a longer time but in a smoother power transition. On the contrary, the process of fast change of power generation is required at second time scale for services such as frequency response. Non-synchronous generator such as wind turbine generator is able to instantaneously provide frequency support due to its converter-based connection. However, the problem of having a SFD is inevitable.

4.3. Primary frequency response

Various frequency controls, depending on the different power reserve form, have been proposed so for. The core purpose of all these controls is to overcome frequency instability problems introduced by wind power integration. Indeed, these control mechanisms enable a WECS to effectively contribute to the frequency support in a system, as will be discussed in detail in this section.

4.3.1. Temporary energy reserves

Mandated by the latest grid code (see COMMISSION REGULATION (EU) 2016/631), WECSs are expected to possess the ability to participate in frequency control when needed to limit the RoCoFs [106]. Temporary energy reserves can be realised by resorting to the kinetic energy stored in the wind turbine's rotor. Relating to temporary energy reserves, over recent years, two control approaches have been introduced: a) droop control and b) fast power reserve. The droop control releases some extra power in proportion to the measured frequency deviation. The fast power reserve approach focuses on fast kinetic energy release in a stepwise incremental manner.

4.3.1.1. Droop control

The aim of the droop control is to mimic similar frequency droop characteristics to that of the governor in a conventional synchronous generator and to contribute to both transient and steady-state frequency regulation. References [107]–[113] discuss the performance of frequency support enabled by the droop control. The slope of the

power-frequency droop characteristic affects the FN and frequency recovery after a loss of generation disturbance [111][114]. The droop control alters the wind turbine output and provides frequency support based on grid frequency deviation, Δf . The following equation refers to this behaviour:

$$\Delta P = P_1 - P_0 = -\frac{f_{meas} - f_{nom}}{R} = -\frac{\Delta f}{R} \tag{4.4}$$

where $\frac{1}{R}$ is the droop coefficient, P_0 and f_{nom} are initial wind turbine power and frequency, respectively. Besides, P_1 and f_{meas} are the adjusted wind turbine power and frequency, respectively. Resulting from this control, the wind turbine output power increases from P_0 to P_1 as the system frequency decreases from f_{nom} to f_{meas}. However, the main drawback of this droop scheme is frequency inadaptability due to the fixed gain chosen in the control loop. In other words, if a large gain is used to improve the FN, it may cause unnecessary over-deceleration of the rotor speed.

An improved droop scheme is proposed in [115], aimed at overcoming the insensitivity of the droop loop to the initial frequency deviation, with the droop gain dynamically tuned based on the RoCoF. The relationship between the droop gain and RoCoF is defined for a fixed rotor speed prior to the disturbance. Nonetheless, this still might cause over-deceleration if an additional disturbance occurs. To resolve this, a slightly modified scheme is proposed in [116] in which the adaptive gain is determined with respect to both the RoCoF and rotor speed. The extra active power P_{extra} can be expressed as:

$$P_{extra} = k_{adap}(\frac{df}{dt}, \omega_r) \cdot \Delta f \tag{4.5}$$

where $k_{adap}(\frac{df}{dt}, \omega_r)$ represents the adaptive gain and Δf represents frequency deviation. The adaptive gain is altered with the RoCoF and rotor speed (see Fig. 4.5). Also the adaptive gain takes the maximum value if the RoCoF is less than -0.05 Hz/s and the rotor speed is at its maximum operating speeding speed. Then k_{adap} decreases with both the RoCoF and rotor speed, until the frequency reaches FN. This is to prevent the system from suffering a SFD when rotor speed decelerates to the minimum

operating limit (0.7 *pu*). After reaching the FN, parameter k_{adap} only decreases with rotor speed to guarantee that no excessive kinetic energy will be released. The main advantage of this control scheme is that it maintains the kinetic energy available for a subsequent disturbance.

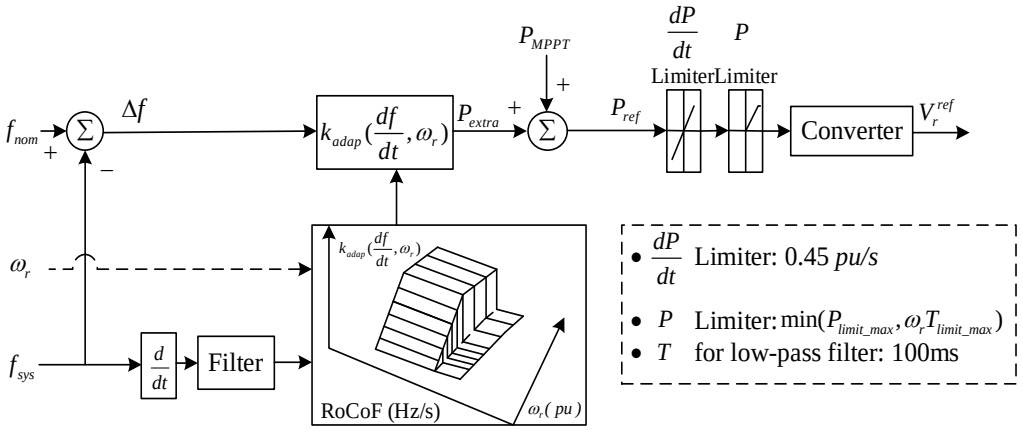

Fig. 4.5: Adaptive short-term frequency support control scheme associated with the concept of an adaptive gain [116].

Reference [111] puts forward a novel time-variable droop scheme. To ensure the pre-disturbance active power reference $P_{ref,pre}$ matches the active power reference generated during the frequency support period, $P_{ref,fs}$, a negative droop is added to the frequency support loop, as shown below:

$$\Delta E_k = \int_{t_{rec}} D'(t)\Delta f(t)dt \tag{4.6}$$

In Equation (4.6), ΔE_k is the kinetic energy change in the wind turbine, $D'(t)$ is the negative droop function and t_{rec} is the recovery time which makes $P_{ref,pre}$ equal to $P_{ref,fs}$. The time-variable droop characteristic follows a function of $\frac{g(t)}{R}$, where $g(t)$ is a properly defined time-variable function. As shown in Fig. 4.6, the droop coefficient remains constant in the first one third of the frequency support period $t_{\sup}$ because maximum wind power is needed to arrest the frequency decline immediately after the disturbance. In the rest of $t_{\sup}$, $g(t)$ is gradually reduced to zero where $P_{ref,pre}$ is still smaller than $P_{ref,fs}$. After system frequency reaches the FN, $g(t)$ continuously decreases to a negative value until $P_{ref,pre}$ matches $P_{ref,fs}$. This gradual droop parameter

change will ensure a smooth exchange of energy between the grid and WECS, in addition to removing the ripples in frequency that otherwise result from cascaded switching caused by the control systems of the WECS.

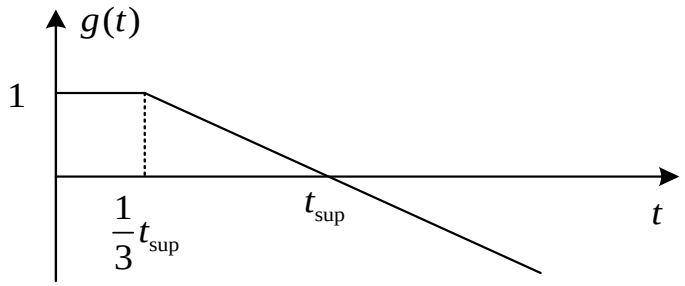

Fig. 4.6: Frequency support control with time-variable droop characteristic proposed in [111].

4.3.1.2. Fast power reserve control

Fast power reserve control is also known as rotor kinetic energy control [117], [118], or step-wise control [83]. In the case of a sudden frequency event, abnormal frequency behaviour can be detected and recovered by temporarily releasing stepwise kinetic energy within a short time window. Compared to a synthetic inertial response, the inertial power using the step-wise control can be properly changed according to different shapes in terms of its magnitude and duration, and thus its temporary frequency support tends to be much faster and stronger [119]–[121].

In [110], delivering some 10% more active power than the nominal active power within 10 seconds is defined as the fast power reserve control, which is implemented to support the frequency following a generation disturbance. The kinetic energy E_k extracted from the wind turbine can be expressed as:

$$E_k = \frac{1}{2} J \omega^2 \tag{4.7}$$

where J and ω are the moment of inertia of the wind turbine and rotor rotational speed, respectively. When a loss of generation disturbance occurs in the power system,

$$\Delta E = P_{const} t = \frac{1}{2} J (\omega_2^2 - \omega_1^2) \tag{4.8}$$

where P_{const} is the constant active power provided by the wind turbine. Besides, t is the fast power delivery time since the disturbance inception, ω_1 represents the rotor rotational speed before the disturbance and ω_2 represents the rotor rotational speed at time t. Therefore, the reference rotor speed is defined as:

$$\omega_{r,ref} = \omega_1 = \sqrt{\omega_2^2 - 2\frac{P_{const}t}{J}} \tag{4.9}$$

as shown in Fig. 4.7. Then the change of rotor rotational speed $\Delta\omega_r$ can be obtained and sent to a PI controller that is used to change the reference active power point P_{ref}.

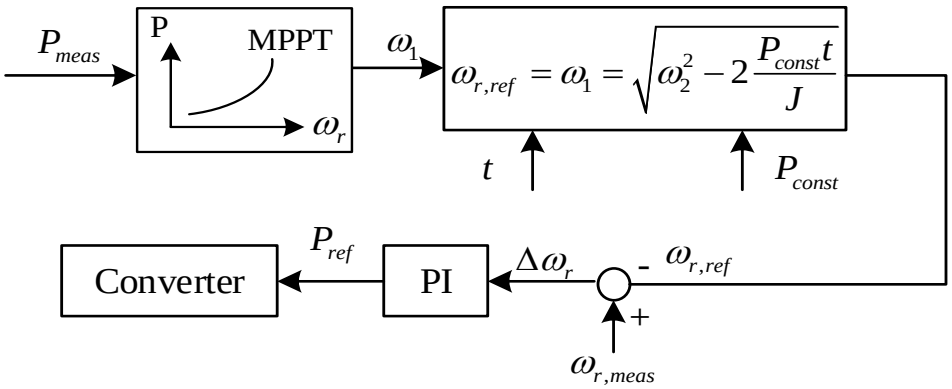

Fig. 4.7: Fast power reserve control loop [110].

A similar approach called temporary over-production approach is presented in [122], addressing the capability of variable speed wind turbines to inject temporary power overproduction. The dashed curve and solid curve shown in Fig. 4.8 are wind turbine (static) production power and a blade's mechanical power under a constant wind speed condition, respectively. The input signal, i.e., the system frequency f, is used to monitor the frequency dip, thus adding active power overproduction ΔP_{OP} to arrest the frequency decline.

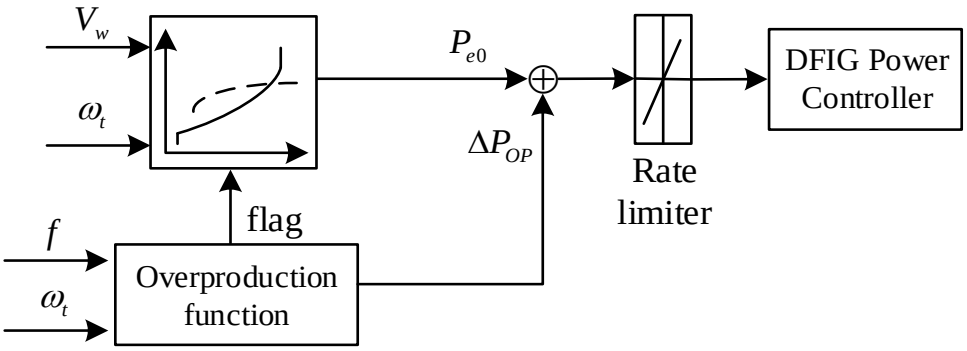

Fig. 4.8: Temporary over-production control [122].

Fig. 4.9 (a) illustrates how the active power changes with the rotor speed, following a sudden frequency event, after implementing the over-production scheme. Frequency support starts at point A. Constant temporary over-produced power ΔP_{OP} is added to the initial reference power point P_{e0} to increase the wind turbine output power to $P_{e0}^{'}$ (between B and C). Once frequency support is no longer required or rotor speed decelerates to its minimum value 0.7 *pu*, the rotor speed starts to recover to its pre-disturbance value from D to E. This results from the application of the accelerating power P_{acc}, which subsequently changes the reference power point to $P_m - P_{acc}$. Indeed, the determination of P_{acc} following the mechanical power trajectory (the blue line) rather than the maximum power point tracking trajectory (the green line) can avoid a SFD due to the smaller active power reduction. Nevertheless, the rotor speed recovery time can be prolonged by applying P_{acc}. Therefore, an optimal trade-off between the rotor speed recovery time and the amplitude of the SFD is deemed necessary.

As the levels of non-synchronous generator increase and synchronous generators continue retiring, system inertia levels are expected to decrease. This introduces a level of vulnerability to failure that could make the grid insecurity. The decreased system inertia brings the problem of having a larger RoCoF in power systems in case of a frequency event which threats the system frequency stability. Therefore, the response speeds for non-synchronous generators (wind turbine) in particular need to be discussed. Most utility-scale wind turbines installed today use electronically enabled variable speed generation to instantaneously adjust electrical torque and marginally increase power delivery. Wind turbines can use these controls to temporarily increase the power output to exceed captured wind power, but this also slows down the rotor.

Wind turbines can respond to a contingency in only a few cycles but require 0.5 to 5 s to reach a full response—power rises at ~20–30% per second [123].

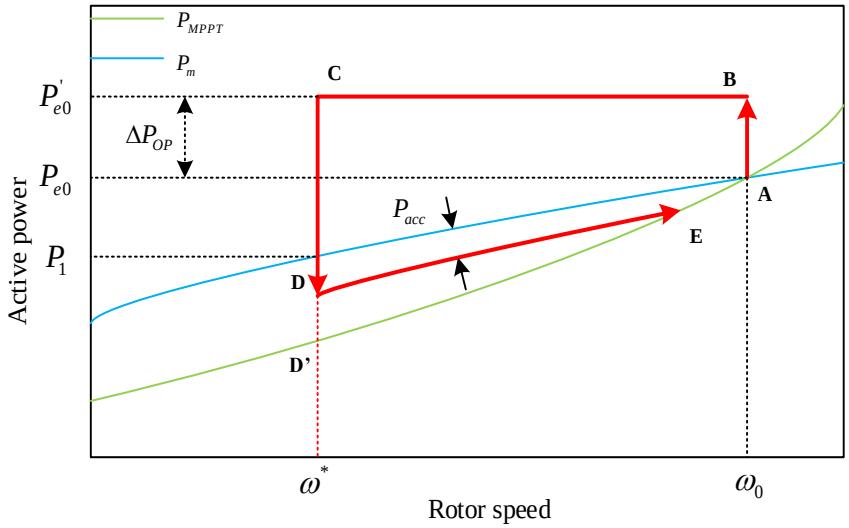

(a) Power-rotor speed trajectory

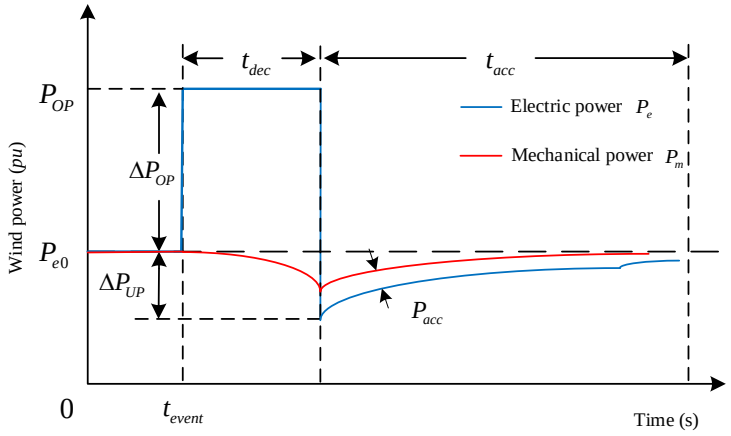

(b) Wind output power in the time domain

Fig. 4.9: Characteristics of the temporary over-production scheme [122].

So far, the frequency support approaches are depicted based on the wind turbine level. Now, the control schemes will be discussed based on wind farm level, as more interesting coordination of various control schemes will be applied among a wind farm, which brings the flexibility of utilisation of these control schemes. Two important aspects which are wake effect and wind speed prediction draw researchers' attention. These variables direct impact on performance of control schemes.

In order to accurately determine the wind power, the impacts brought by the wake effect is considered. Wind speed prediction in ultra-short periods is addressed in [124]–[126]. Therefore, the active power forecasted by high fidelity mathematical models, or deep learning neural networks, can significantly improve the accuracy of wind energy approximation. These studies not only provide layout guidelines for wind farms but also present a more precise wind energy estimation to system operators. In this context, the wake effect refers to the fact that the wind speed arriving at a downstream wind turbine generator drops after travelling through an upstream wind turbine generator. Indeed, different wind turbine generators operate at different MPPT points in a wind farm. The wake effect has been widely explored in [127]–[135], discussing the effects of decaying wind speed from technical and economic perspectives. Reference [129] assumes that wake wind speed is linearly expanded within wind farms due to wind direction and overlapping shadows.

To account for the wake effect, a fixed gain cannot be applied to wind farms because each wind turbine operates at different speed and delivers different power output. As Fig. 4.10 shows, only frequency deviation ΔP_i is used in the additional control loop because the RoCoF calculation may result in potential errors due to inaccurate frequency measurements. The adaptive gain $AG_i(\omega_i)$ is proportional to the available kinetic energy of the wind turbine, i.e., ΔE_i . This kinetic energy can be expressed as follows:

$$AG_i(\omega_i) \propto \Delta E_i = H(\omega_i^2 - \omega_{\min}^2) \tag{4.10}$$

where H is the inertia constant. Besides, ω_i and ω_{min} are instant rotor speed and regulated minimum rotor speed, respectively. Thus, at the beginning of a disturbance, a certain amount of kinetic energy can be released depending on the stored kinetic energy in the wind turbine. wind turbines that have a greater amount of the available kinetic energy are set to have a larger gain, and vice versa:

$$AG_i(\omega_i) = C(\omega_i^2 - \omega_{\min}^2) \quad \text{when } \omega_i < \omega_{\max} \tag{4.11}$$

$$AG_i(\omega_i) = C(\omega_{\max}^2 - \omega_{\min}^2) \quad \text{when } \omega_i \geq \omega_{\max} \tag{4.12}$$

In order to avoid over-deceleration, the adaptive gain is reduced once ω_i is decreased. A large C value may still result in a massive power decrease after reaching the FN, which subsequently may result in a SFD. Simulation results show that both improving FN and preventing over-deceleration can be achieved by implementing the proposed scheme.

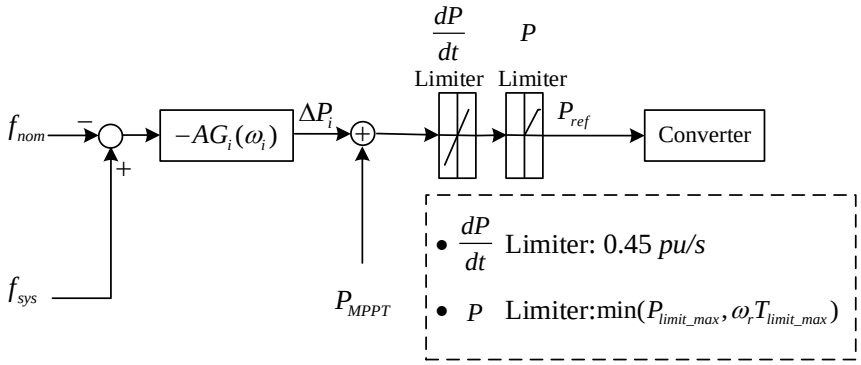

Fig. 4.10: Stable inertial control scheme using adaptive gains $-AG_i(\omega_i)$ [136].

Since the aforementioned schemes result in a significant loss of kinetic energy, the rotor speed may decrease below the minimum operating speed limit. To avoid this, a stepwise decrease in the output for a predetermined time is inevitable to recover the rotor speed. This might cause a subsequent disturbance to the power system and a SFD may occur. Thus, difficulties can arise in determining the amount and duration of an increase/decrease to avoid a SFD. In [120], a modified step-wise inertia control is proposed to counter the SFD problem. The reference signal of the proposed control shown in (4.13) includes the reference signal for an MPPT operation and additional power. The value of MPPT operation P_{MPPT} is set to be proportional to the cube of the rotor speed of DFIG, however, the additional power ΔP is determined by considering the mechanical power curve of DFIG.

$$P_{ref} = P_{MPPT} + \Delta P \tag{4.13}$$

It is noted that the proposed step-wise inertia control adds a constant value ΔP to P_{MPPT}, however, the conventional step-wise inertia control only switches P_{ref} from P_{MPPT} to a constant reference under a frequency event. P_{MPPT} in (4.13) will decrease as the rotor speed decreases during the frequency response stage. In Fig. 4.11 (a), P_{ref} firstly increases from point A to point B, then decreases from point B to point C after

the DFIG completes the frequency support. Both P_{ref} and ΔP will help slowly decrease the rotor speed and reach the rotor speed of the new equilibrium point after disturbance ω^*, because P_{ref} decreases with time. However, if ΔP is too large, a SFD will happen due the quick reduction in rotor speed. Therefore, it is necessary to discuss how to determine a suitable value for ΔP.

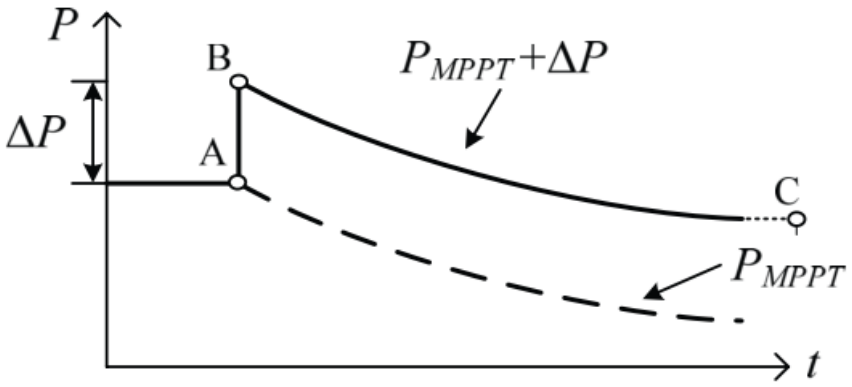

(a) Reference Power

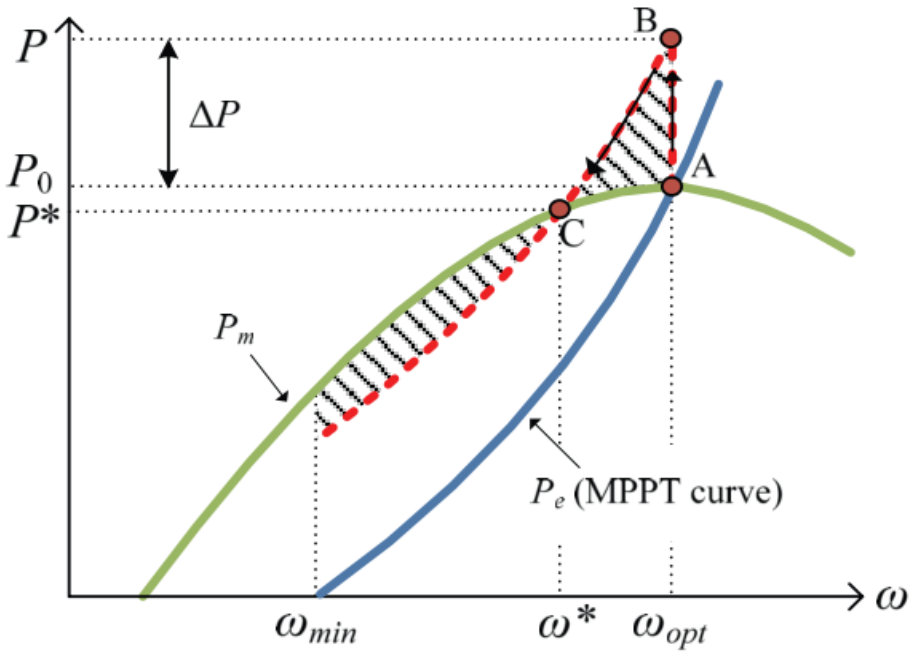

(b) Power-speed trajectory

Fig. 4.11: Operational characteristics of the proposed step-wise inertia control [120].

As shown in Fig. 4.11 (b), the red line and blue line present the electrical power of DFIG P_e during the inertial and MPPT control, respectively. The top shaded area is

the same as that of the bottom shaded area in determining ΔP, which can be expressed in the following mathematical equation:

$$\int_{\omega_{\max}}^{\omega_{\min}} \{P_m - (P_{MPPT} + \Delta P)\} d\omega = 0 \tag{4.14}$$

The top shaded area is the rotor deceleration area, whereas the bottom shaded area is the rotor acceleration area. Therefore, $\omega*$ can be reached after frequency support. ΔP can be calculated by rearranging (4.14):

$$\Delta P = \frac{1}{\omega_{opt} - \omega_{\min}} [\int_{\omega_{opt}}^{\omega_{\min}} P_{MPPT} d\omega - \int_{\omega_{opt}}^{\omega_{\min}} P_m d\omega] \tag{4.15}$$

Moreover, ΔP in this modified control is dependent on the kinetic energy stored in the rotor, which means DFIGs operating at a higher wind speed will generate a bigger ΔP value, thus contributing more power to compensate for the power deficit.

4.3.2. Persistent energy reserves

Regarding the optimal operation of variable speed wind turbines and the use of the available wind energy, they should deliver a maximum active power to the grid with respect to the wind speed. This can be easily achieved by operating along the MPPT curve shown in Fig. 4.12. By doing so, however, the WECS will not be capable of providing prolonged frequency support. To resolve this issue, a certain amount of maximum possible power should be left unextracted by the wind turbine unless there is a justified operational necessity. This is normally referred to as de-loading control, enabling wind turbines to act as a persistent energy reserve. In this context, two commonly used control schemes are explained here, namely rotor speed control and pitch angle control.

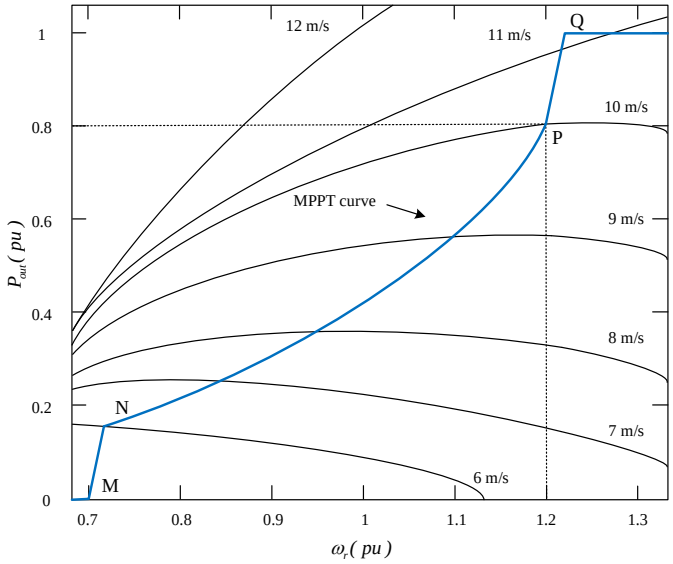

Fig. 4.12: Active power-rotor speed curve of a DFIG for different wind speeds [84].

4.3.2.1. Rotor speed control

A DFIG usually delivers maximum power, determined by the MPPT curve (the blue line shown in Fig. 4.13). To provide persistent frequency support, a de-loading operation is required. This can be achieved by properly shifting the wind turbine operating point to the left or right side of the MPPT curve. Moving from the MPPT curve to the 10% de-loaded curve (red curve) on the left side of MPPT reduces the rotor speed. On contrary, the green line can be obtained by increasing the rotor speed, which is called *over-speed control*. The 10% de-loaded curve on the right-hand side of the MPPT curve is normally the preferred option to avoid interference stability problems caused by the deceleration control [89].

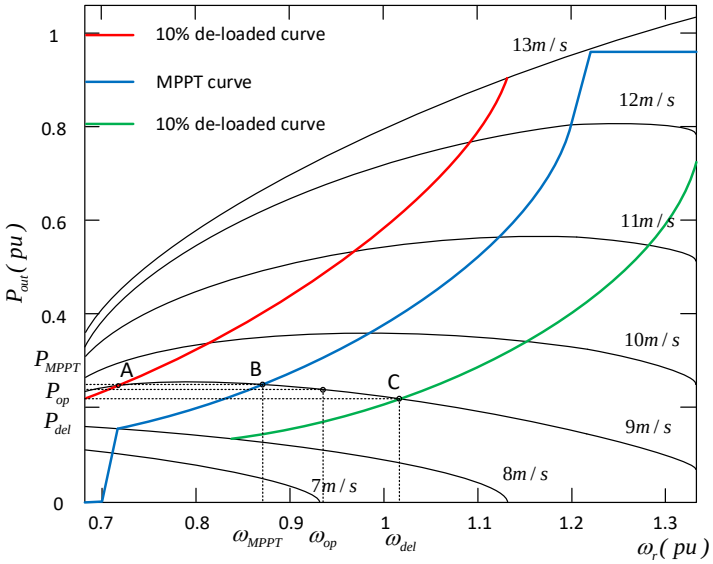

Fig. 4.13: Power-rotor speed curves for a wind turbine deloaded by 10% [93], [118].

To implement the over-speed control, the operating point, P_{op}, lying between points B and C, is obtained according to [137], [89]:

$$P_{op} = P_{del} + (P_{MPPT} - P_{del}) \times (\frac{\omega_{del} - \omega_{op}}{\omega_{del} - \omega_{MPPT}}) \tag{4.16}$$

where P_{del} and P_{MPPT} are de-loading power and maximum power, respectively. The former is the wind turbine power corresponding to the interception point of the green line and mechanical power curve. Here ω_{del}, ω_{op} and ω_{MPPT} denote de-loading rotor speed, operating rotor speed and maximum rotor speed, respectively. With respect to the convertor size, the rotor speed is allowed to vary within a predetermined range, e.g. 0.7 *pu* and 1.2 *pu*. The selection of the speed range is carried out based on the economic optimisation of the investment costs and increased efficiency [66]. Therefore, during high wind speed conditions, the over-speeding control is not suitable due to the rotor speed limits.

4.3.2.2. Pitch angle control

An accurate and complete pitch angle model is crucial for applying de-loading control [138], [139]. In [139], a novel blade pitch model with an optimal pitch control has been designed, manufactured and verified using wind tunnel tests. Regarding de-loading operation, pitch angle control de-loads the wind turbine operating point from

the MPPT curve by increasing the blade's pitch angle. In [69], [140], C_p is reduced according to Equation (3.2), which decreases the wind power output. This control is essentially activated when a wind turbine reaches its rated speed when the speed controller has been disabled or failed to respond [141], [142]. Fig. 4.14 shows the power-rotor speed curves of a typical 1.5 MW wind turbine for different pitch angle values under constant wind speed. The pitch angle controller de-loads the wind turbine at point A at which point the wind turbine's rotational speed reaches its rated speed. Then the operating point of the wind turbine shifts from A to B. This "increased pitch angle" de-loads the wind power by 10%, while the rotational speed remains constant.

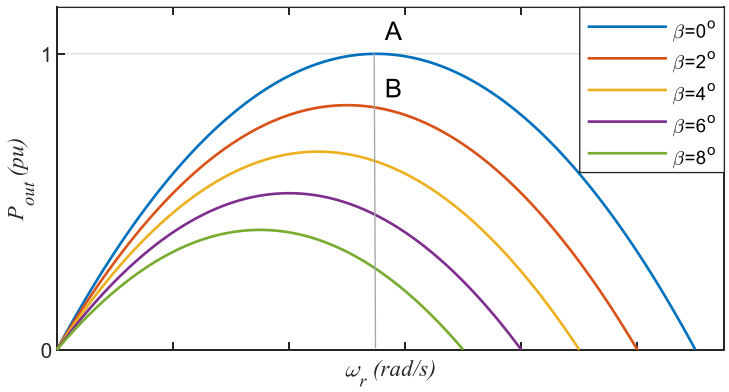

Fig. 4.14: 1.5 MW WECS power-rotor speed curves [65].

A coordinated frequency support control is proposed in [137] by integrating the de-loading control and a variable droop control with a properly selected droop gain. The gain is determined based on the approach presented in [143] using a small-signal approach.

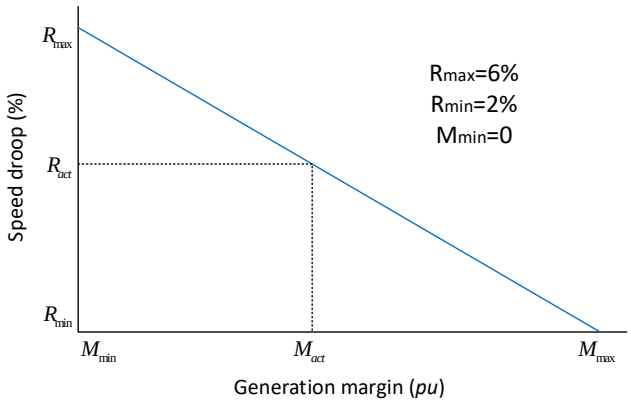

Fig. 4.15: Droop variation for different generation margins [137].

Droop gains are adjusted according to the reserved power of the corresponding wind turbine. The dynamic variation of the droop gain is obtained by linearly decreasing the droop value for larger power reserve margins (see Fig. 4.15). In order to have a maximum wind turbine margin, $M_{\max}$, a minimum droop gain $R_{\min}$ is needed. The droop gain R_{act} is given by:

$$R_{act} = R_{\max} - (R_{\max} - R_{\min}) \times (\frac{M_{act} - M_{\min}}{M_{\max} - M_{\min}}) \tag{4.17}$$

where $M_{\min}$ and $R_{\max}$ are the minimum margin of the wind turbine and its maximum droop gain, respectively. M_{act} is the actual generation margin of the wind turbine. The power margin, P_{margin}, can be expressed as follows:

$$P_{margin} = P_{\max} - P_{out} \tag{4.18}$$

where $P_{\max}$ is the MPPT power point and P_{out} is the wind power output. In this respect, P_{margin} changes from $M_{\min}$ to $M_{\max}$. The wind turbine operates following the MPPT curve at $M_{\min}$, whereas $M_{\max}$ depends on the de-loading curve. Based on the de-loading control, the variable droop control ensures that the wind turbine delivers the maximum output power and operates in a stable condition under low wind speed regimes.

In [108], a SOPPT control is proposed, based on the delta control approach proposed in [144] and the rotor speed-based de-loading control approach. The delta control reserves a constant power or a constant percentage of the available power for emergency conditions.

The SOPPT control takes advantage of the two delta control schemes at various wind speeds. In Fig. 4.16, the orange (dotted) line and the green line represent the SOPPT with a 20% power reserve curve and the SOPPT with a 0.05 *pu* power reserve curve, respectively. To overcome the disadvantages of the delta control, the authors define the point Y', i.e., where the orange and green lines intercept, as the wind speed boundary (which is set to 7.7 m/s). In addition, the same amount of power can be reserved by these two schemes. When the wind speed is smaller than 7.7 m/s, the proposed SOPPT curve follows the green line. However, when the wind speed is above

the boundary, the proposed SOPPT curve switches to the orange line until point *Z'* at which point the constant rotor speed mode is triggered.

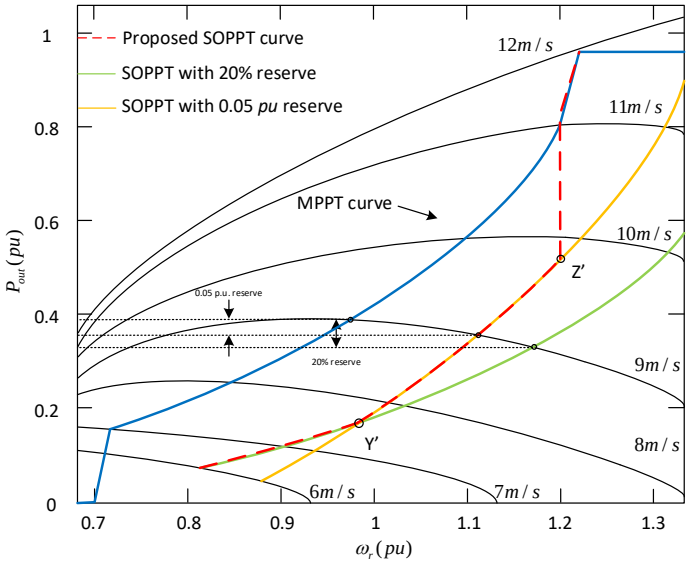

Fig. 4.16: SOPPT strategy – Power-speed characteristics [108].

The amount of reserve power, P_{res}, can be obtained from Equation (3.1) below:

$$P_{rev} = \frac{1}{2}\rho A V_v^3 [C_p(\lambda_1, \beta_1) - C_p(\lambda_2, \beta_2)] \tag{4.19}$$

where $C_p(\lambda_1, \beta_1)$ and $C_p(\lambda_2, \beta_2)$ are the power efficiency under MPPT and SOPPT curves, respectively. Since $C_p(\lambda_1, \beta_1)$ can be obtained by checking the MPPT curve, λ_2 and β_2 are subsequently changed to maintain the required P_{rev}.

Reference [118] elaborates on determining the applicable range of the two above described de-loading methods. Firstly, the limited over-speed de-loading curve is proposed based on the de-loading level, with the de-loading level determined according to both the rotor and wind speeds. A more advanced coordinated active power control is proposed in [145], which precisely defines the coordinated operating zone of the rotor speed and pitch angle control. Nevertheless, robust control of the rotor speed due to the unpredictable wind speed can be challenging in both approaches. This can result in a frequent switching operation between the pitch angle and rotor speed control, exacerbating wear of the mechanical parts.

In order to make the most use of the wind turbines releasable kinetic energy and to increase the revenue of wind farms, the droop control is applied to de-loaded wind turbines [146], [147]. In [137], the approach takes the maximum limit of the de-loaded wind turbine rotor speed into consideration to prevent potential instability due to low rotor speed. However, this approach requires communication between the wind turbine generators in a wind farm.

In [148] a droop coefficient is proposed, based on the reserved energy of wind turbines for a primary frequency response. It also discusses he coordination between wind turbines and synchronous generators. However, both approaches mentioned rely on the performance of wind turbines, which depends on wind speed measurements. To mitigate inaccuracies in wind speed measurements, a so-called efficiency droop control approach is introduced in [149]. In this approach, the de-loaded wind power is related to the tip ratio rather than the wind speed, as discussed in the previous section. In [146], techniques based on torque-droop and power-droop are proposed. Their performances are evaluated in terms of both the transient and steady-state responses. It should be noted that a higher change of power rate due to the implementation of these techniques increases the mechanical tension of the wind turbine, leading to higher maintenance costs. In order to determine the amount of kinetic energy provided by each control scheme, coordination of the droop and de-loading controls is necessary.

In order to reduce the mechanical stress on a WECS, in [150], a *torque limit-based control* technique is proposed. This technique makes the released kinetic energy more flexible by linearising the initially non-linear relationship between rotor speed and its operating point.

Table 4.1: Summary of different control approaches.

Approaches	Controls	Contributions	Concerns
Synthetic inertia control	Adding synthetic inertia power based on RoCoF and frequency deviation	Declining the RoCoF at the beginning of the frequency disturbances	Potential impacts on input signal of RoCoF and occurrence of SFD

Droop control	Adding droop control based on frequency deviation	Improving the frequency nadir	A trade-off between the recovery time of rotor speed and the amplitude of SFD is necessary
Fast power reserve	Temporarily increase a fixed amount of kinetic energy	Fast declining frequency drop	Sudden termination of frequency support causes SFDs
Rotor speed control	Properly changing the WT operating point by changing the rotor speed	Fast compensating frequency drop by releasing pre-reserved energy	Decreasing the annual profit of wind farm
Pitch control	It deloads the WT operating point by increasing the blade's pitch angle.	Long term frequency support	Frequently changing the blade's pitch angle increases the mechanical tension of the WT

4.4. Control techniques to arrest SFDs

Previous sections have discussed frequency control techniques emulating system inertia and contributing to frequency support. However, releasing the kinetic energy stored in the rotor causes rotor deceleration. This means that the frequency support contributed by variable speed wind turbines must be terminated when the rotor speed reaches its minimum value. This minimum value has to do with the stable operation of the variable speed wind turbine. This termination results in a SFD because of the sudden loss of the active power produced by the wind turbine [151]–[156]. The higher the penetration level of the wind energy, the larger the SFD [151]. According to [154], after losing the extra power contribution from wind turbines, a gradual power transition can be an effective approach to avoid the SFD. By comparing Fig. 4.17 with Fig. 4.9 (b), the authors in [84] demonstrate the importance of carefully controlling

the frequency behaviour during the support period. The transition between overproduction and underproduction should follow a cautiously determined slope to avoid over-deceleration and to mitigate a SFD caused by a sudden active power drop.

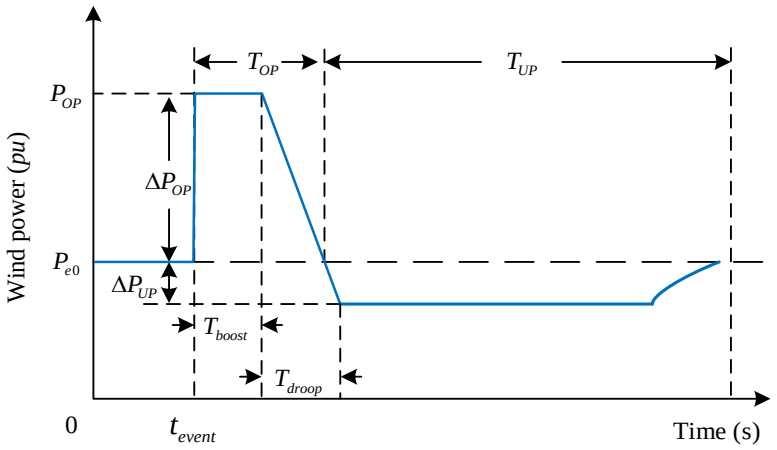

Fig. 4.17: Proposed shape for short-term extra active power [84].

A stable adaptive inertial control scheme is proposed in [156], aimed at improving the FN and RoCoF. Here, the minimal possible SFD is also a target during wind power reduction. During the rotor deceleration period, t_{dec}, a proposed reference power point, $P_{ref}^{'}$, following the power tracking point trajectory (shown in purple in Fig. 4.18(a)) is set to a value larger than P_{MPPT} (from B to C shown in Fig. 4.18(a)) by ΔP_{OP}. Therefore, the approach of releasing more power can improve the FN and RoCoF. The frequency support continues until point C in Fig. 4.18(a). Afterwards, the rotor speed starts recovering. During the rotor acceleration period, t_{acc}, the reference power point, $P_{ref}^{''}$, is switched to a value inside the rotor speed range of ω^{*} and ω_{MPPT} as below:

$$P_{ref}^{''} = P^{*} - 0.03\,pu \tag{4.20}$$

where P^{*} is the active power at which point frequency support is accomplished. Then, $P_{ref}^{''}$ is maintained until the active power output reaches point E. Afterwards, the reference power point returns to P_{MPPT}. Compared to the scheme proposed in [84], the smaller power reduction results in a smaller SFD. The main challenge here concerns the wind speed being difficult to predict during power transition. In this context, coordination between the available wind turbine active power reserve on one hand and

the HVDC interconnectors' active power control/capabilities on the other, has to be considered, as tackled in [157]. The proposed approach compensates for the SFD by changing the frequency response reserve dispatches in various independent nonsynchronous power grids.

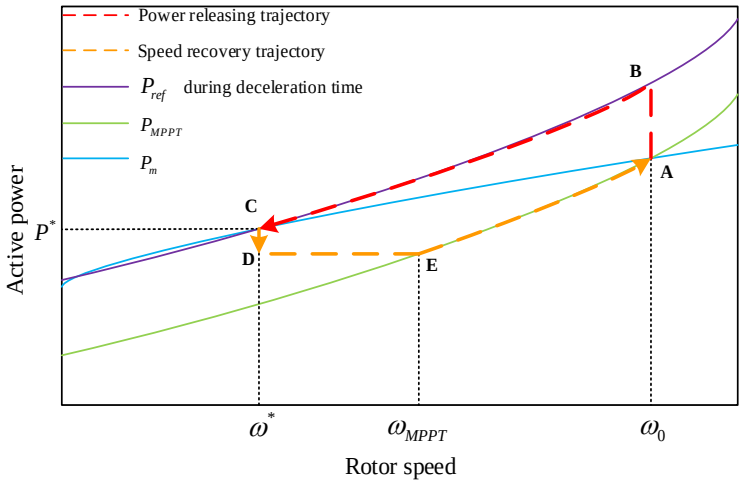

(a) Power-rotor speed

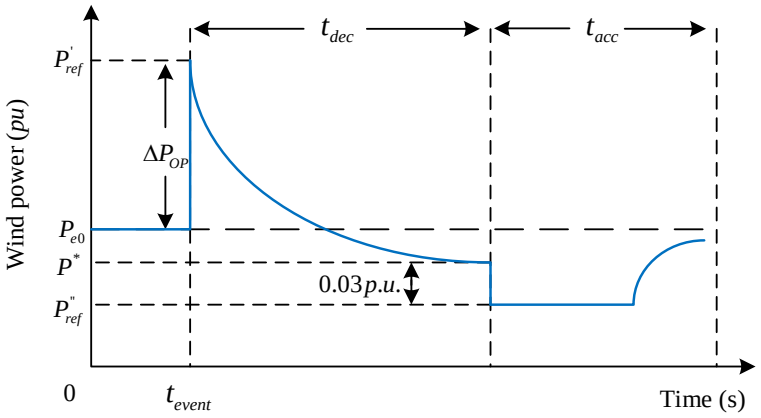

(b) Wind output power in the time domain

Fig. 4.18: Stable adaptive inertial control scheme [156].

To minimise the size of the SFD, which can be dangerous from the perspective of system frequency stability, a novel scheme is proposed in [158] and its application strategy proposed in [159]. Comparing the conventional fast power reserve approaches, this scheme focuses on the correlation between the size of the SFD and the termination time of the frequency support from wind turbines. In [158], the optimal time for terminating the frequency support from wind turbines is analytically derived as a fixed

termination time to minimise the size of the SFD but the parameters of the system frequency response model must be known. In [159], these parameters are estimated and the incremental active power of the fast power reserve approach is also determined. As such, the fixed termination time is suitable for practical application.

4.5. Chapter summary

In this chapter, recently published papers discussing the smart frequency control techniques of DFIGs have been presented. The frequency control schemes reviewed in this chapter have been classified into three categories: synthetic inertia control, temporary energy support and persistent energy support. The synthetic inertia control monitors the RoCoF of the system following a frequency event. However, both temporary and persistent energy support monitor the electrical frequency of the power system. In addition, frequency control schemes to arrest the SFD have also been discussed and will be focused on in the latter chapters with verified simulation results.

Chapter 5 Impacts of Synthetic Inertia Control on Frequency Enhancement in Power Systems

In exploring the frequency support capability of wind turbines, the options for the control and integration of wind turbines based on monitoring the system frequency and wind turbine power can dramatically affect the way the frequency is enhanced after a frequency event. Wind power generation, as one of the most integrated renewable energy sources, has attracted significant attention over recent decades. Then, many power industries in the UK have deployed wind farms based on DFIGs. Meanwhile, unpredictable challenges caused by integration to the conventional power system have resulted in frequency instability. In addition, the integration of wind power generation reduces system inertia due to the rotor of the DFIG being decoupled from the grid frequency. Also, DFIG based variable speed wind turbines always operate in their maximum power point tracking (MPPT) curve. Consequently, there is no reserved power to draw upon as frequency support. In this context, DFIGs can naturally provide little or even no inertia to the frequency control of power systems [160].

The decrease in synchronous inertia brings faster and more significant changes to the frequency deviation, RoCoF and system frequency response following a frequency event. As discussed in the previous chapter, the term synthetic inertia is defined as a process of controlling the active power of a unit such that it is proportional to the RoCoF at the terminal of that unit. The kinetic energy stored in the rotating blades of

wind turbines will not inherently contribute to the frequency regulation of power systems.

In this chapter, the frequency responses of conventional plants versus wind integrated energy plants are presented, with the simulation results verified using DIgSILENT PowerFactory. The adopted DFIG mathematical models are derived in DIgSILENT simulation language (DSL) and the simulation results carried out in DIgSILENT programming language (DPL). Also, the synthetic inertia control developed in [80] is modelled in DIgSILENT PowerFactory, which is used to evaluate the synthetic inertia control performance.

5.1. Comparison of the frequency response of conventional and wind-integrated plants

Conventional power plants consist of synchronously operating generators, characterised by its nominal frequency (50 or 60 Hertz). When the power system is subjected to a frequency event, e.g. loss of a synchronous unit or a sudden load increase, the system can be maintained as an inherent inertial response synchronous generator. For a typical synchronous generator, the inertia constant H ranges from 4 to 7 seconds [13]. As explained above, the inertia constant for wind power generation is barely able to be considered. In order to compare the frequency responses of conventional and wind integrated plants, the simulation results are obtained based on Kundur's two-area test system [45]. The two area network is a stable network with symmetrical topology. Also, the simulation is easy to be carried out because the wind energy sources can be symmetrically connected to the generation bus. Therefore, the power flow in this scenario is same as the original case.

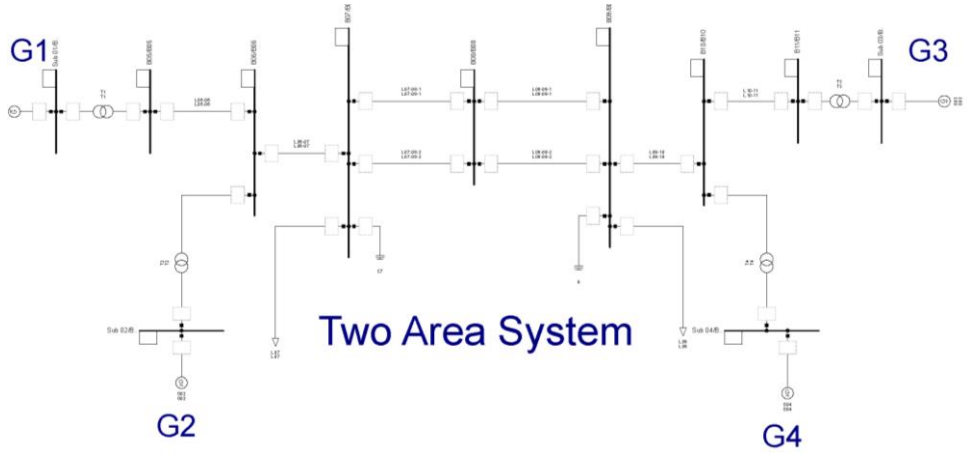

Fig. 5.1: Single line diagram of the modified two-area Kundur test system.

Fig. 5.1 shows a single line diagram of the modified two-area Kundur test system. The system includes two similar areas connected by a weak tie. Each area consists of two synchronous units with a rating of 900 MVA and 20 kV. The total load demand on the system is 2734 MW and 200 Mvar. In the original version of this benchmark system, all the load demands connected to Bus 7 and Bus 9 are supplied by conventional generators.

In the modified version of the system, different types of PE interfaced sources are uniformly integrated into the power system. In other words, the penetration level of PE interfaced sources is set to the calculated level. As the PE interfaced sources affect the voltage levels and power flows in the grid, it is necessary to pay attention to the impact on the grids during the simulations. To change the penetration level of the PE interfaced sources, the power output of DFIGs and synchronous generators are changed automatically by employing DPL.

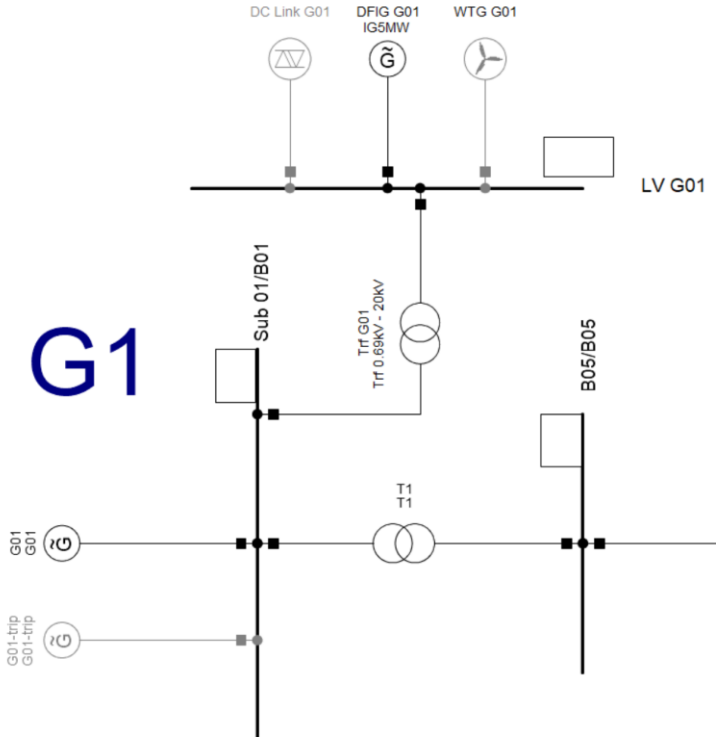

Fig. 5.2: Integration of converter interfaced generations at the generation substation in DIgSILENT.

As shown in Fig. 5.2, different types of PE interfaced sources consisting of a DFIG, FRCG and HVDC link are connected to the generating plant bus via a 0.69/20 kV transformer. The aim of introducing these PE interfaced sources is to modify the penetration level of the system and to investigate the impacts of types of PE interfaced sources on the frequency response following a frequency event. The DFIG model used in this test is the default model in DIgSILENT. The HVDC link and FRCG are modelled as a static generator, which injects a constant amount of active power to the grid. For different types of PE interfaced sources, each one has its constant power output, with the total output from PE interfaced sources at each substation modified by changing the number of devices connected in parallel. In addition, the number of transformers also needs to be changed according to the number of devices, guaranteeing a sufficient grid connection.

5.1.1. Frequency response of a two-area Kundur test system with integrated PE interfaced sources

In this section, the frequency response of a two-area modified system with integrated PE interfaced sources is explored. In order to create a frequency event, the original synchronous generators at each substation are replaced by two synchronous generators, one of which (e.g. 'G04-trip' shown in Fig. 5.1) is presumed to be disconnected from the grid 5s after the simulation start time. The simulation result related penetration levels of the PE interfaced sources are 0% and 33%, respectively.

In order to accurately investigate the impacts on the frequency responses caused by the integration of the PE interfaced sources, a DFIG, as one of the PE interfaced sources, is initially connected to the system. At each substation of the two-area modified system, the total output of a DFIG is 175 MW; therefore, the total active power of the DFIGs in the system is 700 MW. The simulation results are shown between Fig. 5.3 and Fig. 5.7.

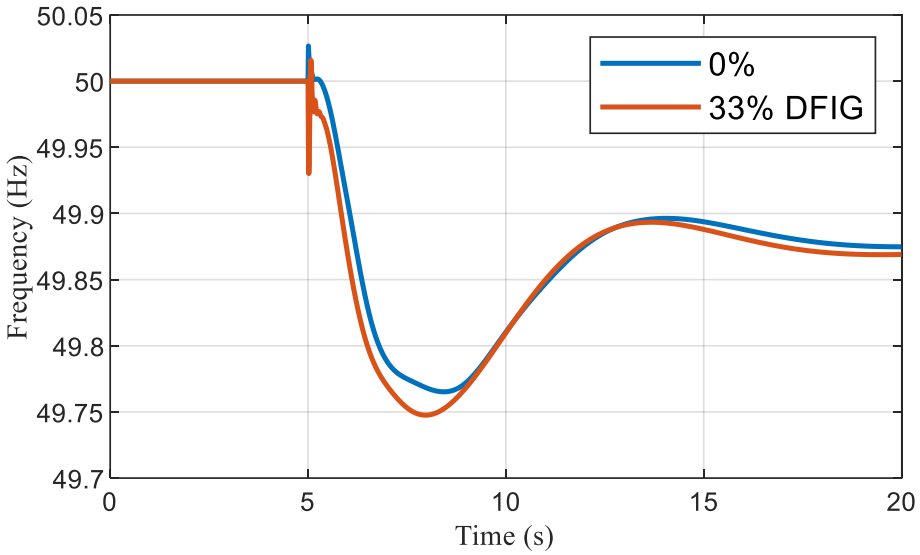

Fig. 5.3: Frequency responses with a loss of 400 MW in generation for a DFIG with penetration levels of 0% and 33%.

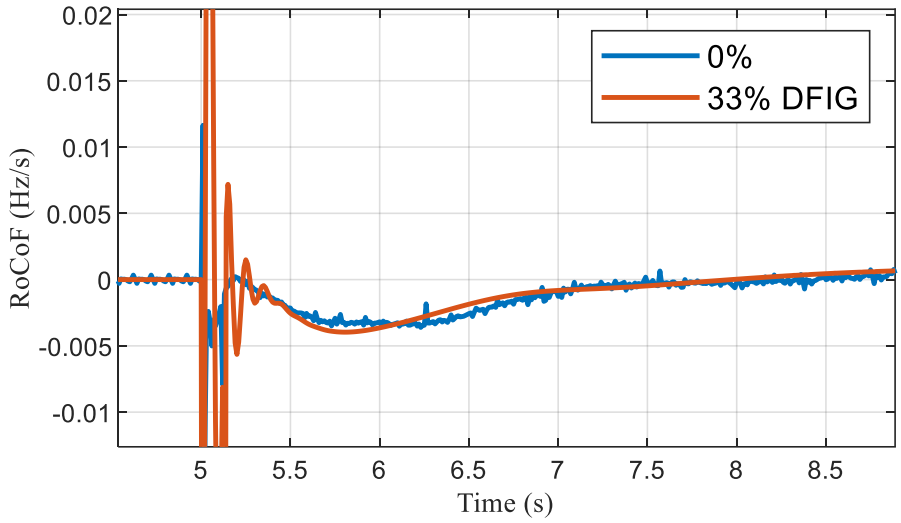

Fig. 5.4: RoCoF with a loss of 400 MW in generation for a DFIG with penetration levels of 0% and 33%.

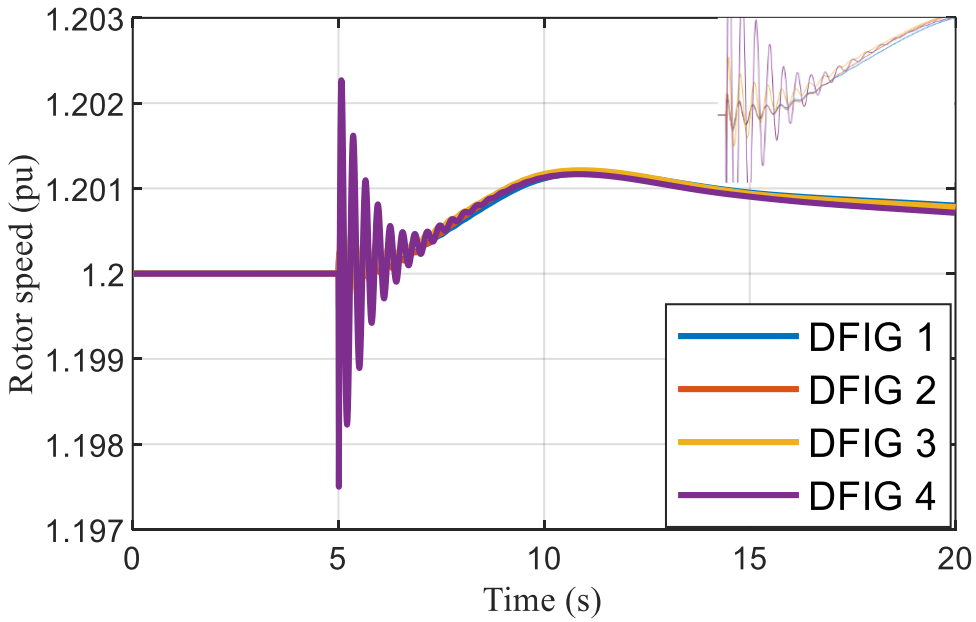

Fig. 5.5: Rotor speed with a loss of 400 MW in generation for a DFIG with a penetration level of 33%.

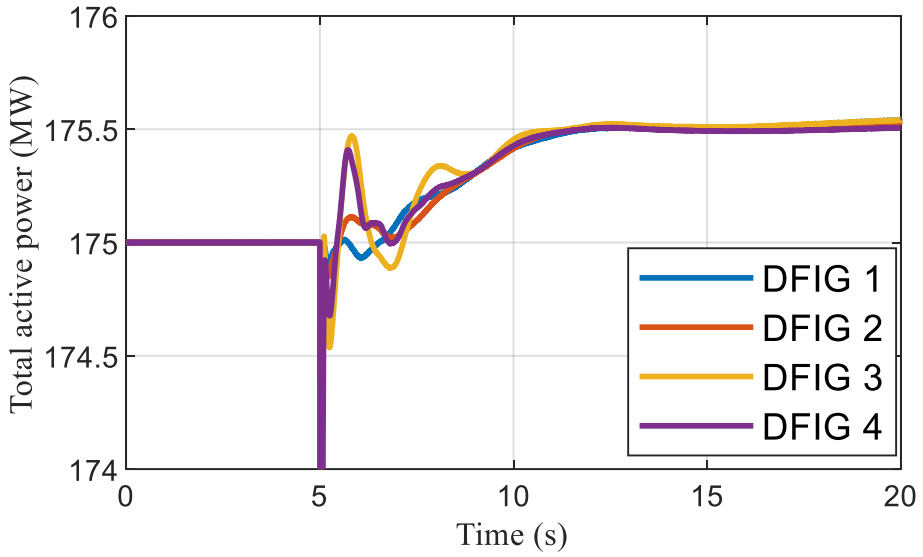

Fig. 5.6: Total active power with a loss of 400 MW in generation for a DFIG with a penetration level of 33%.

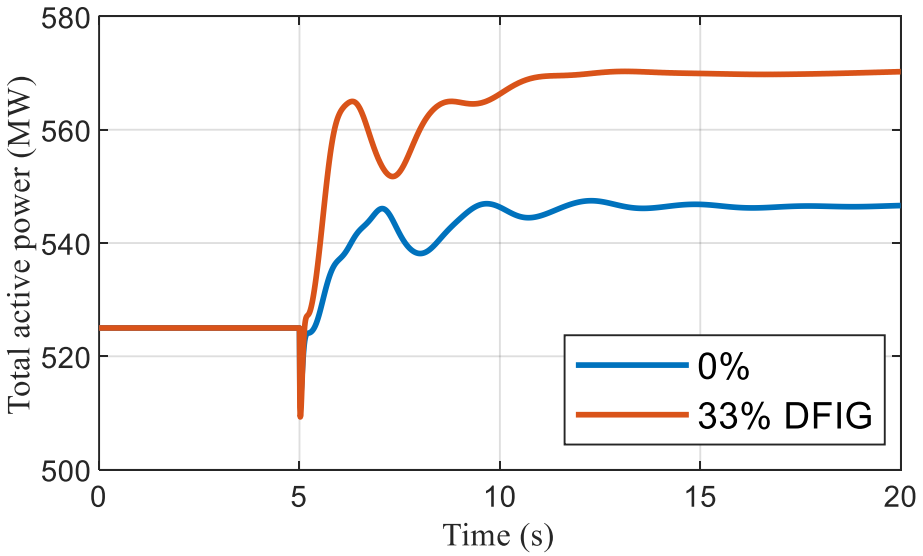

Fig. 5.7: Total active power of SG1 with a loss of 400 MW in generation for a DFIG with penetration levels of 0% and 33%.

Fig. 5.3 and Fig. 5.4 show the frequency and RoCoF for penetration levels of 0% and 33%, respectively. The rotor speed and sum of total active power of the DFIGs at each substation are shown in Fig. 5.5 and Fig. 5.6, respectively. It can be observed that FN and frequency deviation after being subjected to a sudden ‘G04-trip’ both deteriorate at a penetration level of 33% when compared to a penetration level of 0%. The FNs

for the 0% and 33% scenarios are 49.78 Hz and 49.76 Hz, respectively. From the perspective of the DFIGs power change and rotor speed, the output power of the DFIGs does not change dramatically since DFIGs incorporated in the test system are not equipped with a frequency support control. It is also of note that the DFIGs rotor speeds only fluctuate at the very instant of the frequency event and are maintained at their nominal value, 1.2 *pu*. Furthermore, the frequency support burden on SGs had clearly increased for the 33% scenario when compared to the 0% scenario as the conventional synchronous generators are replaced by the DFIGs.

5.1.2. Frequency response of the two-area Kundur test system with variously integrated PE interfaced sources

In order to investigate the frequency response of different PE interfaced sources, three sources connected to the grid have been used to investigate this issue. As explained in the previous section, the DFIG, FRCG and HVDC link replacing the conventional synchronous generators mimic the topology changes of a future modern system, decreasing system inertia and the system reserves available to the whole system. Concerning higher penetration levels, some changes to the systems and their method of operation may be required to accommodate the further integration of wind energy. Since these PE interfaced sources connect to the grid through the voltage source converter, the PE interfaced sources do not contribute to the system inertia response. In this context, the PE interfaced sources do not inherently contribute to the frequency response unless specific control approaches are implemented on them. Comparing DFIG with the other two PE interfaced sources, the DFIGs rotors connect to the grid though a VSC; however, the FRCG and HVDC link directly connect to the grid. The following simulation results describe the differences between the sources with a penetration level of 33%.

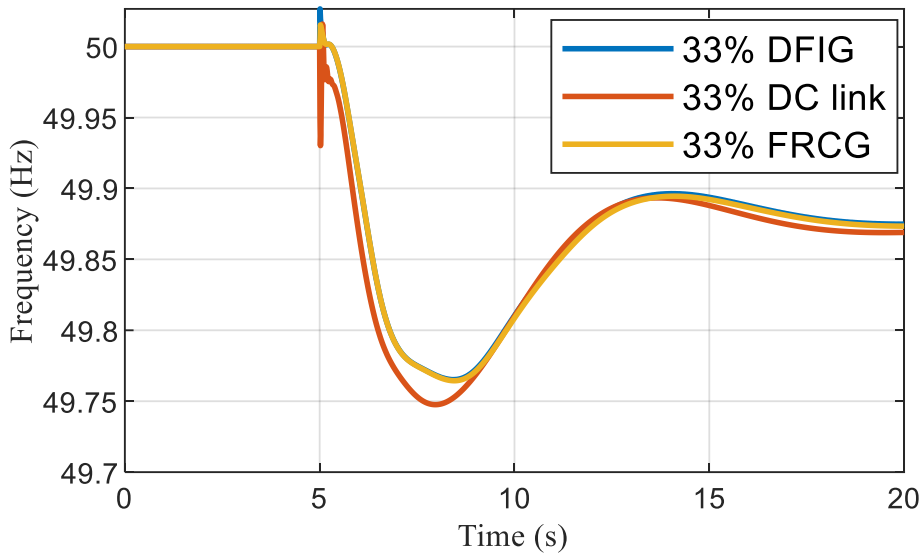

Fig. 5.8: Frequency responses with a loss of 400 MW in generation for different sources with a penetration level of 33%.

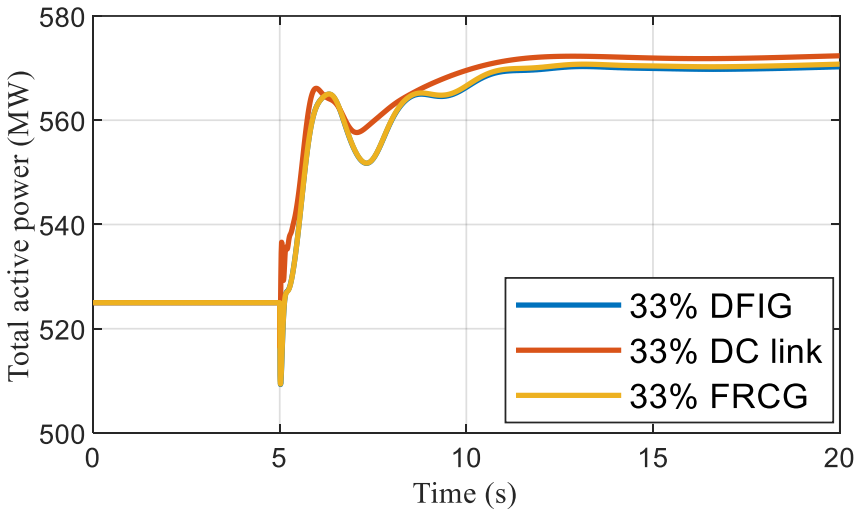

Fig. 5.9: Total active power of SG1 with a loss of 400 MW in generation for different sources with a penetration level of 33%.

Table 5.1: RoCoF with a loss of 400 MW in generation for different sources with a penetration level of 33%.

Size of the frequency event (MW)	Penetration level (%)	RoCoF (Hz/s)	
		DFIG	FRCG
400	33	-0.19	-0.20

As shown in Fig. 5.8, the FNs for the DFIG and FRCG are similar at 49.77 Hz. However, the FN for the HVDC link is slightly lower, 49.74 Hz. From the viewpoint of the total active power of a conventional synchronous generator, the results of these three PE interfaced sources have more or less the same impacts on the contribution to the grid. The time difference from which the nominal frequency decreases to the FN is caused by the different connection topologies.

5.2. Synthetic inertia control

The contribution of DFIGs to the system frequency regulations has become increasingly focused on by many researchers in the field. As discussed in Chapter 4.2, synthetic inertia is proposed and investigated in many literature studies on wind turbines. Generally, wind turbines operate within the MPPT curve and deliver the maximum active power to the grid. When synthetic inertia is implemented in wind turbines, wind turbines are able to provide temporary frequency support stored in their rotating masses after being subjected to a frequency event. The main advantage of using wind turbines to contribute to the frequency is to facilitate frequency support due to the converter-interfaced connection. Also, the frequency support from wind turbines is mandated by the latest grid code (see *COMMISSION REGULATION (EU) 2016/631*), so the wind turbines are expected to have the function ability to be able to participate in controlling the frequency when needed to limit the RoCoFs [106].

5.2.1. Frequency responses in conventional systems

As discussed in previous chapters, the purpose of implementing synthetic inertia control in wind turbines is to mimic how synchronous generators respond when a system is subjected to a frequency event. Before showing that, it is also necessary to present the responses of conventional power systems.

A case study of a conventional power system relating to the damping of the generator and function of the governor is necessary to investigate. Fig. 5.10 shows a simple test network modelled in DIgSILENT. The frequency event applied here is generator outage. The total load is 20 MW.

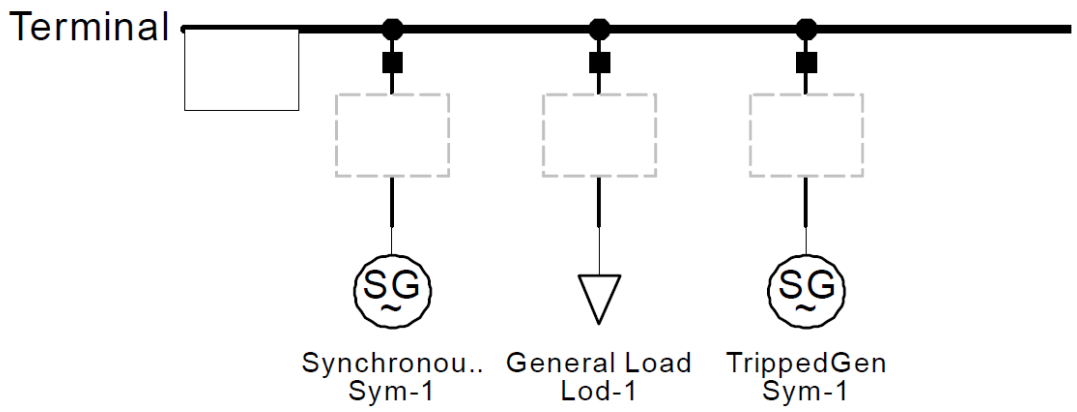

Fig. 5.10: Test network.

Fig. 5.11 shows the speed governor model used in the network. When a load change or generator loss happens in the power system, it is instantaneously reflected as a change in the electrical power output of the generator. According to the equation of motion, the mismatches between mechanical power and electrical power will result in a speed variation, which further causes accelerating power, as expressed by the swing equation.

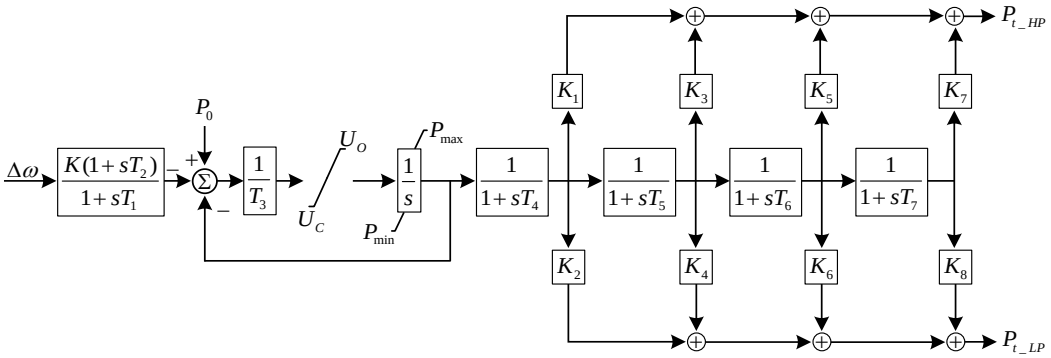

Fig. 5.11: IEEE Type 1 speed-governing model captured from DIgSILENT.

Table 5.2 presents the coefficients of the IEEE Type 1 speed-governor used in synchronous generators.

Table 5.2: Coefficients of the IEEE Type 1 speed-governor.

K	K_1	K_2	K_3	K_4	K_5	K_6	K_7	K_8	P_{MAX}
5	0.3	0	0.25	0	0.3	0	0.15	0	1

T_1	T_2	T_3	T_4	T_5	T_6	T_7	U_O	U_C	P_{MIN}
0.2	1	0.6	0.6	0.5	0.8	1	0.3	-0.3	0

The damping constant in the synchronous generator is expressed as a percent change in generation capacity for every one percent change in frequency. As stated in [13], typical values of D are 1% to 2%. A value of D=2 indicates that a 1% change in frequency will cause a 2% change in generation capacity. The frequency responds to different damping values of the synchronous generator. After the TrippedGen is increased at 2 seconds the frequency drops. It can be concluded that in the absence of a speed governor, the frequency response to a generation capacity change is determined by the inertia constant and damping factor of the synchronous generator.

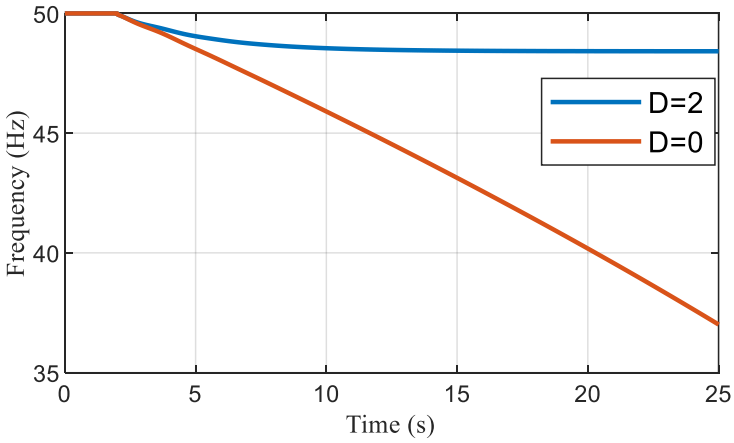

Fig. 5.12: Frequency responses to different damping values of the generator.

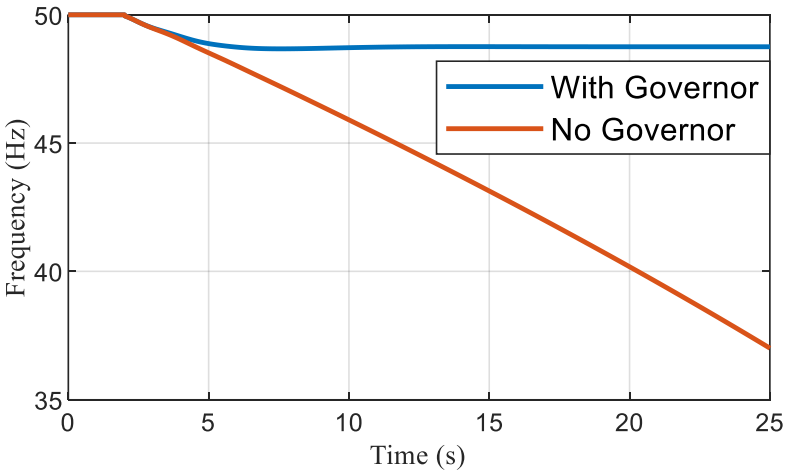

Fig. 5.13: Frequency responses to the governor being activated/deactivated.

When damping of the generator and governor are set to be the same in the system, the only comparison is frequency responses due to the change of gain of the governor. As shown in Fig. 5.14, the gain K of the governor is followed by rotor speed deviations. Therefore, the bigger the gain of the governor, the larger the mechanical power is, which in turn improves the frequency response after being subjected to a frequency disturbance. The simulation results shown in Fig. 5.14 indicate that the FN is 49.21 Hz when $K = 8$, which is higher than the frequency response with the lower gain of the governor. Also, the new frequency steady state is improved around 0.2 Hz by increasing K.

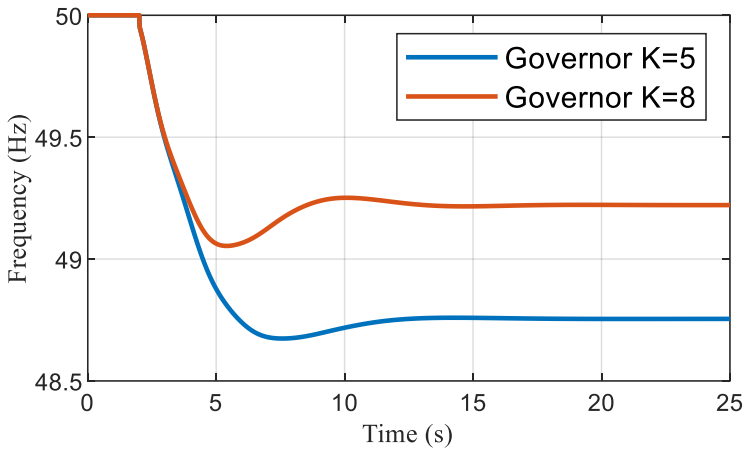

Fig. 5.14: Frequency responses to different gains in the governor.

5.2.2. Frequency responses in a wind-integrated system when considering synthetic inertia control

The synthetic inertia approach is investigated to measure the capability of a DFIG based wind turbine to help frequency responses. Compared with Fig. 5.10, a DFIG is connected to the network through a 0.69/20 kV transformer and a 10 km transmission line.

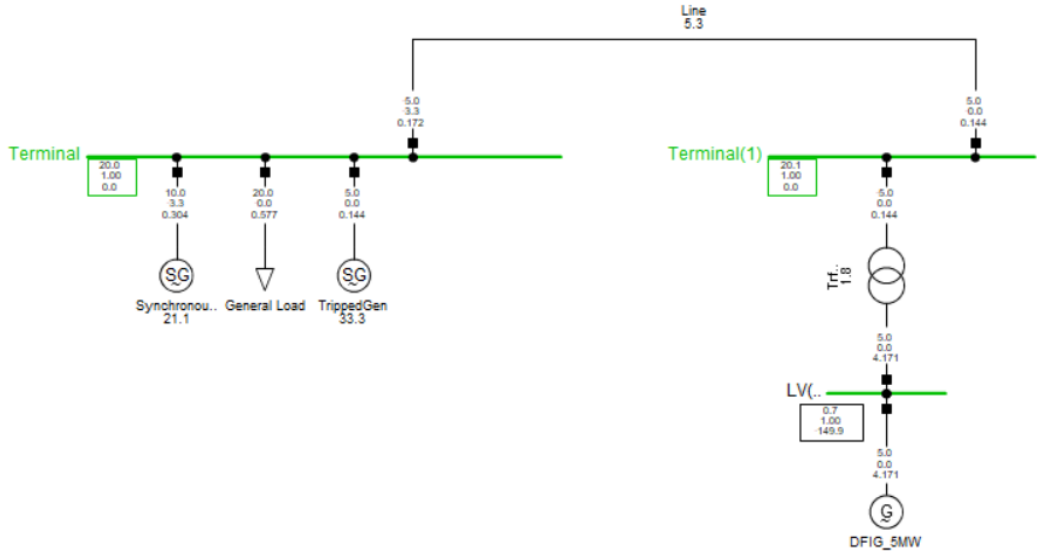

Fig. 5.15: Modified test network.

The generators will be added with an additional governor controller and automatic voltage regulator similar to that set in the previous section. SG1 on the left of the Terminal is used to represent the generation capacity generated in the system and SG2 represents the generator to be tripped in the network. All the simulation results presenting in the following section are achieved using DPL, whilst the synthetic inertia control loop is derived using DSL.

There are three types of synthetic inertial control modelled in this section. The aim of modelling the controls is to examine the performance of each control scheme. The first one is an inertial controller $\frac{df}{dt}$ which temporarily increases the active power related to the input signal of the RoCoF and improves damping in the power system. The second is called droop controller Δf which implies controlling active power related to frequency deviation and behaves similarly to conventional frequency control provided by synchronous generators. The droop gain controller does not improve the RoCoF as it only improves the FN. However, it does not extract any additional kinetic inertia from the rotor like the inertial controller does, therefore some power reserve must be available for this type of controller. The last one is the combined control scheme for the synthetic inertia control and droop gain control. The main advantage of this combined control scheme is to improve the FN and reduce the RoCoF.

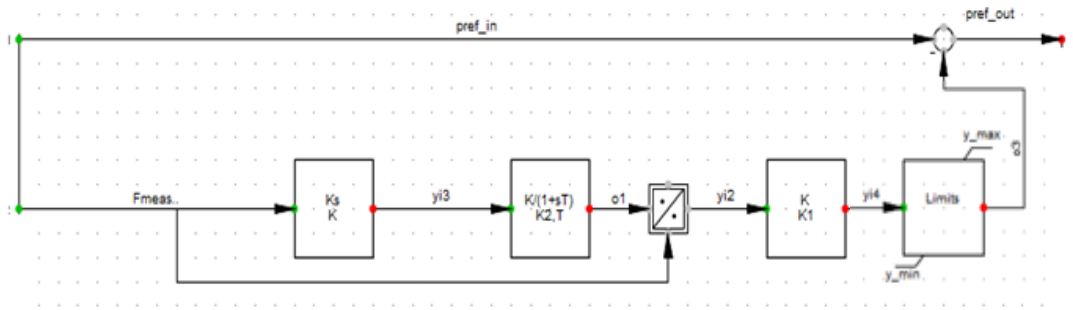

Fig. 5.16: Synthetic inertia control loop.

The synthetic inertia control scheme is presented in Fig. 5.16. In normal operation, power reference P_{ref_out} for the power converter is determined by the MPPT, which is given by P_{ref_in}. During the frequency disturbance, an inertial response value O_3 is added to P_{ref_in} and is given by:

$$O_3 = -K_1 \frac{df}{dt} \tag{5.1}$$

To calculate O_3, system frequency F_{meas} needs to be measured and filtered by mean of a low-pass filter to mitigate noise. As a derivative of the frequency is used to calculate O_3, adequate filtering is needed. The differentiation of a noisy signal may lead to large variation in the value of O_3, which is undesired as it may cause heavy torque pulsations in the drive-train of the wind turbine. Furthermore, the signal value of O_3 is limited to ± 0.1 *pu* to avoid the current limit of the IGBTs in the converter. In other words, when the DFIG works at its rated power operating condition, the total current is less than or equal to 1.1 *pu* during frequency disturbances.

The second control scheme, a droop gain control loop, is shown in Fig. 5.17. A high-pass filter is added to avoid the droop gain control loop contributing in a steady state. Accordingly, the droop gain control is only utilised to provide an inertial response for the wind turbines.

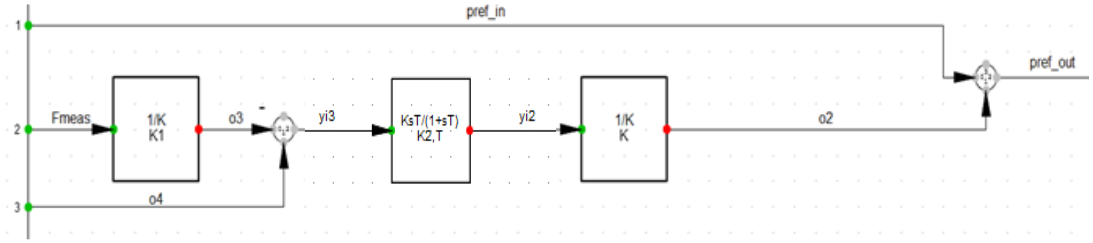

Fig. 5.17: Droop gain control loop.

During the frequency disturbance, droop value O_2 is added to P_{ref_in} and is given by:

$$O_2 = -\frac{\Delta f}{K} \tag{5.2}$$

To calculate O_2, system frequency F_{meas} needs to be measured and compared with the reference frequency value, with the difference between these two values used to calculate the O_2.

The last control introduced here is the combined control for the synthetic inertia control and droop gain control (see Fig. 5.18).

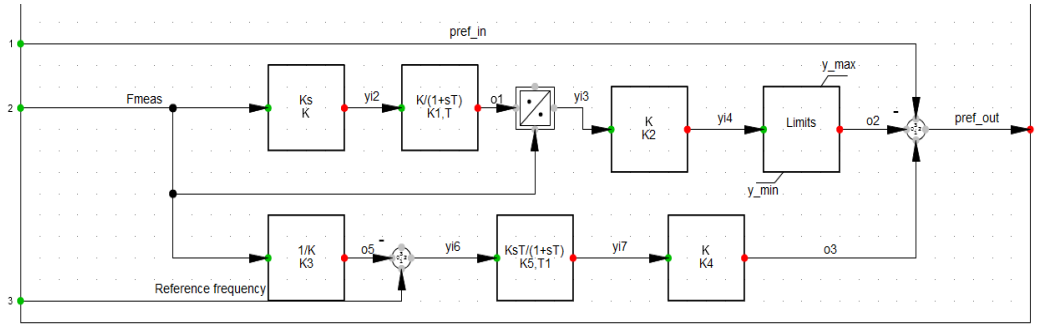

Fig. 5.18: Combined synthetic inertia and droop gain loop control.

The F_{meas} and frequency deviation Δf are two inputs used in this combined control scheme. The two loops have different impacts when improving system frequency stability. The $\frac{df}{dt}$ loop works when the RoCoF in the system is very high and the other Δf loop starts to work when the system frequency is low.

5.2.3. Impacts of synthetic inertia control on system frequency

The inherent characteristics of DFIG based wind turbines depicts that almost no inertial response is able to contribute to support system frequency after a frequency disturbance in the system. Based on the DFIG, the impacts of synthetic inertia control on both frequency and synthetic inertial power are investigated (see Fig. 5.19 to Fig. 5.21). When a generator is tripped at 2 seconds, a frequency drop can be observed in Fig. 5.19. The FN in the case without applying synthetic inertia control is lower than that in the case when a synthetic inertia control is applied as wind power contributes to the frequency response (shown in Fig. 5.20). The kinetic energy stored in the rotating masses of DFIGs increases when employing synthetic inertia control. In this regard, the rotor speed shown in Fig. 5.21 decreases as the kinetic energy in the DFIGs increases. After the frequency is returned to the new steady state with the help of the DFIG and conventional generators, the rotor speed maintains a nominal value of 1.204 *pu*.

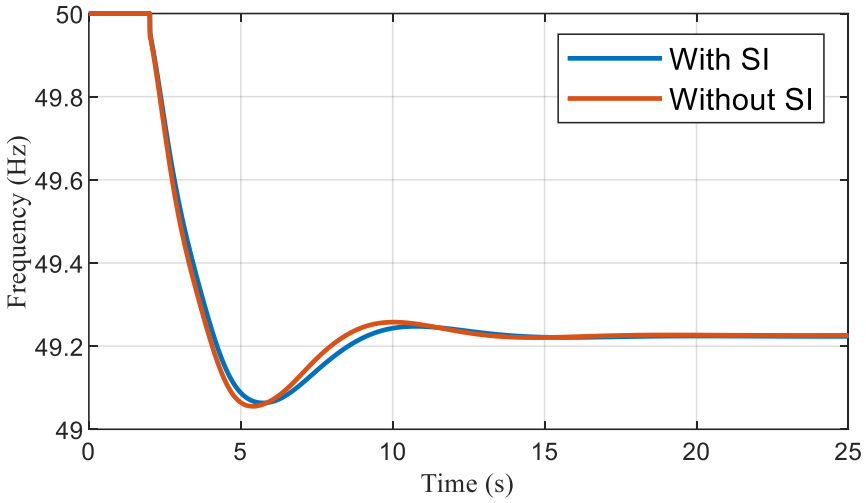

Fig. 5.19: Frequency changes in a DFIG under synthetic inertia control.

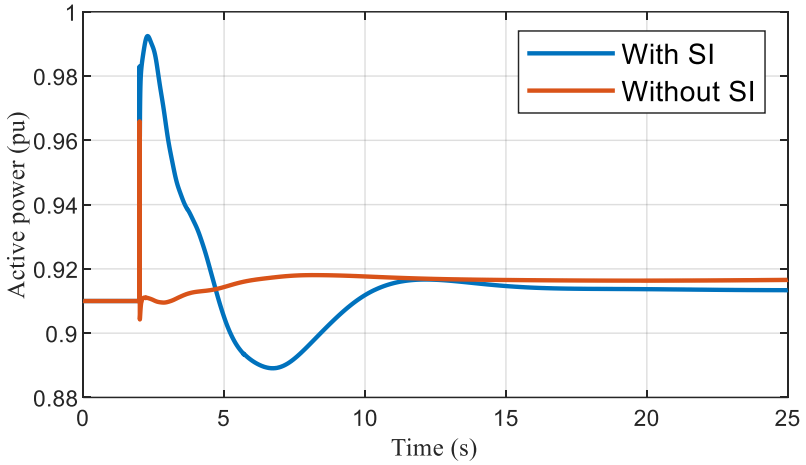

Fig. 5.20: Active power changes in a DFIG under synthetic inertia control.

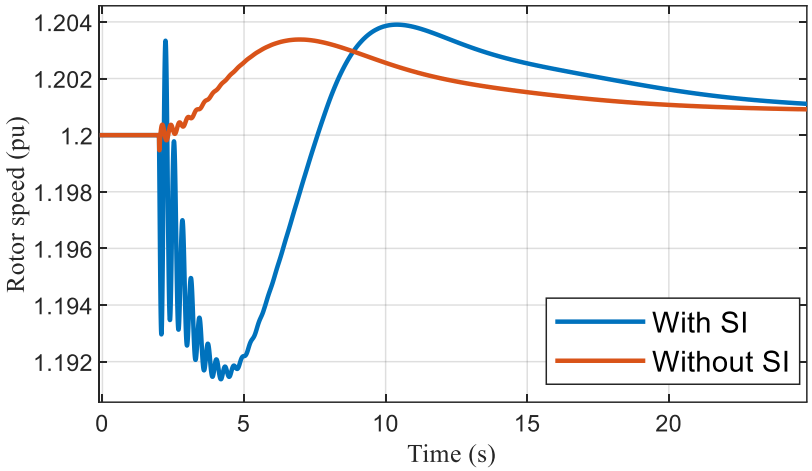

Fig. 5.21: Rotor speed changes in a DFIG under synthetic inertia control.

To make a better comparison, the results of different generator outage sizes are also appended into the above figures. As seen in Fig. 5.19, the FN is much lower when comparing different generator outage sizes in the system because the gain of the synthetic inertia control remains the same. Therefore, DFIGs contribute the same amount of active power to the grid for the frequency responses in these two cases.

In order to more efficiently investigate the frequency responses of DFIGs under a different synthetic inertia control gain, several quantities related to frequency response are shown in Fig. 5.22 to Fig. 5.24. The wind power changes in DFIGs are plotted in Fig. 5.23. It is noteworthy that before the DFIG intentionally increases power and works on a power equal 0.83 *pu* (MPPT mode), so that the additional power

contributed by the DFIG changes proportional to the gain of the synthetic inertia control when the system is subjected to an identical frequency event. In this regard, the DFIGs employing synthetic inertia control are proven to be able to work similarly to the synchronous generator and regulate frequency. In addition, the minor change shown in the frequency responses is because during the simulation the wind energy penetration level and active power reserved by the synchronous generators were kept the same, limiting significant changes to the frequency response.

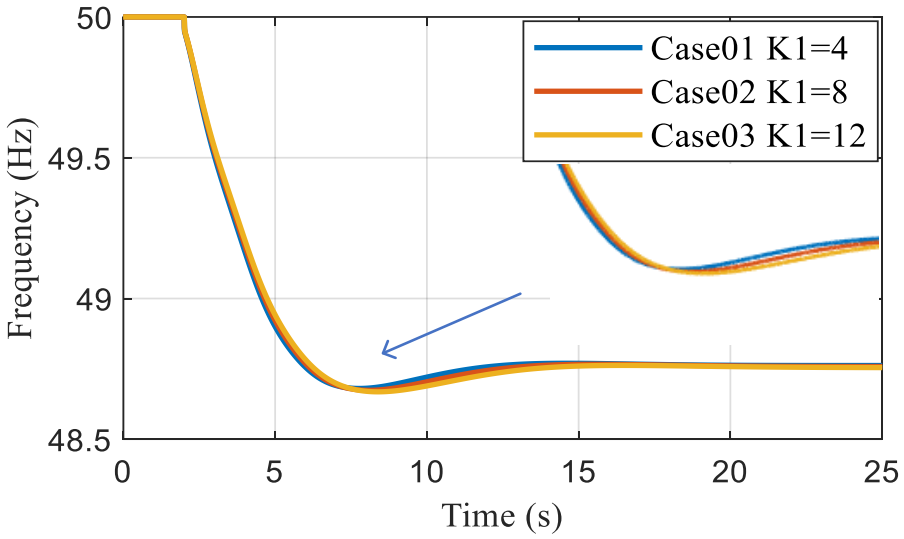

Fig. 5.22: Frequency changes in a DFIG with different synthetic inertia control gain.

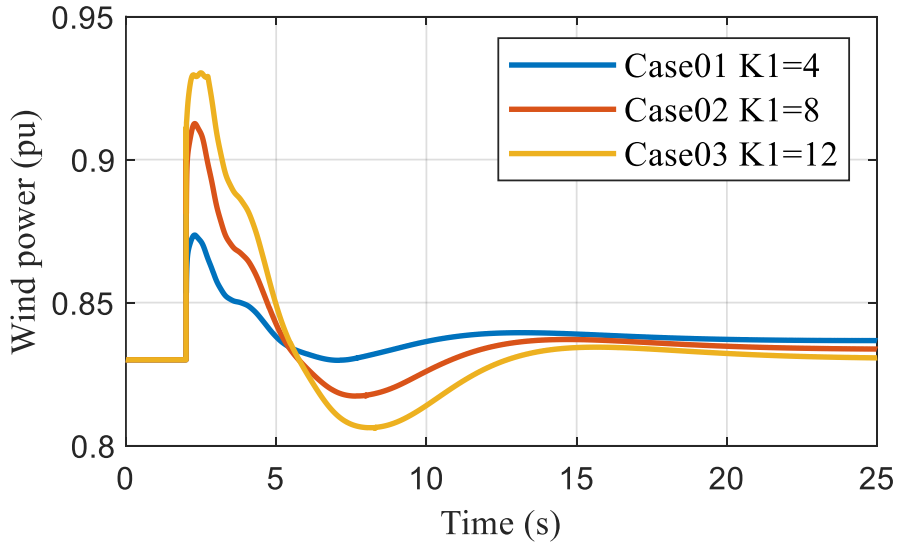

Fig. 5.23: Active power changes in a DFIG with different synthetic inertia control gain.

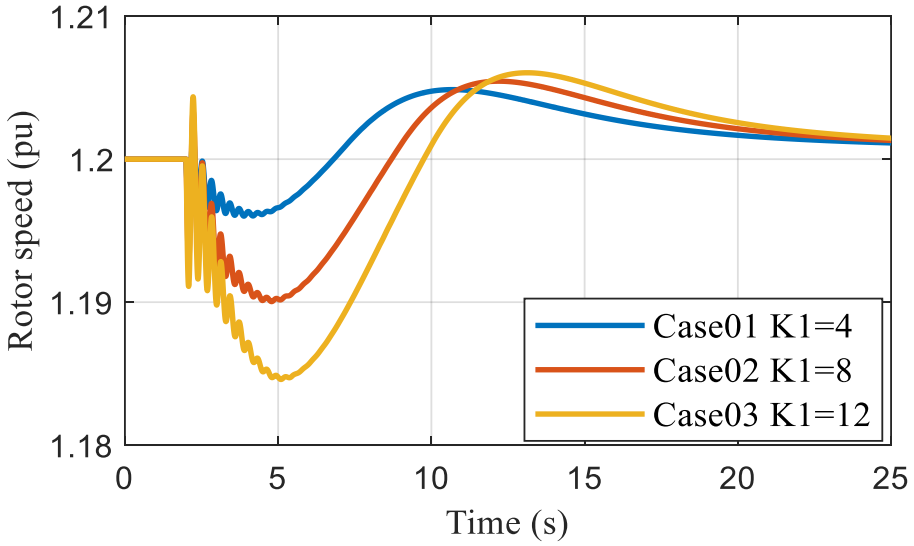

Fig. 5.24: Rotor speed changes in a DFIG with different synthetic inertia control gain.

5.2.4. Impacts of the droop control on system frequency

Based on the DFIG, the impacts of droop control on the frequency and wind turbine power are shown in Fig. 5.25 and Fig. 5.26. The simulation time interval is 50 seconds. When a frequency event occurs, the droop gain control is less dominant during the initial stage of a disturbance but contributes more active power as the frequency deviation becomes increasingly large. This is the due to the droop control loop input being frequency deviation. The FN is 49.1 Hz after applying droop control, which is 0.2 Hz higher than the situation when the DFIG is without droop control.

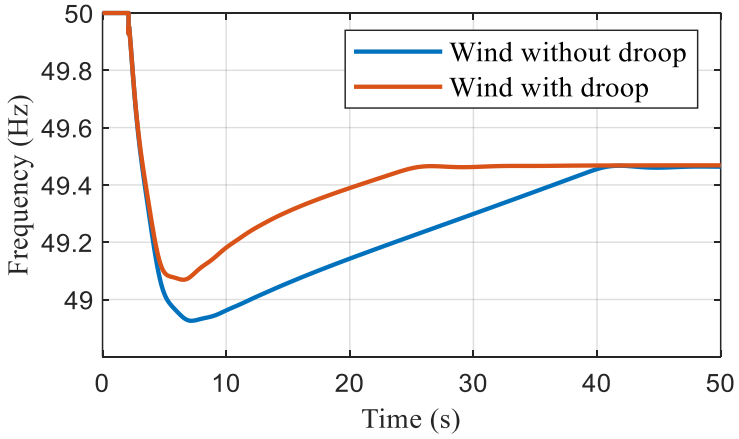

Fig. 5.25: DFIG frequency response changes under droop control.

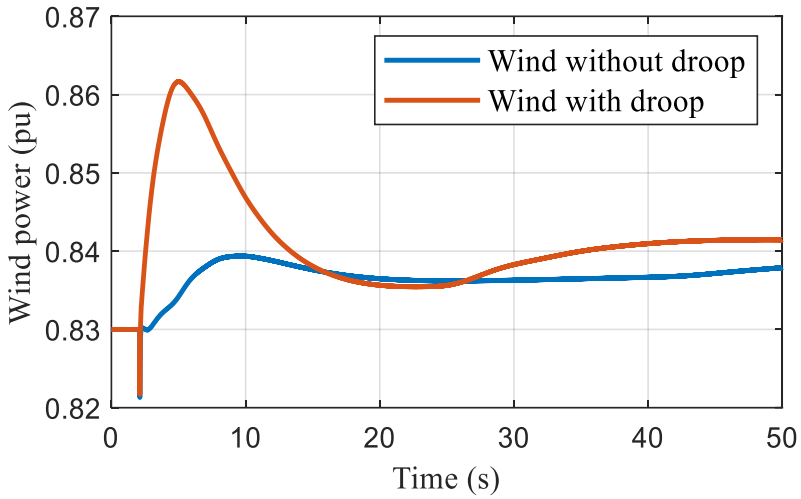

Fig. 5.26: DFIG wind power changes under droop control.

The impact of variations in droop gain constant $\frac{1}{R}$ mentioned in Equation (5.2) on frequency and wind turbine power from a droop control loop are illustrated in Fig. 5.27 and Fig. 5.28. By adopting the controlling variable method, $\frac{1}{R}$ is varied from 0.2 to 0.6 at an interval of 0.1 with the same contingency size applied to the system. It can be seen that the larger the droop gain constant is, the less wind turbine power is sent to the grid.

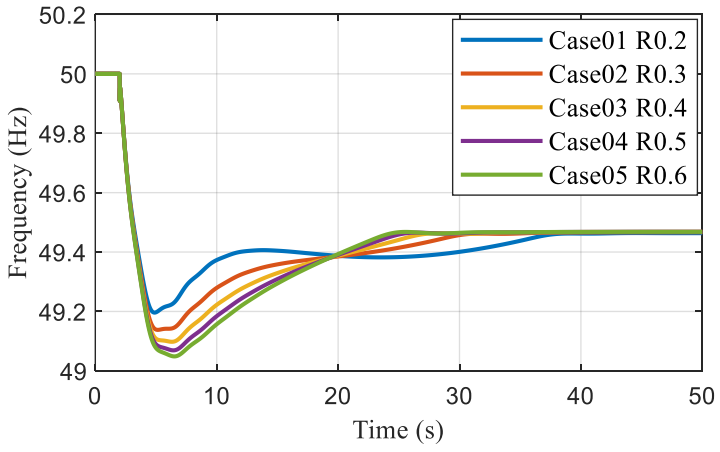

Fig. 5.27: DFIG frequency response changes with droop gain changes.

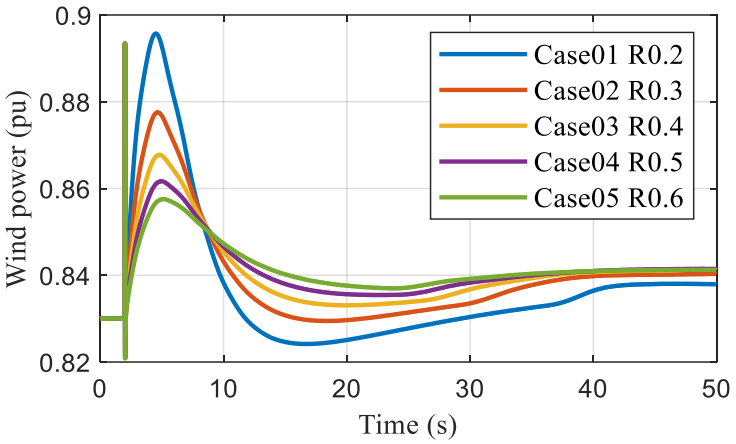

Fig. 5.28: DFIG Wind power changes with droop gain changes.

5.2.5. Impacts of synthetic inertial control and droop control on system frequency

The previous case studies investigated synthetic inertia control and droop control. However, considering the combined control of synthetic inertia and droop control together is the final reason for implementing the temporary energy support in this chapter. To do this, the simulation results of the three controls mentioned in the previous section are shown in Fig. 5.29 and Fig. 5.32.

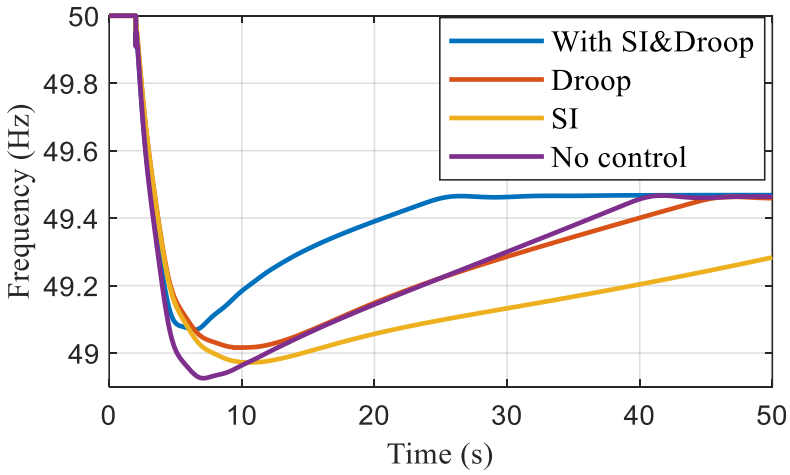

Fig. 5.29: Frequency responses with different control schemes.

After comparing the simulation results, the frequency responses of the different control schemes are more or less the same. However, the combined synthetic inertia control and droop control improved the FN the most. The frequency declines more

slowly in only the droop gain applied case. However, in the only synthetic inertia implemented case, the FN was only slightly increased from 48.86Hz to 48.94 Hz.

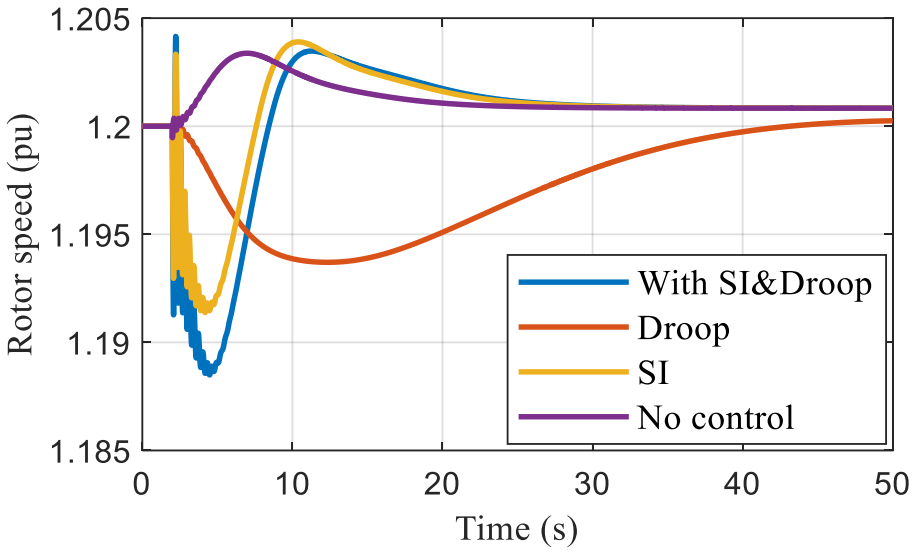

Fig. 5.30: Rotor speed changes with different control schemes.

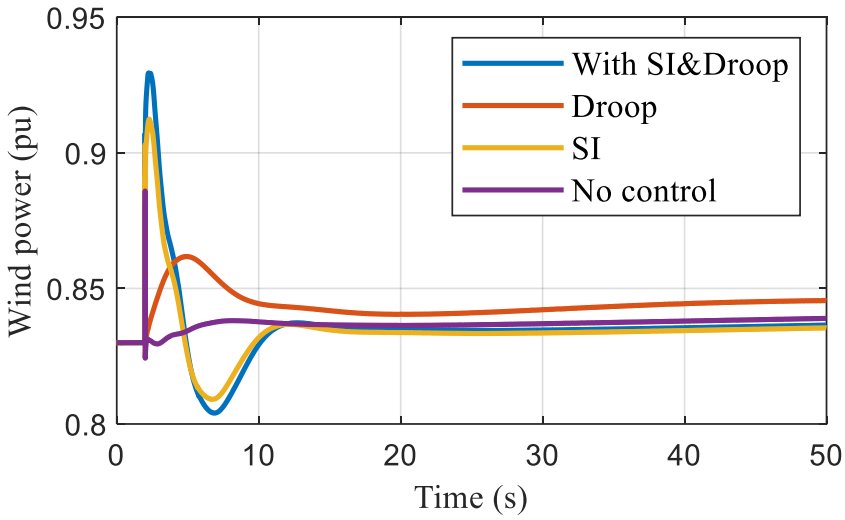

Fig. 5.31: Wind power changes with different control schemes.

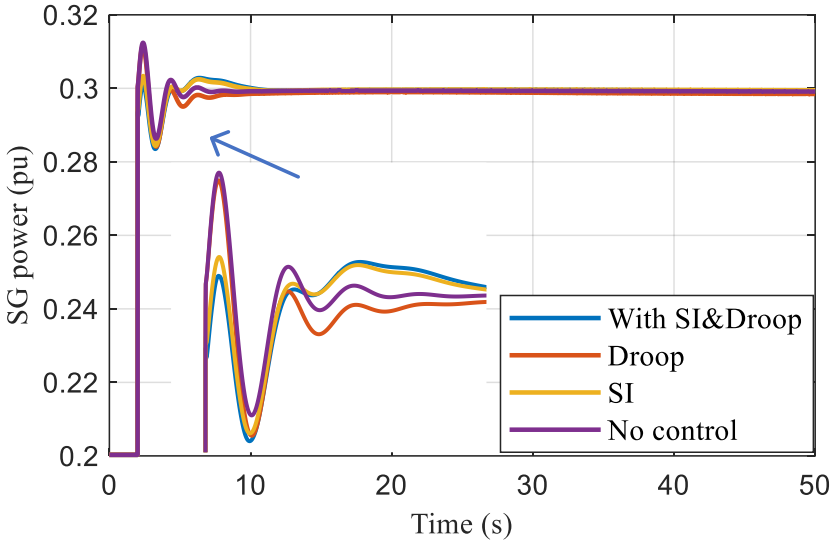

Fig. 5.32: SG power changes with different control schemes.

Concerning DFIG rotor speed changes, the blue line representing the DFIG employing both synthetic inertia and droop control decreases to 1.188 *pu* as most of kinetic energy stored in the DFIG is extracted for frequency regulation. However, in the synthetic inertia control case, the rotor speed only drops to 1.192 *pu*. Comparing the two discussed cases, the DFIG's rotor speed decreased slightly slower to 1.193 *pu* in the droop control scenario.

5.3. Dynamic droop-based control

In this section, a dynamic droop-based control is introduced. This control is able to further improve the frequency response when compared to the droop control. Since both synthetic inertia control and droop-based control are subcategories of temporary energy support (as shown in Fig. 4.1), frequency control is achieved by releasing the kinetic energy stored in the rotating masses, resulting in decelerating rotor speed. If a wind turbine's rotor speed reaches its minimum limit, the slip power of the rotor exceeds the capacity of the rotor side converter. Therefore, a termination of frequency support occurs due to the protection of the rotor side converter being tripped [58]. In this regard, the common problem of applying both controls is shown in Fig. 5.33. A SFD occurs due to the sudden drop of temporary energy contributed by the wind turbine. Also, the amplitude of the SFD is even lower than the first nadir, as the total amount of active power extracted for frequency support is sometimes larger than the size of the frequency event.

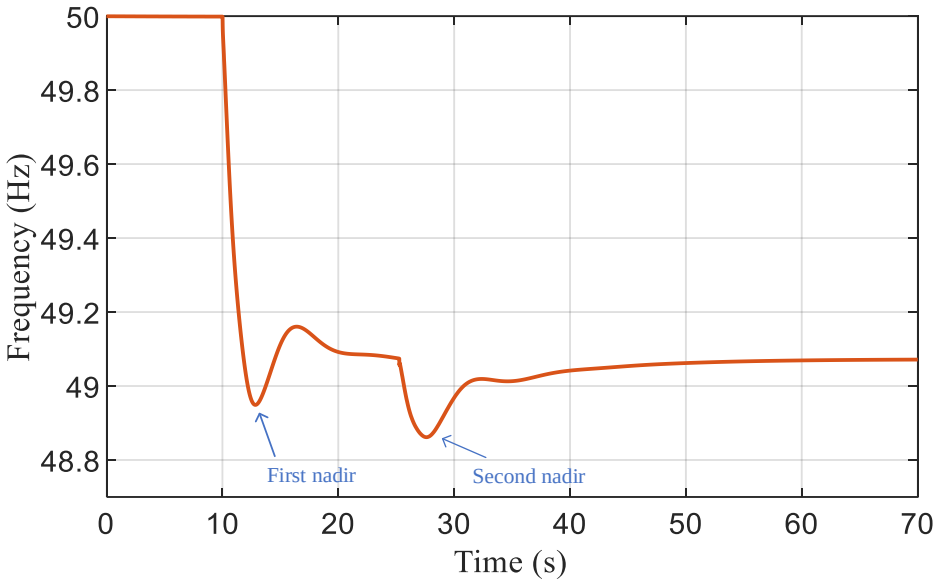

Fig. 5.33: Common problem caused by the termination of temporary energy support.

In order to overcome the shortage of fixed-gain inertial control discussed in [96], the droop loop only contributes less kinetic energy during the initial stage of a contingency because using a large gain can cause the rotor to over-decelerate.

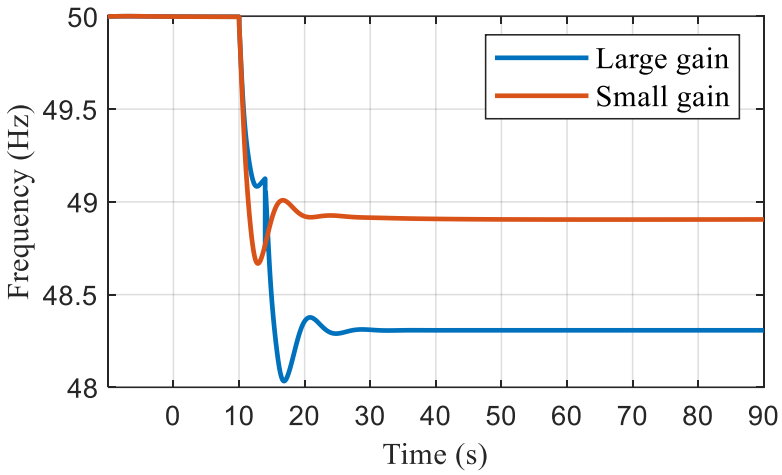

Fig. 5.34: Comparison of frequency to various droop gains.

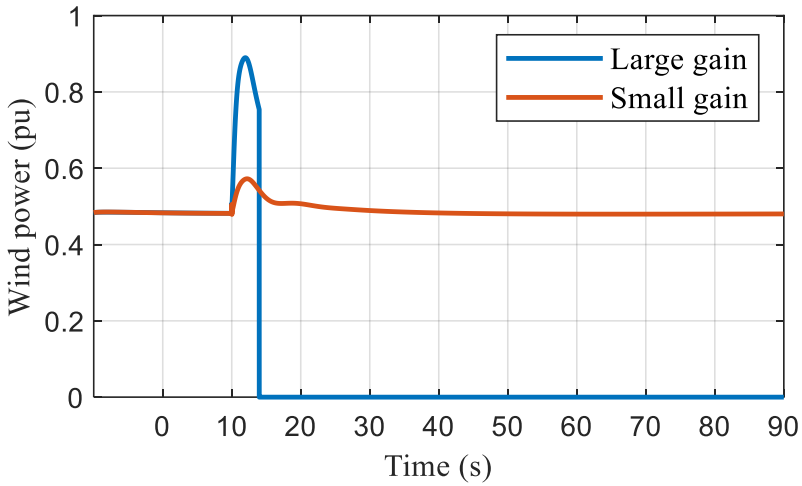

Fig. 5.35: Comparison of wind power to various droop gains.

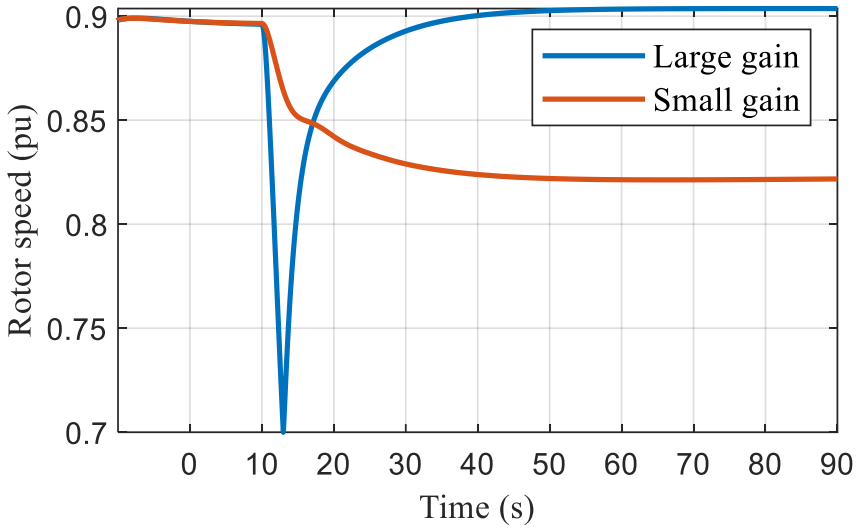

Fig. 5.36: Comparison of rotor speed to various droop gains.

In this comparison, the 5 MW DFIG model is replaced by a 2 MW DFIG model. Therefore, all the DFIG model settings are recalculated according to the characteristics of the DFIGs, as discussed in previous sections. Fig. 5.34 to Fig. 5.36 present the comparisons of system frequency, wind power and rotor speed to fixed droop gains. As seen in the figures, in the case of employing a large droop gain, the first nadir is 49.1 Hz and the SFD is 48.05 Hz, which is lower than the first one. Although almost all the temporary energy from wind turbines is released to stop frequency decline, the rotor speed reaches a minimum limit of 0.7 *pu* in about 2 seconds and trips the rotor

speed protection. Then the frequency support is terminated and the wind power disconnected.

On the other hand, if a small gain is used in the droop control, the first nadir is 48.6 Hz, with only minor kinetic energy extracted to support the frequency recovery. The rotor speed continually decreases from its nominal value and maintains at 0.86 *pu*. This is because the conservative choice of droop gain is made.

In order to increase the primary frequency control from a wind turbine and decrease the burden of synchronous generators, the droop parameter for a wind turbine must be as small as possible. If all the wind turbines in a wind farm are equally set to a lower droop parameter, a sudden increase in the RoCoF will make all the wind turbines outputs surge rapidly. However, if the wind speeds are high, the working operation of the wind turbines is lifted to its capacity. In this regard, a constant small droop setting in this situation may result in instability in such wind turbines when providing frequency support due to insufficient power reserves. Accordingly, a more appropriate and practical droop parameter setting for a generating unit is worth investigating. Therefore, a dynamic droop-based control is employed to deal with this contradiction.

5.3.1. Characteristics of dynamic droop-based control

This section explains the characteristics of the dynamic droop-based scheme to improve the FN as quickly as possible. To overcome the shortcomings of fixed droop gain control, a dynamic droop $R(df/dt)$ can dynamically change depending on the RoCoF (see Equation (5.3)). During the very first instants of a frequency contingency, $R(df/dt)$ is changed to a relatively small value due to a large RoCoF occurring at this stage, which enables DFIGs to release a large amount of ΔP to support the frequency. To prevent the rotor from over-decelerating, $R(df/dt)$ increases with the RoCoF, creating a ΔP decrease. In addition, a reduction in ΔP can also mitigate the amplitude of a SFD due to the termination of the temporal energy support where minimum rotor speed is reached.

The inertial control loop for the dynamic droop-based scheme is shown in Fig. 5.37. The reference power point P_{ref} consists of P_{MPPT} and output of the droop loop ΔP.

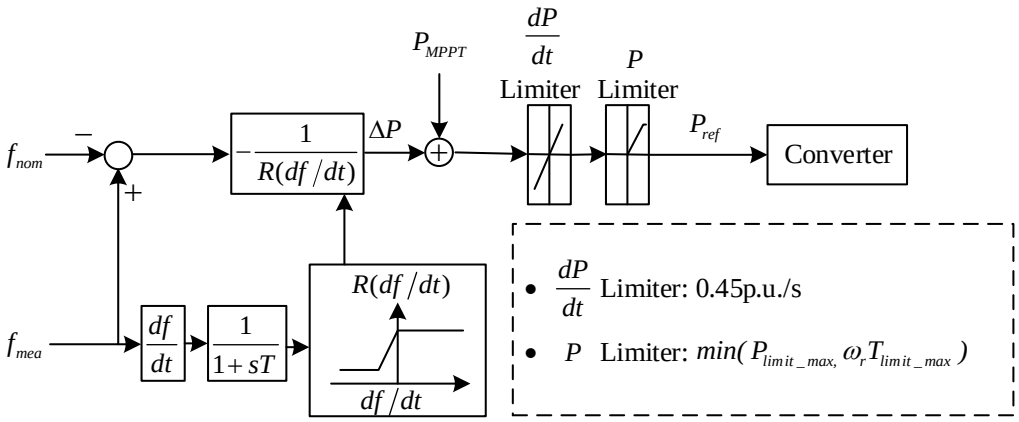

Fig. 5.37: Inertial control loop for the dynamic droop-based scheme.

In this scheme, ΔP is expressed as follows:

$$\Delta P = -\frac{1}{R(df/dt)}(f_{mea} - f_{nom}) \tag{5.3}$$

where $R(df/dt)$ represents the dynamic droop.

5.3.2. System responses with different droop gain combinations.

In this study, the system responses with different droop gain combinations are shown in the following. As shown in Equation (5.3), when RoCoF is less than -0.1 Hz/s, the value of R is set as R1, otherwise R2 is used. In the following simulation results, the system responses show the system frequency, wind power and rotor speed.

Table 5.3: Comparison of RoCoF with various droop gain combinations.

Event	RoCoF (Hz/s)
Case01	-1.22
Case02	-1.21
Case03	-1.18

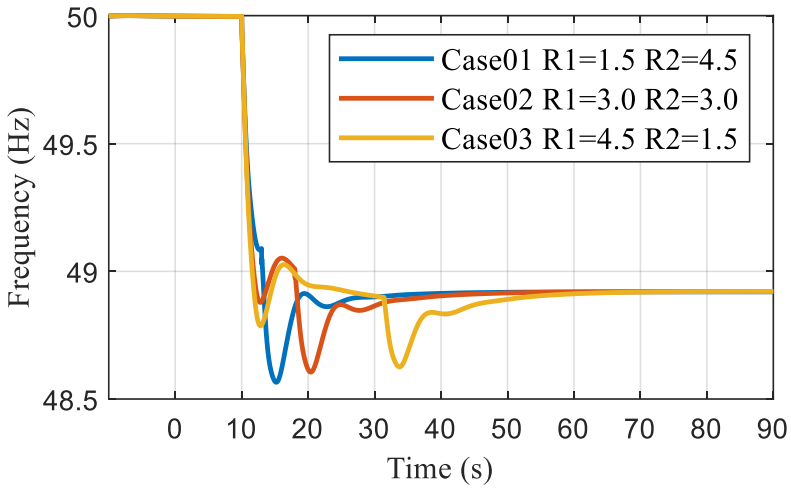

Fig. 5.38: Comparison of frequency with various droop gain combinations.

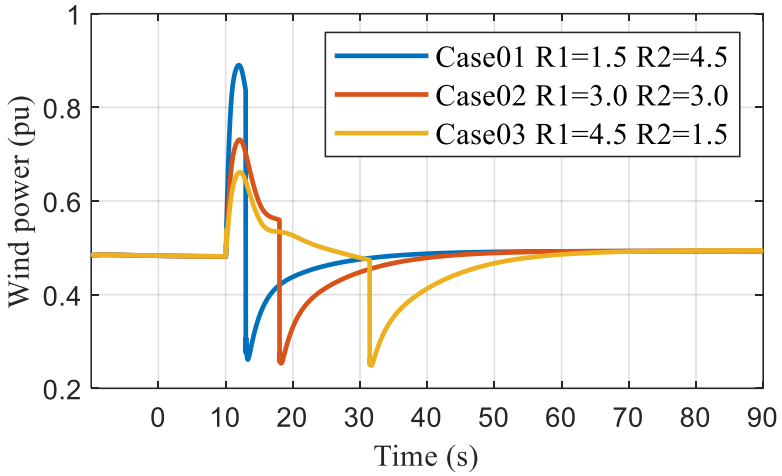

Fig. 5.39: Comparison of wind power with various droop gain combinations.

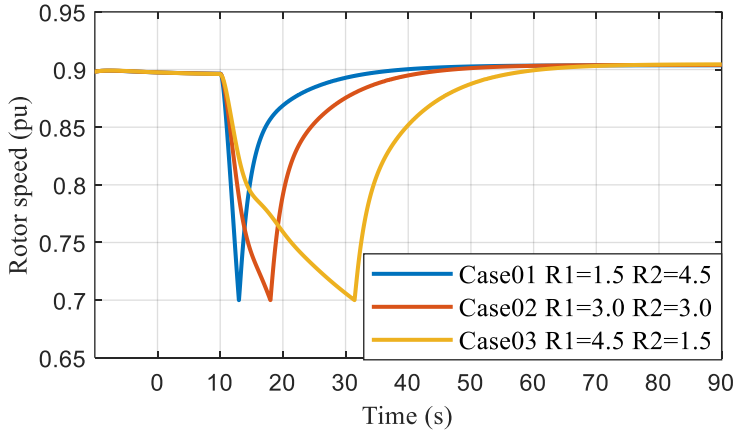

Fig. 5.40: Comparison of rotor speed with various droop gain combinations.

The temporary output of wind turbines is inversely proportional to the value of R. When R1 is chosen to be a rather small value, the active power of DFIGs is relatively large. Most of the temporary energy surges support frequency recovery. By comparing the results for Case01 and Case03, the RoCoF is increased by the release of the amount of energy contributed from DFIGs. Also, it can be noticed that the FN is improved with the decrease of R1, however, the consequent SFD is the lowest in Case01 due to the amount of extracted energy being the largest. For the sake of a better comparison, the simulation results for Case02 are also included in the above table and figures.

5.4. Chapter summary

The dynamics of power system frequency have been investigated in this chapter. A valid dynamic model of a DFIG based variable speed wind turbine model was modelled in DIgSILENT. In order to examine the frequency support capability of DFIGs, synthetic inertia control and droop control were integrated into the DFIG model. The proposed model was tested in different benchmark systems (e.g. a modified two-area system and a simple network) by using the time domain simulation approach.

It can be observed that when wind power is integrated into a power system, system inertia decreases. The frequency response is directly determined by the penetration level of the wind power and active power reserves provided by the synchronous generators. It is also noted in the simple network, the FN and rotor speed changes depend on which control scheme is integrated into the DFIGs. The results show that combining synthetic inertia control and droop control can contribute to the system frequency the most, not only decreasing the RoCoF at the initial stage of the frequency state but also improving the FN. Furthermore, frequency event size is proven to have a large impact on the frequency response when the penetration level of wind power is low in a system.

In addition, a dynamic droop-based control was introduced and investigated. According to system studies in different scenarios, it was observed that dynamic droop-based control can enhance frequency stability in a power system. This decreases the burden of synchronous generators under primary frequency control. Also, the importance of using a

proper droop setting is proved to deal with the contradiction between the amplitude of the FN and SFD.

Chapter 6 A Consecutive Power Dispatch in Wind Farms to Mitigate Secondary Frequency Dips

In exploring the frequency support capability of wind turbines, the options for the control and integration of wind turbines can dramatically affect the way a wind turbine operates. As discussed in the previous chapters, the frequency controls are mainly divided into two subcategories: a) temporary energy support and b) persistent energy support. Temporary energy support was investigated in Chapter 5 the advantages and disadvantages shown and discussed according to the simulation results. This chapter introduces and proposes a consecutive power dispatch scheme to reduce the SFD and prevent wind turbine generators from over-deceleration when used in a large-scale power system integrating wind power. Applying this scheme can cause a relatively small SFD, while improving the first FN and preventing the rotor from over-decelerations under various wind conditions, contingency sizes and wind penetration levels.

Section 6.1 explains the reason how secondary frequency dip occurs in a wind integrated power system. Section 6.2 describes the importance of applying the proposed method. The consecutive power dispatch method will be discussed from the perspective of the difference between temporary and persistent energy support, and how to implement this method in wind power integrated power systems. Section 6.3 presents the modelling of the deloading operation as implemented in DIgSILENT PowerFactory. Section 6.4 demonstrates the test system built in DIgSILENT

PowerFactory. Section 6.5 presents the simulation results and related analysis. Finally, the chapter conclusion is presented in Section 6.6.

6.1. Explanation of a secondary frequency dip

Typical dynamic synthetic inertia control responses are shown in Fig. 6.1 from power output, rotor speed and frequency perspectives. The frequency event occurs at t_1, the synthetic inertia control is activated and lasts for period T_1. This frequency support period ends at t_2 until the minimum rotor speed is reached. During period T_1, extra power P_{extra} contributed by wind turbines is sent to the grid and a decrement of mechanical power occurs due to rotor speed deviation from its initial rotor speed. Then, rotor speed starts to recover at t_2 after termination of the frequency support. In order to accelerate rotor speed, wind power P_m captured by the wind turbines must be larger than the active power output of wind turbines. In this regard, recovery power P_{rec} should be larger than P_m. The rotor speed returns to its initial value after recovery period T_2. Afterword, wind turbines switch to the MPPT curve. However, a SFD also occurs during T_2.

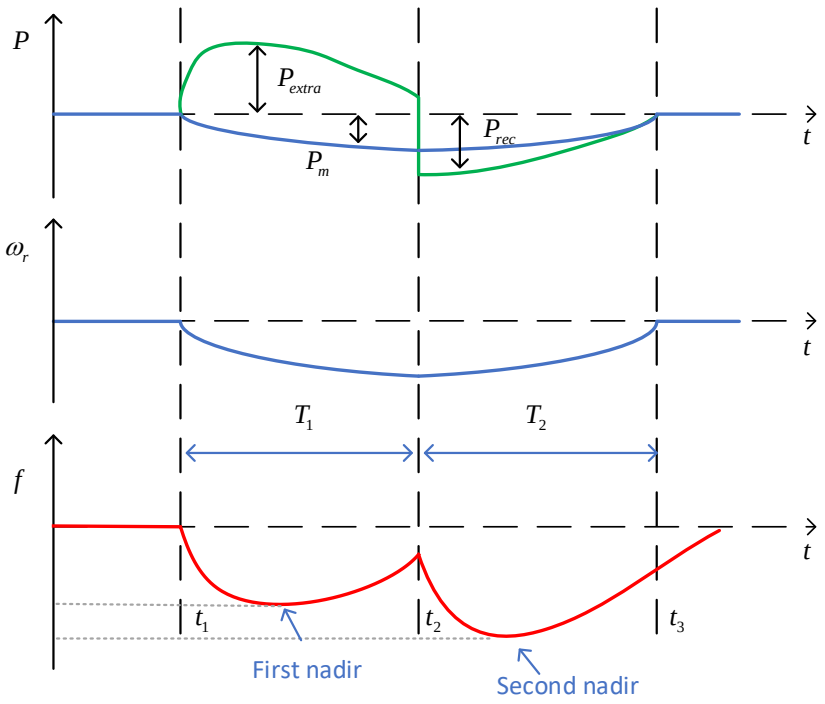

Fig. 6.1: Explanation of secondary frequency dips.

One of the advantages of using wind turbines to mitigate frequency declines is that the fast response due to the converter-based connection. The active power deficit can be quickly compensated by the kinetic energy contributed by frequency support control (such as synthetic inertia control). However, this brings the occurrence of SFD shown in Fig. 6.1, which happens under the condition that nearly all the active power deficit caused by frequency disturbance is compensated by releasing the temporary energy reserves from wind turbines. The frequency support process has to be terminated when the rotor speed protection is tripped. Another active power imbalance occurs here since the energy needs to be extracted from the grid to restore the rotor speed. Especially in medium and high wind speed conditions, the rotor speed of wind turbines is relatively high according to aerodynamic equations thus bigger range between operating rotor speed and lower limits is obtained. In this context, a much larger frequency dip occurs.

6.2. Description of the consecutive power dispatch method

The traditional frequency regulations for conventional power plants offer an extensive and flexible range of solutions for systems operators, especially during system faults and unexpected disturbances. For example, controlling the position of the main supply valve of a steam generator can effectively compensate the active power imbalance, while it is impossible to instantaneously control wind turbine generators or even accurately predict their outputs due to intermittent wind speed. To balance this large non-dispatchable resource, other synchronised generation units need to be regulated more frequently. Although many researchers have developed wind speed forecasting methods to some extent [161]–[164], a low inertia system is more prone to frequency instability. Therefore, wind farms are desperately in need of having a similar performance to conventional generation so that the demand required by system operators can be met.

6.2.1. Explanation of temporary and persistent energy reserves

The energy reserves supplied by a wind farm to control the frequency can be classified into two categories: temporary and persistent energy reserves.

Temporary energy reserves are stored in the rotor of the wind turbine generators operating within the MPPT curve, which contributes to the FN and RoCoF at the very first instance of a frequency disturbance. The duration of the temporary energy reserves depends on the time that the rotor speed of a wind turbine generator decreases from its nominal speed to minimum speed (0.7 *pu*). On the other hand, persistent energy reserves are reserved in a wind turbine generator by shifting the operating point of the wind turbine generator from their MPPT curve to a suboptimal power level, which can provide frequency support. It is worth noting that if no frequency response is required from the wind turbine generators operating under the suboptimal mode, those of which still deliver active powers at a suboptimal level to the grid.

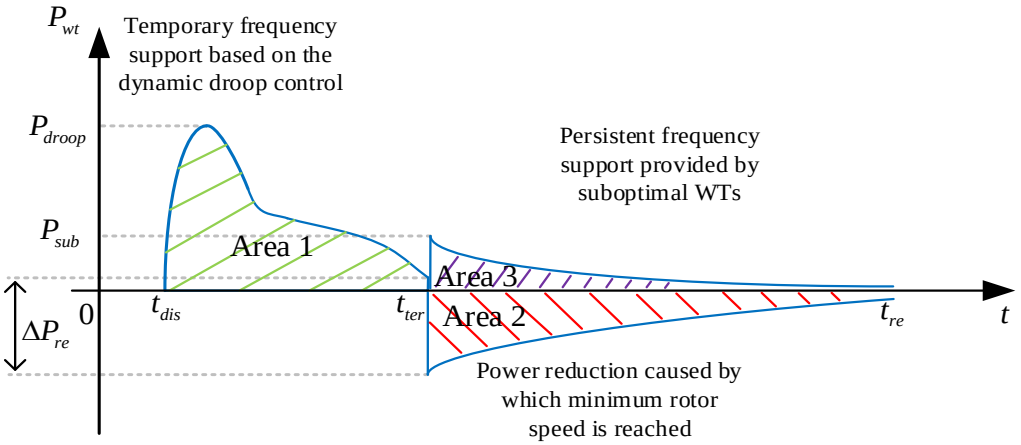

Fig. 6.2: Consecutive dispatch of temporary and persistent energy reserves provided by wind turbine generators operating at an optimal point and suboptimal point, respectively.

How to dispatch the temporary and persistent energy reserves in a wind farm is the key problem to mitigate the impacts caused by a possible occurrence of an SFD. In this process, wind turbine generators operating at the optimal point are designed to employ a dynamic droop-based control to bridge initial active power deficits. However, the persistent energy reserves stored in wind turbine generators operating at the suboptimal point are planned to compensate the power shortage caused by the termination of temporary frequency support. Fig. 6.2 depicts the consecutive dispatch of temporary and persistent energy reserves to arrest a SFD. Area 1 and Area 2 represent the temporary releasable energy and the active power shortage due to the

restoration of the rotor speed, respectively. When a frequency disturbance occurs at t_{dis} , a wind turbine generator operating at the optimal point initially provides temporary power P_{droop}, typically lasting up to tens of seconds, and termination time t_{ter} is determined when the rotor speed of the wind turbine generator reaches 0.7 *pu*. The larger the P_{droop} is, the faster the active power imbalance can be compensated, which brings a severer SFD. Therefore, an adaptive strategy for releasing P_{droop} is discussed in the next section. During the rotor speed restoration period (between t_{ter} and t_{re}), the persistent energy reserves marked as Area 3, counterbalances the power reduction ΔP_{re} . Thus, the difference between Area 2 and Area 3 determines the magnitude of the SFD. In order to make sure the annual revenues of wind farms, the number of wind turbine generators operating at a suboptimal point needs to adapt to the frequency event size. For instance, when the amount of persistent energy reserves is smaller than that of the power reduction, an appearance of a SFD is unavoidable, which may lead to the likelihood of a lower FN when compared to the first FN.

Based on the above explanation, the disadvantages of temporary energy as well as the persistent energy reserves can be alleviated. In a wind farm with all wind turbines operating at MPPT and providing temporary energy support only, the SFD is inevitable as since the activation of rotor speed protection. On the contrary, all wind turbines operate at a suboptimal level point, the annual profit will decrease. Regarding to the time of injecting persistent energy, the amount of temporary energy reserves used is crucial. Because if all the temporary energy reserve is used up, which leads to a termination of temporary energy support due to the protection of rotor speed. If the amount of the temporary energy reserve is enough to compensate the active power imbalance brought by the frequency event, the secondary frequency dip is obviously larger than the first frequency nadir. Thus, the persistent energy would not be necessary to support the potential occurrence of SFD as the synchronous generators take the frequency support responsibility. Therefore, the necessity of Area 3 shown in Fig. 6.2 is dependent on the amount of Area 1.

6.2.2. Consecutive dispatch of temporary and persistent energy reserves

The trade-off between fast inertial response and rotational speed recovery is a vital issue to settle. To suppress the SFD and make the most use of the frequency support capability of wind turbine generators, an application to employ persistent energy reserves will help deliver additional active powers during the rotor restoration stage.

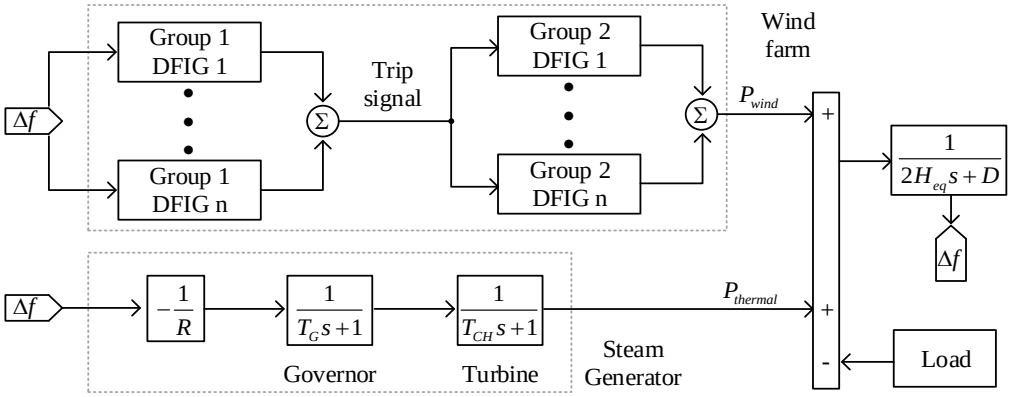

Fig. 6.3: Block diagram of implementing wind turbine generators in frequency control.

This modified power dispatch for DFIG-based wind farms is proposed to deal with the aforementioned problems in a leader-follower manner. To achieve this, all wind turbine generators in a wind farm are divided into two groups depending on operational conditions. The first group (Group 1(G1)) includes DFIGs operating at MPPT with a dynamic droop control, while the second group (Group 2(G2)) contains DFIGs operating at suboptimal mode achieved by overspeeding control. Under normal operating conditions, all DFIGs feed active power to the grid depending on the predefined operation. When a frequency disturbance occurs in the power system, Group 1 achieves fast frequency regulation and terminates the support at which the rotor speed of G1 DFIGs reduces to 0.7 *pu*. Then a trip signal that releases the persistent reserved power is sent to G2 to arrest the sequential frequency dip caused by the termination of temporary frequency support from G1. The persistence of frequency support using reserved power [165] is the main reason why G2 plays as a follower in scheduling. Also, the loss of annual revenue of such a multi-operation mode wind farm is reduced when compared to a wind farm consisting of all deloaded

DFIGs. Moreover, communication between each wind turbine generator requires a central wind farm controller. A latency time of 200 milliseconds [166] between frequency supports originating from the two groups is delayed by communication networks and computation time. Fig. 6.3 shows the schematic for implementing wind turbine generators under frequency control. The dynamic droop-based control implemented in the proposed control has already been introduced in Section 5.3.1. The required deloading control will be introduced in the following section.

6.3. Deloading Operation of DFIGs

In order for DFIGs to have sufficient active powers to provide frequency support; two main deloading methods, pitch angle control and rotor speed control, are widely implemented in wind turbine generators. Pitch angle control changes the pitch angle of the blades, deloading the wind turbine generator operation point from MPPT point to a deloaded level. As can be seen in Equation (3.1) to Equation (3.3), as β becomes larger, it reduces C_P thereby P_m. However, rotor speed control is utilised in the proposed control because the pitch angle control requires frequent pitch angle changes that can affect the lifetime of the pitch controller and increase maintenance costs [137]. Regarding the rotor speed control, wind turbine generators can be deloaded by shifting the operating point towards the left (point B) or right (point C) of the MPPT curve, which is why they are known as underspeeding or overspeeding control, respectively (see Fig. 6.4). In the proposed control, the deloading operation is accomplished by overspeeding control, as an underspeeding controlled turbine can reduce system stability [167]. The wind turbine generators operation follows the dash blue line as the rotor speed changes. For example, rotor speed increases from $\omega_{\max}$ to ω_{de} when wind turbine generator deloads from maximum power $P_{\max}$ to deloaded power P_{de}. When there is a frequency drop, the kinetic energy stored in the rotating mass is released as the rotor speed decreases. Most wind turbine generators are deloaded between 10% to 20%, depending on the instantaneous wind speed and given rotor speed limit [137].

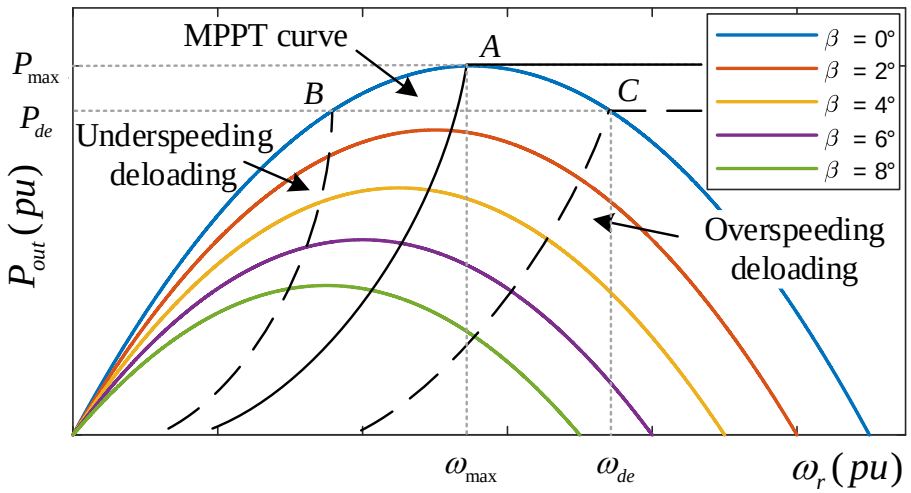

Fig. 6.4: MPPT and deloading power curve for a DFIG.

A deloading coefficient $d = 10\%$ is employed, with the deloaded power expressed by:

$$P_{de} = 0.9P_{MPPT} \tag{6.1}$$

$$P_{de} = (1-d)P_{mppt} = \frac{1}{2}\rho\pi R^2 C_{p,de} v^3 \tag{6.2}$$

where $C_{P,de}$ is the deloading power coefficient.

6.4. Test system

Fig. 6.5 demonstrates a test system built in DIgSILENT PowerFactory to validate the performance of the consecutive dispatch of temporary and persistent energy reserve schemes. The model system consists of four SGs, one aggregated DFIG-based wind farm and a general load of 300 MW. The assumption made in the simulation is that all the wind turbines in the wind farm capture the wind energy without wind speed decaying. In other words, the wake effect discussed in the pre4vious section is neglected.

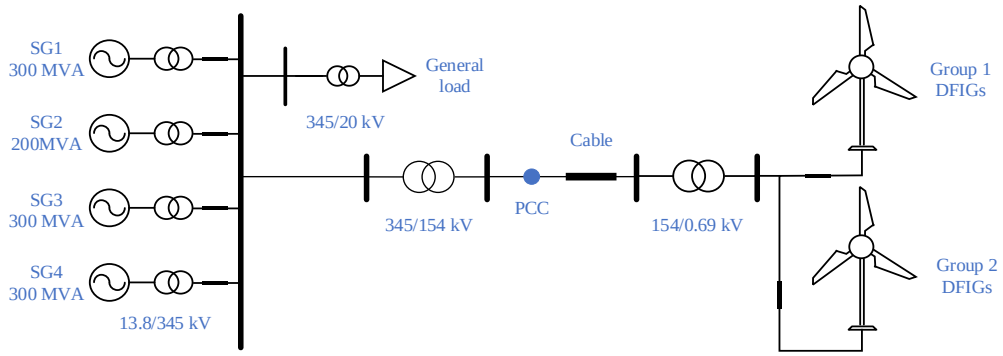

Fig. 6.5: Test system.

6.4.1. Synchronous generators

Four SGs are connected in the system: three 300 MVA SGs and one 200 MVA SG. All SGs in this study are considered to be steam turbine generators. Fig. 5.11 and Table 5.2 show the IEEE Type 1 speed-governor model and the model's coefficients, respectively. The inertia time constants of all SGs are set to 6.25 s. SG1 is selected as a slack machine and SG2 used to simulate a frequency contingency by disconnecting it from the rest of the system.

Due to the automatic generation control (AGC) not being involved in this system, the frequency does not completely recover to the nominal frequency after frequency rebounds.

6.4.2. DFIG-based wind farm

The DFIG-based wind farm is connected to the 0.69/154 kV transformer through the 154 kV submarine cable, then connected to the grid. The wind farm in the system is divided into two groups with 70% of the DFIGs operating at the MPPT curve and 30% of the DFIGs are deloaded. The rated power of each DFIG is 2MW.

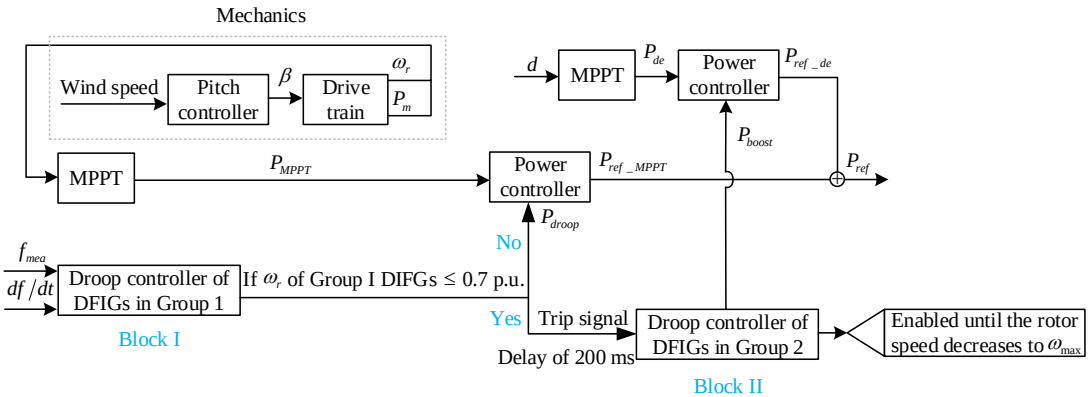

Fig. 6.6: Block diagram of the proposed scheme for a DFIG-based wind farm in DIgSILENT PowerFactory.

In this study, the block diagram for the proposed scheme for the DFIG-based wind farm is modelled in PowerFactory (Fig. 6.6). The mechanical parts of DFIG consist of pitch angle controller and drive train. The pitch angle controller sends the constant pitch angle to the drive train. The drive train uses Equation (3.1) to Equation (3.3) to model the aerodynamics of the DFIG with a single-mass representative because the electromechanical transient dynamic of the drive train is not considered in this study. The MPPT calculates the optimum wind power. The power controller modulates the active power of the wind farm. On the other hand, deloading factor d is sent to the MPPT block in G2 DFIGs, which is used to make G2 DFIGs operate at a deloaded level. Block I shown in Fig. 6.6 is modelled under dynamic droop-based inertial control, as well as a deadband. When frequency deviation is larger than the deadband, the DFIGs in G1 start to provide kinetic energy to support the frequency until their rotor speed is lower than 0.7 *pu*. Then, Block I is disabled and the rotor speed of G1 DFIGs begin to recover until their power output returns to MPPT output at optimum rotor speed. If rotor speed decreases below 0.7 *pu*., then a trip signal with a delay of 200 milliseconds is sent to Block II. Therefore, reserved generation P_{boost} is released by G2 DFIGs until the corresponding optimum rotor speed is reached. The occurrence of a SFD is caused by the sudden loss of P_{droop} due to its temporary power support from the DFIGs. However, the amplitude of the SFD is determined by power P_{boost} reserved in the deloaded DFIGs and the power shortage for the G1 DFIGs restoring the rotor speed. In addition, the duration for P_{boost} for the deloading DFIGs depends on the restoration phase of the G1 DFIGs.

6.5. Simulation results

In this section, the simulation results are obtained to evaluate the performance of the proposed consecutive dispatch of temporary and persistent energy reserves by varying the wind speed, power output and size of the tripping generator (SG2 shown in Fig. 6.5). To do this, the wind speed is varied from 8.5 m/s to 10 m/s in 0.5 m/s steps, the size of the tripped generator is varied from 60 MW to 80 MW in 10 MW steps and the penetration level of the wind power change ranges from 13% to 25%.

As depicted in Table 6.1, the proposed strategy is compared to Scheme 2, which applies the same dynamic droop as in the proposed scheme for all the DFIGs within a wind farm. In addition, it is compared to a case in which a wind farm that is without inertial control through time-domain simulations. All simulations were conducted by writing the DPL code in DIgSILENT PowerFactory. The simulation result is also included in the submitted paper [168].

Table 6.1: Simulation schemes.

Schemes	Wind Turbines
1	Proposed scheme
2	Dynamic droop scheme
3	Without inertial control

6.5.1. Study 1: Effect of wind speed

The performance of the proposed scheme is affected by wind speed, which contributes the various kinetic energy levels over the frequency support period in a wind farm. This section examines the performance of the proposed cases for those cases that have wind speeds of 8.5 m/s and 9 m/s and 9.5 m/s, respectively.

Case 1: Wind Speed of 8.5 m/s, 50 MW Generator Trip, Wind Power Penetration Level of 13%: Fig. 6.7 shows the results for Case 1, in which SG2 is generating 50 MW prior to a disturbance in the model system and tripped at 10 s. As shown in Fig. 6.7(a), the first FNs for the proposed scheme, Scheme 2 and Scheme 3 are 49.09 Hz, 49.13Hz and 48.97 Hz, respectively. Moreover, the SFDs in Scheme 1 and Scheme 2 are 49.18 Hz and 49.07 Hz, respectively.

The proposed scheme prevents the ω_r of G1 DFIGs from reaching $\omega_{\min}$. This is achieved by increasing the $R(df/dt)$ thus temporally decreasing P_{droop} at 16.7 s, as shown in Fig. 6.7(b). However, at the beginning stage of the contingency, ω_{r_de} of G2 DFIGs stays at a deloading level and G2 DFIGs contribute a deloaded level of power to the grid until the trip signal is received. Then ω_{r_de} starts to decrease to the optimum rotor speed ω^* when P_{boost} in the G2 DFIGs is released to compensate for the SFD. In contrast, in Scheme 2, an SFD happens at 21.4 s when the wind farm output starts

decreasing. A larger SFD occurs due to a bigger sudden loss of 12 MW in temporary power than it does in the proposed scheme.

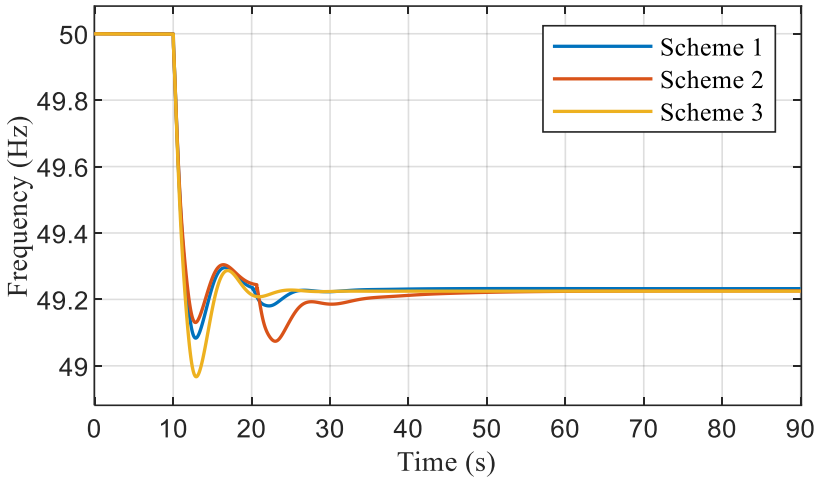

(a)

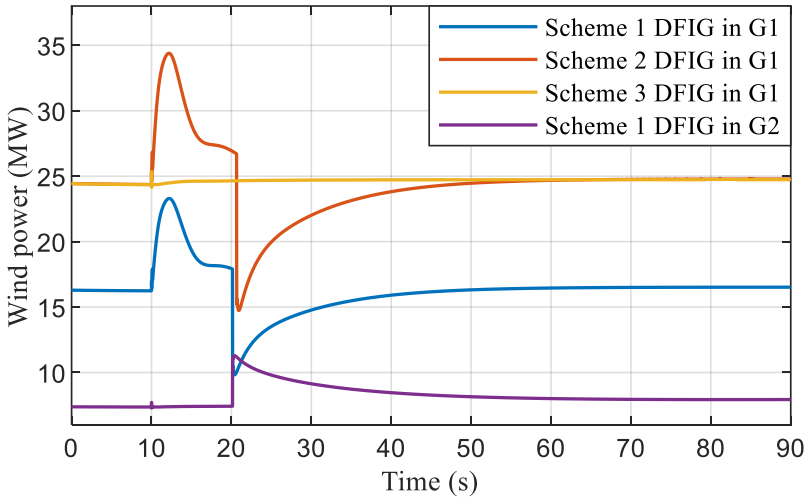

(b)

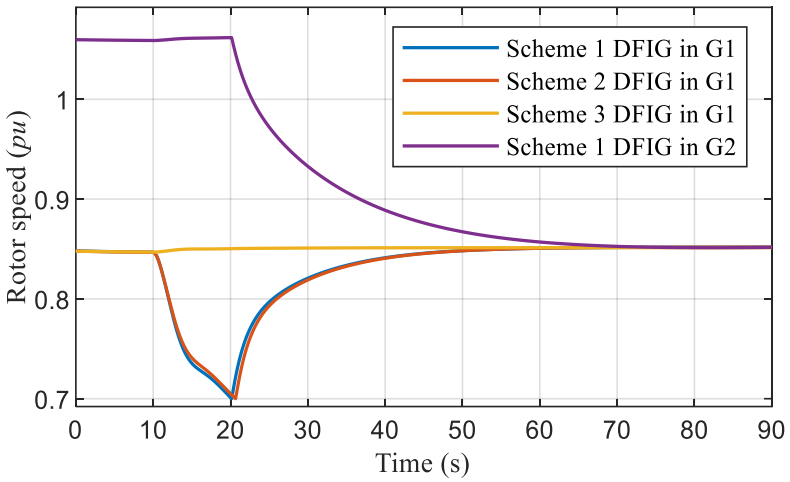

(c)

Fig. 6.7: Results for Case 1. (a) System frequency, (b) WPP output, (c) Rotor speed.

Case 2: Wind Speed of 9 m/s, 50 MW Generator Trip, Wind Power Penetration Level of 13%: Fig. 6.8 shows the results for Case 2, in which the wind speed is bigger than it is in Case 1. Therefore, the kinetic energy of the DFIGs is larger. As shown in Fig. 6.8(a), the first FNs for the proposed scheme, Scheme 2 and Scheme 3 are 49.10 Hz, 49.13Hz and 48.99 Hz, respectively. In addition, the SFD in the proposed scheme is 49.16 Hz, which is 0.06 Hz smaller than the first FN. Moreover, the SFD in Scheme 2 is 49.02 Hz. As in Case 2, the proposed scheme has the smallest SFD among these two schemes, which is identical to Case 1.

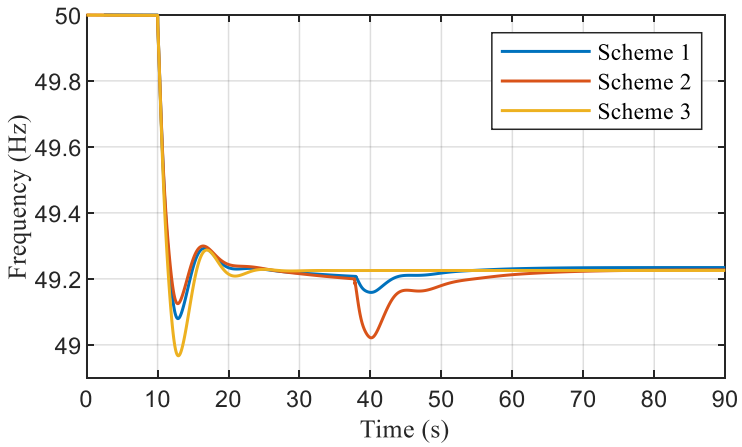

(a)

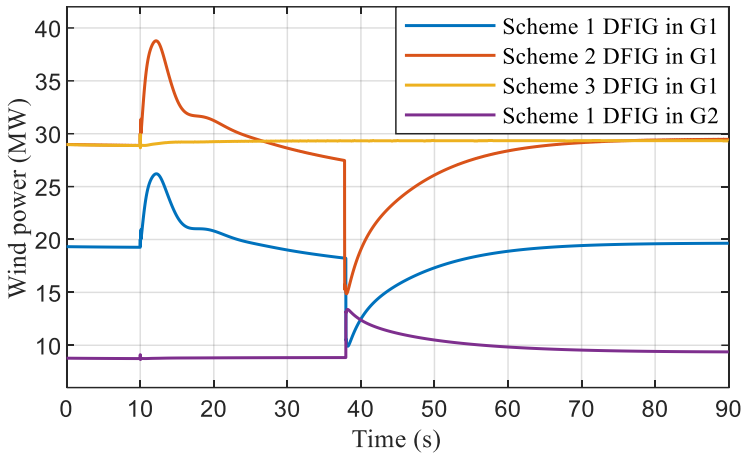

(b)

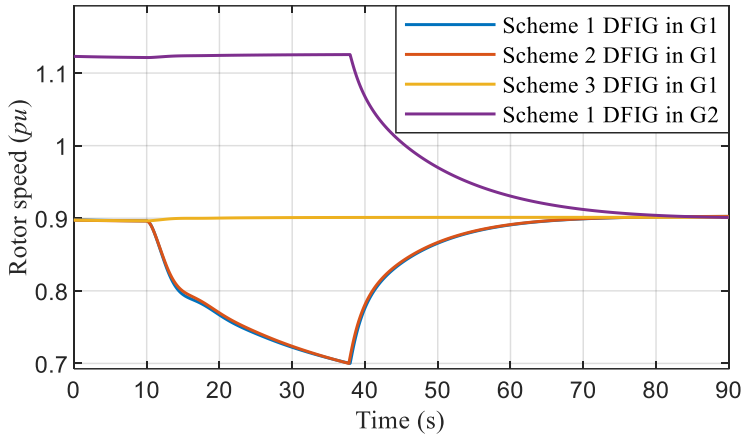

(c)

Fig. 6.8: Results for Case 2. (a) System frequency, (b) WPP output, (c) Rotor speed.

The results of the above two cases prove that the proposed scheme can create a smaller SFD while improving the FN under various wind speeds. However, in Case 2, ω_r recovering to ω^* takes a longer period of time than it does in Case 1. Due to both cases being set to the same dynamic droop value, a DFIG with a larger kinetic energy needs a longer time to reach $\omega_{\min}$.

Case 3: Wind Speed of 9.5 m/s, 50 MW Generator Trip, Wind Power Penetration Level of 13%: Fig. 6.9 shows the results for Case 3. It is noted that the proposed scheme is not activated in this case because the active power output of the DFIGs are increased as the wind speed increases. In this circumstance, the active power deficit can be

compensated by only activating the dynamic droop-based control in G1 DFIGs. In Fig. 6.9(c), the DFIGs rotor speeds in both Scheme 2 and 3 continuously decrease, failing to reach 0.7 *pu*. Hence, the signal for activating G2 DFIG is not tripped. G2 DFIG's rotor speed maintains at its initial speed of 1.188 *pu* during the simulation.

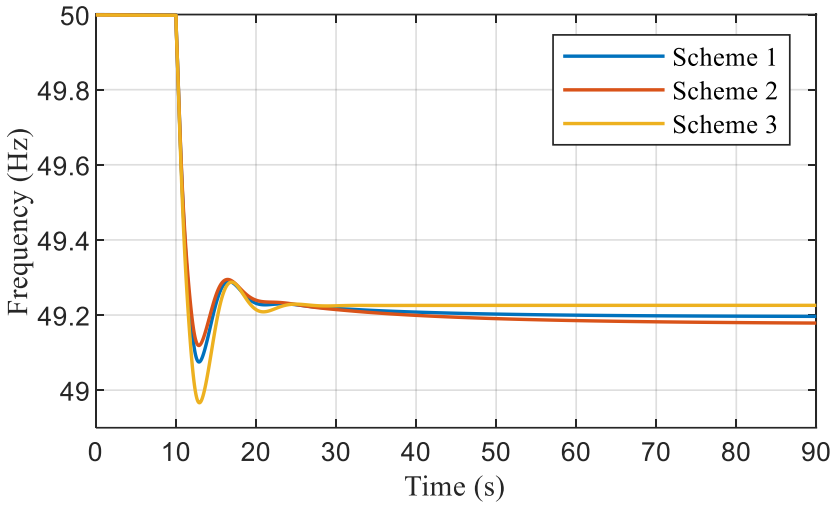

(a)

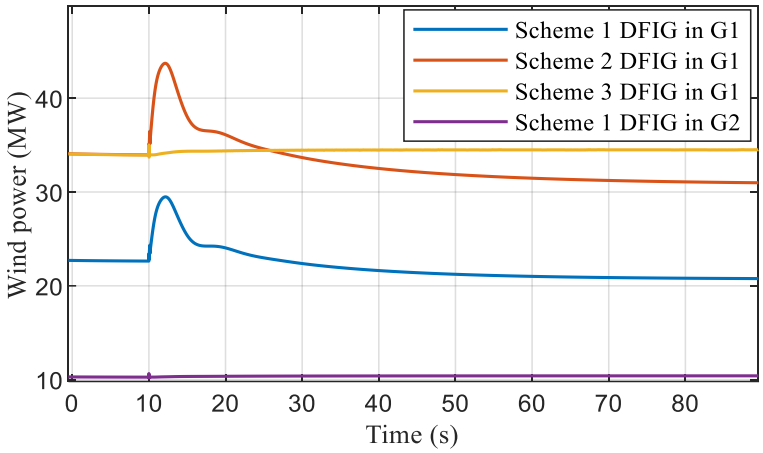

(b)

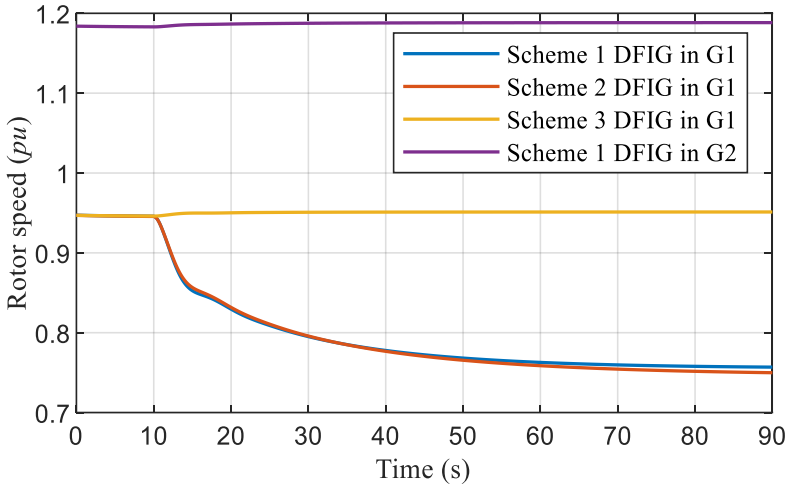

(c)

Fig. 6.9: Results for Case 3. (a) System frequency, (b) WPP output, (c) Rotor speed.

6.5.2. Study 2: Effect of the tripped generator size

This section describes the investigation results for the proposed scheme caused by tripped generator size.

Case 4: Wind Speed of 9 m/s, 60 MW Generator Trip, Wind Power Penetration Level of 13%: Fig. 6.10 shows the simulation results for Case 4. The first nadirs for Scheme's 1, 2 and 3 are 48.95 Hz, 48.9 Hz and 48.76 Hz, respectively. The SFD for Scheme's 1 and 2 are 49.00 Hz and 48.86 Hz, respectively. The amplitude of the SFD is improved 0.14 Hz after applying the proposed control. Compared to the results obtained for Case 2, the time to get the SFD is shorter as more temporary kinetic energy is released after the frequency event. However, the SFD is lower when compared to the amplitude of the SFD for Scheme 2 in both Case's 2 and 4 because a large active power decrement occurs in Case 4 caused by the termination of temporary energy support.

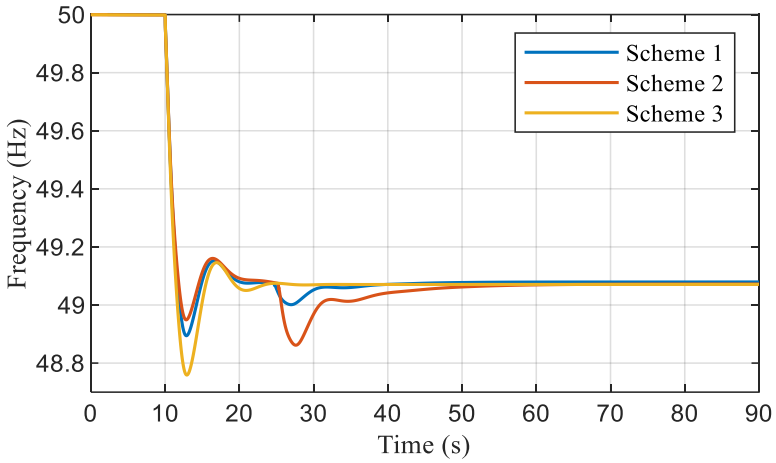
Scheme 1
Scheme 2
Scheme 3
Frequency (Hz)
Time (s)

(a)

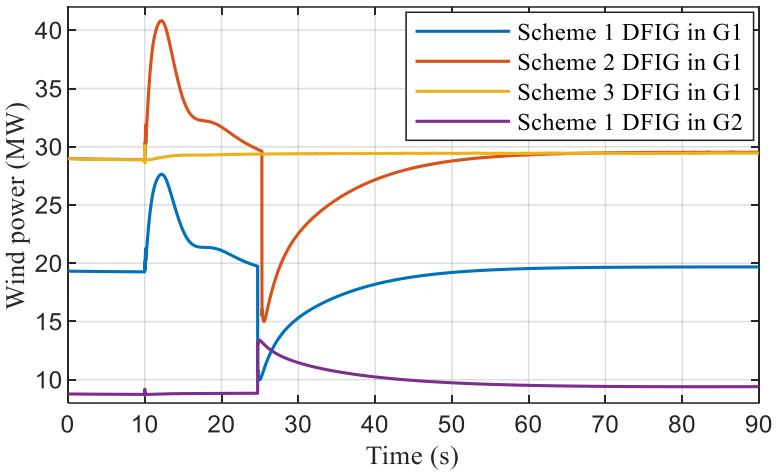
Scheme 1 DFIG in G1
Scheme 2 DFIG in G1
Scheme 3 DFIG in G1
Scheme 1 DFIG in G2
Wind power (MW)
Time (s)

(b)

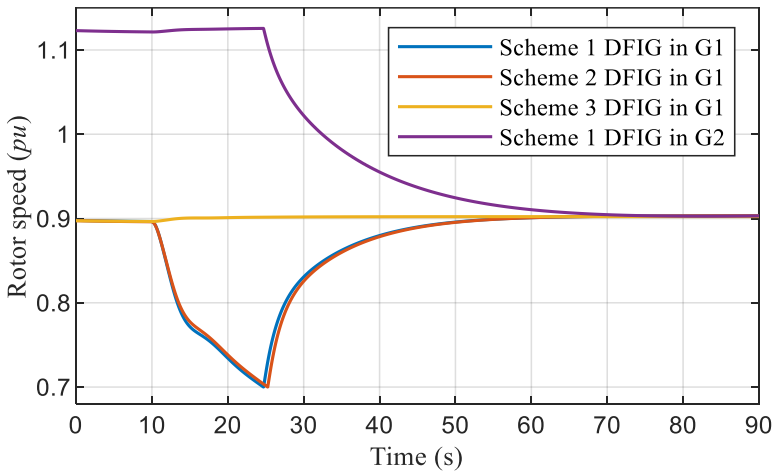
Scheme 1 DFIG in G1
Scheme 2 DFIG in G1
Scheme 3 DFIG in G1
Scheme 1 DFIG in G2
Rotor speed (pu)
Time (s)

(c)

Fig. 6.10: Results for Case 4. (a) System frequency, (b) WPP output, (c) Rotor speed.

Case 5: Wind Speed of 9 m/s, 70 MW Generator Trip, Wind Power Penetration Level of 13%: Fig. 6.11 shows the results for Case 5. The only exception is the size of the tripped generator used. Also, the wind speed is the same as in Case 2, which means the same amount of kinetic energy can be generated by DFIGs. A generator delivering 70 MW to the network is tripped at 10 s prior to a disturbance. This results in a larger frequency drop than in Case 2. The first FNs for the proposed scheme, Scheme 2 and Scheme 3 are 48.71 Hz, 48.77 Hz and 48.55 Hz, respectively. The SFD for the proposed scheme is 48.84 Hz, which is higher than for Scheme 2 by 0.14 Hz and lower than that of Case 2 by 0.32 Hz.

It is worth noting that in this case, the size of the tripped generator is greater than that of Case 2; thus, more power in Case 5 is released to stop the frequency decreasing than it does in Case 2. Additionally, the DFIGs rotor speeds decrease more quickly at the very first instant of the disturbance than in Case 2; however, it still recovers to ω^* within the simulation time.

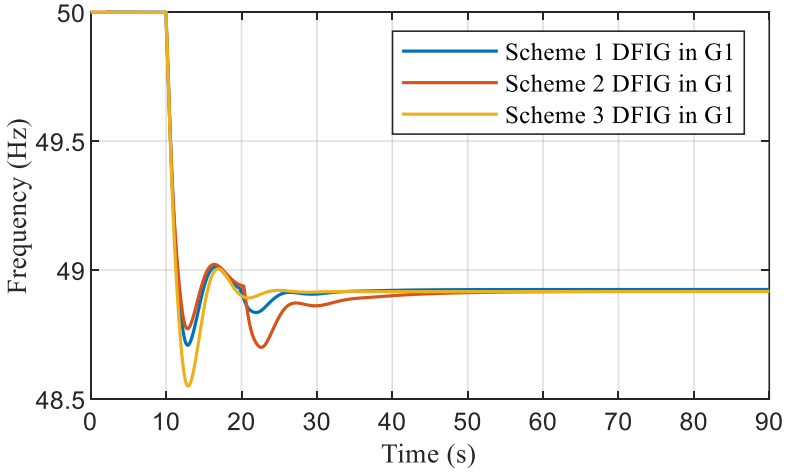

(a)

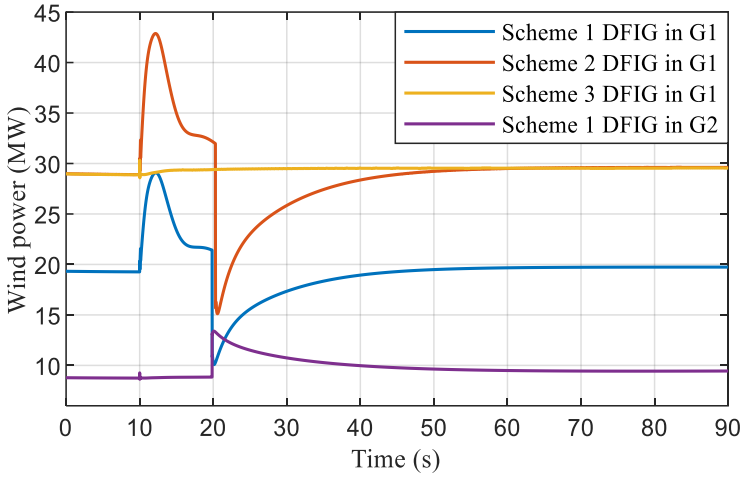

(b)

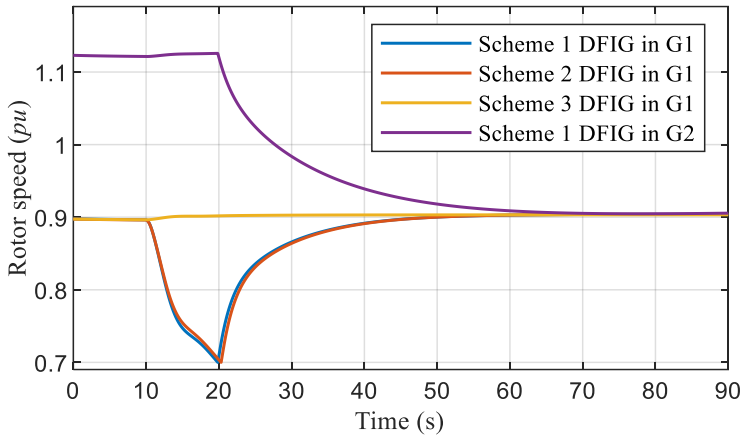

(c)

Fig. 6.11: Results for Case 5. (a) System frequency, (b) WPP output, (c) Rotor speed.

The results for Case 2 and Case 5 demonstrate that the proposed scheme provides more temporary energy to improve the SFD than Scheme 2, even when there is a larger frequency drop due to the larger tripped generator size.

6.5.3. Study 3: Effect of wind power penetration levels

This section investigates the simulation results of the proposed scheme for different wind power penetration levels. To do this, the number of DFIGs is increased, whereas the capacity of SGs is reduced. The comparison is conducted by simulating two wind power penetration levels of 13% and 25%, respectively.

Case 6: Wind Speed of 9 m/s, 70 MW Generator Trip, Wind Power Penetration Level of 25%: Fig. 6.12 shows the results for Cases 6. The simulation settings are identical to Case 5, except for the wind penetration level of 25%. The first FNs for the proposed scheme, Scheme 2 and Scheme 3 are 48.83 Hz, 48.92 Hz and 48.55 Hz, respectively. In addition, the SFD for the proposed scheme is 48.78 Hz, whereas Scheme 2 has an SFD of 48.5 Hz, occurring at 33.9 s.

Comparing Fig. 6.11(a) with Fig. 6.12 (a), the SFD becomes more severe under a higher wind power penetration level. The SFD for Case 6 is 0.06 Hz larger than that for Case 5. Also, ω_r in the proposed scheme starts the recovery from 20.88 s and returns to its ω^*. Compared to Case 5, the recovery time of ω_r is longer to ensure an adequate frequency response in Case 6.

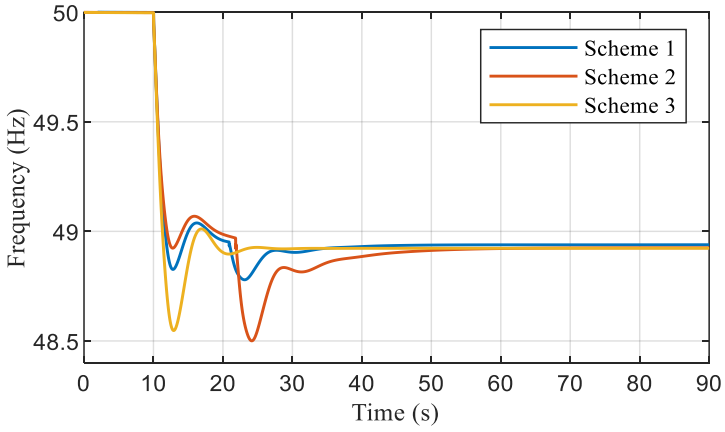

(a)

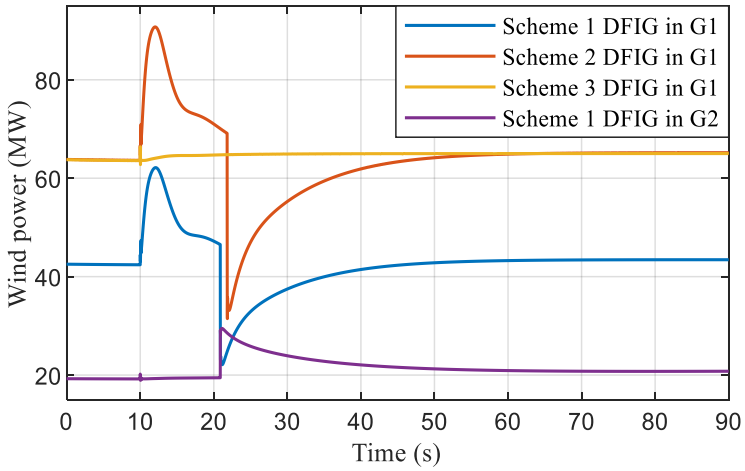

(b)

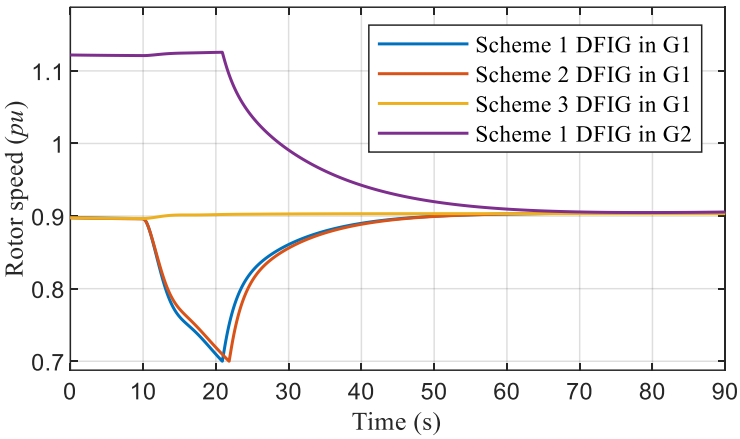

(c)

Fig. 6.12: Results for Case 6. (a) System frequency, (b) WPP output, (c) Rotor speed.

6.5.4. Study 4: Effect of deloading levels

Case 7: Wind Speed of 9 m/s, 70 MW Generator Trip, Wind Power Penetration Level of 13%, Deloading level: 20%: Fig. 6.13 shows the simulation results for Case 7. The deloading level of the G2 DFIGs is assumed to be 10% for Case's 1 to 6. The deloading level is increased from 10% to 20% in Case 7. Therefore, the characteristics of G2 DFIGs must be redefined. The modified parameters of DFIGs can be redefined by calculating the deloading tip-speed ratio λ_{del} and deloading MPPT coefficient $k_{opt\_deloading}$, as per Equation (3.27).

The first nadirs for the proposed scheme, Scheme 2 and 3 are 48.71 Hz, 48.77 Hz, and 48.55 Hz, respectively. The SFDs for Scheme's 1 and 2 are 48.86 Hz and 48.7 Hz, respectively. Comparing Case 5 and Case 7's simulation results, it is noted that the first FN in both cases is 48.71 Hz because the characteristics of G1 DFIGs remain unchanged. In this regard, the active power output and the amount of temporary energy contributed by the G1 DFIGs is the same in both cases. On the other hand, the amplitude of the SFD is increased 0.02 Hz by further deloading the G2 DFIGs 10% more when compared to the simulation results in Case 5. Since the 20% deloading level is applied, the initial rotor speed of the G2 DFIGs is equal to 1.23 *pu*, with 20%

of generated power reserved in the G2 DFIGs. More persistent energy is available to compensate for the wind power decreases caused the termination of temporary energy. Furthermore, the G2 DFIGs rotor speeds take a longer time to reach the MPPT rotor speed in this case.

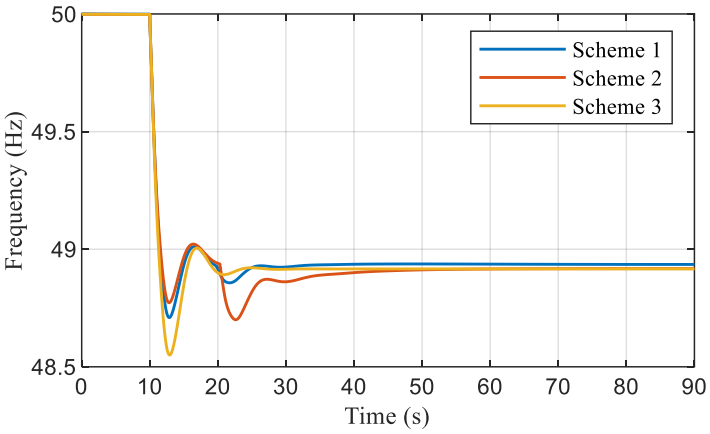

(a)

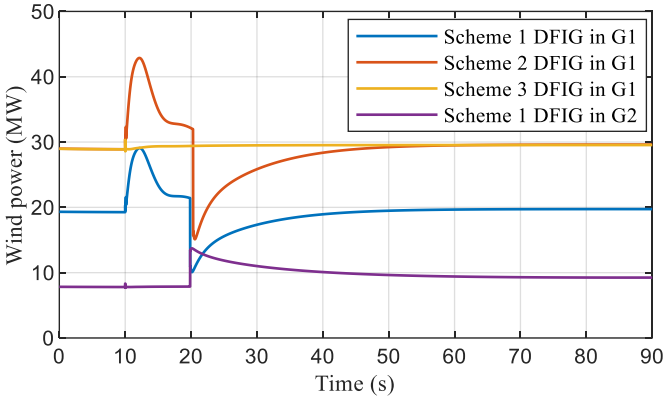

(b)

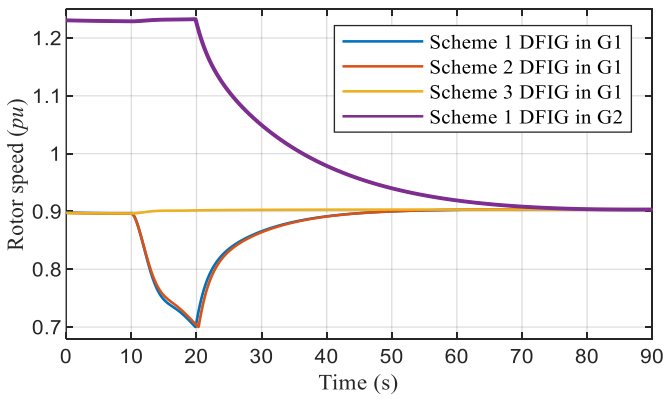

(c)

Fig. 6.13: Results for Case 7. (a) System frequency, (b) WPP output, (c) Rotor speed.

6.5.5. Study 5: Sensitivity analysis for communication times

In this part, the performance of the proposed dispatch is investigated under different assumed communication times. The system frequency responses, active powers of G2 wind turbines and rotor speeds of G2 wind turbines are depicted in the following figures. Four different communication times are employed in the simulations with a 250 ms gap. As can be seen in Fig. 6.14 (a), the frequency responses are carried out. The general pattern can be obtained is that the magnitude of secondary frequency dip is lower as the larger communication delay is used in the simulation, which worsens the system frequency stability. This is because the larger communication time is used, the later the persistent energy reserved in G2 wind turbine is injected into grid. Moreover, lower magnitude of SFD may increase the possibility of causing unnecessary UFLS activated.

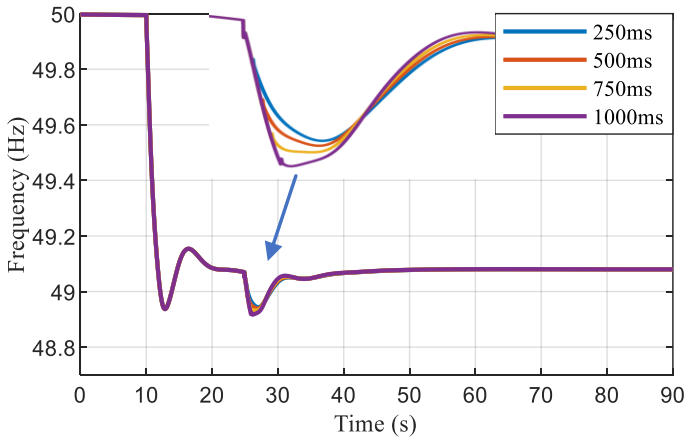

(a)

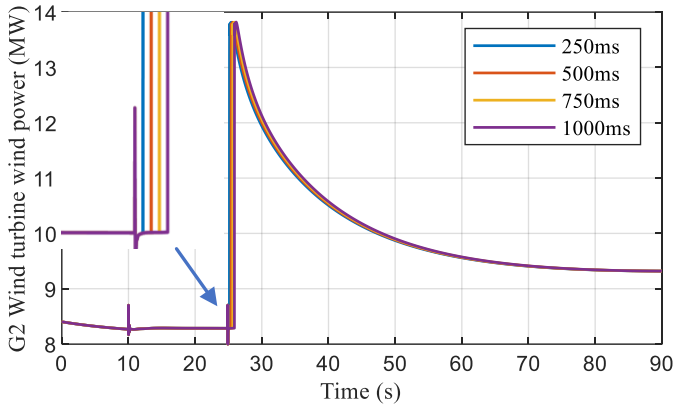

(b)

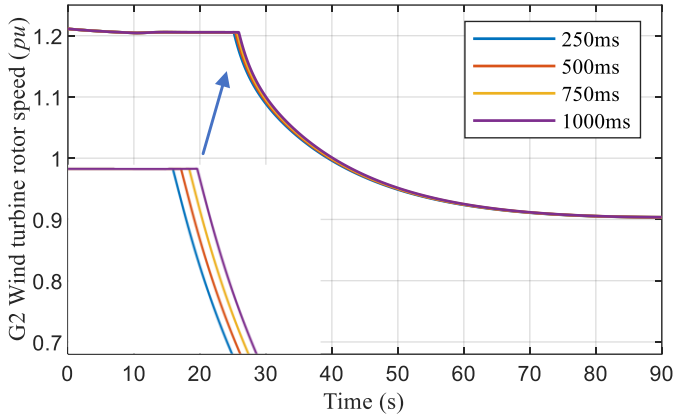

(c)

Fig. 6.14: Results for sensitivity analysis. (a) System frequency, (b) WPP output, (c) Rotor speed.

6.5.6. Study 6: Optimization of G1 and G2 wind turbines

To explore the best performance of the proposed scheme, determining the number of wind turbines located in Group 1 and 2 is crucial. Table 6.2 shows the three combinations of Group 1 and 2 used in this simulation. The percentage of G2 is increased to maximum 30% as the consideration of annual profit of wind farms; because more wind turbines operate at suboptimal power level, the less profit wind farms make.

Table 6.2: Combination of G1 and G2.

Combination	G1	G2

1	90%	10%
2	80%	20%
3	70%	30%

Fig. 6.15 (a) shows the frequency response with different combination of G1 and G2 wind turbines, It can be found that the first nadirs caused by frequency event decrease as the number of wind turbines in G2 increases, because the number of wind turbines in G1 decreases resulting in a less temporary energy reserves. Thus, less power originated from G1 wind turbine is available to compensate the active power imbalance. However, the magnitude of secondary frequency dip is improved the most in the Combination 3 among three cases. The yellow line shown in Fig. 6.15 (c) represents the G2 wind turbine power in Combination 3, which shows the largest amount of persistent energy reserves in G2 wind turbine. In this context, the secondary frequency decline caused by the termination of temporary energy support from G1 wind turbine will be mitigated most. The magnitude of SFD in Combination 1, 2 and 3 are 48.86 Hz, 48.92 Hz, and 48.97 Hz, respectively.

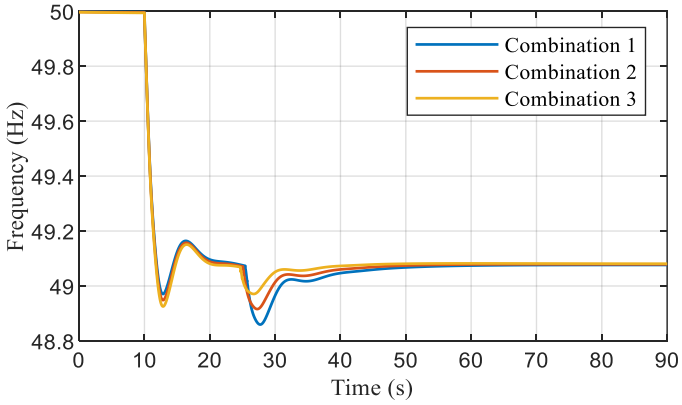

(a)

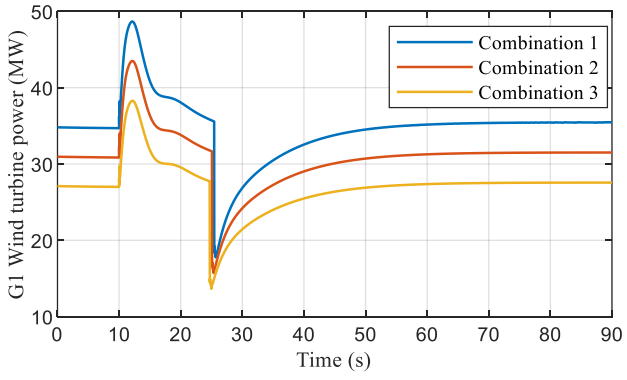

(b)

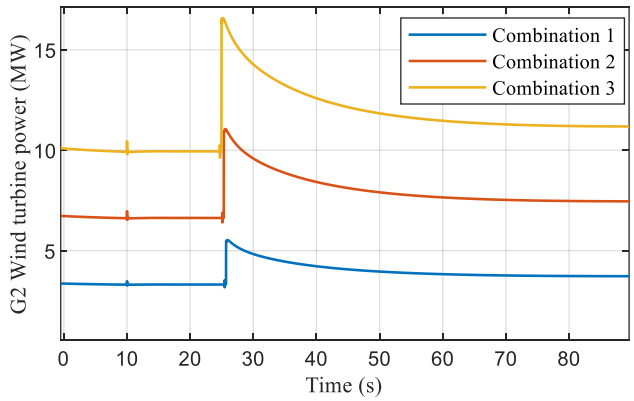

(c)

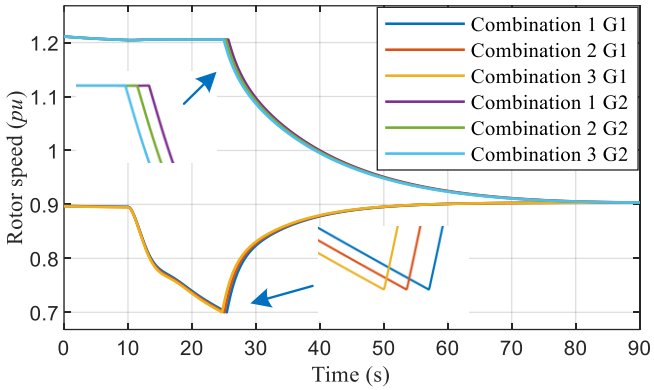

(d)

Fig. 6.15: Results for optimisation of G1 and G2. (a) System frequency, (b) G1 wind turbine output, (b) G2 wind turbine output, (d) Rotor speed.

6.6. Chapter summary

This chapter proposed a consecutive power dispatch scheme for DFIG-based wind farms. This scheme can mitigate SFDs and appropriately recover rotor speed when DFIGs support the frequency.

In order to mitigate the SFD caused by the disablement of DFIGs temporary energy reserves, this scheme coordinates temporary energy reserves with persistent energy reserves by dividing all DFIGs in a wind farm into two groups. G1 DFIGs operate in

accordance with the MPPT curve, whereas the rest of DFIGs in G2 operate with deloading power. At the initial stage of a disturbance, G1 DFIGs start to provide frequency support based on a dynamic-droop based control. A trip signal is sent to G2 DFIGs when the G1 DFIGs rotor speeds reach their minimum limit; therefore, the magnitude of the SFDs can be compensated by the additional boost power from the G2 DFIGs.

The simulation results were conducted from the perspective of wind speed, contingency size, wind power penetration level and the DFIGs deloading levels. It is noted that the proposed scheme can mitigate the size of the SFD, while improving the first FN and preventing the rotor from over-deceleration. Also, it ensures the stable operation of DFIGs under various wind conditions, contingency sizes and wind penetration levels. Furthermore, it will increase annual revenue when compared to wind farms that apply deloading control to all DFIGs.

Chapter 7 System Integrity Protection Schemes - Under Frequency Load Shedding

A System Integrity Protection Scheme (SIPS) is properly designed in modern power systems and a valuable way of assessing the system security [169], unlike conventional protection devices that are adopted to selectively disconnect faulty devices. However, the aims of a SIPS is not only to protect the equipment but also maintain the integrity of the power system, or even a portion of the power system experiencing the contingency. A key characteristic of a SIPS is that it monitors the elements of the power system, rather than controlling them. For example, a SIPS can monitor the power flow along the transmission lines, therefore deciding whether the disconnection of generation or load is necessary to get those devices relieved. A comprehensive review of SIPSs led by the IEEE Power System Relaying Committee is discussed in [170].

Section 7.1 introduces a SIPS that is comprised of the classification, architecture and input of the SIPS. Section 7.2.1 introduces UFLS from philosophical, methodological and operating principle perspectives. Moreover, a systematic approach for designing an UFLS system is also presented. Section 7.3 and 7.4 elaborates on the simulation results obtained from the modified two-area system and GB 29-zone system, respectively. Section 7.5 concludes this chapter.

7.1. Introduction to SIPS

With increasing demand for electricity, the requirement for a carbon dioxide reduction and integration of RESs bring technical challenges to modern power systems. The

potential faults to be dealt with are contingencies occurring along the transmission line, power systems operating close to their security limits, power imbalance due to the intermittence of RESs, etc. Especially, system stability will degrade alongside the penetration level of RESs. Most RESs are converter-interfaced sources, which means those sources cannot contribute to system inertia. In other words, system inertia declines as the RESs displace synchronous generators. The FN is lower and frequency excursion is faster in a RES integrated system after being subjected to a frequency event. Furthermore, it increases the risk of tripping a relevant SIPS and cascading outages.

The classification of a SIPS must be clear before assessing the SIPS design. The SIPS can be classified into four subcategorises, as shown in Fig. 7.1.

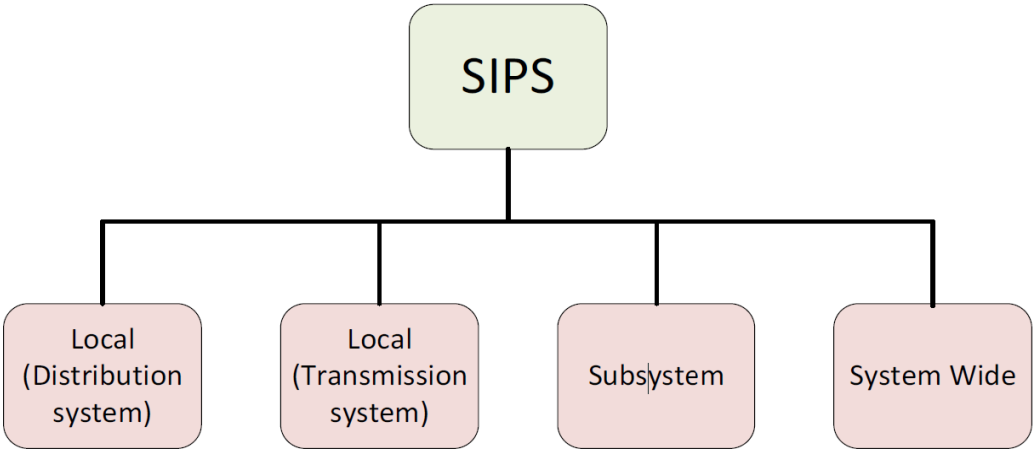

Fig. 7.1: Classification of SIPS [170].

A SIPS is installed in a power system to protect the integrity of the system or its strategic portions. A SIPS is used to ensure the entire system or strategic parts are functioning to maintain system stability, retain overall system connectivity and avoid the serious damage to the equipment when under contingencies. Consequently, the SIPS requires numerous detection, actuation and communication devices.

Local (Distribution system): SIPS devices are equipped with a dedicated function. The monitoring, decision-making and control devices are connected to one distribution bus. The operation of this type of SIPS generally only impacts on a portion of a distribution system (e.g. radial feeder or small network).

Local (Transmission system): The monitoring, decision-making and control devices are connected to one transmission bus. The operation of this type of SIPS usually impacts on a small power company and has rather limited effects on neighbouring interconnected systems.

Subsystem: The action of this type of SIPS affects a large geographic area that consists of several transmission system and generating facilities. The monitoring device adopted here needs to sense the parameters and operating states of various power systems. A decision-making device is required to perform at one location. Also, telecommunication is mandatory to collect the data and send/receive the control signal.

System wide: This type of SIPS is most complex among the four types of SIPS and consists of multiple level of arming, decision-making and communications. Collecting local and remote data from various locations and consistently sending/receiving control signals can be achieved as per the real-time system operator's requirement.

The actions of this type of SIPS can have a significant impact on a whole interconnected system.

7.1.1. Architecture of a SIPS

The SIPS architecture is determined by the practical location of the monitoring, decision-making and control devices that make up the scheme and impact on the power system [171]. A SIPS can be classified into two main subcategories: flat and hierarchical architecture.

Flat architecture: The measurement and operating devices of a SIPS are located in the same location. Moreover, the decision making devices collecting remote data and initiating actions require communication links between them. A typical instance of a flat architecture SIPS is UFLS.

Hierarchical architecture: This type of architecture consists of several steps during the SIPS's corrective actions. Local measurement and various predetermined parameters at different locations are exchanged between decision making devices. The design of this architecture considering the logic and actions involves the use of operating nomograms, state estimation and contingency analysis [171].

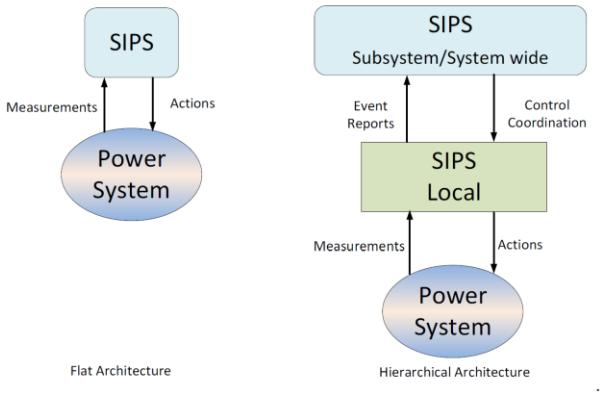

Fig. 7.2: Architecture of a SIPS [172].

Fig. 7.2 shows the architecture of a SIPS.

7.1.2. Inputs of SIPS

The inputs by a SIPS depend on the types of disturbance [173]:

- Power flow congestion.
- System instability.
- Thermal overloading.

To deal with the aforementioned problems, a list of input variables for a typical SIPS is shown in the following. The input measurements can be either collected locally or received through multiple layers of monitoring devices.

- Power system voltage and/or current: These measurements is timely local or system-wide synchronised and ranges from magnitude, phase angle and scale factors.
- Power system frequency.
- Control signals: E.g. automatic voltage regulator, power system stabiliser, generator speed-governor and reactive power compensation, including converters, FACTS and static voltage compensator.
- Working status: Status of the circuit breaker, status of the transformer tap changer, etc.
- Last valid state: System state estimation and telemetry data in case of communication link disconnection.

- Arming status: Status of the SIPS, system equipment chosen to be involved in the corrective action.

From a technical perspective, the contingency analysis is predetermined during the design of a relevant SIPS [174]. Fig. 7.3 shows the operating schematic of a SIPS. A disturbance is detected in many ways, such as amplitude of system parameters and working status of various protection relays, etc. These signals will be transmitted and utilised as the input of a SIPS. Then, the decision-making devices react according to predesigned actions once the disturbance has been identified.

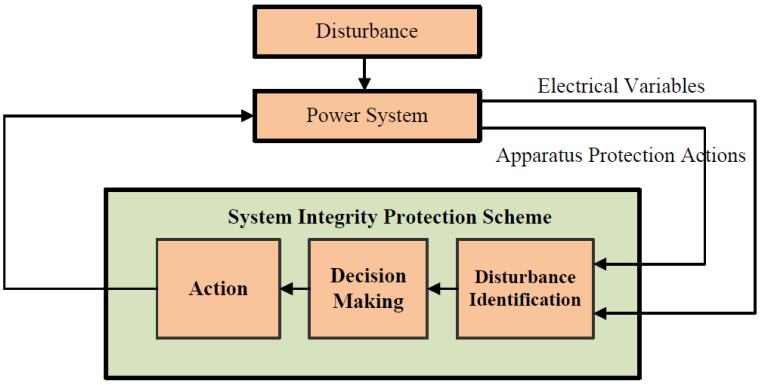

Fig. 7.3: Operating schematic of a SIPS [172].

As depicted in [170], a SIPS consists of various levels or schemes: Special Protection Schemes (SPS), Remedial Action Schemes (RAS) and more specific schemes, such as UFLS, UVLS and out-of-step (OOS).

7.2. Introduction to UFLS

In order to keep the power system in an equilibrium operating state, the balance between generation and consumption needs to be maintained. A power system is prone to lose frequency stability due to a sudden load increase, loss of a major generating unit or coherence between a group of generators, tripping transmission lines. An over frequency situation can be caused by excess generation, whereas an underfrequency situation can result from a sudden load increase. UFLS is undoubtedly one of the critical areas in a SIPS because the activation of UFLS is the last automated countermeasure against severe frequency decreases [175]. Also, in order to prevent propagation of a cascading outage and minimise the risk the damage to significant equipment in power systems, UFLS relays are installed at specific load sites.

The UFLS used in this project can be divided into three steps. Firstly, system frequency is monitored. Secondly, when the detected abnormal frequency drops below the acceptable range, an instruction will be sent to the control centre, shedding a certain load to prevent the power system from experiencing frequency instability. The final step is to monitor the system frequency again and check whether system frequency returns to an acceptable range.

When the power system operates in a steady state, the mechanical power is always equal to the electrical power required from the load side. According to [47], the Grid Code states that system frequency should be maintained at 50 Hz in the UK. Due to contingencies such as loss of generator and sudden load increase potentially happening in a system, the system's electrical frequency drops at a certain rate depending on the power difference between electrical power and mechanical power, and the system inertia constant [176].

Table 7.1: Maximum operating time of a steam turbine under abnormal frequency operation [177].

Frequency deviation from nominal value	Maximum operating time
±1%	Continuously
±2%	100 mins
±3%	10 mins
±4%	1 min
±5%	6 s
±6%	1 s

Table 7.1 depicts the maximum operating time of a steam turbine under an abnormal frequency condition captured from [177]. It can be concluded that the larger the frequency deviation occurring in a power system, the smaller maximum operating time a steam turbine is allowed to operate in the power system. An underfrequency condition existing for a long time can cause severe damage to the equipment installed in a power system. The underfrequency operation of power systems is unsustainable since it can adversely affect the performance and lifetime of generating units and lead to further generation deficits due to tripping of remaining generators caused by a lack of underfrequency protection. Therefore, protection schemes for the equipment is mandatory in power systems.

7.2.1. UFLS philosophy

The need to protect power system equipment from damage during underfrequency operation of a power system calls for countermeasures that can rectify system frequency back to the nominal value in the event of a frequency drop. Concern relates to retaining a balance between power generation and load before the decaying frequency impacts the performance of the power system equipment, especially generators and other plant auxiliaries. Shedding a suitable load under low frequency conditions is one corrective action that can arrest a drop in frequency, other than generation reserve and demand relief [178]. UFLS is a protective scheme that implements this corrective action to restore nominal system frequency and also one of the most representative and widely used SIPSs.

Automatic operation of UFLS is utilised to get rid of abnormal frequency conditions after being subjected to a generation deficit that can be caused by tripping of generators and major transmission lines. Load shedding operations are usually achieved across the entire system by installing underfrequency relays at major transmission and distribution substations so that loads can be automatically disconnected when needed by controlling the circuit breakers in the substations. The operation of UFLS has to be automatic since generation deficits or overloads are generally caused by unpredictable outages and disturbances. It is a simple method and directly solves the problem by mitigating the imbalance between power generation and load.

Underfrequency protection is also applied to generating units to prevent them from damage during underfrequency operations because of the lifetime issue associated with generating units. The interaction between UFLS and the underfrequency protection of generators can lead to potential cascading effects, with the tripping of generators due to underfrequency protection further increasing the generation deficit and leading to deteriorating frequency conditions. Excessive loss of capacity in generating units can also result in a system inertia reduction and the capability to provide reactive support that can cause further issues associated with voltage instability. Hence, it is critically important to appropriately coordinate the UFLS and underfrequency protection of generators. As discussed in [178], the frequency threshold of the underfrequency protection of generators should be lower than those

of UFLS, so that UFLS sheds the load before generators are disconnected after activation of the underfrequency protection. Or, there should be a suitable amount of additional load shedding assigned to compensate the loss of generation caused by underfrequency protection [178].

Many studies have to be carried out when designing UFLS to maintain the integrity of the power system by shedding a suitable load during abnormal frequency conditions without degrading the frequency and voltage stability of the system. In general, UFLS is used to shed the load in multiple steps to deal with the differently sized frequency events. As discussed above, to avoid potential interaction between UFLS and other underfrequency protection schemes, it is necessary to consider the abnormal frequency performance of generators, system inertia constant, generator capacity and also reactive power support capability. In this regard, the number of load shedding steps and the amount of load shed at each step will able to be determined. When designing the UFLS system, the maximum possible generation deficit is a critical parameter to set as the total amount of load shed in all steps. It is equally important to define an optimal load percentage for each step that could result in overshedding, and thus resulting in a potential overfrequency. On the other hand, if the load shed is less than required at each step, system frequency will continuously decrease. Consequently, the UFLS settings should be focused on the protected transmission/distribution devices in turn, with coordination among the protection schemes ensuring an effective approach.

7.2.2. UFLS methods

UFLS must be accomplished as fast as possible in the event of generation deficits to arrest system frequency decay by decreasing power load in the system. UFLS can be initiated manually by system operators through a supervisory control and data acquisition (SCADA) system, which is comparatively slow and may not be able to arrest the frequency decay within an acceptable time range. A faster UFLS approach is to implement automatic schemes by installing underfrequency relays at load connected substations to initiate load disconnection when measured the system frequency is below a predefined threshold, with all these steps accomplished automatically without human intervention. UFLS methods can also be categorised into local schemes where the load is monitored and shed at the same location, and wide-area schemes where the load is shed at multiple locations.

Monitoring or measuring the frequency is achieved by voltage transformers in cooperation with underfrequency relays. Voltage transformers are installed in substations to transform the high voltages to low voltage signals that fall within the acceptable input range of underfrequency relays. These transformed voltage signals are then transmitted to relays that are also installed in the same substation through leads. Upon the receipt of voltage signals, underfrequency relays measure the frequency of input voltages by different methods according to the type of relay used.

Manual UFLS: A load shedding command can be initiated by system operators manually if there is a firm need to disconnect an excessive load. Although it is not recommended to initiate manual UFLS because it is relatively slow, manual operation of load shedding and/or disconnection of tie lines to other utilities is actually permitted when the operation of all available automatic UFLS can not prevent the frequency from decaying and further unplanned load shedding is required. Manual operation of UFLS is generally considered as an emergency control action that can be accomplished in control centres by sending tripping signals via SCADA systems.
Automatic UFLS: Automatic operation of UFLS is a more common practice in modern power systems in which load shedding commands are automatically initiated according to predefined criteria and without human intervention. It can provide faster responses to underfrequency conditions because there is no complex planning and decision making processes involved in the automatic methods, and its performance is more reliable compared to that of manual methods since human error can be avoided in most cases during operation. Underfrequency relays, the central logic of UFLS, are usually installed in transmission and distribution substations for convenient access to monitoring and actuating devices. Substations can provide UFLS sites with monitoring devices, e.g. voltage transformers and easy access to circuit breakers that can be used to disconnect a line to shed a large amount of load at the transmission level or a feeder to shed a block of loads at the distribution level.

Local UFLS: In local UFLS schemes, monitoring of frequency and actuating of load shedding is accomplished at the same location, typically within a substation. Due to this proximity, there is no need for a long-distance communications system, which not only reduces the capital and subsequent maintenance costs of the additional equipment but also avoids a possible decrease in reliability. Local UFLS can be further classified

down to centralised architecture UFLS and distributed architecture UFLS. It should be noted that in both architectures, the main equipment is still located within a substation.

Centralised UFLS utilises only one underfrequency relay measuring frequency at a single location, typically a bus within a substation. With the aid of control logic, the centralised UFLS scheme still has access to all substation circuit breakers to disconnect feeders and/or lines for load shedding purposes. Hardwiring and short-distance digital communication between the central logic and circuit breaker control circuits enables the realisation of centralised UFLS. The simple architecture brings with it several advantages when compared to distributed architecture but it does also have some shortcomings. Capital and maintenance costs can be reduced due to reduced need for frequency measurement devices, i.e. each substation will only need one underfrequency relay. Single control logic that has full access to all feeders and lines facilitates prioritising all loads so that non-prioritised loads can be shed first followed by high priority loads, with load shedding schedule shifts easily achieved by modifying the control logic. The main disadvantage of centralised UFLS is that extensive coding is required in a substation with a large number of feeders and lines connected. Such large scale coding is expensive at the initial setup stage and complex, bringing difficulties when it comes to maintenance and trouble-shooting.

Distributed UFLS has become a more preferable option for load shedding design since the proliferation of numeric relays. The underfrequency function can be added into these multifunctional relays at no extra cost and UFLS can be integrated into existing feeder protection systems. In contrast to its centralised counterpart, distributed UFLS has multiple frequency monitoring devices within a substation rather than one, increasing reliability because failure of one frequency monitoring device will only affect a part of the UFLS scheme. In general, each feeder or line within the substation has its own monitoring and control logic that can initiate load shedding when required, controlling the disconnection of specific load circuits in a more precise way. However, the disadvantages of a distributed UFLS scheme arises from the number of underfrequency relays. Equipping each feeder/line with a relay means a large database noting the settings of all relays has to be maintained, and whenever there is a need to

change the load shedding schedule, the settings of all relays have to be modified, which is both time consuming and increases the possibility of errors.

Wide-area UFLS: In a wide-area UFLS scheme, monitoring and load shedding does not necessarily take place at the same location. Frequency monitoring is accomplished where frequency measuring is convenient, usually still in substations, but the load to be shed can be located remotely and the circuit breakers to be opened can be outside and far from the substation where monitoring occurs. This method can be implemented to achieve more intelligent load shedding manoeuvres where only a set of particularly selected set of load is to be connected to enhance the overall performance. For example, shedding a load that is nearer to the loss of generation location is preferable because it can avoid overloading some transmission lines and help maintain voltage stability by shedding reactive power demand locally, without leading to the need for long-distance reactive power transmission. Additionally, a wide-area approach can achieve more selective load shedding by only disconnecting a portion of users that are connected to substations via remote distribution transformers [169][29]. This can avoid tripping high-priority loads that can happen in local UFLS schemes when high-priority and low-priority loads are connected to substations through a common radial feeder [178].

Extra communication is needed to accomplish wide-area UFLS as opposed to local UFLS where hardwiring suffices. This can increase capital and the subsequent scheme implementation maintenance costs. The reliability of the communication channel and delay time due to information transmission has to be studied before implementing this type of scheme. Most existing UFLS schemes are based on local architecture that is simpler and more reliable, with years of experience evidencing itself. However, there is increasing research focused on the wide-area approach, with increasing implementation expected in the future.

7.2.3. UFLS operating principles

The operating principles of UFLS are relatively simple compared to other SIPS applications. UFLS disconnects a set of prearranged loads whenever the measured system frequency indicates an excessive load above that generated. Conventionally, system frequency is the only input in an UFLS scheme, with it dropping below a set of predefined thresholds implying the severity of the imbalance. An additional input,

RoCoF, has been used in UFLS schemes to improve performance. Hence, there are variations in UFLS schemes in terms of the protection elements used according to the different operating principles employed, e.g. a fixed frequency element, RoCoF element and fixed frequency supervised RoCoF element.

Fixed frequency: Conventional UFLS schemes only utilise underfrequency relays that operate whenever the measured frequency drops below predefined and fixed frequency thresholds. This type of UFLS scheme is relatively simple to implement and easy to coordinate with UFLS schemes applied in other parts of the system or other protection schemes based on frequency since it only considers the frequency measurement. The main disadvantage of this type of UFLS scheme is that it can be slow to respond to generation deficits because the system frequency has to already low enough before load shedding can be activated.

Load shedding is usually designed to be implemented in multiple steps with different frequency thresholds and time delays. It is a common practice that the setting of a UFLS scheme uses a trial and error approach in which settings are adjusted after each trial, according to the simulation results, until a suitable set of settings is obtained. Experience shows that setting a UFLS scheme in three to five steps is preferable because it is easier to coordinate and fewer load amounts need to be shed [179]. In common practice, the first step of UFLS sheds 10% of the total system load, with the remaining steps shedding arbitrarily determined loads as long as the total load shedding is nearly equal to the maximum possible generation deficit. It is not necessary to ensure that the UFLS steps restore the frequency back to the exact nominal frequency. The governor control in generators can enable the pick-up of the remaining generation deficit if the generators have sufficient pick-up capability. If this is not possible, bringing the frequency back to near nominal frequency by UFLS can still provide system operators with enough time to take other measures to recover frequency by shedding additional loads manually or activating generation reserves. However, it is not recommended to shed fewer loads than required to avoid potential damage to turbines if underfrequency conditions are sustained for too long [180].

It is also necessary to include safety margins and selectivity in the design of UFLS schemes like in other protection schemes. Time delay is implemented in each load shedding step to avoid unwanted load shedding due to frequency oscillations.

Frequency oscillations can cause temporary frequency to drop below a certain threshold. Unnecessary activation of the next step of load shedding will result in overshedding. A suitably set time delay can successfully prevent this from happening as the frequency will shortly recover and be above the threshold after the delay without shedding any load.

Rate of change of frequency: Since final system frequency after loss of generation is a combined result of the RoCoF due to power imbalance and the time after the initial event, it takes time before a UFLS scheme based on fixed frequency function can respond to the power imbalance. A more desirable way is to take RoCoF into consideration when UFLS is applied because it is a direct indicator of power imbalance and can reduce service interruption time by activating shedding commands right after the initial event.

According to the swing equation, RoCoF is proportional to the power imbalance and inversely proportional to the system inertia constant. The amount of generation deficit after the loss of generation event can easily be estimated by measuring the RoCoF, with appropriate load shedding steps initiated to arrest the dropping frequency. Such a load shedding function requires an additional input, which is the system inertia constant. The additional information can be transmitted to the relay but it is not fixed and changes its value after system separation. If the system separation pattern is not known to system operators, i.e., an unintentional system separation happens, an accurate estimation of the system inertia constant is not possible and the UFLS scheme based on the RoCoF function will not work properly. Another disadvantage of using the RoCoF element relates to the oscillatory nature of frequency and also the RoCoF. While oscillatory frequency does not adversely affect fixed frequency elements when the pickup delay function is utilised, RoCoF elements are very sensitive to the oscillations of the RoCoF. It is therefore preferable to place the relay next to the centre of inertia where minimum RoCoF oscillation is observed. However, his is not always possible because the location of the centre of inertia changes case by case. Hence, it is quite difficult to obtain an accurate RoCoF measurement.

A more secure way is to use the average RoCoF, which is the average rate of change during a period of time, rather than using the instantaneous RoCoF. It is calculated by monitoring the frequency change over a predefined time window and dividing it by

the length of the time window. It can serve as a frequency trend indicator but is slightly slower than the instantaneous RoCoF element.

Modern digital relays are capable of incorporating all these elements for implementation to meet different criteria. The relay can be switched to using a fixed frequency supervised RoCoF element for faster response, or from using average RoCoF to using the fixed frequency element if the delay introduced by the estimation window does not meet stability requirements [181].

7.2.4. UFLS design – Systematic approach for setting UFLS relays

A UFLS scheme can be optimally designed according to the systematic approach described in [180]. The swing equation shown in Equation (2.1), derived from the equation of motion of a rotating machine (and shown below), can precisely describe the relationships between electrical and mechanical power, and their implications on the frequency operation of power systems.

The frequency threshold of the first step is set at the minimum acceptable frequency, which is regulated in grid code and varies from country to country. If the system inertia time constant and the contingency size are known, the average RoCoF immediately after loss of generation can be determined using:

$$Excess\ load\ \ factor\ L = \frac{L_{\max} - G_{re}}{G_{re}} \tag{7.1}$$

$$Average\ RoCoF_i = \frac{PF \times L}{H} \times \frac{th_i - f_{i-1}}{1 - \left(\frac{th_i}{f_{i-1}}\right)^2} \tag{7.2}$$

where $L_{\max}$ is the maximum possible generation loss in the system and G_{re} is the remaining generation available in the system. th_i and f_i are the ith frequency threshold and the frequency at which the ith stage is accomplished, respectively. The time that frequency takes to reach the first threshold can be calculated. It should be noted that load shedding does not happen at exactly the moment when the frequency threshold is met. Time delay due to the pick-up function in the relay and operation of circuit breakers should be considered. To provide a logical safety margin, this delay can be considered between 15 to 20 cycles [180]. The load will be shed after this time delay

elapses. If frequency continues to drop, further load shedding steps will be required. The threshold of the next step should be set 0.1 Hz lower to allow an appropriate safety margin between steps.

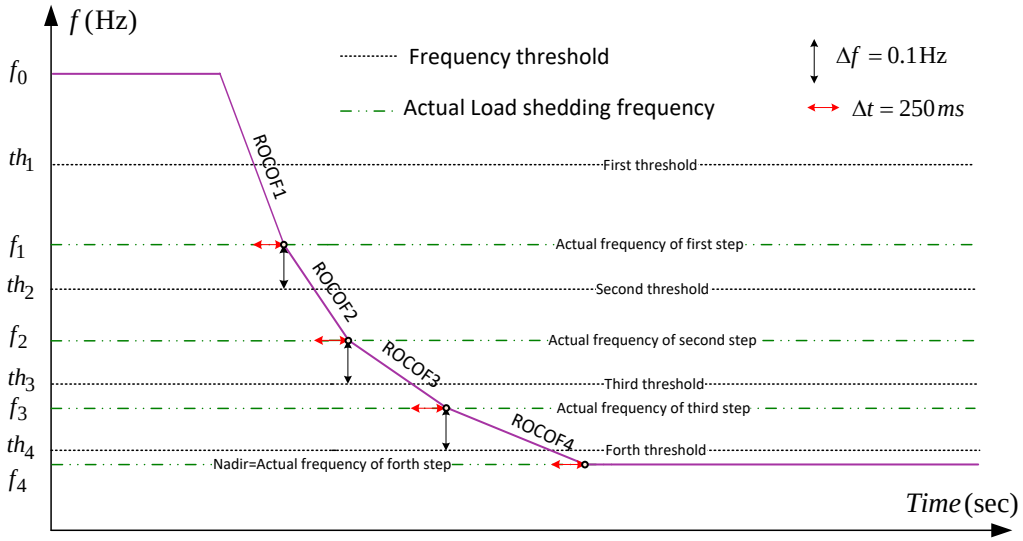

Fig. 7.4: Systematic approach for setting UFLS relays [180].

Fig. 7.4 shows the systematic approach for setting UFLS relays. Load shedding is designed to be carried out in four stages. As stated, th_i is the threshold at which the i th load shedding step is triggered to be carried out. Besides, f_i is the minimum frequency at which that the load shedding step will be accomplished considering a maximum time delay of Δt. And next threshold is obtained considering this point and a frequency safety margin of Δf. In other words,

$$th_{i+1} = f_i + \Delta f \tag{7.3}$$

This procedure is continued until all frequency thresholds are obtained.

It is noted that the frequency dependency of the load and the contribution of generators in frequency support is totally neglected. This is why after implementation of the last step, the frequency becomes constant since generation and consumption reach a new equilibrium state after a suitable load is shed. It follows that the frequency trajectory drawn here is a pessimistic one and its minimum value (nadir) is not reached in practice. For generating units not to trip due to low system frequency, a certain margin

(around 0.5 Hz) should be considered below so-calculated nadir. This allows them to continue operating without tripping, thereby not aggravating the situation.

7.3. Two-area test system

The test system used in the simulations is modified from Kundur's two-area system already used in this study and presented in Fig. 5.1. The generators and loads in the original test system have been adapted to facilitate the study of the impacts of UFLS on system frequency response in the event of the loss of generation. As seen in Fig. 5.1, PE sources are connected to the original two-area system equably, which means the PE penetration level is equal to the actual PE penetration at each generator substation. Under this condition, the PE-interfaced generator and the corresponding output are systematically loaded in the modified two-area system using DPL codes.

7.3.1. UFLS configuration

To monitor the performance of the SIPS under different PE penetration levels, the SIPS relays are set at 0%, 25%, 50% and 70% PE levels, respectively. Thus, the system responses under different actual PE penetration levels can be summarised and concluded.

In order to simulate loss of generation events with different contingency sizes, the synchronous generator at each generator bus is split into two generators, with one representing the tripped generation capacity and the other representing the remaining generation capacity. The size of the contingency can be set by changing the active power despatch of the two generators, given that the sum of the two generators' active power remains constant. In each simulation case with a different contingency size, the rated power of both the tripped and remaining generators has to be adjusted accordingly to ensure that each generator contributes a predetermined amount of inertia to the overall system inertia.

To enable load shedding with multiple steps, each load in the original system is split into several independent loads, with each one representing a feeder or a line outlet in a physical transmission or distribution substation. The active and reactive power of each load can be adjusted as long as the sum of the active and reactive power of all loads does not change the power flow of the system. This technique is used to adjust the load amount to be shed in each step. It is noted that the LSA shown in the Table

7.2 is two multiplies 81.25MW. This is because the test system has two load buses, bus 7 and bus 9, to assure that the load is shed uniformly in the system, with the total load shedding amount required at each UFLS step halved and shed at bus 7 and bus 9 respectively and simultaneously. In [177], the time delay for triggering the UFLS is discussed, with it generally being obtained from 15 to 20 cycles of power system frequency. The time and frequency margins Δt and Δf are considered to be 250 ms and 0.1 Hz, respectively. The load shedding starts directly after the time delay. If the frequency continuously decreases after the first load shedding step, then the second load shedding stage has to be activated with a 0.1 Hz lower frequency threshold than the frequency threshold set at the first step. For the two-area modified test system, the load shedding procedure is divided into four steps to carry out. Fig. 7.2 shows the UFLS settings under different PPEs.

Table 7.2: UFLS settings under different presumed PE penetration levels.

Step	Load shedding amount (MW)	PPEs		
		0%	25%	50%
		Frequency thresholds (Hz)		
1	2×81.25	49.5	49.5	49.5
2	2×81.25	49.1	48.9	48.8
3	2×81.25	48.8	48.6	48.3
4	2×81.25	48.6	48.3	47.9

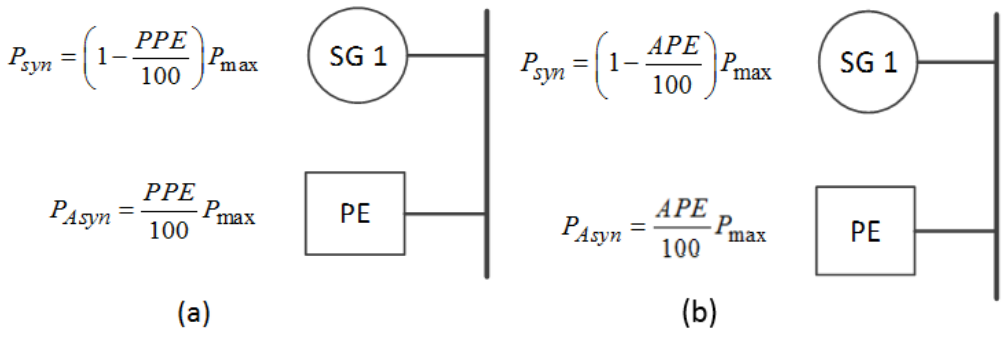

Fig. 7.5: PPE and APE are configured in the test system.

Due to the intermittency of RESs, the corresponding electrical power will not be constantly available due to some factors beyond direct control. This means that for a known installed capacity of PE-interfaced sources, the actual PE penetration level (APE) will be continually changing on a daily/hourly basis. Therefore, taking one fixed level of PE penetration as the base for designing a SIPS will not necessarily yield

the most acceptable performance in the respective power system. The presumed PE penetration level (PPE) for which SIPS relays are configured is referred in the following sections. Fig. 7.5 shows how PPE and APE are configured in DIgSILENT PowerFactory.

In order to investigate the impacts of PE penetration on the performance of the existing UFLS scheme, the two-area test system is modified to include PE-based generators. As shown in the single line diagram of the generating plant, three PE-based generators representing the HVDC link, DFIG and fully rated converter wind turbine are connected to the generating plant bus respectively, via a transformer. The purpose of introducing three types of PE-based generators is to investigate if the type of PE penetration source affects the UFLS performance differently. The HVDC link is modelled as a static generator, injecting a fixed amount of active power. The DFIG is modelled as a converter interfaced generation. The fully rated converter wind turbine is also modelled as a static generator. Control models based on IEC Standard 61400-27-1 are applied to both the DFIG and fully rated converter wind turbine. Each wind turbine has a fixed active power output. Detailed models of both wind turbines are not required in this study as the penetration level of the PE based generator is controlled by adjusting the number of parallel generators. It should be noted that the number of parallel transformers should also be changed accordingly to provide sufficient grid connection capability. The activation status of PE-based generators and the output of these generators are controlled automatically by a DPL code according to the given PE penetration level.

7.3.2. Frequency responses with various PE penetration levels

The simulation scenario set in this section is based on a fact that the nature of RESs is intermittent, meaning that generation deficits/surpluses can always occur in the power supply process. In other words, the PPE levels implemented in the simulation may not equal the APE levels. To study the impacts of the various PPEs and APEs on the modified system, sixteen simulation cases were conducted. The simulation cases are undertaken using four PE penetration levels of 0%, 25%, 50% and 70%. The renewable energy resources connected to the generating bus require the active output to be changed according to the APE levels.

Table 7.3: COI RoCoF following the various disturbance sizes.

Disturbance size (MW)	RoCoF (Hz/s)
162	-0.10
325	-0.28
488	-0.49
650	-0.73

Table 7.3 tabulates the rate of change of frequency change following the various disturbance sizes. The COI RoCoF is obtained by taking the frequency difference changing in a 0.1 second time window and dividing it by 0.1. It can be concluded that RoCoF increases as the disturbance size increases.

Table 7.4: The amount of load shedding following various PPE and APE levels.

PPE (%)	0			25			50		
APE (%)	0	25	50	0	25	50	0	25	50
Disturbance size (MW)	Total load shedding amount (MW)								
162	0	0	0	0	0	0	0	0	0
325	0	162	162	0	162	162	0	162	162
488	162	162	325	162	162	325	162	162	325
650	325	325	650	162	325	650	325	325	650

In Table 7.4, the simulation results cover the UFLS under various PPE levels and APE levels, with the only exception being when the APE level equals 70%, the reason for which will be discussed in the rest of this section. The table shows that the total load shedding amount increases when the disturbance size increases. Also, the PPE level for which the relay has been configured does impact on the total load shedding amount because the Δt and Δf are large and de-emphasise the presence of the inertia constant time with respect to the formula utilised when configuring relay settings.

Table 7.5: Final frequency following various PPE and APE levels.

PPEs (%)	0			25			50		
APEs (%)	0	25	50	0	25	50	0	25	50
Disturbance size (MW)	Final frequency (Hz)								
162	49.66	49.75	49.78	49.88	49.84	49.77	49.88	49.84	49.77
325	49.50	49.70	49.58	49.75	49.78	49.66	49.75	49.78	49.66
488	49.66	49.65	49.50	49.70	49.58	49.50	49.70	49.58	49.50
650	49.88	49.84	49.77	49.53	49.50	49.66	49.53	49.50	49.65

Table 7.5 shows the final COI frequency after being subjected to various disturbance sizes. The conclusion is that system frequency returns to the acceptable range above 49.5 Hz in all simulation cases.

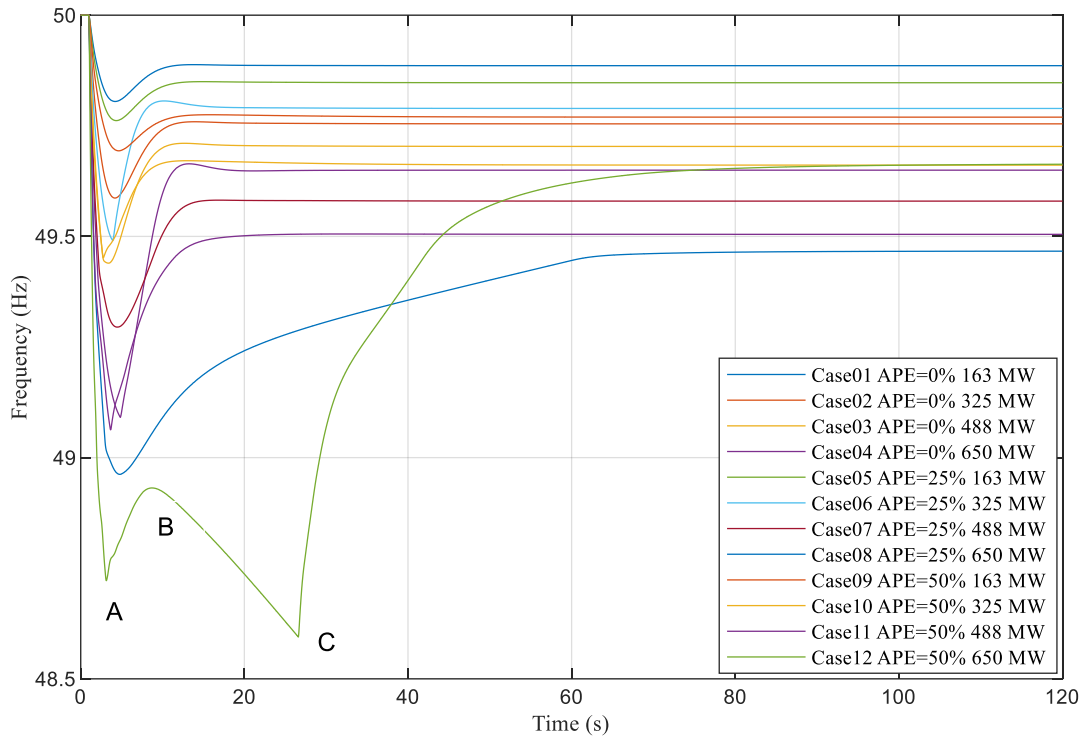

Fig. 7.6: f_{COI} for disturbance sizes under various APE levels.

As shown in Fig. 7.6, the f_{COI} for disturbance sizes under various APE levels is obtained and drawn using MATLAB. The simulation time is set to 120 seconds to guarantee that the f_{COI} for each case reaches the stable state. For all the simulations, only the f_{COI} for Case08 does not to return to minimum frequency margin of 49.5 Hz.

As Fig. 7.6 shows, the f_{COI} for all simulation cases performs in a similar trend, except for Case12. The third UFLS stage is enabled at point A in Fig. 7.6. Meanwhile, 487.5 MW of load is shed due to the large generation lost in the system. Then, the system frequency starts to increase as the imbalance between generation and load decreases. However, the increase in load offsets the frequency support provided by the governors. Thanks to the voltage dependent load, the active power of the load increases as the load voltage gains. When the f_{COI} reaches point C, the fourth UFLS stage triggers; at this time, 162.5 MW of excess load needs to be shed to prevent the system from experiencing frequency instability. After point C, the f_{COI} starts to recover again as balance between the generations and demands occurs.

Table 7.6: The load shedding amount following a 70% APE level and various PPEs.

PPEs (%)	0	25	50
APEs (%)	70		
Disturbance sizes (MW)	Total load shedding amount (MW)		
162	0	0	0
325	325	325	325
488	650	650	650
650	650	650	650

As shown in Table 7.6, the total load shedding amount highlighted in yellow indicates that the total load shedding amount is larger than the disturbance sizes in all the cases because the load is a voltage dependent load and no frequency support is provided by the generators. In the two-area test system, when the generation contributed by synchronous generation is less than 10%, synchronous generation cannot provide support to the excess load because of the increased load.

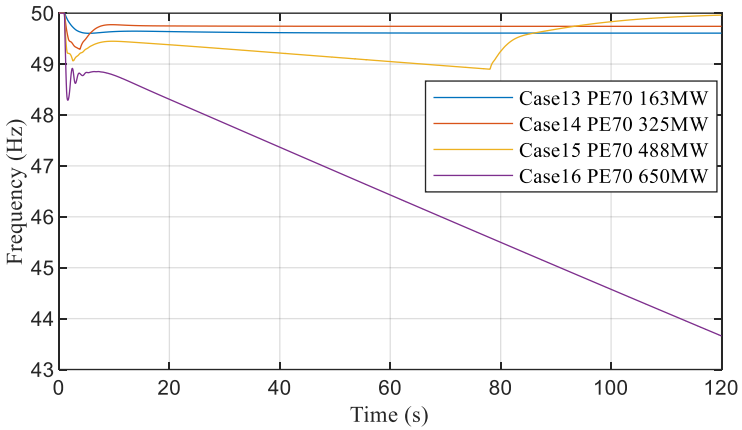

Fig. 7.7: f_{COI} following disturbance sizes when the APE is 70%.

Fig. 7.7 shows the f_{COI} responses following various disturbance sizes when the APE is set to 70%. It is noted that the f_{COI} for Case16 decreases dramatically after the 650 MW generation is tripped in the system. This is due to the impact of the governor of the generation on the frequency support being insignificant. In addition, the active power transferred between the generation and load decreases substantially in the tie-lines, meaning that the voltage increases where the load blocks are connected. Since the load utilised in the system is a voltage dependent load, accordingly, the voltage increase in the system causes the frequency instability to occur in this case.

7.3.3. Frequency responses with different types of wind turbines

Table 7.7: The FN of various of wind turbines.

APE (%)	PPE (%)	0		25		50	
	Wind turbine type	DFIG	Type 4	DFIG	Type 4	DFIG	Type 4
	Disturbance size (MW)	FN (Hz)					
0	163	49.45	49.80	49.80	49.80	49.80	49.80
	325	49.06	49.58	49.58	49.58	49.58	49.58
	488	48.59	49.44	49.44	49.44	49.44	49.44
	650	49.80	49.09	49.07	49.07	49.07	49.07
25	163	49.58	49.76	49.76	49.76	49.76	49.76
	325	49.44	49.48	49.49	49.48	49.49	49.48
	488	49.09	49.26	49.29	49.26	49.29	49.26
	650	49.76	48.91	48.92	48.87	48.76	48.75
50	163	49.49	49.69	49.69	49.69	49.69	49.69
	325	49.29	49.43	49.45	49.43	49.45	49.43
	488	48.96	49.03	48.97	48.95	48.79	48.78
	650	49.69	48.59	48.29	48.29	47.89	47.89

Table 7.7 shows the FN for a DFIG and Type 4 wind turbine. It can be seen from the table that the lower FN that the system frequency is able to reach, the higher the PE penetration the renewable sources are able to supply in the power system. This is due to system inertia decreasing as the PE penetration of the PE-interfaced source increases. In addition, the frequency margin between the UFLS operation and underfrequency protection of generation narrows as the PE penetration increases.

7.3.4. Discussion

As shown in the simulation results, the performance of the designed UFLS changes as the PE penetration level increases. Two points can be summarised from the results:

a) A decrease in FN

As the PE penetration level increases, the FN decreases after being subjected to a frequency event because the total system inertia constant decreases accordingly. In this regard, the frequency is prone to drop. As shown in the results, when the APE and PPE are 50% and disturbance size is 650 MW, the FN is 47.89 Hz, which is quite close to the frequency of protection of generators at 47.5 Hz.

b) A potential increase in LSA

The results also show that the frequency is recovered within the acceptable range by applying UFLS until the PE penetration level reaches 70%. When UFLS is set with enough space between multiple frequency thresholds, it is important to determine a suitable frequency margin in the scheme. However, when the PE penetration level is 70%, the LSA is larger than the disturbance size in the case of a 488 MW generation deficit, resulting in unnecessary load shedding.

7.4. GB 29-zone system

To evaluate the SIPS performance in a more realistic system, a number of dynamic models in DIgSILENT PowerFactory are utilised and that represent the Great Britain (GB) system at present and in future horizon years. These models are respectively called base-case and transition scenarios. The transition scenarios are a set of models that consider the expected installed capacity of conventional synchronous generators and renewable generators, load changes and potential grid reinforcements in years 2020 and 2025.

As the 29-zone system suggests explicitly, each transition model consists of 29 zones, which are connected by a total number of 99 transmission lines. These transmission lines represent existing power flow routes throughout the GB transmission system. The nominal voltage of the transmission lines in the southern part is mostly 400kV, whereas the lines in the northern part operate at a nominal voltage of 275 kV.

The buses installed in the synchronous generator model are set as PV buses, while the rest of the buses without generators are configured as PQ buses. Various RESs are connected to the station through the compatible transformers, as shown in Fig. 7.8. These sources in all the models are considered to be wind turbine and wind park models. The system load is modelled directly at the high voltage nodes as constant impedance static loads. In order to investigate the SIPS performance, load is represented by the dynamic model to better feature actual load characteristics (mainly a combination of constant impedance and constant power loads). The typical structure of a zone interconnected in the 29-zone model is shown in Fig. 7.8.

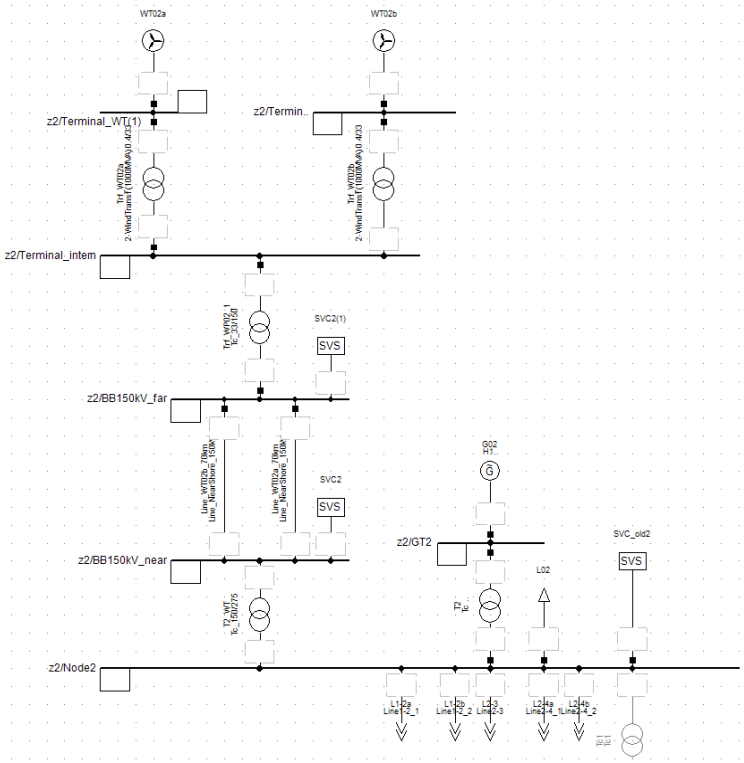

Fig. 7.8: Typical topology of a zone in the DIgSILENT 29-zone model.

According to the files provided by the National Grid, the “No Progression Scenario” represents future systems in which only new capacities that are presently under construction or already well-planned will be in service. It is a particularly rare scenario compared to the “Gone Green Scenario”. The “Gone Green Scenario” is a more realistic scenario that assumes all RES targets and environmental considerations will have been achieved until respective years. The PE penetration level in any of the “No Progression Scenario” models is as large as its counterpart in the “Gone Green Scenario”. For this reason, the SIPS performance will need to be investigated on systems with higher degrees of PE, which are the “Gone Green Scenario” models.

The GB transmission network is divided into 5 regions (see Fig. 7.9):

1. Scotland
2. North England
3. West England (Wales and the Midlands)
4. East England
5. South England

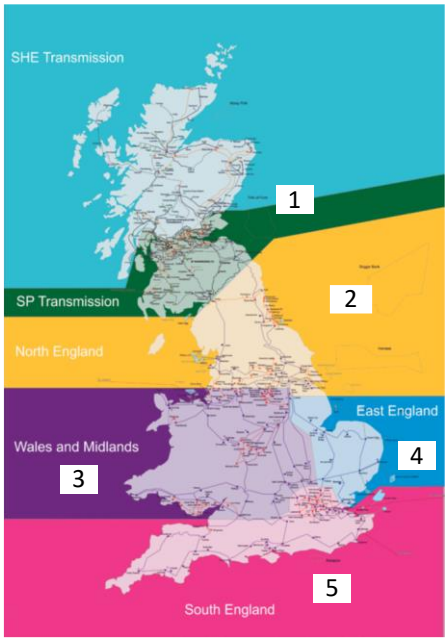

Fig. 7.9: Five regions in GB's system.

Zones inside each of the five regions in the GB system are tabulated in Table 7.8.

Table 7.8: GB's system network.

GB 29-zone model mapping	Related zones in the 29-zone system
Scotland	1, 2, 3, 4, 5, 6, 7, 8
North England	9, 10, 11, 16
West England	12, 13, 14, 15, 17, 18
East England	19, 20
South England	21, 22, 25, 23, 24, 28, 26, 27, 29

The generation and load data are first predicted for the above five regions in GB's system. Then, the regional values are divided by the number of zones in each region to provide values for each node of the 29-zone model. Table 7.8 shows how the 29 zones are mapped into 5 regions. After obtaining all the generation and load data, they are reflected in the relevant horizon models in DIgSILENT PowerFactory.

The total generation capacity (by identifying synchronous and PE penetration levels) for the base-case and "Gone Green Transition Scenarios" for different horizon years in DIgSILENT PowerFactory models are presented in Table 7.9.

Table 7.9: Generation and load characteristics of GB's system.

Model		Total load (MW)	Synchronous generation (MW)	PE penetration level (%)	PE generation (MW)	
					Type 3 WT	Type 4 WT
Base-case		52450	43650	17	3789	5781
Transition scenarios	2020	48750	32363	34	4624	12951
	2025	49350	18100	63	7077	26584

Table 7.10 shows the inertia constants in the GB 29-zone system for different horizon years, under their original APE levels and half of them.

Table 7.10: Inertia constants for the GB 29-zone system in different years under various APE levels.

Model	Base-case		2020		2025	
APE (%)	8	17	17	34	32	63
H (s)	9.5	7.6	8.0	6.7	6.7	4.8

7.4.1. Results for the GB 29-zone system

Simulation results obtained from the 29-zone system are shown in the following section. Various simulations were conducted on this system when equipped with the UFLS scheme designed according to the systematic approach. The simulation results for the system were then analysed accordingly.

7.4.2. Description of the UFLS settings and contingencies

The modified 29-zone GB system is utilised to evaluate the performance of UFLS on system frequency response after being subjected to a loss generation event. To simulate such events with different disturbance sizes, the entire GB system is split into five regions. The disturbance size is achieved by altering the number of generators tripped in each region from one to as many as the number of generators connected in that region. These contingencies are large and change the system structure. These changes will impact on the system dynamic characteristics and result in highlighting the deficiencies in the original PSSs when dealing with new inter-area oscillations.

This is why for some of the disturbances it takes time for arising oscillations to be completely damped out.

As shown in the previous section discussing the systematic approach, the settings for the UFLS relays in the GB test system in different horizon years are predetermined. The Δt and Δf used are 250 ms and 0.1 Hz, respectively. Table 7.11 The load shedding amount (LSA) and frequency threshold of the UFLS relays at each step are presented in Table 7.11. The UFLS relays are installed at the load buses in regions 1, 2, 9, 11, 12, 13, 19, 20, 27 and 29. In each of these regions, the load blocks are divided into five sub-blocks, four of which are used to apply the four load shedding steps shown in Table 7.11. Moreover, the LSA of each step will be calculated as the ratio between the maximum disturbance size divided by the number of steps.

Table 7.11: Settings of the UFLS relays on GB's test system for different years.

Model	Base-case			2020			2025		
PPE (%)	8	17	LSA (MW)	17	34	LSA (MW)	32	63	LSA (MW)
Step No	FT (Hz)	FT (Hz)		FT (Hz)	FT (Hz)		FT (Hz)	FT (Hz)	
1	49.5	49.5	2225	49.5	49.5	2620	49.5	49.5	2000
2	49.2	49.2	2225	49.1	49.0	2620	49.1	49.0	2000
3	49.0	48.9	2225	48.8	48.6	2620	48.8	48.6	2000
4	48.8	48.7	2225	48.5	48.3	2620	48.6	48.3	2000

7.4.3. UFLS performance under various PE penetration levels

In this section, a large number of cases are simulated on the GB 29-zone system for different years. Various cases are analysed to tabulate their various PE penetration levels. Four indices, namely FN, final frequency, RoCoF and LSA, are tabulated to evaluate the performance of the UFLS.

i). Base-case model

The generation and load characteristics of the base-case GB test system are summarised and tabulated in Table 7.9. The PE penetration level of this system is calculated to be 17%. In total, 38 simulation cases are able to be defined using the procedure explained in the previous section. The predetermined contingencies are simulated under APEs of 17% and 8%.

a) UFLS performance under different APEs with relays set for a PPE of 17%

Fig. 7.10 shows f_{COI} for the system when the UFLS scheme is implemented in the system. To this end, 19 cases are simulated in this system with both the APE and PPE set at 17%.

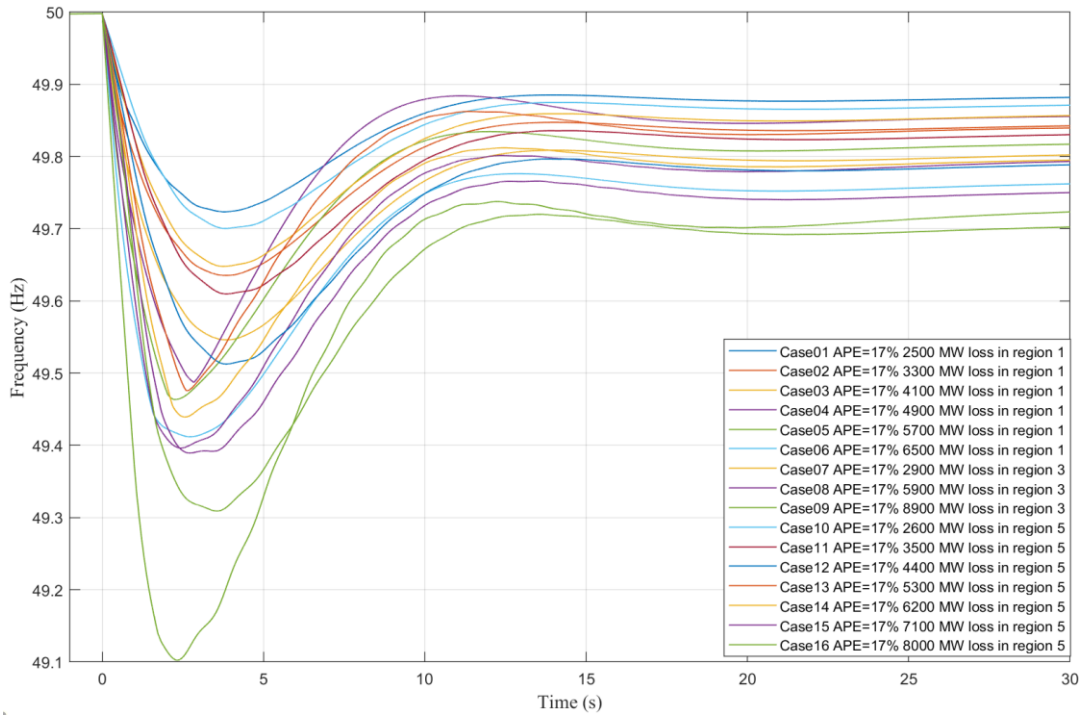

Fig. 7.10: f_{COI} for the base-case system with an APE of 17% and a PPE of 17%.

The frequency responses for the GB test system are similar with and without UFLS. However, the lowest FN among all cases, which is Case 09, improved from 48.69 Hz to 49.1 Hz. This proves the effectiveness of UFLS in improving the frequency response of the system. Moreover, the f_{COI} in all cases returned to the permissible range after implementing UFLS.

Now, the frequency response is investigated for a system with an APE of 8%, when the relays are set with a PPE of 17%. By using more of the available capacity contributed by synchronous generators, less capacity in those generators is available to support the frequency during a contingency event. This is the situation when the inertia constant of the system remains the same since no additional generators are committed and the whole load in the system is the same as before. It can be seen in Fig. 7.11 that the FN of the worst case is 49.05 Hz. When the APE drops to 8%,

synchronous generators contribute less in active power injection after the contingency compared to a case in which the APE is 17%.

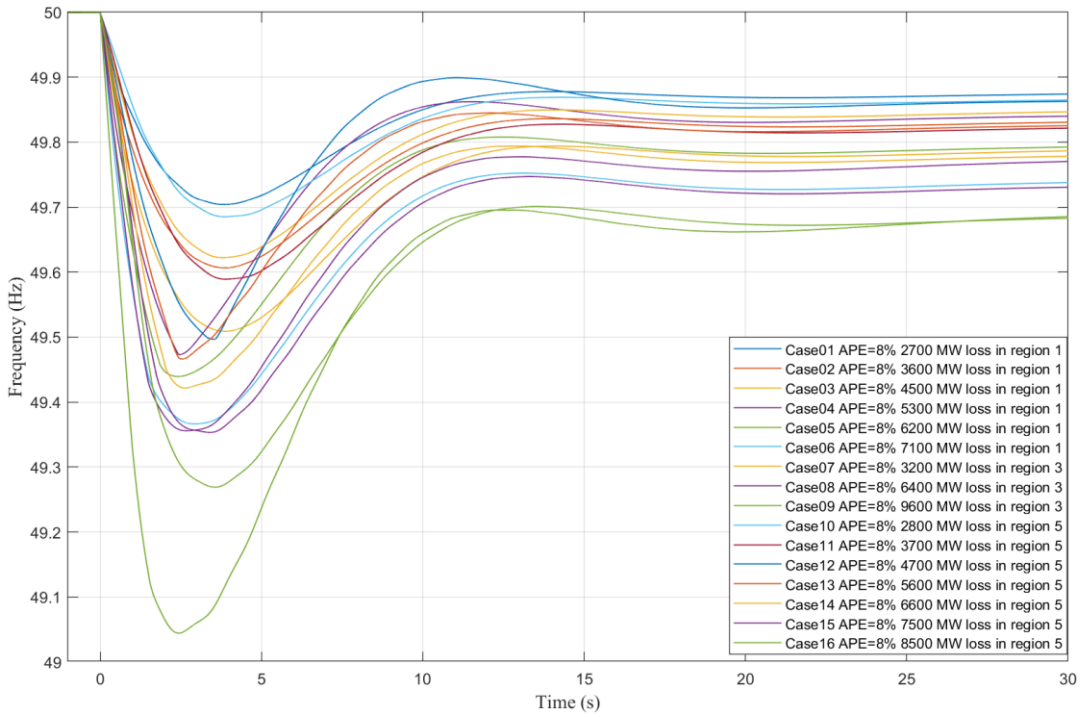

Fig. 7.11: f_{COI} for the base-case system with an APE of 8% and a PPE of 17%.

Table 7.12 and Table 7.13 show the results on the base-case GB test system. The system frequency returns to the permissible range as shown in Table 7.12 and Table 7.13 when just one step of the UFLS is triggered. In only two simulation cases out of all cases did the system require two UFLS steps because the contingency size was large enough in the other cases.

Table 7.12: UFLS performance in the base-case system with an APE of 17% and relays set for a PPE of 17%.

Region	Contingency size (MW)	FN (Hz)	Final frequency (Hz)	RoCoF (Hz/s)	LSA (MW)
1	2500	49.72	49.88	-0.18	0
1	3300	49.64	49.84	-0.18	0
1	4100	49.55	49.80	-0.28	0
1	4900	49.49	49.86	-0.35	1890
1	5700	49.46	49.82	-0.41	2000

1	6500	49.41	49.76	-0.46	2000
3	2900	49.65	49.86	-0.18	0
3	5900	49.40	49.79	-0.42	2000
3	8900	49.10	49.72	-0.64	4000
5	2600	49.70	49.87	-0.14	0
5	3500	49.61	49.83	-0.16	0
5	4400	49.51	49.79	-0.19	0
5	5300	49.48	49.84	-0.20	2000
5	6200	49.44	49.80	-0.23	2000
5	7100	49.39	49.75	-0.24	2000
5	8000	49.31	49.70	-0.28	2000

Table 7.13: UFLS performance in the base-case system with an APE of 8% and relays set for a PPE of 17%.

Region	Contingency size (MW)	FN (Hz)	Final frequency (Hz)	RoCoF (Hz/s)	LSA (MW)
1	2700	49.70	49.87	-0.18	0
1	3600	49.61	49.83	-0.24	0
1	4500	49.51	49.79	-0.31	0
1	5300	49.47	49.84	-0.36	2000
1	6200	49.44	49.79	-0.43	2000
1	7100	49.37	49.74	-0.48	2000
3	3200	49.62	49.85	-0.19	0
3	6400	49.36	49.77	-0.45	2000
3	9600	49.04	49.69	-0.68	4000
5	2800	49.69	49.86	-0.14	0
5	3700	49.59	49.82	-0.16	0
5	4700	49.50	49.86	-0.20	1800
5	5600	49.47	49.83	-0.21	2000
5	6600	49.42	49.78	-0.23	2000
5	7500	49.35	49.73	-0.25	2000
5	8500	49.27	49.68	-0.28	2000

According to the UFLS scheme's setting, a 2225 MW load is required to be shed at each step. The frequency can be recovered in near all cases when one UFLS step is triggered. When the contingency size is large enough to trip a second UFLS stage, the

LSA increases to 4000 MW to restore the frequency. In the system with an APE of 8%, on average, the ratio between the LSA and disturbance size is 33%, while it is 30% in system with an APE of 17%, which is due to the synchronous generators having more capacity to contribute to active power injection in the latter case.

b) UFLS performance under different APEs with relays set for a PPE of 8%

The system frequencies under different APEs set for PPEs of 17% and 8% are similar. Table 7.14 and Table 7.15 provide the frequency response when relays are set for a PPE of 8%. Overall, the frequency response is quite acceptable. By comparing the results of Table 7.12 to Table 7.15, one pattern can be identified. The FN increases as the relays are set for a smaller PPE. In addition, in systems with a larger inertia constant, the RoCoF decreases, resulting in a higher nadir.

Table 7.14: UFLS performance in the base-case system with an APE of 17% and relays set for a PPE of 8%.

Region	Contingency size (MW)	FN (Hz)	Final frequency (Hz)	RoCoF (Hz/s)	LSA (MW)
1	2500	49.74	49.88	-0.14	0
1	3300	49.65	49.84	-0.14	0
1	4100	49.57	49.80	-0.23	0
1	4900	49.49	49.86	-0.28	1890
1	5700	49.47	49.82	-0.34	2000
1	6500	49.43	49.76	-0.38	2000
3	2900	49.67	49.86	-0.14	0
3	5900	49.42	49.79	-0.33	2000
3	8900	49.13	49.72	-0.52	4000
5	2600	49.72	49.87	-0.11	0
5	3500	49.63	49.83	-0.13	0
5	4400	49.54	49.78	-0.15	0
5	5300	49.49	49.84	-0.16	2000
5	6200	49.46	49.79	-0.18	2000
5	7100	49.41	49.75	-0.20	2000
5	8000	49.34	49.70	-0.23	2000

Table 7.15: UFLS performance in the base-case system with an APE of 8% and relays set for a PPE of 8%.

Region	Contingency size (MW)	FN (Hz)	Final frequency (Hz)	RoCoF (Hz/s)	LSA (MW)
1	2700	49.71	49.87	-0.16	0
1	3600	49.62	49.83	-0.21	0
1	4500	49.52	49.79	-0.27	0
1	5300	49.48	49.84	-0.31	2000
1	6200	49.45	49.79	-0.38	2000
1	7100	49.38	49.74	-0.43	2000
3	3200	49.64	49.85	-0.17	0
3	6400	49.38	49.77	-0.38	2000
3	9600	49.07	49.68	-0.60	4000
5	2800	49.70	49.86	-0.12	0
5	3700	49.60	49.82	-0.14	0
5	4700	49.51	49.78	-0.17	111
5	5600	49.47	49.83	-0.18	2000
5	6600	49.41	49.78	-1.20	2000
5	7500	49.37	49.73	-0.22	2000
5	8500	49.29	49.68	-0.25	2000

ii). The 2020 model

In this part, the UFLS performance in the GB 2020 test system is evaluated. The original APE in the system is 34%. To explore the frequency response of the system, relays are set for two PPEs of 17% and 34%. In total, there are 29 simulation cases where the potential disturbance sizes are large enough to decrease the frequency below 49.5 Hz, which is able to trigger at least one of the designed UFLS steps.

a) UFLS performance under different APEs with relays set for a PPE of 34%

In this part, UFLS performance is studied in the GB 2020 test system with relays set for a PPE of 34%. Table 7.16 and Table 7.17 present the results obtained under two APEs of 17% and 34%, respectively. Fig. 7.12 and Fig. 7.13 show the frequency responses under different APE levels.

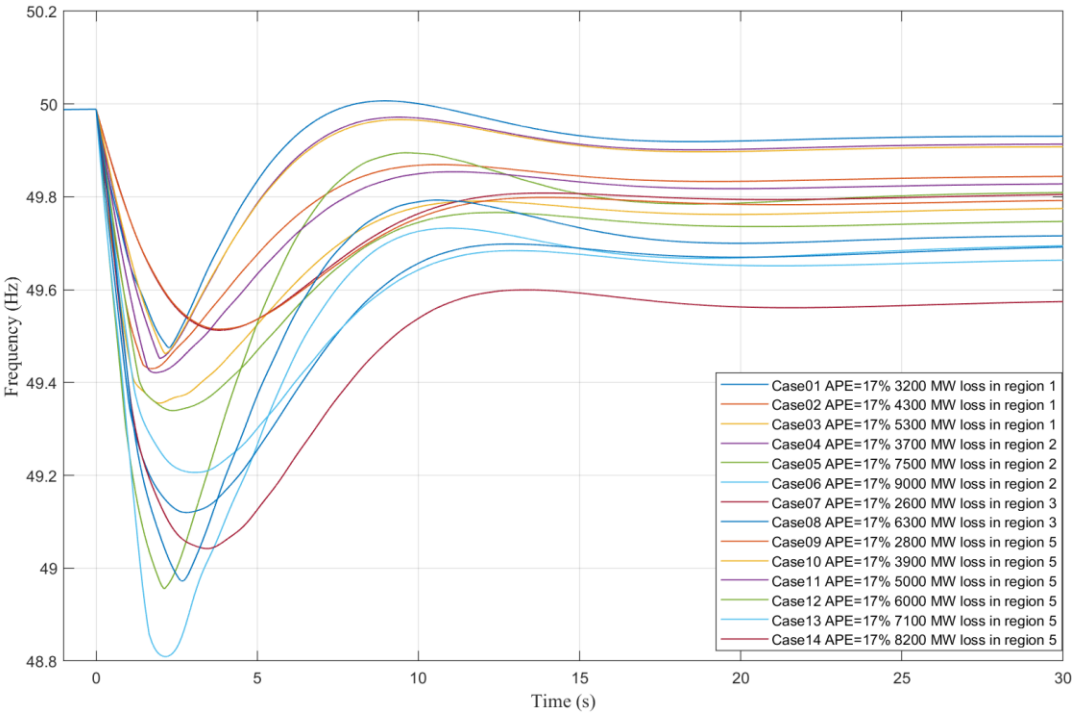

Fig. 7.12: f_{COI} for the 2020 model with an APE of 17% and a PPE of 34%.

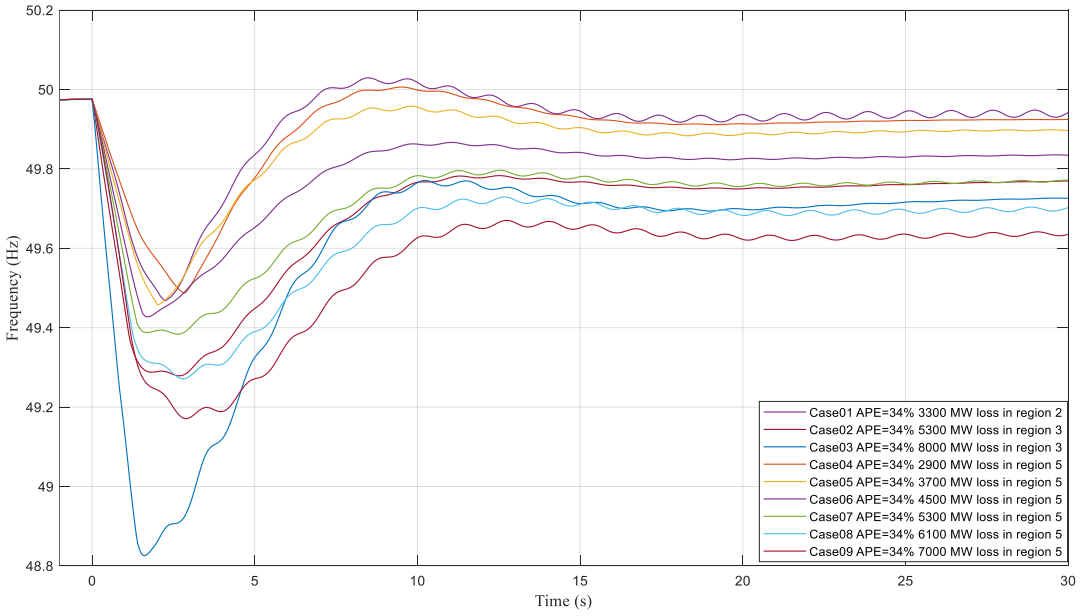

Fig. 7.13: f_{COI} for the 2020 model with an APE of 34% and a PPE of 34%.

Table 7.16: UFLS performance in the 2020 model with an APE of 17% and relays set for a PPE of 34%.

Region	Contingency size (MW)	FN (Hz)	Final Frequency (Hz)	RoCoF (Hz/s)	LSA (MW)
1	3200	49.48	49.93	-0.41	2618
1	4300	49.43	49.84	-0.57	2618
1	5300	49.36	49.77	-0.69	2618
2	3700	49.45	49.91	-0.35	2618
2	7500	48.96	49.81	-0.80	5236
2	9000	48.81	49.69	-0.85	5236
3	2600	49.51	49.81	-0.24	0
3	6300	49.12	49.69	-0.64	2618
5	2800	49.51	49.79	-0.24	0
5	3900	49.46	49.91	-0.30	2618
5	5000	49.42	49.83	-0.37	2618
5	6000	49.34	49.75	-0.42	2618
5	7100	49.21	49.66	-0.45	2618
5	8200	49.04	49.57	-0.50	2618

Table 7.17: UFLS performance in the 2020 model with an APE of 34% and relays set for a PPE of 34%.

Region	Contingency size (MW)	FN (Hz)	Final Frequency (Hz)	RoCoF (Hz/s)	LSA (MW)
2	3300	49.47	49.94	-0.30	2618
3	5300	49.28	49.77	-0.53	2618
3	8000	48.83	49.73	-0.83	5235
5	2900	49.49	49.92	-0.83	2120
5	3700	49.46	49.90	-0.30	2618
5	4500	49.43	49.83	-0.32	2618
5	5300	49.38	49.77	-0.32	2618
5	6100	49.27	49.70	-0.40	2618
5	7000	49.17	49.64	-0.36	2618

To show how effectively the UFLS scheme activates, the f_{COI} for the GB 2020 test system with an APE of 17% is shown in Fig. 7.12. As this figure and Table 7.16 show, the frequency response can be brought to an acceptable range activating UFLS.

b) UFLS performance under different APEs with relays set for a PPE of 17%

Table 7.18 and Table 7.19 show the frequency responses obtained with relays set for a PPE of 17%, when the APE is 34% and 17%, respectively. It is noted that the LSA increases as the PE penetration level rises. For example, when there is a 3300 MW generation loss in region 2 and a 2900 MW loss in region 5, the LSA increases 16% and 43% respectively as the APE changes from 17% to 34%. However, an exception occurs when 8000 MW generation loss occurs in region 3. In this case, the LSA decreases 72 MW as the PE penetration level increases, with this small difference due to the relay installed at the local substation only monitoring the local load bus frequency. In this regard, the f_{COI} will be slightly different in various cases.

Table 7.18: UFLS performance in the 2020 model with an APE of 34% and relays set for a PPE of 17%.

Region	Contingency size (MW)	FN (Hz)	Final Frequency (Hz)	RoCoF (Hz/s)	LSA (MW)
2	3300	49.48	50.13	-0.20	2194
3	5300	49.35	50.03	-0.35	2618
3	8000	48.99	50.09	-0.55	5307
5	2900	49.52	50.08	-0.17	1205
5	3700	49.48	50.07	-0.21	2618
5	4500	49.46	50.05	-0.23	2618
5	5300	49.43	49.98	-0.24	2618
5	6100	49.33	49.90	-0.26	2618
5	7000	49.24	49.85	-0.25	2618

Table 7.19: UFLS performance in the 2020 model with an APE of 17% and relays set for a PPE of 17%.

Region	Contingency size (MW)	FN (Hz)	Final Frequency (Hz)	RoCoF (Hz/s)	LSA (MW)
1	3200	49.49	49.93	-0.28	2618
1	4300	49.46	49.84	-0.39	2618
1	5300	49.41	49.77	-0.48	2618
2	3700	49.47	49.91	-0.24	2618
2	7500	49.07	49.81	-0.53	5236
2	9000	48.98	49.69	-0.56	5236

3	2600	49.56	49.80	-0.16	0
3	6300	49.22	49.69	-0.42	2618
5	2800	49.56	49.79	-0.17	0
5	3900	49.48	49.91	-0.20	2618
5	5000	49.45	49.83	-0.26	2618
5	6000	49.39	49.74	-0.29	2618
5	7100	49.28	49.66	-0.31	2618
5	8200	49.13	49.57	-0.34	2618

iii). The 2025 model

In this part, the performance of the UFLS scheme is evaluated in the GB 2025 test system. The total load in this system is 49350 MW, of which the synchronous generation is 18100 MW. PE generators contribute 33661 MW in total, with the type 3 wind turbine and type 4 wind turbine sharing 21% and 79%, respectively. Accordingly, the relays will be set for a PPE of 63% and 32%. In the 2025 test system, 14 simulations for each relay were conducted with APEs of 63% and 32%. Table 7.20 and Table 7.21 summarise the simulation results when the relay was set for a 63% PPE level. As can be seen, the frequency in all cases can be recovered to the permissible range with the triggering of one or two UFLS steps.

a) UFLS performance under different APEs with relays set for a PPE of 63%

Table 7.20 and Table 7.21 present the UFLS performance in the GB 2025 test system under APEs of 63% and 32%, respectively. The UFLS relays are set for a PPE of 63%.

Table 7.20: UFLS performance in the 2025 model with an APE of 63% and relays set for a PPE of 63%.

Region	Contingency size (MW)	FN (Hz)	Final Frequency (Hz)	RoCoF (Hz/s)	LSA (MW)
2	5300	49.13	49.34	-0.53	2000
3	3600	49.41	49.86	-0.35	2000
3	6600	48.89	49.76	-0.66	4000
5	2600	49.52	49.80	-0.16	0
5	3400	49.47	49.89	-0.18	2000
5	4200	49.43	49.83	-0.20	2000

5	5000	49.37	49.77	-0.23	2000
5	5900	49.25	49.68	-0.29	2000

Table 7.21: UFLS performance in the 2025 model with an APE of 32% and relays set for a PPE of 63%.

Region	Contingency size (MW)	FN (Hz)	Final Frequency (Hz)	RoCoF (Hz/s)	LSA (MW)
1	3300	49.40	49.86	-0.57	2000
1	4200	49.28	49.75	-0.70	2000
2	3400	49.46	49.89	-0.38	2000
3	5600	49.12	49.71	-0.57	2000
5	2500	49.54	49.81	-0.20	0
5	3500	49.48	49.89	-0.23	2000

Fig. 7.14 present the f_{COI} for the 2025 model with an APE of 63%. It can be observed that the lowest FN among all the simulation cases is 48.86 Hz. In this system, the frequency threshold of the third UFLS step is 48.6 Hz. Accordingly, to conclude, only two UFLS steps were enough to maintain the system frequency within a permissible frequency range under possible generation deficits. It is also clear that the FN decreases with an increase in contingency size.

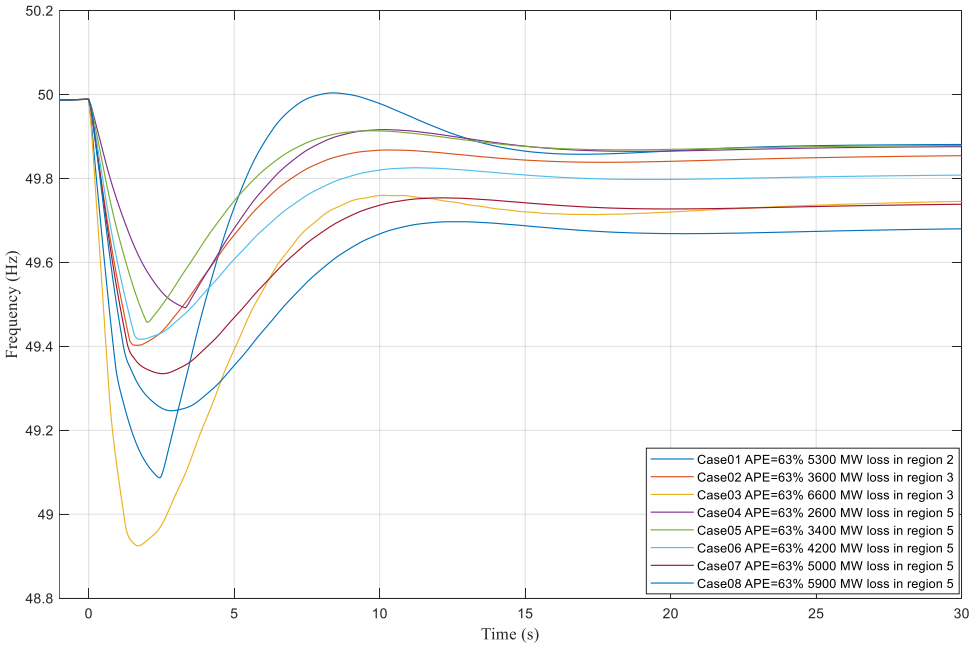

Fig. 7.14: f_{COI} for the 2025 model with an APE of 63% and relays set for a PPE of 63%.

Fig. 7.15 shows the f_{COI} for the 2025 model with an APE of 32%. When the APE is dropped to 32%, the frequency response becomes more oscillatory due to a change in load flow dispatch and the dynamic characteristics of the system. When the contingency size is 9200 MW, the FN drops below 48.6 Hz. On its way down, the frequency reaches the third frequency threshold of the UFLS scheme. As a result, a 6000 MW load is shed in total to ensure system stability.

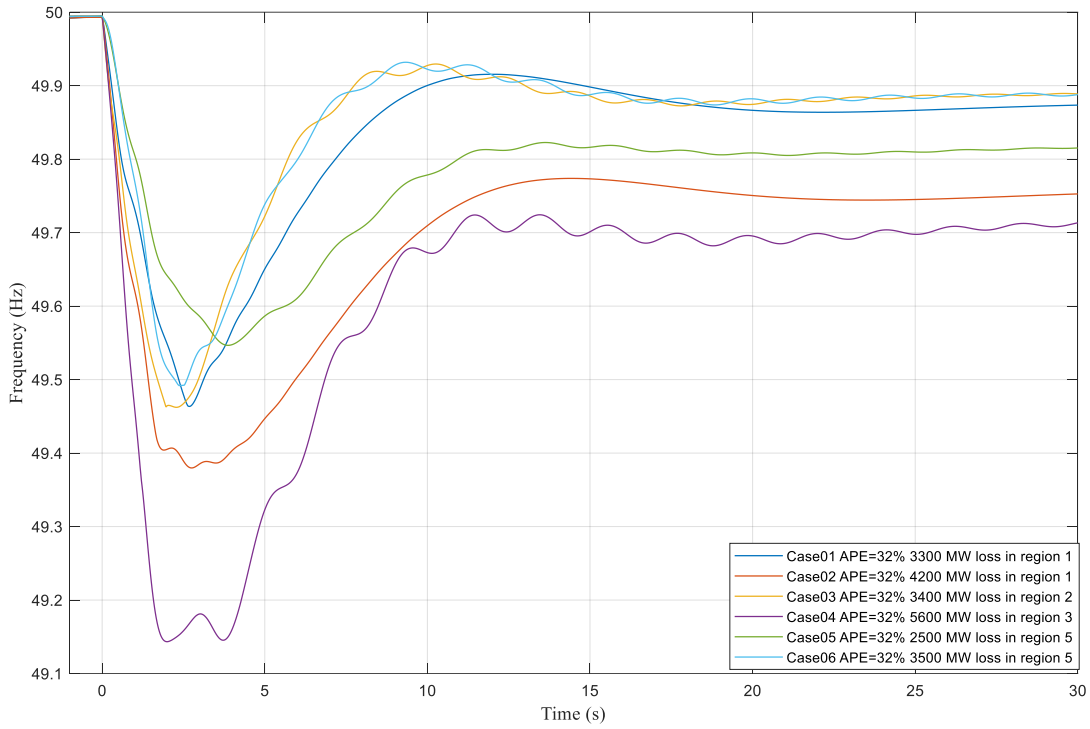

Fig. 7.15: f_{COI} for the 2025 model with an APE of 32% and relays set for a PPE of 63%.

b) UFLS performance under different APEs with relays set for a PPE of 32%

Table 7.22 and Table 7.23 present the frequency response of the GB 2025 test system under APEs of 63% and 32%, respectively. In this respect, the UFLS relays are set for a PPE of 32%. The general pattern on the FN and RoCoF follows that of the other horizon years.

Table 7.22: UFLS performance in the 2025 model with an APE of 63% and relays set for a PPE of 32%.

Region	Contingency size (MW)	FN (Hz)	Final Frequency (Hz)	RoCoF (Hz/s)	LSA (MW)
2	5300	49.17	49.88	-0.45	2000
3	3600	49.44	49.85	-0.28	2000
3	6600	49.00	49.74	-0.55	4000
5	2600	49.53	49.88	-0.14	0
5	3400	49.47	49.87	-0.16	2000
5	4200	49.45	49.81	-0.20	2000
5	5000	49.38	49.74	-0.23	2000
5	5900	49.30	49.68	-0.21	2000

Table 7.23: UFLS performance in the 2025 model with an APE of 32% and relays set for a PPE of 32%.

Region	Contingency size (MW)	FN (Hz)	Final Frequency (Hz)	RoCoF (Hz/s)	LSA (MW)
1	3300	49.47	49.87	-0.36	2000
1	4200	49.38	49.75	-0.46	2000
2	3400	49.46	49.83	-0.28	2000
3	5600	49.16	49.52	-0.46	2000
5	2500	49.55	49.64	-0.17	366
5	3500	49.47	49.69	-0.20	2000

7.4.4. Discussion

This section discusses the impact of various parameters on the performance of UFLS under different PE generator levels. From Fig. 7.16 to Fig. 7.18, the frequency responses are shown with respect to H_{APE} , H_{PPE} and Δt . Also, the frequency response shows the worst scenarios in which the speed-governor is not included in the synchronous generators.

i). Impacts of time margin Δt on frequency threshold settings

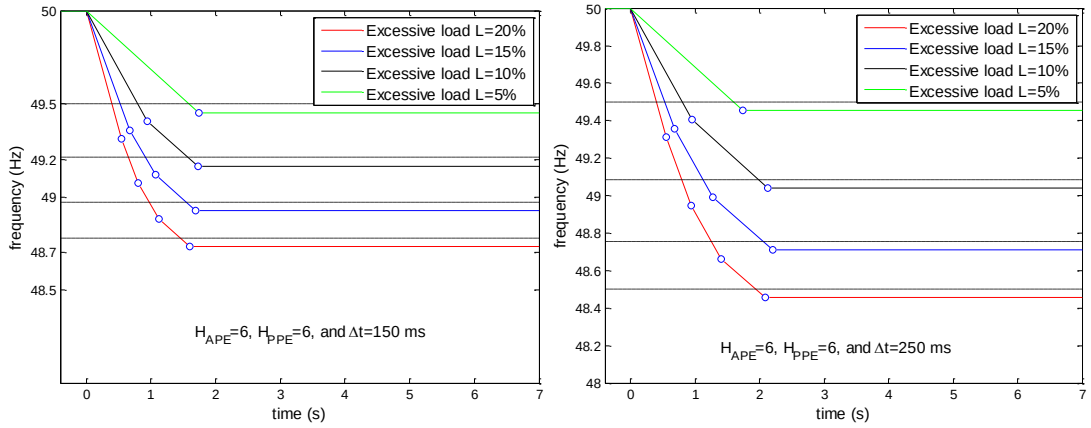

Fig. 7.16: Impact of Δt on the frequency response to UFLS relay settings [182].

Fig. 7.16 shows the impacts of Δt on the frequency response after configuring the UFLS relays. The Δt used in the left figure is 150 ms, while for the right one it is 250 ms. As can be seen clearly, the UFLS with a larger Δt will stop the frequency decline later than that with a smaller Δt. This indicates that the system frequency is prone to fall into the impermeable frequency range specified by National Grid Electricity Transmission plc [183]. For the given example shown in Fig. 7.16, the larger Δt is still preferred because there is still enough room between 48.5 Hz and 47.5 Hz to activate the last UFLS step. In addition, a late circuit breaker operation can be achieved which less chance of overshedding occurring.

ii). Impacts of the inertia constant for which the relays are configured.

As shown in Fig. 7.17, if H_{PPE} is used to configure the UFLS frequency thresholds is larger than H_{APE}, the frequency thresholds will be more compressed. Therefore, the frequency can be prevented from substantial decline. Nonetheless, such a predetermined H_{PPE} will cause problems when H_{APE} is small. For example, the blue line and red line represent a H_{APE} of 3 s and 1.5 s, respectively, due to there not being enough time for UFLS to be triggered at each step.

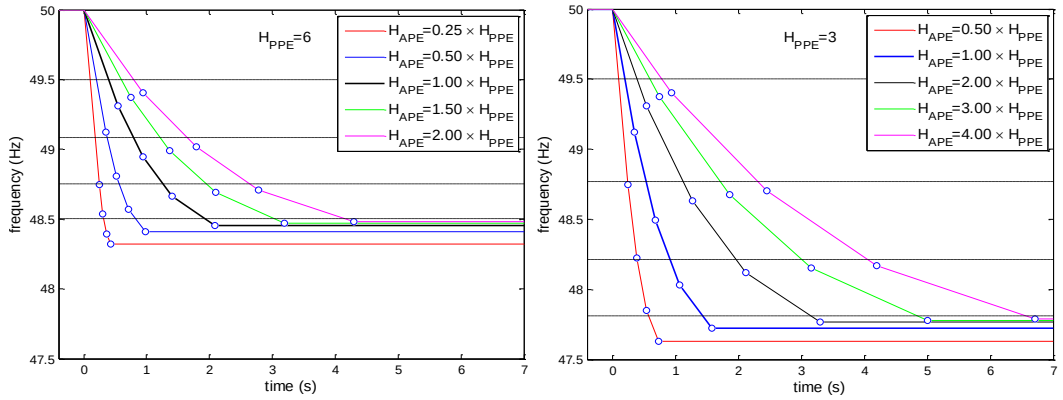

Fig. 7.17: Impacts on the inertia constant for which the relays are configured [182].

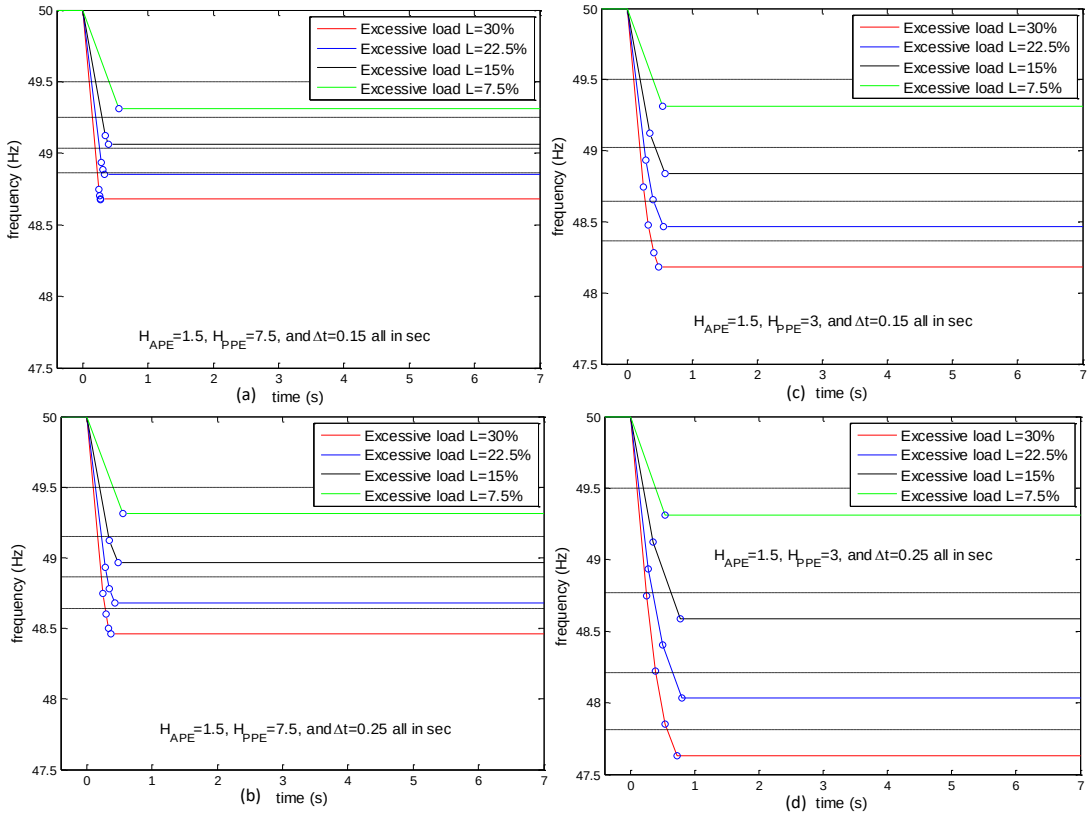

Fig. 7.18: Potential overshedding in contingencies whose sizes are smaller than the biggest one that the UFLS relays are set for [182].

In more detail, the frequency thresholds where the UFLS is too closed for each step, which is shown in Fig. 7.18 (a) and (b). A problem may occur if the contingency the size is smaller than the biggest possible generation deficit, whose excessive load is less than 30%. For example, the UFLS is triggered later than it is supposed to where the frequency threshold is predefined. Even the frequency already reaches the next frequency threshold or below, which causes the overshedding. However, when H_{APE}

is close to H_{PPE}, overshedding is less likely to happen due to the enough space existing between neighbouring UFLS frequency thresholds.

To conclude the UFLS design, if a large Δt is adopted, the FN is lower and prone to be closer to the impermissible range. However, if a small Δt is used, the late operation of the circuit breaker may cause overshedding. In this regard, the trade-off between overshedding and the FN should be investigated. On the other hand, the potential overshedding occurs when the H_{APE} is far smaller than H_{PPE} because the frequency thresholds will compress together.

7.5. Chapter summary

In this chapter, SIPS was initially discussed from classification, architecture and input perspectives. An UFLS scheme designed according to the systematic approach was then introduced. Simulation tests were conducted on both the modified two-area system and the GB 29-zone system, evaluating the performance of applying UFLS. However, the intermittency of RESs have significant impacts on load sharing in power systems. The simulations also presented that H_{APE}, H_{PPE} and Δt have various effects on the frequency response, with each of these parameters discussed with respect to the UFLS trigger time and FN. In the process of designing the UFLS scheme, the presumed penetration level needs to be carefully determined in order to deal with the trade-off between the FN and overshedding. Therefore, unnecessary overloading or interferences among various protection schemes can be mitigated and the frequency stability of power systems maintained.

Chapter 8 Conclusions

This chapter summarises the intent of the research presented in this thesis (see Section 8.1). It then presents conclusions regarding the success of the research in relation to its original goals (see Section 8.2). The contributions made by this research are discussed in Section 8.3, before some recommendations for further research are presented in Section 8.4.

8.1. Introduction

The research presented in this thesis mainly focused on the creation of novel frequency controls that ensure frequency stability in a power system with a high penetration level of RESs. Conventional DFIG-based RES are unable to provide frequency support as they are decoupled from the system frequency. As the penetration level of the RESs increase, the total system inertia constant drops, making system frequency much more prone to drop. The traditional frequency controls used to support the frequency mimic the behaviours of a speed-governor in a synchronous generator. However, DFIGs work within the MPPT curve in general, providing a limited amount of active power to support the system frequency. Additionally, the kinetic energy required for recovering the rotor speed of DFIGs is potentially larger than the contingency size, leading to SFD events. On the other hand, UFLS, as the last measure to maintain frequency stability within the entire power system, was introduced, and based on the systematic approach. Applying UFLS can effectively retain the impacts on the system operation and economic performance without disconnecting unwanted loads, and by proxy disturbing demand side users.

The background of this research can be defined as the continuing increase of the fossil energy deficiency and the improvement of the human-living environment, with RESs so called converter interfaced generation having become the mainstream in power

systems. In addition, wind power accounts for the highest proportion among all types of RESs in distribution systems [184]. Moreover, the conventional operation, control and protection paradigms employed for the secure operation of a power system are becoming increasingly inappropriate due to the different dynamic characteristics introduced by RESs, such as wind turbines [8]. This is adversely impacting the performance of approaches traditionally used for the design, operation and control of energy production, transmission and distribution. The novel frequency control of DFIGs was chosen as a strong candidate to fill the gap in existing research. They are well established in power systems and have become a critical tool for improving frequency stability. Unlike conventional frequency controls that only target the FN, the reasons responsible for a SFD are often neglected. For example, with only temporary energy contributed by wind turbines, SFDs occur after the minimum rotor speed is reached, thereby terminating frequency support. In this regard, the requirements placed on frequency control need extending.

The motivation of this research was to make the most use of the available energy of integrated wind turbines by adopting low-cost, reliable manners in the wind turbines. Temporary energy support and persistent energy support have their advantages and disadvantages, which provides the opportunity to create more intelligent controls to support the frequency. Without detailed models, any frequency control scheme based on generic assumptions is unable to perform accurately. The dynamic characteristics of different forms of response provided by wind turbines have been investigated and demonstrated, with one of the key aspects of the work being to test and understand the capabilities of different frequency controls. In addition, UFLS, as a wide-area protection scheme, can prevent an entire power system from frequency instability if wind turbines are incapable of supporting the frequency in extreme circumstances. All the dynamic models and controllers were built and applied in a simulation of the GB 29-zone test system. The simulation tests were conducted using DIgSILENT PowerFactory.

8.2. Thesis conclusions

Fast frequency response is considered like any form of active power injection or load reduction within half a second after being subjected to a disturbance, targeted at providing frequency support for the increased requirements as a primary frequency

response in a low inertia system. In this sense, most literature focuses on the capability of RESs for frequency control. Since wind power accounts for a large percentage of the generation among all RESs, implementing frequency control in wind turbines is one area important to investigate.

Accordingly, Chapter 2 mainly reviewed power system stability in conventional systems and the systems integrating RESs. The definition and classification were firstly presented, as were the corresponding time scales for various other stabilities. As the integration of RESs in power systems, resonance and converter-driven stability are brought into researchers' vision. More importantly, the frequency stability emphasised at the end of Chapter 2 by analysing the swing equation, RoCoF, droop characteristics. Also, the impact of the integration of a WECS on the frequency stability was discussed from system inertia and active power reserve perspectives. Consequently, one of the main research areas of this research was to understand the potential treats brought by the integration of RESs and develop fast, reliable and accurate methodologies that can contribute to the frequency response.

Chapter 3 introduced the modelling and control of a DFIG-based variable speed wind turbine. Section 3.1 briefly introduced the configuration of a DFIG. The reason why a wind turbine is termed as being 'doubly fed' was also discussed, presenting that the voltage on the stator is supplied from the grid, whereas the voltage on the rotor is induced by the VSC. The purpose of a VSC is to compensate for the difference between mechanical and electrical frequency by injecting rotor current at a variable frequency. As discussed in the previous chapter, a DFIG can be divided into two systems, mechanical system and electrical system. A mechanical system consists of an aerodynamic system, drive train system and pitch system, whereas an electrical system includes a generator, converter, transformer and crowbar protection. Section 3.4 and 3.5 presented a steady state model and dynamic modelling of DFIGs, respectively. Finally, Section 3.6 demonstrated the DFIG modelling adopted in DIgSILENT PowerFactory, which was built for the simulations presented in the following chapters. These models and controls were generically built according to the literature review to develop a standard real-time test system.

Chapter 4 elaborated on the existing smart frequency control schemes in the literature. In a bulk power system with a high integration of WECS, they are required to

participate in the primary frequency response following a frequency excursion. An appropriate and well-designed model is important to ensure power system security. A classification of these schemes is provided by considering the energy types and monitored input signals. The active power of a variable speed wind turbine usually follows the MPPT curve, which was introduced in Section 4.1. Considering the simulation was conducted based on the curve, a precisely defined MPPT curve was critically important for the reliability of the results. Then, the energy used for frequency support was divided into two types: temporary energy and persistent energy. The temporary energy support was applied to the wind turbines operating the MPPT curve, with the wind turbines controlled to behave like conventional synchronous generators by adding supplementary control loops and releasing the temporary energy during frequency excursions. On the other hand, persistent energy support was adopted by the wind turbines by deloading the active power of the wind turbines. This was achieved using either speed or pitch angle control. Compared to the speed control, pitch angle control usually takes longer and the constant operation of pitch angle changes, resulting in a mechanical loss of the wind turbines. Additionally, the occurrence of a secondary frequency dip was also explored in Section 4.4.

Chapter 5 introduced a synthetic inertia control design for a WECS to take part in frequency control by making them temporary release the kinetic energy to emulate the inertial response of synchronous generators. In the supplemented inertial emulator, the monitored input signals were frequency deviation and RoCoF changes. The active power of wind turbines was raised to the maximum generated power by decreasing the rotor speed. The frequency support was terminated if the rotor speed protection was triggered when the minimum rotor speed was reached. Although synthetic inertia control provides frequency support at the beginning of a contingency, the active power deficits caused by the termination of frequency support as the need for rotor speed recovery, causing a SFD. Consequently, a dynamic droop-based control was introduced. The simulation results proved that the implementation of dynamic droop gain can effectively reduce the SFD since the active power was changed with RoCoF. Thereby the proposed control not only arrested the frequency drop but also mitigated the amplitude of the SFD.

Chapter 6 proposed a consecutive power dispatch in wind farms to mitigate SFDs. The simulation results, based on temporary energy support, were analysed in Chapter 5 . In addition, a deloading control was deployed in wind turbines. The deloading control of wind turbines degrades their active power output, which is achieved by the overspeeding control. However, the main disadvantage of the deloading control is that the annual revenue is largely impacted if the deloading control is activated in a wind farm. In this regard, this study firstly explored consecutive dispatch schemes. We divided all the wind turbines in a wind farm into two groups, making two groups of wind turbines to be triggered in two steps to support the frequency as the core idea. As such, the wind turbines operating at suboptimal level would release the persistent energy after which the termination of wind turbines using inertia emulator to support the frequency. The active power deficits caused by the termination could be compensated by the persistent energy, therefore mitigating the magnitude of SFDs. The performance of the proposed schemes was evaluated using various wind speeds, contingency sizes, penetration levels and deloading levels. To end this, the amount of frequency response ancillary services required from RESs can be enhanced. This would permit the UK's national grid to integrate a larger amount of RESs and reduce the need for frequency support from synchronous generators.

Chapter 7 introduced a UFLS design based on the systematic approach. In the previous chapters, frequency control was discussed from the generation side, whereas the attention focused on the load side in this chapter. SIPS have become progressively prevalent in recent years and UFLS is the last countermeasure to prevent the entire system from frequency excursions. This UFLS scheme used the presumed inertia constant and largest possible loss in the system as inputs. The simulation was conducted on a two-area test system and GB's 29-zone transmission system. In this regard, the impacts of presumed system inertia, frequency thresholds and communication delay on the UFLS performance were revealed.

8.3. Specific thesis contributions

The main contributions of the research presented in this thesis are the following:

1) Developed a DFIG model in DIgSILENT PowerFactory and investigated its dynamic performance in a built system with a high penetration of DFIGs. The entire research required a detailed understanding of DFIG operating conditions

and confidence in high-fidelity DFIG models, both during steady state and transient conditions.

2) Quantified MPPT curve for WECS, to determine the operating point of DFIG in terms of its aerodynamic control using modified power coefficient representations. It is essential to build an aerodynamic system of DFIGs which specifically presents the relationship between different parameters and the DIFG operations modes.
3) Built and evaluated an appropriate WECS with well-designed synthetic inertia control for large scale power systems with a high penetration of RESs, which verified the presumed results. And this accurate WECS model is prepared to be connected to where needed for further simulations.
4) Developed a novel dynamic droop based control for DFIGs to mitigate SFDs following the termination of synthetic inertia control. In most of previous research, researchers only considered the first frequency dip due to the generation deficit. However, the SFD caused by termination of synthetic inertia control of DFIGs is usually out of the researchers' view. Implementing dynamic droop based control can consider the frequency changes in the two mentioned situations.
5) Built a deloading control based on WECS, allowing DFIGs to provide persistent energy support during frequency events, which utilises different approaches to analyse the frequency support issues.
6) Proposed a consecutive power dispatch in wind farms to quickly and reliably mitigate SFDs in a large scale wind farm. This consecutive power dispatch is developed to provide a more complete process of frequency support.
7) The sensitivity analyses carried out for the consecutive power dispatch demonstrate the impacts of various combination of G1 and G2 wind turbines as well as the communication delay on the system frequency response, which contributes the evaluation of proposed scheme and raises the further research direction. The research direction consists of more accurate optimization of grouping, impacts of wake effect on the grouping, annual profits of wind farms, etc.

8) Presented a GB 29-zone transmission system based on National Grid data and modelling developed to support research into future power systems. All the data are accurately set for the following horizon years.
9) Designed a practical UFLS scheme based on a systematic approach using presumed system inertia and the largest possible active power deficits.

8.4. Future work

The research presented in this thesis has successfully delivered on most of its objectives and succeeded in making several valuable contributions. Moreover, a number of possible areas for the future development of this research are presented in this section.

- For wind farm modelling:
  In this thesis, all the simulation results were conducted under the assumption that wind turbines experience the same wind speed across the entire wind farm. However, the overall contribution of kinetic energy would be of major difference for individual wind turbine. Each wind turbine operates under a varied operational state and delivers different kinetic energy. Therefore, a more realistic wind farm model is worthy of further exploration by considering the wake effect and wind turbine deployment.
- For transmission line modelling:
  HVDC transmission links in RES dominated systems are becoming crucially important because HVDC links based on PEs can be permanently damaged within microseconds. HVDC link modelling needs to be carefully designed and should consider more factors, such as temperature difference and sag, in terms of its overloading capability.
- For methodology optimisation:
  Future work should focus on optimising the methodology for the proposed consecutive power dispatch. The objective of this research was to provide the optimal combination to mitigate SFDs. Further research should consider elements such as wind turbine share in different groups, deloading level, penetration level of wind energy, wind speed, contingency size and wind farm profitability.
- A new market mechanism:

The implementation of ancillary service providers, such as wind energy, PV, battery energy storage system, to provide a fast frequency response is worth considering in a new commercial model. By defining an incentive mechanism, ancillary service providers are encouraged to provide fast frequency support. Not only can the frequency response market be more competitive but the frequency excursion can be also recovered by producing less carbon emissions.

- Collaboration between RESs and UFLS:

  Before applying the novel consecutive power dispatch in a wind farm, the influence of its performance within the rest of the system must be pre-accessed. The implementation of frequency control must not result in any consequent disturbance across the system. Potential collaboration between RESs and UFLS in relation to frequency support should also be explored.

References

[1] J. Wu, J. Yan, H. Jia, N. Hatziargyriou, N. Djilali, and H. Sun, “Integrated energy systems,” *Appl. Energy*, vol. 167, pp. 155–157, 2016, doi: 10.1016/j.apenergy.2016.02.075.

[2] OECD (2016), *World electricity generation by source of energy: Terawatt hours (TWh)*. Paris: OECD Publishing, 2016.

[3] European Commission, “The Road from Paris: assessing the implications of the Paris Agreement and accompanying the proposal for a Council decision on the signing, on behalf of the European Union, of the Paris agreement adopted under the United Nations Framework Convention on Cl,” *Commun. from Comm. to Eur. Parliam. Counc.*, vol. 110, no. final, pp. 1–10, 2016, [Online]. Available: https://eur-lex.europa.eu/legal-content/EN/TXT/?uri=CELEX:52016DC0110%0Ahttp://eur-lex.europa.eu/legal-content/EN/TXT/PDF/?uri=CELEX:52016DC0110&from=EN.

[4] H. Holttinen *et al.*, “Currents of change,” *IEEE Power Energy Mag.*, vol. 9, no. 6, pp. 47–59, 2011, doi: 10.1109/MPE.2011.942351.

[5] U.S. Energy Information Administration, “Nuclear Power and the Environment.” https://www.eia.gov/energyexplained/index.php?page=nuclear_environment#.W4lnIewtd_Y.mendeley (accessed Aug. 31, 2018).

[6] I. Pineda and W. Pierre Tardieu, “Annual combined onshore and offshore wind energy statistics,” 2018, doi: 10.1016/j.preghy.2016.08.046.

[7] S. Evans, “Analysis: UK renewables generate more electricity than fossil fuels for first time,” 2019. [Online]. Available: https://www.carbonbrief.org/analysis-uk-renewables-generate-more-electricity-than-fossil-fuels-for-first-time.

[8] L. Hu *et al.*, “Sliding mode extremum seeking control based on improved invasive weed optimization for MPPT in wind energy conversion system,” *Appl. Energy*, vol. 248, no. January, pp. 567–575, 2019, doi: 10.1016/j.apenergy.2019.04.073.

[9] M. L. Kubik, P. J. Coker, and J. F. Barlow, “Increasing thermal plant flexibility in a high renewables power system,” *Appl. Energy*, vol. 154, no. 2015, pp. 102–111, 2015, doi: 10.1016/j.apenergy.2015.04.063.

[10] J. J. Vidal-Amaro, P. A. Østergaard, and C. Sheinbaum-Pardo, “Optimal energy mix for transitioning from fossil fuels to renewable energy sources - The case of the Mexican electricity system,” *Appl. Energy*, vol. 150, pp. 80–96, 2015, doi: 10.1016/j.apenergy.2015.03.133.

[11] W. Zappa, M. Junginger, and M. van den Broek, “Is a 100% renewable European power system feasible by 2050?,” *Appl. Energy*, vol. 233–234, no. January 2018, pp. 1027–1050, 2019, doi: 10.1016/j.apenergy.2018.08.109.

[12] A. Malik and J. Ravishankar, “A hybrid control approach for regulating frequency through demand response,” *Appl. Energy*, vol. 210, no. April 2017, pp. 1347–1362, 2018, doi: 10.1016/j.apenergy.2017.08.160.

[13] P. Kundur, *Power System Stability and Control*. New York: Mc- Graw-Hill, 1994.

[14] B. Kroposki *et al.*, “Achieving a 100% Renewable Grid: Operating Electric Power Systems with Extremely High Levels of Variable Renewable Energy,” *IEEE Power Energy Mag.*, vol. 15, no. 2, pp. 819–826, 2017, doi: 10.1109/MPE.2016.2637122.

[15] Australian Energy Market Operator (AEMO), “Wind integration in electricity grids : International practice and experience,” no. October, pp. 1–50, 2011.

[16] S. C. Johnson, J. D. Rhodes, and M. E. Webber, “Understanding the impact of non-synchronous wind and solar generation on grid stability and identifying mitigation pathways,” *Appl. Energy*, vol. 262, no. January, p. 114492, 2020, doi: 10.1016/j.apenergy.2020.114492.

[17] M. F. M. Arani and E. F. El-Saadany, “Implementing virtual inertia in DFIG-

based wind power generation," *IEEE Trans. Power Syst.*, vol. 28, no. 2, pp. 1373–1384, 2013, doi: 10.1109/TPWRS.2012.2207972.

[18] National Gird, "Enhanced frequency control capability (EFCC)," 2014. Accessed: Dec. 13, 2018. [Online]. Available: https://www.nationalgrideso.com/innovation/projects/enhanced-frequency-control-capability-efcc.

[19] S. Azizi *et al.*, "Development and tests of new protection solutions when reaching 100 % PE penetration," *EU H2020 MIGRATE Proj. Deliv. 4.3*, 2018.

[20] N. Miller, D. Lew, and R. Piwko, "Technology capabilities for fast frequency response," 2017. [Online]. Available: https://www.aemo.com.au/-/media/Files/Electricity/NEM/Security_and_Reliability/Reports/2017/2017-03-10-GE-FFR-Advisory-Report-Final---2017-3-9.pdf.

[21] J. H. Eto, J. Undrill, C. Roberts, P. Mackin, and J. Ellis, "Frequency control requirements for reliable interconnection frequency response," no. February, pp. 1–116, 2018.

[22] Z. Zhuo, N. Zhang, C. Kang, R. Dong, and Y. Liu, "Optimal operation of hybrid AC/DC distribution network with high penetrated renewable energy," *IEEE Power Energy Soc. Gen. Meet.*, vol. 2018-Augus, pp. 0–4, 2018, doi: 10.1109/PESGM.2018.8585802.

[23] S. Temtem, K. Creighton, D. Cashman, and R. Skillen, "Summary of studies on rate of change of frequency events on the all-island system August 2012," no. August 2012, pp. 1–8, 2012.

[24] C. P. Steinmetz, "Power control and stability of electric generating stations," *Trans. Am. Inst. Electr. Eng.*, vol. 39, pp. 1215–1287, 1920, doi: 10.1109/T-AIEE.1920.4765322.

[25] P. Kundur *et al.*, "Definition and classification of power system stability," *IEEE Trans. Power Syst.*, vol. 19, no. 3, pp. 1387–1401, 2004, doi: 10.1109/tpwrs.2004.825981.

[26] N. Hatziargyriou, J. V. Milanović, and C. Rahmann, "Stability definitions and characterization of dynamic behavior in systems with high penetration of power

electronic interfaced technologies," 2020.

[27] P. Kundur, J. Paserba, and S. Vitet, "Overview on definition and classification of power system stability," *CIGRE/IEEE PES Int. Symp. Qual. Secur. Electr. Power Deliv. Syst. CIGRE/PES 2003*, pp. 1–4, 2003, doi: 10.1109/QSEPDS.2003.159786.

[28] P. Kundur *et al.*, "Definition and Classification of Power System Stability IEEE/CIGRE Joint Task Force on Stability Terms and Definitions," *IEEE Trans. Power Syst.*, vol. 19, no. 3, pp. 1387–1401, 2004, doi: 10.1109/TPWRS.2004.825981.

[29] U. Rudez and R. Mihalic, "WAMS-Based Underfrequency Load Shedding with Short-Term Frequency Prediction," *IEEE Trans. Power Deliv.*, vol. 31, no. 4, pp. 1912–1920, 2016, doi: 10.1109/TPWRD.2015.2503734.

[30] IEEE Power and Energy Society, "Dynamic Models for Turbine-Governors in Power System Studies," 2013. doi: PES-TR1.

[31] R. R. Londero, C. M. Affonso, J. P. A. Vieira, and U. H. Bezerra, "Impact of different DFIG wind turbines control modes on long-term voltage stability," *IEEE PES Innov. Smart Grid Technol. Conf. Eur.*, pp. 1–7, 2012, doi: 10.1109/ISGTEurope.2012.6465694.

[32] C. V. T. Van Cutsem, *Voltage stability*. .

[33] A. E. Leon and J. A. Solsona, "Sub-Synchronous Interaction Damping Control for DFIG Wind Turbines Andres," *IEEE Trans. Power Syst.*, vol. 30, no. 1, 2015, doi: 10.1021/acs.jpcb.5b02886.

[34] IEEE Committee Report, "Reader's guide to subsynchronous resonance," *IEEE Trans. Power Syst.*, vol. 7, no. 1, pp. 150–157, 1992.

[35] IEEE Subsynchronous Resonance Working Group of the System Dynamic Performance Subcommittee Power System Engineering Committee, "Terms, definitions and symbols for subsynchronous oscillations," *IEEE Power Eng. Rev.*, vol. PER-5, no. 6, p. 37, 1985, doi: 10.1002/9781118541555.wbiepc210.

[36] R. K. Varma, S. Auddy, and Y. Semsedini, "Mitigation of subsynchronous

resonance in a series-compensated wind farm using FACTS controllers," *IEEE Trans. Power Deliv.*, vol. 23, no. 3, pp. 1645–1654, 2008, doi: 10.1109/TPWRD.2008.917699.

[37] O. Dudurych and M. Conlon, "Impact of reduced system inertia as a result of higher penetration levels of wind generation," *Proc. Univ. Power Eng. Conf.*, 2014, doi: 10.1109/UPEC.2014.6934801.

[38] N. Shams, P. Wall, and V. Terzija, "Adaptive Under Frequency Load Shedding Scheme Based on Dynamic Security Assessment."

[39] Y. Tofis, S. Timotheou, and E. Kyriakides, "Minimal Load Shedding Using the Swing Equation," *IEEE Trans. Power Syst.*, vol. 32, no. 3, pp. 2466–2467, 2017, doi: 10.1109/TPWRS.2016.2614886.

[40] S. Liu, G. Li, and M. Zhou, "Power system transient stability analysis with integration of DFIGs based on center of inertia," *CSEE J. Power Energy Syst.*, vol. 2, no. 2, pp. 20–29, 2016, doi: 10.17775/CSEEJPES.2016.00018.

[41] D. Jones, S. Pasalic, M. Negnevitsky, and M. E. Haque, "Determining the frequency stability boundary of the Tasmanian system due to voltage disturbances," *2012 IEEE Int. Conf. Power Syst. Technol. POWERCON 2012*, 2012, doi: 10.1109/PowerCon.2012.6401272.

[42] P. Tielens and D. van Hertem, "Grid Inertia and Frequency Control in Power Systems with High Penetration of Renewables," *Status Publ.*, vol. 0, no. 2, pp. 1–6, 2012, [Online]. Available: https://lirias.kuleuven.be/handle/123456789/345286.

[43] P. M. Anderson and A. A. Fouad, *Power System Control and Stability*. 2008.

[44] Z. DIMITRIOS, "Power System Inertia Estimation and Frequency Response Assessment," KTH, 2019.

[45] Prabha Kundur and P. Kundur, *Power system stability and control*. 1994.

[46] N. Oliferovich, D. Hryniuk, and I. Orobei, "Harmonic Identification of Technological Objects in Real Time," *2016 Open Conf. Electr. Electron. Inf. Sci.*, no. Mi, pp. 1–4, 2016.

[47] P. Energy and F. S. Road, “Rate of change of frequency (RoCoF) review of TSO and generator submissions final report,” no. May 2013, 2013.

[48] G. Lalor, J. Ritchie, S. Rourke, D. Flynn, and M. J. O’Malley, “Dynamic frequency control with increasing wind generation,” in *2004 IEEE Power Engineering Society General Meeting*, 2004, vol. 2, no. July, pp. 1715–1720, doi: 10.1109/pes.2004.1373170.

[49] V. V Terzija and H.-J. Koglin, “Adaptive underfrequency load shedding integrated with a frequency estimation numerical algorithm,” *Gener. Transm. Distrib. IEE Proc.*, vol. 149, no. 6, pp. 713–718, 2002.

[50] V. V. Terzija, “Adaptive underfrequency load shedding based on the magnitude of the disturbance estimation,” *IEEE Trans. Power Syst.*, vol. 21, no. 3, pp. 1260–1266, 2006, doi: 10.1109/TPWRS.2006.879315.

[51] M. Karimi, P. Wall, H. Mokhlis, and V. Terzija, “A new centralized adaptive underfrequency load shedding controller for microgrids based on a distribution state estimator,” *IEEE Trans. Power Syst.*, vol. 32, no. 1, pp. 370–380, 2017.

[52] C. Li *et al.*, “Continuous under-frequency load shedding scheme for power system adaptive frequency control,” *IEEE Trans. Power Syst.*, vol. 35, no. 2, pp. 950–961, 2020.

[53] J. Zhao, Y. Tang, and V. Terzija, “Robust online estimation of power system center of inertia frequency,” *IEEE Trans. Power Syst.*, vol. 34, no. 1, pp. 821–825, 2019.

[54] J. Quirós-Tortós, P. Demetriou, M. Panteli, E. Kyriakides, and V. Terzija, “Intentional controlled islanding and risk assessment : A Uuified framework,” *IEEE Syst. J.*, vol. 12, no. 4, pp. 3637–3648, 2018.

[55] L. Ding, P. Wall, and V. Terzija, “Graph spectra based controlled islanding for low inertia power systems,” *IEEE Trans. Power Syst.*, vol. 32, no. 1, pp. 302–309, 2017, doi: 10.1109/TPWRD.2016.2582519.

[56] L. Ding, Y. Guo, P. Wall, K. Sun, S. Member, and V. Terzija, “Identifying the timing of controlled islanding using a controlling UEP based method,” *IEEE Trans. Power Syst.*, vol. 33, no. 6, pp. 5913–5922, 2018, doi:

10.1109/TPWRS.2018.2842709.

[57] L. Ding, F. M. Gonzalez-longatt, S. Member, P. Wall, V. Terzija, and S. Member, "Two-step spectral clustering controlled islanding algorithm," *IEEE Trans. Power Syst.*, vol. 28, no. 1, pp. 75–84, 2013.

[58] T. Ackermann, *Wind Power in Power Systems*. 2012.

[59] P. Shen, L. Guan, Z. Huang, L. Wu, and Z. Jiang, "Active-current control of large-scale wind turbines for power system transient stability improvement based on perturbation estimation approach," *Energies*, vol. 11, no. 8, 2018, doi: 10.3390/en11081995.

[60] J. Lee, E. Muljadi, P. Sørensen, and Y. C. Kang, "Releasable kinetic energy-based inertial control of a DFIG wind power plant," *IEEE Trans. Sustain. Energy*, vol. 7, no. 1, pp. 279–288, 2016, doi: 10.1109/TSTE.2015.2493165.

[61] M. A. Rodr, J. Lo, L. Marroyo, and E. Engineers, "Introduction to a wind energy generation system," in *Doubly Fed Induction Machine: Modeling and Control for Wind Energy Generation*, 2011, pp. 1–85.

[62] T. Lei, "Doubly-Fed Induction Generator Wind Turbine Modelling , Control and Reliability," 2014.

[63] S. Heier, *Grid Integration of Wind Energy*. 2014.

[64] J. M. Kennedy, B. Fox, T. Littler, and D. Flynn, "Validation of fixed speed induction generator models for inertial response using wind farm measurements," *IEEE Trans. Power Syst.*, vol. 26, no. 3, pp. 1454–1461, 2011, doi: 10.1109/TPWRS.2010.2081385.

[65] D. Palejiya and D. Chen, "Performance improvements of switching control for wind turbines," *IEEE Trans. Sustain. Energy*, vol. 7, no. 2, pp. 526–534, 2016, doi: 10.1109/TSTE.2015.2502262.

[66] T. Ackermann, *Wind Power in Power Systems*, vol. 8. 2005.

[67] Z. Chen, J. M. Guerrero, F. Blaabjerg, and S. Member, "A Review of the State of the Art of Power Electronics for Wind Turbines," *IEEE Trans. Power Electron.*, vol. 24, no. 8, pp. 1859–1875, 2009, doi:

10.1109/TPEL.2009.2017082.

[68] R. J. Ye, H. Li, Z. Chen, and Q. Gao, “Comparison of transient behaviors of wind turbines with DFIG considering the shaft flexible models,” *Proc. 11th Int. Conf. Electr. Mach. Syst. ICEMS 2008*, pp. 2585–2590, 2008.

[69] S. Ghosh and N. Senroy, “Electromechanical dynamics of controlled variable-speed wind turbines,” *IEEE Syst. J.*, vol. 9, no. 2, pp. 639–646, 2015, doi: 10.1109/JSYST.2013.2280037.

[70] M. A. Rodr, J. Lo, L. Marroyo, and E. Engineers, “Steady State of the Doubly Fed Induction Machine,” in *Doubly Fed Induction Machine: Modeling and Control for Wind Energy Generation*, 2011, pp. 209–239.

[71] L. Shuhui and T. A. Haskew, “Analysis of decoupled d-q vector control in DFIG back-to-back PWM converter,” *2007 IEEE Power Eng. Soc. Gen. Meet. PES*, pp. 1–7, 2007, doi: 10.1109/PES.2007.385461.

[72] L. M. Fernandez, C. A. Garcia, and F. Jurado, “Comparative study on the performance of control systems for doubly fed induction generator (DFIG) wind turbines operating with power regulation,” vol. 33, pp. 1438–1452, 2008, doi: 10.1016/j.energy.2008.05.006.

[73] T. R. Ricciardi, D. Salles, W. Freitas, and X. Wang, “Dynamic modeling of inverter-based distributed generators with voltage positive feedback anti-islanding protection,” *2010 IREP Symp. - Bulk Power Syst. Dyn. Control - VIII, IREP2010*, 2010, doi: 10.1109/IREP.2010.5563283.

[74] S. Paladhi and S. Ashok, “Solid state transformer application in wind based DG system,” *2015 IEEE Int. Conf. Signal Process. Informatics, Commun. Energy Syst. SPICES 2015*, 2015, doi: 10.1109/SPICES.2015.7091563.

[75] G. Abed, J. Lopez, M. A. Rodriguez, L. Marroyo, and G. Iwanski, *Doubly Fed Induction Machine: Modeling and Control for Wind Energy Generation*. 2011.

[76] A. M. A. Haidar, K. M. Muttaqi, and M. T. Hagh, “A Coordinated Control Approach for DC link and Rotor Crowbars to Improve Fault Ride-Through of DFIG based Wind Turbines,” *IEEE Trans. Ind. Appl.*, vol. 9994, no. c, pp. 1–1, 2017, doi: 10.1109/TIA.2017.2686341.

[77] G. Pannell, D. J. Atkinson, and B. Zahawi, “Minimum-threshold crowbar for a fault-ride-through grid-code-compliant DFIG wind turbine,” *IEEE Trans. Energy Convers.*, vol. 25, no. 3, pp. 750–759, 2010, doi: 10.1109/TEC.2010.2046492.

[78] J. B. Ekanayake, L. Holdsworth, and N. Jenkins, “Dynamic modeling of doubly fed induction generator wind turbines,” *IEEE Trans. Power Syst.*, vol. 18, no. 2, pp. 803–809, 2003, doi: 10.1109/TPWRS.2003.811178.

[79] M. A. Rodr, J. Lo, L. Marroyo, and E. Engineers, “Dynamic Modeling of the Doubly Fed Induction Machine,” in *Doubly Fed Induction Machine: Modeling and Control for Wind Energy Generation*, 2011, pp. 209–239.

[80] N. W. Miller and J. J. Sanchez-gasca, “Modeling of GE Wind Turbine-Generators for Grid Studies,” 2010.

[81] R. Azizipanah-abarghooee, “Wide - Area Monitoring based Smart Frequency Control in Future Low - Variable Inertia Systems with CCGT / Wind / PV / BES / Load,” University of Manchester, 2018.

[82] Y. Fu, X. Zhang, Y. Hei, and H. Wang, “Active participation of variable speed wind turbine in inertial and primary frequency regulations,” *Electr. Power Syst. Res.*, vol. 147, pp. 174–184, 2017, doi: 10.1016/j.epsr.2017.03.001.

[83] Z. Wu *et al.*, “Improved inertial control for permanent magnet synchronous generator wind turbine generators,” *IET Renew. Power Gener.*, vol. 10, no. 9, pp. 1366–1373, 2016, doi: 10.1049/iet-rpg.2016.0125.

[84] S. El Itani, U. D. Annakkage, and G. Joos, “Short-term frequency support utilizing inertial response of DFIG wind turbines,” *IEEE Power Energy Soc. Gen. Meet.*, pp. 1–8, 2011, doi: 10.1109/PES.2011.6038914.

[85] M. Yin, Z. Yang, Y. Xu, J. Liu, L. Zhou, and Y. Zou, “Aerodynamic optimization for variable-speed wind turbines based on wind energy capture efficiency,” *Appl. Energy*, vol. 221, no. November 2017, pp. 508–521, 2018, doi: 10.1016/j.apenergy.2018.03.078.

[86] L. G. González, E. Figueres, G. Garcerá, and O. Carranza, “Maximum-power-point tracking with reduced mechanical stress applied to wind-energy-

conversion-systems," *Appl. Energy*, vol. 87, no. 7, pp. 2304–2312, 2010, doi: 10.1016/j.apenergy.2009.11.030.

[87] H. Fathabadi, "Novel high-efficient unified maximum power point tracking controller for hybrid fuel cell/wind systems," *Appl. Energy*, vol. 183, pp. 1498–1510, 2016, doi: 10.1016/j.apenergy.2016.09.114.

[88] D. Song, X. Fan, J. Yang, A. Liu, S. Chen, and Y. H. Joo, "Power extraction efficiency optimization of horizontal-axis wind turbines through optimizing control parameters of yaw control systems using an intelligent method," *Appl. Energy*, vol. 224, no. January, pp. 267–279, 2018, doi: 10.1016/j.apenergy.2018.04.114.

[89] M. Dreidy, H. Mokhlis, and S. Mekhilef, "Inertia response and frequency control techniques for renewable energy sources: A review," *Renew. Sustain. Energy Rev.*, vol. 69, no. July 2016, pp. 144–155, 2017, doi: 10.1016/j.rser.2016.11.170.

[90] R. Eriksson, N. Modig, and K. Elkington, "Synthetic inertia versus fast frequency response: a definition," *IET Renew. Power Gener.*, vol. 12, pp. 507–514, 2017, doi: 10.1049/iet-rpg.2017.0370.

[91] F. Gonzalez-Longatt, "Impact of synthetic inertia from wind power on the protection / control schemes of future power systems : Simulation study," *11th IET Int. Conf. Dev. Power Syst. Prot. (DPSP 2012)*, 2012.

[92] F. Gonzalez-Longatt, E. Chikuni, and E. Rashayi, "Effects of the Synthetic Inertia from wind power on the total system inertia after a frequency disturbance," *Proc. IEEE Int. Conf. Ind. Technol.*, no. July, pp. 826–832, 2013, doi: 10.1109/ICIT.2013.6505779.

[93] D. Pudjianto, D. Pudjianto, C. Ramsay, C. Ramsay, G. Strbac, and G. Strbac, "Frequency support from doubly fed induction generator wind turbines," *Renew. Power Gener. IET*, vol. 1, no. 1, pp. 10–16, 2007, doi: 10.1049/iet-rpg.

[94] H. Dharmawardena, K. Uhlen, and S. S. Gjerde, "Modelling wind farm with synthetic inertia for power system dynamic studies," *2016 IEEE Int. Energy Conf.*, no. 2, pp. 1–6, 2016, doi: 10.1109/ENERGYCON.2016.7514098.

[95] Z. Wang and W. Wu, “Coordinated Control Method for DFIG-Based Wind Farm to Provide Primary Frequency Regulation Service,” *IEEE Trans. Power Syst.*, vol. 33, no. 3, pp. 1–1, 2017, doi: 10.1109/TPWRS.2017.2755685.

[96] J. Morren, S. W. H. de Haan, W. L. Kling, and J. A. Ferreira, “Wind turbines emulating inertia and supporting primary frequency control,” *IEEE Trans. Power Syst.*, vol. 21, no. 1, pp. 433–434, 2006, doi: 10.1109/TPWRS.2005.861956.

[97] C. Rahmann, J. Jara, and M. B. C. Salles, “Effects of inertia emulation in modern wind parks on isolated power systems,” *IEEE Power Energy Soc. Gen. Meet.*, vol. 2015-Septe, pp. 1–5, 2015, doi: 10.1109/PESGM.2015.7285749.

[98] H. T. Nguyen, G. Yang, A. H. Nielsen, and P. H. Jensen, “Frequency stability enhancement for low inertia systems using synthetic inertia of wind power,” pp. 2–5, 2017.

[99] V. Terzija and M. Djuric, “Direct estimation of voltage phasor, frequency and its rate of change using Newton’s iterative method,” *Int. J. Electr. Power Energy Syst.*, vol. 16, no. 6, pp. 423–428, 1994, doi: 10.1016/0142-0615(94)90030-2.

[100] M. B. Djurić and V. V. Terzija, “An algorithm for frequency relaying based on the Newton-Raphson method,” *Electr. Power Syst. Res.*, vol. 31, no. 2, pp. 119–124, 1994, doi: 10.1016/0378-7796(94)90089-2.

[101] V. Terzija, M. B. Djurić, and N. Ž. Jeremić, “A recursive Newton type algorithm for digital frequency relaying,” *Electr. Power Syst. Res.*, vol. 36, no. 1, pp. 67–72, 1996.

[102] V. V. Terzija, M. B. Djuric, and B. D. Kovacevic, “Voltage phasor and local system frequency estimation using newton type algorithm,” *IEEE Trans. Power Deliv.*, vol. 9, no. 3, pp. 1368–1374, 1994, doi: 10.1109/61.311162.

[103] V. V. Terzija, “Improved recursive Newton-type algorithm for frequency and spectra estimation in power systems,” *IEEE Trans. Instrum. Meas.*, vol. 52, no. 5, pp. 1654–1659, 2003, doi: 10.1109/TIM.2003.817152.

[104] G. Rietveld, P. S. Wright, and A. J. Roscoe, “Reliable Rate-of-Change-of-

Frequency Measurements: Use Cases and Test Conditions," *IEEE Trans. Instrum. Meas.*, vol. 69, no. 9, pp. 6657–6666, 2020, doi: 10.1109/TIM.2020.2986069.

[105] ENTSO-E, "Frequency Measurement Requirements and Usage," no. January, Final Version 7, pp. 1–11, 2018.

[106] European commission, "Commission Regulation (EU) 2016/631 Establishing a network code on requirements for grid connection of generators," *Off. J. Eur. Union*, no. 14 April 2016, p. 68, 2016, doi: 10.1017/CBO9781107415324.004.

[107] Z.-S. Zhang, Y.-Z. Sun, J. Lin, and G.-J. Li, "Coordinated frequency regulation by doubly fed induction generator-based wind power plants," *IET Renew. Power Gener.*, vol. 6, no. 1, p. 38, 2012, doi: 10.1049/iet-rpg.2010.0208.

[108] Y. Tan, S. Member, L. Meegahapola, K. M. Muttaqi, and S. Member, "A suboptimal power-point-tracking-based primary frequency response strategy for DFIGs in hybrid remote area power supply systems," *IEEE Trans. Energy Convers.*, vol. 31, no. 1, pp. 1–13, 2015, doi: 10.1109/TEC.2015.2476827.

[109] F. Díaz-González, M. Hau, A. Sumper, and O. Gomis-Bellmunt, "Participation of wind power plants in system frequency control: Review of grid code requirements and control methods," *Renew. Sustain. Energy Rev.*, vol. 34, pp. 551–564, 2014, doi: 10.1016/j.rser.2014.03.040.

[110] Y. Sun, Z. Zhang, G. Li, and J. Lin, "Review on frequency control of power systems with wind power penetration," *2010 Int. Conf. Power Syst. Technol.*, pp. 1–8, 2010, doi: 10.1109/POWERCON.2010.5666151.

[111] G. Verbiˇ, S. Member, and D. J. Hill, "Frequency support from wind turbine generators with a time-variable droop characteristic," *IEEE Trans. Sustain. ENERGY*, vol. 9, no. 2, pp. 676–684, 2018.

[112] J. Van de Vyver, J. D. M. M. De Kooning, B. Meersman, L. Vandevelde, and T. L. Vandoorn, "Droop control as an alternative inertial response strategy for the synthetic inertia on wind turbines," *IEEE Trans. Power Syst.*, vol. 31, no. 2, pp. 1129–1138, 2016, doi: 10.1109/TPWRS.2015.2417758.

[113] J. F. Conroy and R. Watson, "Frequency response capability of full converter

wind turbine generators in comparison to conventional generation," *IEEE Trans. Power Syst.*, vol. 23, no. 2, pp. 649–656, 2008, doi: 10.1109/TPWRS.2008.920197.

[114] Y. Zhang and B. T. Ooi, "Stand-Alone doubly-fed induction generators (DFIGs) with autonomous frequency control," *IEEE Trans. Power Deliv.*, vol. 28, no. 2, pp. 752–760, 2013, doi: 10.1109/TPWRD.2013.2243170.

[115] M. Hwang, E. Muljadi, J.-W. Park, P. Sørensen, and Y. C. Kang, "Dynamic droop–based inertial control of a doubly-fed induction generator," *IEEE Trans. Sustain. ENERGY*, vol. 7, no. 6, pp. 2971–2979, 2016.

[116] M. Hwang, E. Muljadi, G. Jang, and Y. C. Kang, "Disturbance-adaptive short-term frequency support of a DFIG associated with the variable gain based on the RoCoF and rotor speed," *IEEE Trans. Power Syst.*, vol. 32, no. 3, pp. 1873–1881, 2017, doi: 10.1109/TPWRS.2016.2592535.

[117] F. Wilches-Bernal, J. H. Chow, and J. J. Sanchez-Gasca, "A fundamental study of applying wind turbines for power system frequency control," *IEEE Trans. Power Syst.*, vol. 31, no. 2, pp. 1496–1505, 2016, doi: 10.1109/TPWRS.2015.2433932.

[118] X. Zhang, X. Zha, S. Yue, and Y. Chen, "A frequency regulation strategy for wind power based on limited over-speed de-loading curve partitioning," *IEEE Access*, vol. 6, pp. 22938–22951, 2018, doi: 10.1109/ACCESS.2018.2825363.

[119] L. Miao, J. Wen, H. Xie, C. Yue, and W. J. Lee, "Coordinated Control Strategy of Wind Turbine Generator and Energy Storage Equipment for Frequency Support," *IEEE Trans. Ind. Appl.*, vol. 51, no. 4, pp. 2732–2742, 2015, doi: 10.1109/TIA.2015.2394435.

[120] M. Kang, J. Lee, K. Hur, S. H. Park, Y. Choy, and Y. C. Kang, "Stepwise inertial control of a doubly-fed induction generator to prevent a second frequency dip," *J. Electr. Eng. Technol.*, vol. 10, no. 6, pp. 2221–2227, 2015, doi: 10.5370/JEET.2015.10.6.2221.

[121] G. C. Tarnowski, P. C. Kjær, P. E. Sørensen, and J. Østergaard, "Variable speed wind turbines capability for temporary over-production," *2009 IEEE Power*

Energy Soc. Gen. Meet. PES '09, pp. 1–7, 2009, doi: 10.1109/PES.2009.5275387.

[122] G. C. Tarnowski, P. C. Kjær, P. E. Sørensen, and J. Østergaard, "Variable speed wind turbines capability for frequency response," *EWEC 2009 Sci. Proc.*, pp. 190–193, 2009.

[123] N. Miller, D. Lew, and R. Piwko, "Technology capabilities for fast frequency response.," Schenectady, NY, 2017.

[124] D. Y. Hong, T. Y. Ji, M. S. Li, and Q. H. Wu, "Ultra-short-term forecast of wind speed and wind power based on morphological high frequency filter and double similarity search algorithm," *Int. J. Electr. Power Energy Syst.*, vol. 104, no. July 2018, pp. 868–879, 2019, doi: 10.1016/j.ijepes.2018.07.061.

[125] L. Li *et al.*, "An adaptive time-resolution method for ultra-short-term wind power prediction," *Int. J. Electr. Power Energy Syst.*, vol. 118, no. December 2019, p. 105814, 2020, doi: 10.1016/j.ijepes.2019.105814.

[126] Z. Lin, X. Liu, and M. Collu, "Wind power prediction based on high-frequency SCADA data along with isolation forest and deep learning neural networks," *Int. J. Electr. Power Energy Syst.*, vol. 118, no. January, p. 105835, 2020, doi: 10.1016/j.ijepes.2020.105835.

[127] M. De Prada Gil, O. Gomis-Bellmunt, and A. Sumper, "Technical and economic assessment of offshore wind power plants based on variable frequency operation of clusters with a single power converter," *Appl. Energy*, vol. 125, pp. 218–229, 2014, doi: 10.1016/j.apenergy.2014.03.031.

[128] X. Gao *et al.*, "Investigation and validation of 3D wake model for horizontal-axis wind turbines based on filed measurements," *Appl. Energy*, vol. 260, no. November 2019, 2020, doi: 10.1016/j.apenergy.2019.114272.

[129] N. O. Katic, I., Hojstrup, J., Jensen, "A simple model for cluster efficiency," in *European wind energy association*, 1986, no. October, pp. 407–410.

[130] S. Grassi, S. Junghans, and M. Raubal, "Assessment of the wake effect on the energy production of onshore wind farms using GIS," *Appl. Energy*, vol. 136, pp. 827–837, 2014, doi: 10.1016/j.apenergy.2014.05.066.

[131] A. Abraham and J. Hong, "Dynamic wake modulation induced by utility-scale wind turbine operation," *Appl. Energy*, vol. 257, no. September 2019, p. 114003, 2020, doi: 10.1016/j.apenergy.2019.114003.

[132] X. Gao *et al.*, "Investigation of wind turbine performance coupling wake and topography effects based on LiDAR measurements and SCADA data," *Appl. Energy*, vol. 255, no. June, p. 113816, 2019, doi: 10.1016/j.apenergy.2019.113816.

[133] R. Brogna, J. Feng, J. N. Sørensen, W. Z. Shen, and F. Porté-Agel, "A new wake model and comparison of eight algorithms for layout optimization of wind farms in complex terrain," *Appl. Energy*, vol. 259, no. November 2019, p. 114189, 2019, doi: 10.1016/j.apenergy.2019.114189.

[134] J. Xu *et al.*, "Demand side industrial load control for local utilization of wind power in isolated grids," *Appl. Energy*, vol. 243, no. March, pp. 47–56, 2019, doi: 10.1016/j.apenergy.2019.03.039.

[135] F. González-Longatt, P. P. Wall, and V. Terzija, "Wake effect in wind farm performance: Steady-state and dynamic behavior," *Renew. Energy*, vol. 39, no. 1, pp. 329–338, 2012, doi: 10.1016/j.renene.2011.08.053.

[136] J. Lee, G. Jang, E. Muljadi, F. Blaabjerg, Z. Chen, and Y. Cheol Kang, "Stable short-term frequency support using adaptive gains for a DFIG-based wind power plant," *IEEE Trans. Energy Convers.*, vol. 31, no. 3, pp. 1068–1179, 2016, doi: 10.1109/TEC.2016.2532366.

[137] K. V. Vidyanandan and N. Senroy, "Primary frequency regulation by deloaded wind turbines using variable droop," *IEEE Trans. Power Syst.*, vol. 28, no. 2, pp. 837–846, 2013, doi: 10.1109/TPWRS.2012.2208233.

[138] Y. Jin, P. Ju, C. Rehtanz, F. Wu, and X. Pan, "Equivalent modeling of wind energy conversion considering overall effect of pitch angle controllers in wind farm," *Appl. Energy*, vol. 222, no. September 2017, pp. 485–496, 2018, doi: 10.1016/j.apenergy.2018.03.180.

[139] Y. L. Xu, Y. X. Peng, and S. Zhan, "Optimal blade pitch function and control device for high-solidity straight-bladed vertical axis wind turbines," *Appl.*

Energy, vol. 242, no. November 2018, pp. 1613–1625, 2019, doi: 10.1016/j.apenergy.2019.03.151.

[140] R. G. de Almeida, E. D. Castronuovo, and J. A. Peças Lopes, "Optimum generation control in wind parks when carrying out system operator requests," *IEEE Trans. Power Syst.*, vol. 21, no. 2, pp. 718–725, 2006, doi: 10.1109/TPWRS.2005.861996.

[141] X. Yuan and Y. Li, "Control of variable pitch and variable speed direct-drive wind turbines in weak grid systems with active power balance," *IET Renew. Power Gener.*, vol. 8, no. 2, pp. 119–131, 2014, doi: 10.1049/iet-rpg.2012.0212.

[142] K. A. Naik and C. P. Gupta, "Fuzzy logic based pitch angle controller for SCIG based wind energy system," in *2017 Recent Developments in Control, Auto mation & Power Engineering*, vol. 3, pp. 1–6.

[143] E. Barklund, N. Pogaku, M. Prodanovic, C. Hernandez-Aramburo, and T. C. Green, "Energy management in autonomous microgrid using stability-constrained droop control of inverters," *IEEE Trans. Power Electron.*, vol. 23, no. 5, pp. 2346–2352, 2008, doi: 10.1109/TPEL.2008.2001910.

[144] I. D. Margaris, S. A. Papathanassiou, N. D. Hatziargyriou, A. D. Hansen, and P. Sorensen, "Frequency control in autonomous power systems with high wind power penetration," *IEEE Trans. Sustain. Energy*, vol. 3, no. 2, pp. 189–199, 2012, doi: 10.1109/TSTE.2011.2174660.

[145] H. Luo, Z. Hu, H. Zhang, and H. Chen, "Coordinated Active Power Control Strategy for Deloaded Wind Turbines to Improve Regulation Performance in AGC," *IEEE Trans. Power Syst.*, vol. PP, no. c, p. 1, 2018, doi: 10.1109/TPWRS.2018.2867232.

[146] M. F. M. Arani and Y. A. R. I. Mohamed, "Analysis and mitigation of undesirable impacts of implementing frequency support controllers in wind power generation," *IEEE Trans. Energy Convers.*, vol. 31, no. 1, pp. 174–186, 2016, doi: 10.1109/TEC.2015.2484380.

[147] S. De Rijcke, P. Tielens, B. Rawn, D. Van Hertem, and J. Driesen, "Trading energy yield for frequency regulation: optimal control of kinetic energy in wind

farms," *IEEE Trans. Power Syst.*, vol. 30, no. 5, pp. 2469–2478, 2015, doi: 10.1109/TPWRS.2014.2357684.

[148] Y. Fu, Y. Wang, and X. Zhang, "Integrated wind turbine controller with virtual inertia and primary frequency responses for grid dynamic frequency support," *IET Renew. Power Gener.*, vol. 11, no. 8, pp. 1129–1137, 2017, doi: 10.1049/iet-rpg.2016.0465.

[149] M. F. M. Arani and Y. A.-R. I. Mohamed, "Dynamic Droop Control for Wind Turbines Participating in Primary Frequency Regulation in Microgrids," *IEEE Trans. Smart Grid*, vol. 9, no. 6, pp. 1–1, 2017, doi: 10.1109/TSG.2017.2696339.

[150] R. Azizipanah-abarghooee, M. Malekpour, F. Blaabjerg, and V. Terzija, "A linear inertial response emulation for variable speed wind turbines," *IEEE Trans. Power Syst.*, vol. 35, no. 2, pp. 1198–1208, 2020.

[151] M. Kang, J. Lee, and Y. C. Kang, "Modified stepwise inertial control using the mechanical input and electrical output curves of a doubly fed induction generator," *9th Int. Conf. Power Electron. - ECCE Asia "Green World with Power Electron. ICPE 2015-ECCE Asia*, pp. 357–361, 2015, doi: 10.1109/ICPE.2015.7167810.

[152] W. Bao, L. Ding, S. Yin, K. Wang, and V. Terzija, "Active rotor speed protection for DFIG synthetic inertia control," *IET Conf. Publ.*, vol. 2016, no. CP711, pp. 1–5, 2016.

[153] Z. Liu, L. Ding, K. Wang, Z. Ma, W. Bao, and Q. Liu, "Control strategy to mitigate secondary frequency dips for DFIG with virtual inertial control," *China Int. Conf. Electr. Distrib. CICED*, vol. 2016-Septe, no. Ciced, pp. 10–13, 2016, doi: 10.1109/CICED.2016.7576211.

[154] K. Liu, Y. Qu, H. M. Kim, and H. Song, "Avoiding frequency second dip in power unreserved control during wind power rotational speed recovery," *IEEE Trans. Power Syst.*, vol. 33, no. 3, pp. 3097–3106, 2018, doi: 10.1109/TPWRS.2017.2761897.

[155] M. Kang, K. Kim, E. Muljadi, J. W. Park, and Y. C. Kang, "Frequency control

support of a doubly-fed induction generator based on the torque limit," *IEEE Trans. Power Syst.*, vol. 31, no. 6, pp. 4575–4583, 2016, doi: 10.1109/TPWRS.2015.2514240.

[156] M. Kang, E. Muljadi, K. Hur, and Y. C. Kang, "Stable adaptive inertial control of a doubly-fed induction generator," *IEEE Trans. Smart Grid*, vol. 7, no. 6, pp. 2971–2979, 2016, doi: 10.1109/TSG.2016.2559506.

[157] K. Sun *et al.*, "Frequency secure control strategy for power grid with large-scale wind farms through HVDC links," *Int. J. Electr. Power Energy Syst.*, vol. 117, no. November 2019, p. 105706, 2020, doi: 10.1016/j.ijepes.2019.105706.

[158] W. Bao *et al.*, "Analytically derived fixed termination time for stepwise inertial control of wind turbines Part I: Analytical derivation," *Int. J. Electr. Power Energy Syst.*, vol. 121, no. April 2020, p. 106120, 2020, doi: 10.1016/j.ijepes.2020.106120.

[159] Y. Guo *et al.*, "Analytically derived fixed termination time for stepwise inertial control of wind turbines—Part II: Application strategy," *Int. J. Electr. Power Energy Syst.*, vol. 121, no. April 2020, p. 106106, 2020, doi: 10.1016/j.ijepes.2020.106106.

[160] G. Lalor, A. Mullane, and M. O'Malley, "Frequency control and wind turbine technologies," *IEEE Trans. Power Syst.*, vol. 20, no. 4, pp. 1905–1913, 2005, doi: 10.1109/TPWRS.2005.857393.

[161] Q. Xu *et al.*, "A short-term wind power forecasting approach with adjustment of numerical weather prediction input by data mining," *IEEE Trans. Sustain. Energy*, vol. 6, no. 4, pp. 1283–1291, 2015, doi: 10.1109/TSTE.2015.2429586.

[162] A. Kusiak, Z. Zhang, and A. D. Description, "Short-Horizon Prediction of Wind Power : A Data-Driven Approach," vol. 25, no. 4, pp. 1112–1122, 2010.

[163] R. Ak, O. Fink, and E. Zio, "Two Machine Learning Approaches for Short-Term Wind Speed Time-Series Prediction," *IEEE Trans. Neural Networks Learn. Syst.*, vol. 27, no. 8, pp. 1734–1747, 2016, doi: 10.1109/TNNLS.2015.2418739.

[164] M. Khalid and A. V. Savkin, "A method for short-term wind power prediction

with multiple observation points," *IEEE Trans. Power Syst.*, vol. 27, no. 2, pp. 579–586, 2012, doi: 10.1109/TPWRS.2011.2160295.

[165] R. G. de Almeida and J. a P. Lopes, "Participation of doubly fed induction wind generators in system frequency regulation," *Power Syst. IEEE Trans.*, vol. 22, no. 3, pp. 944–950, 2007, doi: 10.1109/TPWRS.2007.901096.

[166] J. Madsen, M. Findrik, T. Madsen, and H. P. Schwefel, "Optimizing Data Access for Wind Farm Control over Hierarchical Communication Networks," *Int. J. Distrib. Sens. Networks*, 2016, doi: 10.1155/2016/5936235.

[167] N. A. Janssens, G. Lambin, and N. Bragard, "Active power control strategies of DFIG wind turbines," *2007 IEEE Lausanne POWERTECH, Proc.*, no. July, pp. 516–521, 2007, doi: 10.1109/PCT.2007.4538370.

[168] Y. Cheng and V. Terzija, "A consecutive power dispatch in wind power plants to mitigate secondary frequency dips," *IEEE Trans. Sustain. Energy*, vol. Submitted.

[169] V. Terzija *et al.*, "Wide-area monitoring, protection, and control of future electric power networks," *Proc. IEEE*, vol. 99, no. 1, pp. 80–93, 2011, doi: 10.1109/JPROC.2010.2060450.

[170] V. Madani *et al.*, "IEEE PSRC report on global industry experiences with System Integrity Protection Schemes (SIPS)," *IEEE Trans. Power Deliv.*, vol. 25, no. 4, pp. 2143–2155, 2010, doi: 10.1109/TPWRD.2010.2046917.

[171] V. Madani and M. Adamiak, "Application Considerations in System Integrity Protection Schemes (SIPS)," pp. 25–30.

[172] C. Yuhang, "Synchronized Measurement Technology Supported Operational Tripping Schemes," University of Manchester, 2015.

[173] S. Horowitz, D. Novosel, V. Madani, and M. Adamiak, "Adaptive Protection," *Power and Energy Magazine, IEEE*, no. October, pp. 34–42, 2008.

[174] "8 Countries that Produce the Most Wind Energy in the World | REVE." https://www.evwind.es/2016/06/23/8-countries-that-produce-the-most-wind-energy-in-the-world/56665 (accessed Aug. 01, 2018).

[175] T. Amraee, M. Ghaderi Darebaghi, A. Soroudi, and A. Keane, “Probabilistic Under Frequency Load Shedding Considering RoCoF relays of Distributed Generators,” *IEEE Trans. Power Syst.*, vol. 33, no. 4, pp. 3587–3598, 2017, doi: 10.1109/TPWRS.2017.2787861.

[176] D. Kim, Y. Moon, and H. Nam, “A New Simplified Doubly Fed Induction Generator Model for Transient Stability Studies,” vol. 30, no. 3, pp. 1030–1042, 2015.

[177] P. Alexander, J. Apple, A. Elneweihi, R. Haas, and G. W. Swift, *Power System Protection*. 2006.

[178] H. You, S. Member, V. Vittal, X. Wang, and S. Member, “Slow Coherency-Based Islanding,” vol. 19, no. 1, pp. 483–491, 2004.

[179] P. Wall and V. Terzija, “Simultaneous estimation of the time of disturbance and inertia in power systems,” *IEEE Trans. Power Deliv.*, vol. 29, no. 4, pp. 2018–2031, 2014, doi: 10.1109/TPWRD.2014.2306062.

[180] S. H. Horowitz and A. G. Phadke, *Power System Relaying*. 2008.

[181] D. A. Tziouvaras and D. Hou, “Out-of-step protection fundamentals and advancements,” *Annu. Conf. Prot. Relay Eng.*, pp. 282–307, 2004, doi: 10.1109/cpre.2004.238495.

[182] Work Package 4, “D4.2: Limitations of present power system AC protection schemes and SIPS technologies to properly operate in systems with high penetration of PE during faults in DC and AC systems,” 2017.

[183] “The Grid Code,” 2017.

[184] X. Yingcheng and T. Nengling, “Review of contribution to frequency control through variable speed wind turbine,” *Renew. Energy*, vol. 36, no. 6, pp. 1671–1677, 2011, doi: 10.1016/j.renene.2010.11.009.

Appendix A. List of Publication

Journal

1. Y. Cheng, R. Azizipanah-Abarghooee, S. Azizi, L. Ding, and V. Terzija, "Smart frequency control in low inertia energy systems based on frequency response techniques: A review," *Appl. Energy*, vol. 279, no. September, p. 115798, 2020, doi: 10.1016/j.apenergy.2020.115798. Accepted.
2. Y. Cheng and V. Terzija, "A consecutive power dispatch in wind power plants to mitigate secondary frequency dips," *IEEE Trans. Sustain. Energy*, Submitted.

Report

1. M. Villén, E. Martínez, S. Borroy, M. Popov, R. Dubey, Y. Cheng, et al., "D4.2: Limitations of present power system AC protection schemes and SIPS technologies to properly operate in systems with high penetration of PE during faults in DC and AC systems". *WP4.2, MIGRATE Project.*